Hot Stars in Globular Clusters

Der Naturwissenschaftlichen Fakultät I (Mathematik/Physik)
der Friedrich-Alexander Universität Erlangen-Nürnberg
als Habilitationsschrift

vorgelegt von
Dr. Sabine Moehler
aus
Bamberg

Contents

Abstract

Globular clusters are densely packed, gravitationally bound conglomerates of several thousand to more than one million stars. The fact that they are old and had only a short period of star formation in the beginning makes them an ideal laboratory to study the evolution of low-mass stars. In this work we concentrate on three types of hot stars observed in globular clusters: horizontal branch stars, UV bright stars, and white dwarfs. We start with an overview on the history of hot star research in globular clusters and briefly describe the analysis methods used in this thesis.

It has been found early on that the distribution of stars along the **horizontal branch** (HB) in globular clusters moves towards hotter temperatures as metallicity decreases. Colour-magnitude diagrams of many metal-poor globular clusters, however, show variations in their HB morphologies like blue tails (i.e. extensions towards hotter temperatures) and gaps, that are not expected from standard stellar evolution. We observed and analysed stars along the blue tails in the globular clusters M 15 and NGC 6752 to verify the various models that have been suggested to explain this unexpected behaviour:

The stars below the gap in M 15 are cooler than ≈20,000 K and best described by hot horizontal branch evolutionary tracks, although their surface gravities and masses are systematically lower than predicted by canonical HB models.

The situation is somewhat different for NGC 6752: The stars below the gap are hotter than ≈20,000 K and their atmospheric parameters and masses are well described by evolutionary tracks for extreme HB (EHB) stars. The cooler stars above the gap are hot HB stars similar to the stars *below the gap* in M 15. Like those they have lower surface gravities and masses than theoretically expected. All stars analysed in NGC 6752 are found to be helium deficient, indicative of gravitational settling of helium in their atmospheres.

A comparison with results for HB stars in other globular clusters shows that these puzzling results represent a common phenomenon: Stars with 11,500 K$\leq T_{\text{eff}} \leq$20,000 K show low gravities and masses, while hotter stars agree well with theoretical predictions in both regards. Stars cooler than 11,500 K have gravities and temperatures consistent with canonical HB evolution, but low masses. The comparison also reveals that most of the gaps seen along the horizontal branches are not visible in the distribution of physical parameters. The only two exceptions are a gap at about 20,000 K separating extreme HB stars from hot HB stars and a narrow gap at $T_{\text{eff}} \approx$10,000 K – 12,500 K. Thus the gaps seen along the HB's are in most cases due to statistical fluctuations.

Three possible scenarios to explain the distribution of atmospheric parameters (T_{eff}, $\log g$) and masses are discussed: *Helium mixing on the red giant branch* would produce low surface gravities for hot HB stars, but not for EHB stars. An increase in the *distances to globular clusters* would increase the masses of all stars within one cluster without changing their atmospheric parameters. *Radiative levitation of heavy elements* in the atmospheres of the HB stars would change the metallicities in these atmospheres and the low gravities would be artifacts from the metallicity mismatch between theoretical and observed stellar atmospheres.

NGC 6752 is a perfect test case for these scenarios: Its distance is undebated and the stars analysed in this cluster cover a large temperature range. While the atmospheric parameters of hot HB stars and EHB stars in all clusters studied so far are well described by helium-mixed tracks, the low masses obtained for the hot HB stars in NGC 6752 (in combination with the canonical EHB star masses and the undebated distance) argue against helium mixing as the only explanation. A closer look at the spectra of the hot HB stars in NGC 6752 reveals the presence of Mg II and Fe II lines, which indicate an iron enrichment by a factor 50 on average with respect to the cluster abundance whereas the magnesium abundances are consistent with the cluster metallicity. These abundances suggest that radiative levitation of heavy elements (like iron) plays a significant role in the atmospheres of hot HB stars. Using metal-rich model atmospheres for the analyses of these stars yields physical parameters that agree well with canonical evolution theory for 11,500 K$\leq T_{\text{eff}} \leq$15,500 K. Some discrepancy remains for the temperature range 15,500 K to 19,000 K, which may indicate changes in the abundance patterns in

this temperature range, that are not well described by our simple model atmospheres. The masses determined for HB stars cooler than about 11,500 K (which should be unaffected by diffusion) in the globular clusters M 92, NGC 6397, and NGC 288 strongly support the long distance scale for globular clusters. We thus verified for the first time that taking into account the effects of radiative levitation and using the long distance scale strongly reduces the discrepancy between canonical evolutionary theory and the atmospheric parameters and masses derived for hot HB stars.

Since the distribution of stars along the horizontal branch moves towards cooler temperatures as metallicity increases, hot horizontal branch stars are generally rare in metal-rich globular clusters. The observed UV excess of (metal-rich) elliptical galaxies, however, suggests that hot HB and/or EHB stars can also be produced at high metallicities. The discovery of such stars in several metal-rich globular clusters prompted us to study them spectroscopically:

The horizontal branches observed in the bulge globular clusters NGC 6388 and NGC 6441 show long blue tails and a puzzling slope towards brighter magnitudes for hotter stars. Several non-canonical evolutionary scenarios have been suggested to explain such behaviour. The results of our spectroscopic analyses are marginally inconsistent with the predictions of canonical evolutionary theory (which can explain neither the presence of so many hot stars in these clusters nor the sloped HB's), but disagree strongly with all non-canonical scenarios (that reproduce the sloped horizontal branches and yield many hot stars). This contradiction between photometric and spectroscopic properties of these hot HB stars cannot be solved with the currently available data.

Far-UV observations with the Ultraviolet Imaging Telescope (UIT) suggested the presence of hot stars in the globular clusters 47 Tuc and NGC 362, which so far have been known to contain primarily red HB stars. Spectroscopic analyses of these stars reveal, however, that most of the hot stars seen in NGC 362 are probably background stars belonging to the Small Magellanic Cloud. The parameters of those stars that are members of 47 Tuc and NGC 362 (3 stars in each cluster) agree well with canonical HB evolution. These stars are thus probably produced from red giants with unusually high mass loss, which is consistent with the small number of hot stars.

Turning towards the evolutionary stages after the horizontal branch we observed **UV-bright stars** discovered by UIT in globular clusters. Comparing their effective temperatures, surface gravities, and helium abundances to evolutionary tracks shows that none of the stars is a “true” post-AGB star. All stars lie along either post-EHB or post-early AGB evolutionary tracks. The post-early AGB stars have solar helium abundances, while the post-EHB stars are helium deficient, similar to their EHB progenitors. The lack of “true” post-AGB stars suggests that mass loss on the AGB may be higher than assumed in standard evolution (resulting in an early termination of the AGB phase). The slower evolution of post-early AGB stars could also explain the lack of planetary nebulae in globular clusters.

To get more information on the post-AGB phase of stellar evolution we determined abundances for two hot post-AGB stars, ROA 5701 (ω Cen) and Barnard 29 (M 13). Iron abundances derived from UV data together with abundances for He, C, N, O, and Si are compared to the abundances of other stars in these globular clusters. While the abundances of the light elements agree with those of the red giants in these clusters, the iron abundances are very low in both stars. This iron depletion could be explained by the condensation of iron onto dust grains in the AGB star's atmospheres, which were then removed from the atmosphere by a radiatively driven wind (gas-dust separation). No 3$^{\rm rd}$ dredge-up is necessary to explain the observed abundance patterns.

Finally we observed the very first spectra of stars along the **white dwarf** sequences in globular clusters, which turn out to be hydrogen-rich DA white dwarfs. Estimates of atmospheric parameters suggest that the brightest star analysed may be a luminous, low-mass helium-core white dwarf. The masses and absolute magnitudes of the stars are estimated by comparing their physical parameters to evolutionary calculations. We use the absolute magnitudes to derive distances to the globular cluster NGC 6397 and find that the assumption of a constant mass for all white dwarfs in NGC 6397 will yield incorrect distance values.

Glossary

Acronyms

AGB	Asymptotic Giant Branch
ANS	Astronomical Netherlands Satellite
BHB	Blue Horizontal Branch
BT	Blue Tail
CASPEC	CAssegrain echelle SPECtrograph
CCD	Charge Coupled Device
CMD	Colour-Magnitude Diagram
CSPN	Central Star of Planetary Nebula
EAGB	Early Asymptotic Giant Branch
EFOSC	Eso Faint Object Spectrograph and Camera
EHB	Extreme Horizontal Branch
EMMI	Eso Multi Mode Instrument
ESO	European Southern Observatory
FORS	FOcal Reducer/low resolution Spectrograph
FWHM	Full Width at Half Maximum
GHRS	Goddard High Resolution Spectrograph
HB	Horizontal Branch
HBA	Horizontal Branch A type (star)
HBB	Horizontal Branch B type (star)
HST	Hubble Space Telescope
HUT	Hopkins Ultraviolet Telescope
IRAS	InfraRed Astronomical Satellite
IUE	International Ultraviolet Explorer
LINFOR	LINe FORmation (program package)
LMC	Large Magellanic Cloud
LTE	Local Thermal Equilibrium
LWP	Long Wavelength Prime
LWR	Long Wavelength Reserve
MIDAS	Munich Image Data Analysis System
MS	Main Sequence
NLTE	Non-Local Thermal Equilibrium
NTT	New Technology Telescope
OAO	Orbiting Astronomical Observatory
PN	Planetary Nebula
STIS	Space Telescope Imaging Spectrograph
RGB	Red Giant Branch
sdB	subdwarf B (star)
sdOB	subdwarf OB (star)
sdO	subdwarf O (star)
SMC	Small Magellanic Cloud
SWP	Short Wavelength Prime
TAHB	Terminal-Age Horizontal Branch
UIT	Ultraviolet Imaging Telescope
UVBS	UV Bright Star
VLT	Very Large Telescope
WFPC2	Wide Field and Planetary Camera 2
ZAHB	Zero-Age Horizontal Branch

Symbols

χ_n	excitation energy of level n
ΔX_{mix}	difference in hydrogen abundance between envelope of a red giant and the innermost point reached by mixing currents
E_{B-V}	reddening
ε_{th}	thermal emission coefficient
ε_s	scattering emission coefficient
$\log \epsilon_{\mathrm{X}}$	(logarithmic) number abundance of the element X with $\log \epsilon_X = \log (X/H) + 12$
f	oscillator strength
$\log g$	(logarithmic) surface gravity
g_n	statistical weight of level n
i	angle between stellar rotation axis and line-of-sight
κ	absorption coefficient
L	stellar luminosity
$L_\odot$	solar luminosity
M	stellar mass
$\mathrm{M}_\odot$	solar mass
M_V	absolute V magnitude
$(m - M)_V$	apparent distance modulus in V
$(m - M)_0$	true distance modulus
[M/H]	metallicity, i.e. logarithmic abundance of metals relative to the solar abundance (metal meaning every element except H and He)
μ	molecular weight
ρ	matter density
σ	r.m.s. error
σ_{SB}	Stefan Boltzmann constant
T_{eff}	effective temperature
$v \sin i$	rotational velocity of a star as observed (i being the inclination angle)
$v_{\mathrm{rad,hel}}$	radial velocity corrected to heliocentric system
W_λ	equivalent width
ξ	microturbulent velocity
Y	helium abundance by mass
Y_{MS}	helium abundance by mass on the main sequence

Chapter 1

Historical Background

Readers unfamiliar with stellar evolution (Appendix A) or with the use of photometric observations in astronomy (Appendix B) may profit from reading the respective appendices before this chapter.

Globular clusters are the closest approximation to a physicist's laboratory in astronomy. They are densely packed, gravitationally bound systems of several thousands to about one million of stars. The dimensions of the globular clusters are small compared to their distance from us: half of the light is generally emitted within a radius of less than 10 pc, whereas the closest globular cluster has a distance of 2000 pc and 90% lie more than 5000 pc away. We can thus safely assume that all stars within a globular cluster lie at the same distance from us. With an age of more than 10^{10} years globular clusters are among the oldest objects in our Galaxy. Contrary to the field of the Galaxy stars in globular clusters formed only once in the beginning. Because the duration of that star formation episode is short compared to the current age of the globular clusters the stars within one globular cluster are essentially coeval. In addition all stars within one globular cluster show the same primordial abundance patterns (which may differ from one cluster to another).

As we know today that galactic globular clusters are old stellar systems people are often surprised by the presence of hot stars in these clusters. The following paragraphs will show that hot stars have been known to exist in globular clusters for quite some time:

About a century ago Barnard (1900) reported the detection of stars in globular clusters that were much brighter on (blue-sensitive) photographic plates than they appeared visually: *"Of course the simple explanation of this peculiarity is that these stars, so bright photographically and so faint visually, are shining with a much bluer light than the stars which make up the main body of the clusters."* .

In 1915 Shapley started a project to obtain colours and magnitudes of individual stars in globular and open clusters (Shapley 1915a) hoping that *"considerable advance can be made in our understanding of the internal arrangement and physical characteristics"* of these clusters. In the first globular cluster studied this way (M 3, Shapley 1915b) he found a double peaked distribution of colours, with a red maximum and a blue secondary peak. He noticed that – in contrast to what was known for field dwarf (i.e. main sequence) stars – the stars in M 3 became bluer as they became fainter. Ten Bruggencate (1927, p.130) used Shapley's data on M 3 and other clusters to plot magnitude versus colour (replacing luminosity and spectral type in the Hertzsprung-Russell diagram) and thus produced the first colour-magnitude diagrams[1] ("FARBENHELLIGKEITSDIAGRAMME"). In these colour-magnitude diagrams (CMD's) ten Bruggencate noted the presence of a red giant branch that became bluer towards fainter magnitudes, in agreement with Shapley (1915b). In addition, however, he saw a horizontal branch ("HORIZONTALER AST") that parted from the red giant branch and extended far to the blue at constant brightness.

---

[1] Shapley (1930, p.26, footnote) disliked the idea of plotting individual data points – he thought that the small number of measurements might lead to spurious results.

Greenstein (1939) produced a colour-magnitude diagram for M 4 (also noting the presence of a sequence of blue stars at constant brightness) and mentioned that *"the general appearance of the colour-magnitude diagram of M4 is almost completely different from that of any galactic* (i.e. open) *cluster."* He also noticed that – while hot main-sequence stars were completely missing – there existed a group of bright stars above the horizontal branch and on the blue side of the giant branch. Similar stars appeared also in the CMD's presented by Arp (1955).

As more CMD's of globular clusters were obtained it became obvious that the horizontal branch morphology varies quite considerably between individual clusters. The clusters observed by Arp (1955) exhibited extensions of the blue horizontal branch towards bluer colours and fainter visual magnitudes, i.e. towards hotter stars[2] (see Fig. 1). In some of Arp's CMD's (e.g. M 15, M 2) these **blue tails** are separated from the horizontal part by gaps at varying brightness (see also Fig. 5). A more detailed discussion of these features can be found in Chapter 3.

About 25 years after their discovery first ideas about the nature of the horizontal branch stars began to emerge: Hoyle & Schwarzschild (1955) were the first to identify the horizontal branch stars with post-red giant branch stars that burn helium in the central regions of their cores.

Sandage & Wallerstein (1960) noted a correlation between the metal abundance and the horizontal branch (HB) morphology seen in globular cluster CMD's: the horizontal branch became bluer with decreasing metallicity. Faulkner (1966) managed for the first time to compute zero age horizontal branch (ZAHB) models that qualitatively reproduced this trend of HB morphology with metallicity (i.e. for a constant total mass stars become bluer with decreasing metallicity) without taking into account any mass loss but assuming a rather high helium abundance of Y = 0.35. Iben & Rood (1970), however, found that *"In fact for the values of Y and Z most favored ($Y \geq 0.25 \rightarrow 0.28$, $Z = 10^{-3} \rightarrow 10^{-4}$), individual tracks are the stubbiest. We can account for the observed spread in color along the horizontal branch by accepting that there is also a spread in stellar mass along this branch, bluer stars being less massive (on the average) and less luminous than redder stars. It is somewhat sobering to realize that this conclusion comes near the end of an investigation that has for several years relied heavily on aesthetic arguments against mass loss and has been guided by the expectation of obtaining, as a final result, individual tracks whose color amplitudes equal the entire spread in color along the observed horizontal branches."* In the same paper they found for post-HB stars that *"During most of the double-shell-source phase, models evolve upwards and to the red along a secondary giant branch*[3] *that, for the models shown, approaches the giant branch defined by models burning hydrogen in a shell."*

Comparing HB models to observed globular cluster CMD's Rood (1973) found that an HB that *"... is made up of stars with the same core mass and slightly varying total mass, produces theoretical c-m diagrams very similar to those observed. (...) A mass loss of perhaps 0.2 $M_\odot$ with a random dispersion of several hundredths of a solar mass is required somewhere along the giant branch."* The assumption of mass loss also diminished the need for very high helium abundances.

Sweigart & Gross (1974, 1976) computed HB tracks including semi-convection and found that this inclusion considerably extends the temperature range covered by the tracks. However, Sweigart (1987) noted that *"For more typical globular cluster compositions, however, the track lengths are clearly too short to explain the observed effective temperature distributions along many HB's, and thus semiconvection does not alleviate the need for a spread in mass (or some other parameter), a point first emphasized by Rood (1973)"*

---

[2] The change in slope of the horizontal branch for hotter stars is caused by the decreasing sensitivity of $B-V$ to temperature on one hand and by the increasing bolometric correction for hotter stars on the other hand, which results in fainter visual magnitudes for hotter stars.

[3] This secondary giant branch is called asymptotic giant branch (AGB) later in the text and consists of stars with a hydrogen and a helium burning shell.

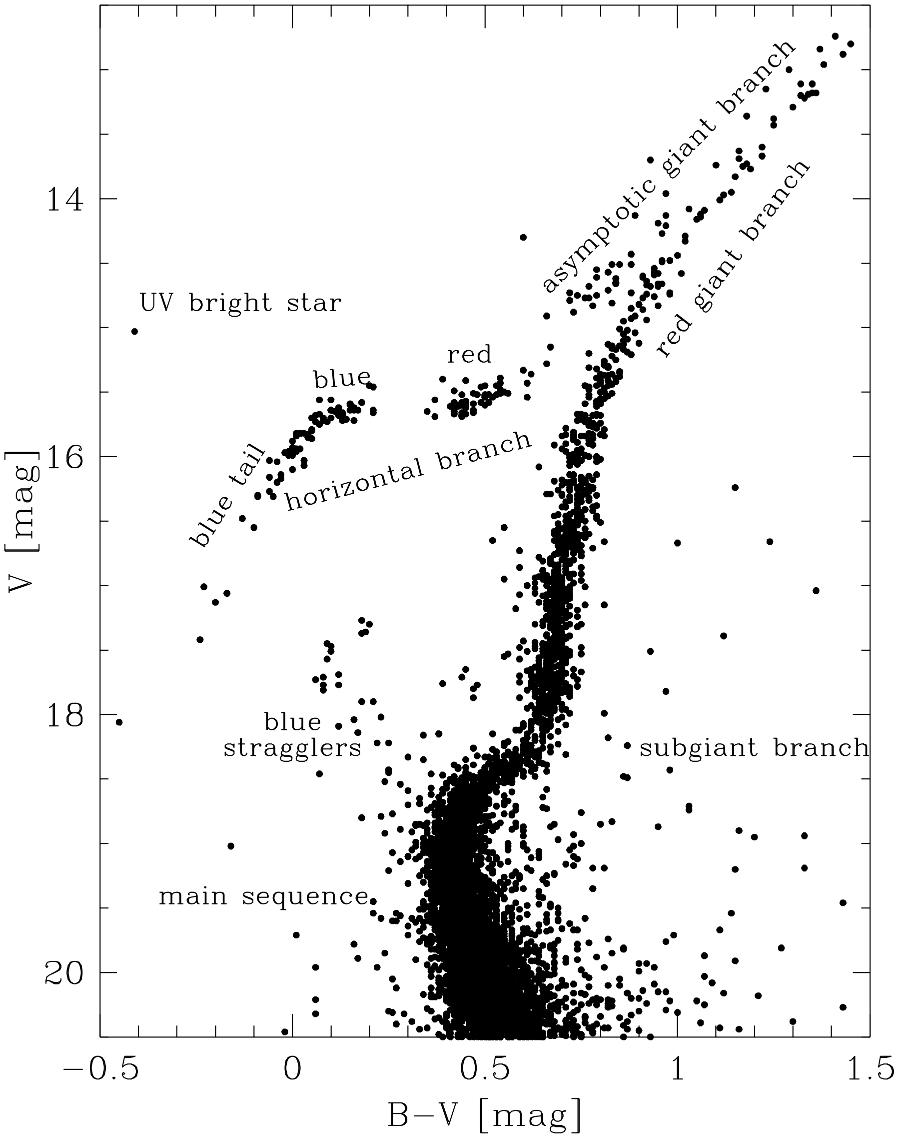

Fig. 1. Colour-magnitude diagram of M 3 (Buonanno et al. 1994) with the names of the principal sequences

Caloi (1972) investigated zero age HB locations of stars with very low envelope masses (≤ 0.02 $M_\odot$; extended or **extreme HB** = EHB) and found that they can be identified with the subdwarf B stars known in the field (Greenstein 1971). Sweigart et al. (1974) and Gingold (1976) studied the post-HB evolution and found that – in contrast to the more massive blue HB stars – EHB models do not ascend the second (asymptotic) giant branch (AGB).

Thus our current understanding sees **hot horizontal branch stars** as stars that burn helium in the center of a core of about 0.5 $M_\odot$ and hydrogen in a shell. Their hydrogen envelopes vary between 0.02 $M_\odot$ (less massive envelopes belong to EHB stars which do not have any hydrogen shell burning) and up to 0.2 $M_\odot$ for metal-poor HB stars. Depending on the mass of their hydrogen envelopes they evolve to the asymptotic giant branch (hot HB stars) or directly to the white dwarf domain (EHB stars, also called AGB manqué stars [Greggio & Renzini 1990]). For a review on HB evolution see Sweigart (1994).

But hot horizontal branch stars are neither the brightest nor the bluest stars in globular clusters: Already Shapley (1930, p.30) remarked that *"Occasionally, there are abnormally bright blue stars, as in Messier 13, but even these are faint absolutely, compared with some of the galactic B stars".*

This statement refers to stars like those mentioned by Barnard (1900) which in colour-magnitude diagrams lie above the horizontal branch and blueward of the red giant branch (see Fig. 1). This is also the region where one would expect to find central stars of planetary nebulae, which are, however, rare in globular clusters: Until recently Ps1 (Pease 1928), the planetary nebula in M 15 with its central star K 648, remained the only such object known in globular clusters (see also Jacoby et al. 1997, Chapter 6).

Apart from analyses of individual stars like vZ 1128 in M 3 (Strom & Strom 1970, and references therein) and Barnard 29 in M 13 (Traving 1962, Stoeckley & Greenstein 1968) the first systematic work on these bright blue stars was done by Strom et al. (1970). All stars analysed there show close to solar helium content, contrary to the hot horizontal branch stars, which in general are depleted in helium (Heber 1987, see also Chapter 3). Strom et al. identified the brightest and bluest UV bright stars with models of post-AGB stars (confirming the ideas of Schwarzschild & Härm 1970) and the remaining ones with stars evolving from the horizontal branch towards the AGB. This means that all of the stars in their study are in the double-shell burning stage. Zinn et al. (1972) performed a systematic search for such stars using the fact that they are brighter in the U band than all other cluster stars. This also resulted in the name **UV Bright Stars** for stars brighter than the horizontal branch and bluer than the red giant branch[4]. Zinn (1974) found from spectroscopic analyses of UV bright stars in 8 globular clusters *"a strong correlation between the presence of supra-HB stars in a globular cluster and the presence of HB stars hotter than log* $T_{eff} = 4.1$*"*

Harris et al. (1983) extended the compilation of UV bright stars in globular clusters and de Boer (1987) gave yet another list of such stars in globular clusters, together with estimates of effective temperatures and luminosities. De Boer (1985) found from analyses of vacuum UV spectra (observed with the IUE satellite) of UV bright stars in 7 globular clusters that their contribution to the total cluster intensity ranges *"from, on average, over 50% at 1200 Å to a few percent at 3000 Å."*

Most of the UV bright stars found in ground based searches are cooler than 30,000 K, although theory predicts stars with temperatures up to 100,000 K (e.g. Schönberner 1983, Renzini 1985). The ground based searches, however, are biased towards cooler stars due to the large bolometric corrections for hotter stars. It is therefore not very surprising that space based searches in the vacuum UV (Ultraviolet Imaging Telescope, Stecher et al. 1997) discovered a considerable number of additional *hot* UV bright stars in a number of globular clusters (see also Chapter 6).

Space based observatories also contributed a lot of other information about hot stars in globular clusters: UIT observations showed the unexpected presence of blue HB stars in metal-rich globular clusters like NGC 362 (Dorman et al. 1997) and 47 Tuc (O'Connell et al. 1997). At about the same time Hubble Space Telescope (HST) observations of the core regions of globular clusters showed long blue tails in metal-rich bulge globular clusters (Rich et al. 1997). These metal-rich globular clusters are discussed in more detail in Chapter 5. The interest in old hot stars like blue horizontal branch and UV bright stars has been revived and extended by the discovery of the UV excess in elliptical galaxies (Code & Welch 1979; de Boer 1982) for which they are the most likely sources (Greggio & Renzini 1990, Dorman et al. 1995, Dorman 1997, Brown et al. 1997, see also Chapters 5 and 6).

The most recent addition to the family of hot stars in globular clusters are the white dwarfs seen in HST observations of M 4 (Richer et al. 1995, 1997), NGC 6752 (Renzini et al. 1996) and NGC 6397 (Paresce et al. 1995, Cool et al. 1996), for which we obtained the first spectroscopic observations with the ESO Very Large Telescope in 1999 (see Chapter 8).

---

[4] To be precise this is true only for cool and/or luminous UV bright stars, while hot UV bright stars do not fulfil this criterion. As the flux maximum moves to ever shorter wavelengths for increasing temperatures, hot UV bright stars may be rather faint not only in V, but also in the U band (see also Chapter 6).

Chapter 2

Analysis Methods

Most analyses of stars use one (or both) of the following observations: Photometry[5], i.e. the observation of stars through a defined set of filters, and spectroscopy. Photometric observations allow to study many stars at once using large two-dimensional detectors. In addition, as light is integrated over a large wavelength range (20–100 nm for the two traditional and widely used Strömgren and Johnson filter systems) faint stars can be observed with this method. However, this same integration is also a disadvantage as it can mask existing differences between stars. It is thus preferable to use a combination of photometric and spectroscopic data to determine the physical status of a star. Spectrophotometry, i.e. spectroscopic observations with special emphasis on a correct measurement of absolute fluxes, provide more details on the flux distribution of a star than purely photometric observations.

To derive effective temperatures and surface gravities we compare various spectroscopic and photometric observations to their theoretical counterparts. For this purpose we need theoretical calculations that establish a connection between the physical status of a star and the light it emits, i.e. a model atmosphere (see Sect. 2.4). Depending on the available observational and theoretical data and the amount of software sophistication a wide variety of analysis methods is currently available. The following sections give an overview – more detailed descriptions can be found in the respective chapters.

2.1 Effective Temperature

The ideal temperature indicator is insensitive to variations of surface gravity because it then allows to derive the effective temperature independently from the surface gravity. For the stars we discuss in this work the vacuum UV flux distribution (shortward of 3000 Å) and the Balmer jump fulfill this requirement for effective temperatures between about 11,000 K and 30,000 K, although both become less sensitive to temperature in the hotter stars[6] (see Fig. 2). As interstellar extinction changes (reddens) the flux distribution of a star the observational data must be corrected for this effect.

Temperature determinations that include **vacuum UV data** (e.g. spectrophotometric observations with the International Ultraviolet Explorer IUE) are in general more reliable than those relying solely on optical observations, as the vacuum UV flux distribution (shortward of 3000 Å) is more sensitive to temperature variations of hot stars than the optical continuum.

If only **optical spectrophotometry** is available the overall continuum slope and the Balmer jump should be fitted simultaneously, including – if possible – optical photometric data as well.

---

[5] A more detailed description of photometry can be found in Appendix B.

[6] Johnson *UBV* photometry becomes rather gravity independent for the stars discussed here at temperatures above about 20,000 K – at the same time, however, it also loses temperature sensitivity. Strömgren *uvby* photometry stays temperature sensitive up to higher effective temperatures but is not available for most globular clusters.

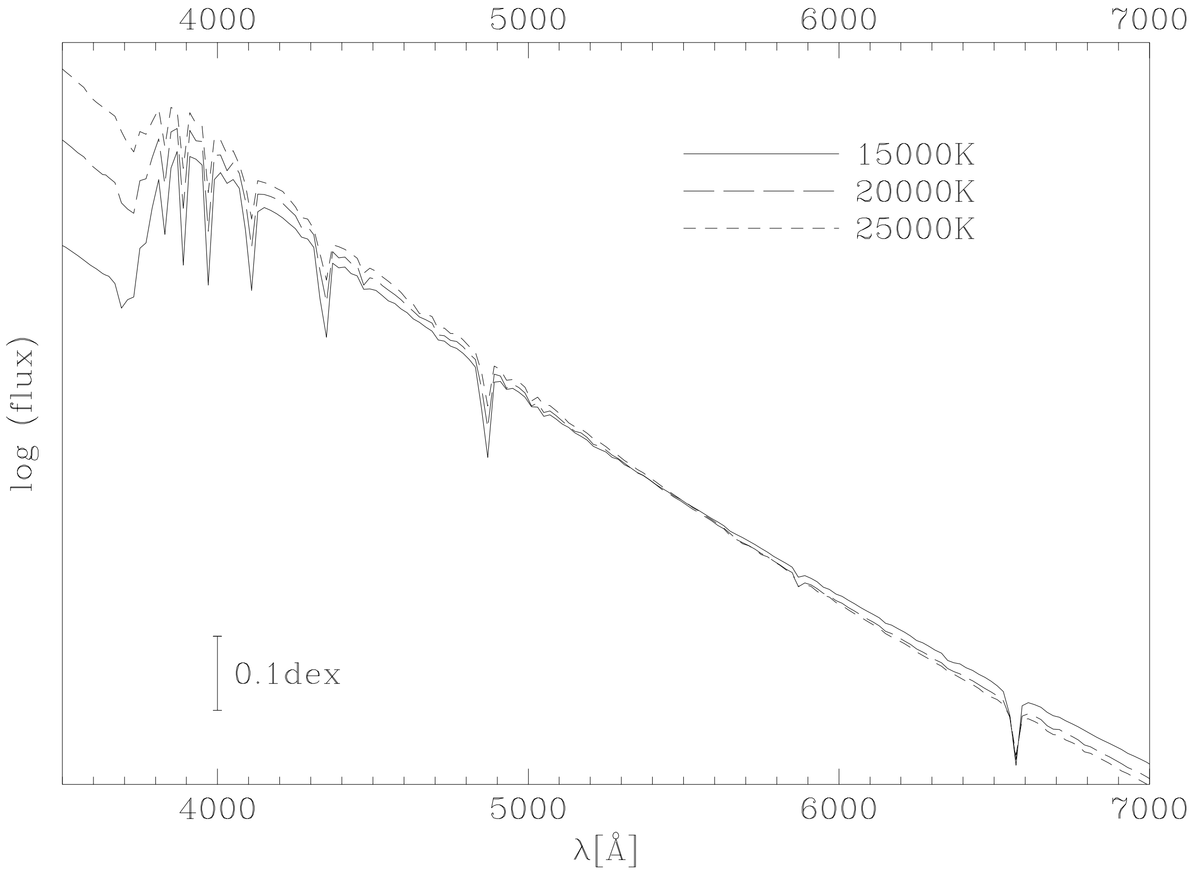

Fig. 2. Theoretical flux distributions for solar metallicity and helium content. Models for 15,000 K, 20,000 K, and 25,000 K (all for $\log g = 4.0$) are shown. The models are normalized to a common V magnitude.

2.2 Surface Gravity

Provided the effective temperature has been determined independently the surface gravity can be derived by fitting the shape of the Balmer line profiles at a fixed temperature (see Fig. 3). For this purpose the spectra are normalized and corrected for Doppler shifts introduced by the radial velocities of the stars. The model spectra have to be convolved with a profile representing the instrumental resolution, which was generally determined from the FWHM of the calibration lines (for more details see Sect. 3.2.2).

2.3 Simultaneous Determination of $T_{\rm eff}$ and $\log g$

For the cooler stars (below about 20,000 K) one can use a combination of **optical photometry** and **Balmer line profile fits** to determine effective temperature and surface gravity simultaneously: Reddening free indices (Q for Johnson UBV photometry; $[c1]$, $[u-b]$ for Strömgren *uvby* photometry) in comparison with theoretical values from model atmospheres allow to determine a relation between effective temperature and surface gravity. Fits to the lower Balmer line profiles (H_β to H_δ) yield another relation between $T_{\rm eff}$ and $\log g$ and from its intersection with the photometric relation effective temperature and surface gravity can be derived (for examples see Fig. 4, de Boer et al. 1995, and Moehler & Heber 1998).

For stars below about 8,500 K (Sect. 3.2.2, M 15) the Balmer line profiles depend more on $T_{\rm eff}$ than on $\log g$. In these cases the Balmer lines are used to estimate the temperature and $\log g$ is derived from photometric data.

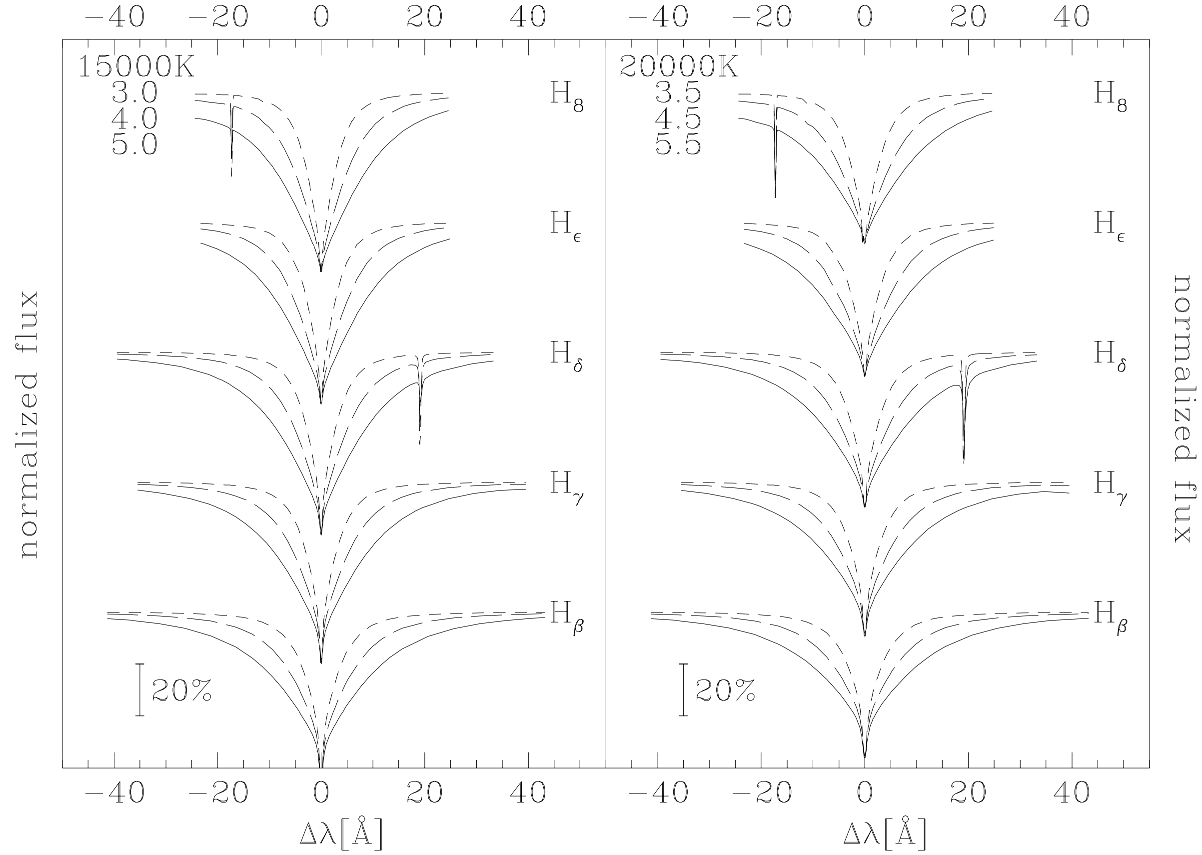

Fig. 3. Theoretical Balmer and He I (3872 Å, 4120 Å) line profiles for solar metallicity and helium content. Models for 15,000 K, $\log g = 3.0,4.0,5.0$ (**left panel**) and 20,000 K, $\log g = 3.5,4.5,5.5$ (**right panel**) are shown

Including also the higher Balmer lines (H_ϵ to at least H_{10}) allows to derive the effective temperature together with the surface gravity by fitting **all Balmer lines (H_β to H_{10})** simultaneously (Bergeron et al. 1992; Saffer et al. 1994).

2.4 Model atmospheres

Most of the stars discussed here are in a temperature–gravity range where LTE (local thermal equilibrium) is a valid approximation for the calculation of model atmospheres (Napiwotzki 1997). For a short and simplified description of the calculation of LTE model atmospheres see Appendix C. For the data described in Sects. 3.2, 3.3 published ATLAS9 model spectra were used (Kurucz 1992). The stars discussed in Sect. 3.3 required an extension of the ATLAS9 model atmosphere grid to higher surface gravities, for which we used an updated version of the code of Heber (1983).

The new fit procedures (Bergeron et al. 1992, Saffer et al. 1994) which we employed for the more recent data (Chapters 4, 5, 6) required line profiles for the higher Balmer lines (shortward of H_δ) that are not available from Kurucz. We therefore calculated model atmospheres using ATLAS9 (Kurucz 1991, priv. comm.) and used Lemke's version[7] of the LINFOR program (developed originally by Holweger, Steffen, and Steenbock at Kiel university) to compute grids of theoretical spectra (for various metallicities) that contain the Balmer lines H_α to H_{22} and He I lines.

For those stars which show He II lines in their spectra (and are thus considerably hotter than the bulk of our programme stars) it is necessary to take non-LTE effects into account (Napiwotzki 1997,

---

[7] For a description see http://a400.sternwarte.uni-erlangen.de/~ai26/linfit/linfor.html

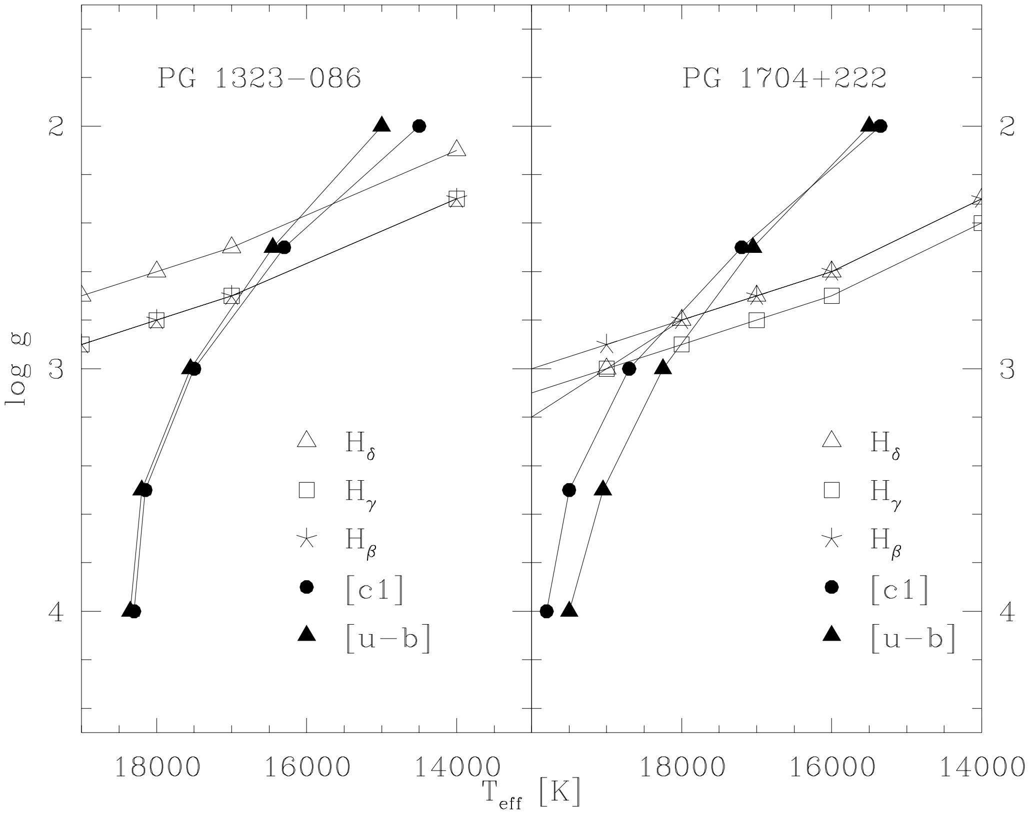

Fig. 4. Effective temperature and surface gravity derived from Strömgren photometry and from fits to the lower Balmer lines (from Moehler & Heber 1998)

Chapter 6). For the white dwarf spectra discussed in Chapter 8 we used Koester's LTE models as described in Finley et al. (1997) and the NLTE grid described in Napiwotzki et al. (1999).

As the abundance distribution within a stellar atmosphere influences the temperature and pressure distribution and thus the emergent flux distribution, we usually took to use model atmospheres of a similar metallicity as the studied globular cluster.

Chapter 3

Horizontal Branch Stars in Metal-Poor Globular Clusters – First Results and Problems

3.1 Gaps and Blue Tails

As mentioned in Chapter 1 the blue tails seen in the colour-magnitude diagrams (CMD's) of many globular clusters are often separated from the more horizontal part of the HB by gaps at varying brightness (see Fig. 5). For a list of globular clusters with blue tails see Fusi Pecci et al. (1993). Catelan et al. (1998) and Ferraro et al. (1998) give comprehensive lists of clusters that show gaps and/or bimodal horizontal branches. Such gaps can be found already in Arp's (1955) CMD's and are also known for distributions of field HB stars (Newell 1973, Heber et al. 1984). When discussing the blue tails and the gaps along the blue horizontal branch one should ensure not to introduce biases by naming conventions. Several authors call the stars seen along the blue tail subdwarfs or sdB stars, which implicates that they are twins to the hot sdB stars known from the field (for analyses and discussions of field sdB stars see Heber 1986, Moehler et al. 1990b, Saffer et al. 1994, 1997). However, as will be shown below, stars along the blue tails are not necessarily as hot as field subdwarf B stars and should therefore not be identified by this misleading name. In order not to introduce further confusion into an already complicated subject the acronyms used here will be defined below:

Definitions from colour-magnitude diagrams (see Fig. 1)

- ⋆ **BHB** identifies the **B**lue **H**orizontal **B**ranch, meaning stars along the mostly horizontal part of this sequence bluewards of the RR Lyrae region
- ⋆ **BT** stands for **B**lue **T**ail, meaning the stars along the almost vertical extension of the BHB towards higher effective temperatures. This part is vertical in $V, B-V$ colour-magnitude diagrams due to the decreasing sensitivity of $B-V$ to effective temperature for stars hotter than 10,000 K and to the increasing bolometric correction (i.e. the maximum of stellar flux is radiated at ever shorter wavelengths for increasing temperatures, making stars fainter at V). The effective temperature of stars along the blue tail thus increases towards fainter V magnitudes.

Spectroscopic definitions [8] *(see also Moehler et al. 1990a)*

- ⋆ **HBB/HBA** means **H**orizontal **B**ranch stars corresponding to the MK spectral types **B** resp. **A**. Such stars show mainly Balmer lines (deeper and more narrow for cooler type A stars than for

---

[8] More detailed discussion of the spectroscopic classification of hot subdwarfs can be found in Drilling (1996).

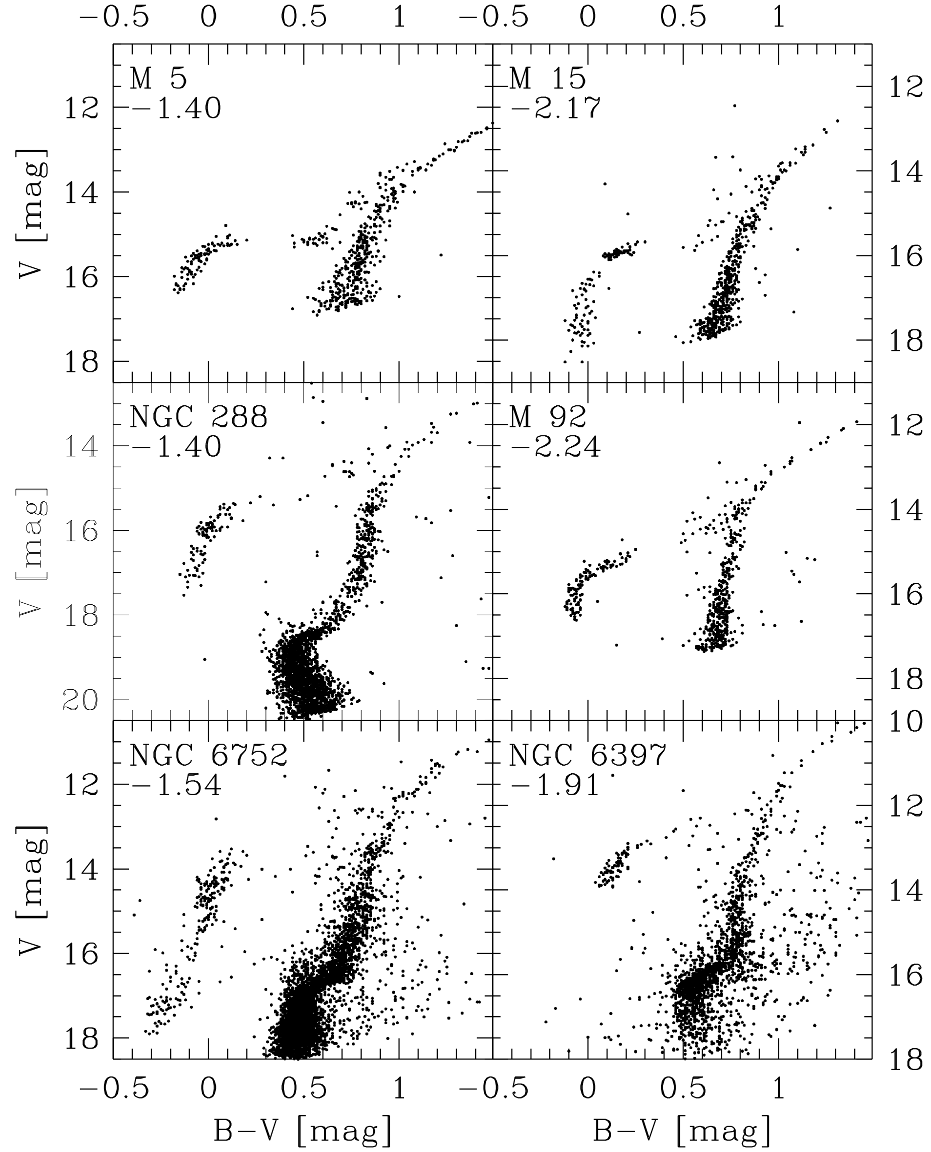

Fig. 5. Colour-magnitude diagrams of NGC 6752 (Buonanno et al. 1986), NGC 288 (Buonanno et al. 1984), M 5 (Buonanno et al. 1981), NGC 6397 (Alcaino et al. 1987), M 92 (Buonanno et al. 1983b), M 15 (Buonanno et al. 1983a). The numbers noted for each cluster give the mean metallicity of the cluster (from Zinn & West 1984). The wide gaps in the brighter and more horizontal part of some HB's are in reality populated by (variable) RR Lyrae stars, which are omitted from the plots. The gaps discussed here are located at fainter magnitudes in the (mostly vertical) blue tails (most pronounced in NGC 6752, NGC 288, and M 15). The CMD of M 3 ([M/H] = −1.66) can be found in Fig. 1.

type B stars) and the hotter B-type stars may also show lines of He I. HBA stars have effective temperatures between ≈ 7500 K and ≈ 10,000 K whereas the hotter HBB stars have temperatures between ≈10,000 K and ≈20,000 K.

⋆ **sdB** means **s**ub**d**warf **B** stars, which are hotter than ≈20,000 K and show less deep Balmer lines than HBB stars accompanied by lines of He I. Their Balmer lines merge earlier (at H_{11}–H_{12}) indicating higher gravities than for the HBB stars, which show discernible Balmer lines up to H_{16} and more (see Fig. 14, p. 32: B 1509 is an HBB star, B 3915 is an sdB star). **sdOB** and **sdO** stars extend the hot subdwarf sequence to higher temperatures, showing (besides Balmer lines) lines of both He I and He II (sdOB) resp. only He II (sdO).

Theoretical definitions (see also Appendix A)

- ⋆ **hot HB** stars are HB stars hotter than the variable RR Lyrae stars, with a helium-burning core of ≈ $0.5\,M_\odot$, a hydrogen-burning shell, and a hydrogen-rich envelope of varying mass. The more massive this hydrogen envelope is the cooler is the resulting star and at constant hydrogen envelope mass stars become hotter (= bluer) with decreasing metallicity. The minimum envelope mass for a hot HB star is about $0.02\,M_\odot$ while the maximum mass depends strongly on metallicity and can reach $0.2\,M_\odot$ for very metal-poor stars. The effective temperatures of hot HB stars are between 7500 K and ≈20,000 K. Hot HB stars evolve from the horizontal branch to the asymptotic giant branch and from there on to white dwarfs.
- ⋆ **EHB** stars are **E**xtreme **HB** stars with a hydrogen-rich envelope of less than $0.02\,M_\odot$, which is too small to sustain hydrogen-shell burning. These stars do not evolve to the asymptotic giant branch (therefore they are sometimes also called AGB-manqué stars, Greggio & Renzini 1990) but instead evolve directly to the white dwarf domain. They are supposed to be the main source of the UV upturn seen in elliptical galaxies (see also Chapter 5).

While analyses of field sdB and HBB/HBA stars have shown that they can be identified with EHB resp. hot HB stars, the situation is not so clear for the blue stars in globular clusters. An identification of the BHB stars with hot HB models is consistent with photometric observations (colour-magnitude diagrams), but the evolutionary status of the stars along the blue tails remained unclear for quite some time. The main problem of the gaps (which appear at varying absolute magnitudes and thus temperatures) is that they are not expected from canonical evolutionary scenarios. Various explanations have been suggested during the past 25 years and some of them are given below (more detailed descriptions of possible explanations for the gaps can be found in Crocker et al. 1988, Catelan et al. 1998, and Ferraro et al. 1998):

- ⋆ **Diverging evolutionary paths**

  As mentioned above stars evolve away from the zero-age HB (ZAHB) in different directions (to the asymptotic giant branch or directly to the white dwarf region) depending on the mass of their hydrogen envelope. Such evolution could in principle transform a uniformly populated ZAHB into a bimodal one as stars evolve. Newell (1973) was the first to suggest this idea as an explanation for the gap seen in *UBV* photometry of field horizontal branch stars at temperatures corresponding to ≈12,900 K. Heber et al. (1984) suggested that the small gap at ≈20,000 K between field HBB and sdB stars could be explained by diverging evolution.

  Support for the explanation of the HB gaps by diverging evolutionary paths came from Lee et al. (1994), but other calculations show that the effect is not large enough to explain the gaps along the horizontal branches as HB stars spend most of their lifetime close to the ZAHB (see e.g. Dorman et al. 1991, Catelan et al. 1998). D'Cruz et al. (1996) found that bimodal horizontal branches become more probable for increasing metallicity as the range in mass loss required to produce an extreme HB star stays constant, whereas only a very narrow range of mass loss can produce hot HB stars at high metallicities. While this scenario offers a good explanation for the sdB stars and the large gap seen in the metal-rich open cluster NGC 6791 (Liebert et al. 1994) it cannot explain the gaps seen in the mostly rather metal-poor globular clusters.
- ⋆ **Differences in some properties like [CNO/Fe], rotation etc.**

  Rood & Crocker (1989) suggest differences in CNO or He abundances or rotation rates between stars above and below the gaps as possible causes for the gaps. For hot HB stars a decrease in *CNO abundances* results in bluer colours (a similar effect as seen for a decrease in overall metallicity). Increasing the *He abundance* in the hydrogen envelope of a hot HB star will increase the energy production in the H-burning shell, thereby resulting in brighter horizontal branch stars (see Sect. 4.1 or Sweigart 1997b for more details). *Rotation* would delay the helium core flash in a red giant thereby leading to an increase in the helium core mass and more mass loss, resulting in bluer and brighter

HB stars (see also Buonanno et al. 1985 for a discussion of rotation and blue tails). Differences in any of these parameters may thus lead to gaps along the horizontal branch. Neither the CNO abundance nor the He abundance can be easily determined for HB stars as their atmospheres may be affected by diffusion (see Sect. 4.2).

The finding of Peterson (1985) that the relative number of blue HB stars correlates with the rotational velocities observed for blue HB stars in M 3, M 4, M 5, M 13 (clusters with bluer HB morphologies show higher rotation velocities among their HB stars) supports the idea that rotation affects the distribution of stars along the HB. However, the analysis of Peterson et al. (1995b) shows that while the stars in M 13 (which has a long blue tail) rotate on average faster than those in M 3 (which has only a short blue HB), the stars in NGC 288 show *slower* rotation velocities at *higher* temperatures – the opposite of what would be expected if bluer HB morphology were correlated with higher rotation rates of HB stars. The results for NGC 288 are consistent with those reported for blue HB and blue tail stars in M 13 by Behr et al. (1999b), who determined rotational velocities for stars as hot as 19,000 K (considerably hotter than the stars analysed by Peterson et al. 1995b). They found that stars hotter than about 11,000 K have significantly lower rotational velocities than cooler stars and that the change in mean rotational velocity may coincide with the gap seen along the blue HB of M 13. These results could be understood if the enhanced mass loss due to rotation on the red giant branch is accompanied by an above average loss of angular momentum. Such an explanation, however, would argue against the correlation reported by Peterson et al. (1995b) that clusters with bluer HB morphologies show higher rotational velocities among their HB stars. More data, especially on hotter HB stars, are needed to verify whether the tendency of slower rotation for hotter HB stars is a common phenomenon.

⋆ **Different creation processes for stars above and below gaps**

A gap would be easy to understand if the stars above and below the gap were created by different mechanisms: If the stars below the gaps do not descend from red giants there is no reason why they should form a smooth extension of the sequence defined by red giants descendants. The most prominent candidates for such different formation mechanisms are binary interactions:

1. Common envelope evolution can lead to the formation of subluminous O and B stars if Roche lobe overflow occurs during the ascend of the first (case B) or second (case C) giant branch (Iben & Tutukov 1985, 1993, Iben 1986, Iben & Livio 1993). Well studied examples are HD 128220 (sdO+ FIV) and AA Dor. For case B evolution the sdB masses are somewhat smaller than the canonical 0.5 $M_\odot$ (e.g. AA Dor, $M = 0.3$ $M_\odot$, Kudritzki et al. 1982), while for case C they are slightly larger than the canonical value (e.g. HD 128220, $M > 0.55 M_\odot$, Howarth & Heber 1990).
2. Mengel et al. (1976) explored the possibility that sdB stars could evolve from binaries in which mass transfer is initiated at the tip of the red giant branch, i.e. shortly before the ignition of the core helium flash, resulting in sdB masses very close to the canonical $0.5 M_\odot$.
3. sdB stars can also result from the merger of a double helium-core white dwarf system (Iben & Tutukov 1984, Iben 1990) with final masses ranging from $0.3 M_\odot$ to $0.9 M_\odot$. Bailyn et al. (1988) suggested collisions followed by mergers of main-sequence and white dwarf stars, while Iben & Tutukov (1986) propose the merging of two helium-core white dwarfs into one He-rich star with a thin hydrogen shell (see also Iben 1990). Bailyn & Iben (1989) have explored these possibilities for globular cluster sdB's and argue that a few tens of sdB's can be formed in a typical globular cluster, because binary-single star interactions increase the merger rate considerably, especially for the central regions of the cluster. An extensive review of the scenarios sketched above as well as other possibilities can be found in Bailyn et al. (1992).

These scenarios create stars that resemble the sdB, sdOB, and sdO stars known from the field of the Milky Way, but predict quite different mass distributions: The single-star EHB hypothesis and Mengel's binary scenario predict an sdB mass of $(0.5 \pm 0.02) M_\odot$, while the common-envelope binary scenario and the merger model predict a mass varying between 0.3 and $0.9 M_\odot$, where the low-mass stars are hotter and live considerably longer than the heavier ones (Iben 1990). The narrow mass range predicted by the EHB model has been used to derive distances and to study the population characteristics of field subdwarfs (Heber 1986, Moehler et al. 1990b, Theissen et al. 1993, indirectly also Villeneuve et al. 1995, Mitchell 1998). A broad mass range for sdB stars would render these results invalid. The main objection to the merger scenarios is that in this case the relative numbers of red giant (RGB/AGB) to "true" HB stars, which gives an estimate of the cluster's original helium abundance, would vary between clusters and pretend varying primordial helium abundances (see Buonanno et al. 1985, Fusi Pecci et al. 1993). Another objection is the tight sequence in temperature and surface gravity reported by Heber et al. (1986) for stars below the gap in NGC 6752. Crocker et al. (1988) cite the similar blue tails in M 15 and NGC 288, which are dynamically very different, as argument against the production of blue tail stars by dynamical interactions like merging (Ferraro et al. 1997 argue in the same way with respect to M 13 and M 3, which are dynamically very similar but have very different HB morphologies). See, however, Buonanno et al. (1997) for a discussion of the relation between cluster density and the presence of blue tails.

⋆ **Atmospheric processes**
Quite recently, Caloi (1999) proposed the change from convection to diffusion in the stellar atmospheres as an explanation for the gaps around $(B-V)_0 = 0$. This scenario would predict chemical peculiarities in the stars below the gaps. A more detailed discussion of the rôle of diffusion in hot HB stars can be found in Sect. 4.2.

⋆ **Statistical fluctuations**
Catelan et al. (1998) argued quite convincingly that at least some of the gaps may be due to statistical fluctuations.

The obvious need for more information on the stars along the blue tails led to our project to obtain atmospheric parameters and masses for blue HB and blue tail stars in several globular clusters. Sect. 3.2 describes the analysis of blue HB and blue tail stars in M 15 and the conclusions we drew at the time of the analysis (1995). Prompted by the puzzling results for M 15 we decided to obtain spectra of the blue tail stars in NGC 6752 to enlarge the sample studied by Heber et al. (1986) and verify their conclusion that the stars below the gap in NGC 6752 are sdB stars. This work is described in Sect 3.3. To enlarge the samples discussed we also used the data on NGC 6397 (de Boer et al. 1995), and on NGC 288, M 3, M 5, and M 92 (Crocker et al. 1988). The CMD's of all these clusters can be found in Figs. 1 and 5.

3.2 M 15

The following section gives a quite detailed description of the data reduction to which later sections will refer.

3.2.1 Observations and Data reduction

We tried to select stars that do not have obvious close companions (i.e. closer than about 4″) on the finding charts of Buonanno et al. (1983a) and Battistini et al. (1985). The targets are listed in Table 1 and marked in the colour-magnitude diagram of M 15 (Fig. 6). All observations described in this Section were obtained with the Cassegrain Twin Spectrograph of the 3.5m telescope at the Calar Alto observatory during 1989 – 1992. The observational parameters are given in Table 2. The seeing normally lay around 2″, except for one night in 1992 where the seeing was 1″ or below. During this night we observed B 276, B 421, and B 686 (see also Sect. 3.2.2). Of the medium resolution spectra we have at least two for each star. We used ESO's Munich Image Data Analysis System (MIDAS) for all data analysis.

Table 1. Coordinates, photometric data, and heliocentric radial velocities for the targets in M 15. The numbers of the stars refer to Buonanno et al. (1983a) and Battistini et al. (1985). The absolute magnitudes M_V are based on an apparent distance modulus of $(m - M)_V = 15.43$.

number	α_{2000}	δ_{2000}	V	$B - V$	M_V	$v_{\rm rad,hel}$ [km/s]
Stars above the gap						
18	$21^{\rm h}30^{\rm m}02\overset{\rm s}{.}5$	$+12^\circ14'04''$	$16\overset{\rm m}{.}10$	$+0\overset{\rm m}{.}11$	$+0\overset{\rm m}{.}67$	−128
440	$21^{\rm h}29^{\rm m}52\overset{\rm s}{.}1$	$+12^\circ08'44''$	$15\overset{\rm m}{.}79$	$+0\overset{\rm m}{.}22$	$+0\overset{\rm m}{.}36$	−98
484	$21^{\rm h}29^{\rm m}53\overset{\rm s}{.}5$	$+12^\circ08'16''$	$16\overset{\rm m}{.}04$	$+0\overset{\rm m}{.}09$	$+0\overset{\rm m}{.}61$	−133
Stars below the gap						
1	$21^{\rm h}30^{\rm m}02\overset{\rm s}{.}3$	$+12^\circ14'49''$	$17\overset{\rm m}{.}85$	$+0\overset{\rm m}{.}01$	$+2\overset{\rm m}{.}42$	−129
20	$21^{\rm h}30^{\rm m}01\overset{\rm s}{.}2$	$+12^\circ14'02''$	$17\overset{\rm m}{.}75$	$-0\overset{\rm m}{.}02$	$+2\overset{\rm m}{.}32$	−83
27	$21^{\rm h}30^{\rm m}04\overset{\rm s}{.}4$	$+12^\circ13'40''$	$16\overset{\rm m}{.}66$	$-0\overset{\rm m}{.}03$	$+1\overset{\rm m}{.}23$	−116
208	$21^{\rm h}30^{\rm m}08\overset{\rm s}{.}3$	$+12^\circ11'29''$	$18\overset{\rm m}{.}05$	$-0\overset{\rm m}{.}02$	$+2\overset{\rm m}{.}62$	−95
258	$21^{\rm h}30^{\rm m}08\overset{\rm s}{.}6$	$+12^\circ10'56''$	$16\overset{\rm m}{.}49$	$+0\overset{\rm m}{.}06$	$+1\overset{\rm m}{.}06$	−106
276	$21^{\rm h}30^{\rm m}12\overset{\rm s}{.}7$	$+12^\circ10'41''$	$18\overset{\rm m}{.}52$	$-0\overset{\rm m}{.}12$	$+3\overset{\rm m}{.}09$	−105
325	$21^{\rm h}30^{\rm m}06\overset{\rm s}{.}3$	$+12^\circ10'00''$	$16\overset{\rm m}{.}78$	$+0\overset{\rm m}{.}11$	$+1\overset{\rm m}{.}35$	−126
348	$21^{\rm h}29^{\rm m}46\overset{\rm s}{.}9$	$+12^\circ09'54''$	$16\overset{\rm m}{.}69$	$+0\overset{\rm m}{.}01$	$+1\overset{\rm m}{.}26$	−89
421	$21^{\rm h}30^{\rm m}11\overset{\rm s}{.}9$	$+12^\circ08'43''$	$18\overset{\rm m}{.}52$	$-0\overset{\rm m}{.}03$	$+3\overset{\rm m}{.}09$	−117
574	$21^{\rm h}29^{\rm m}42\overset{\rm s}{.}3$	$+12^\circ07'32''$	$17\overset{\rm m}{.}84$	$-0\overset{\rm m}{.}06$	$+2\overset{\rm m}{.}41$	−102
686	$21^{\rm h}30^{\rm m}15\overset{\rm s}{.}5$	$+12^\circ14'21''$	$18\overset{\rm m}{.}42$	$-0\overset{\rm m}{.}01$	$+2\overset{\rm m}{.}99$	−118

We always took wavelength calibration spectra ahead of and after each observation in order to account for eventual shifts in wavelength due to bending differences during the observation. The dark currents cited below were derived from three or more dark current frames of 2700 sec or more each. We took at least 5 bias frames each night, normally 10, and averaged them separately for each night. For the bias correction we scaled the mean bias with overscan values obtained for the science frames.

All spectra were corrected for atmospheric extinction using the extinction coefficients of La Silla (Tüg 1977) and standard MIDAS routines; since there are no published data for the Calar Alto observatory we used the La Silla coefficients. The error introduced that way should not affect the results seriously (cf. Rufener 1986).

To correct for the wavelength-dependent response of the system (telescope, spectrograph, and CCD) we derived response curves from the spectra of flux-standard stars (cf. Moehler et al. 1990b) For the flux calibration we fitted third order polynomials (except for the spectra obtained in 1992, for which we used a spline fit) as response curves. We then averaged the response curves for each night separately. As standard stars we used BD+28°4211 (1989, 1991, 1992), BD+33°2642 (1989, 1990, 1992), Feige 98 (1989), Hiltner 102 (1990), all taken from Stone (1977), and HZ 44 (1991), taken from Oke (1974).

Observations 1989 – 1991

The dark frames of the RCA chip did not show any structure and resulted in a mean dark current of 6.5 ± 2.5 counts/hr/pixel. We corrected the dark current by subtracting an averaged (over all nights of each run) dark frame (corrected for cosmic events by comparing several frames) scaled with exposure time.

To correct the column structure of the RCA chip we took flat fields of varying but short exposure times. These flats were averaged for each exposure level over all nights. The intensity distribution of the mean flat (for each exposure level) was taken out using a large median filter and subtracting the filtered frame from the original one. To reduce the noise further we averaged the resulting frames along the columns, thus creating a one-dimensional column mask which was afterwards grown again along the columns. The correction of column structure was achieved by subtracting from the science frame the column mask that originated from the flat whose intensity came closest to the background

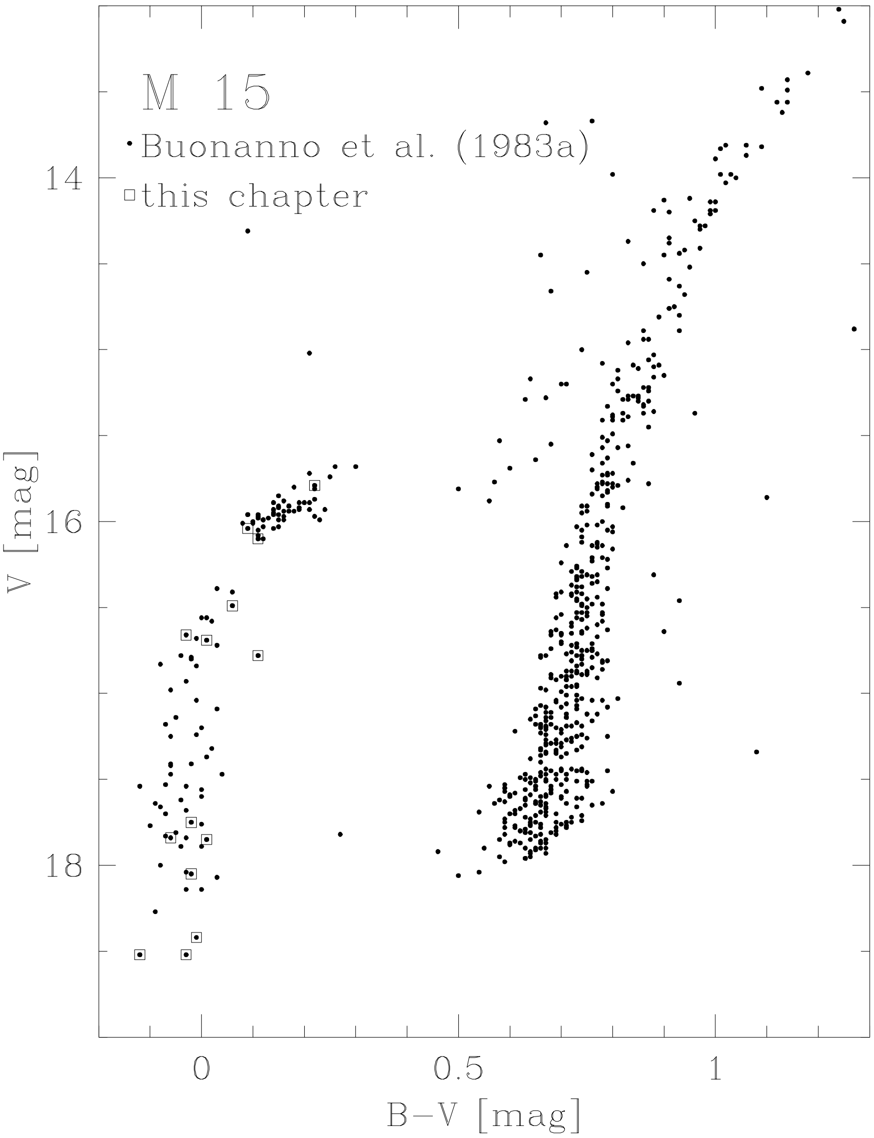

Fig. 6. The colour-magnitude diagram of M 15 (Buonanno et al. 1983a). Stars analysed in this section are marked by open squares. Star B 686 is taken from Battistini et al. (1985).

intensity of the respective science frame. To correct the pixel-to-pixel variation we used flat fields with exposure levels up to 10,000 counts. They were averaged separately for each night and normalized by fitting a third order polynomial to their spectral intensity distribution.

The wavelength calibration was performed by fitting a third order polynomial to the dispersion relation of each column separately. Then the mean dispersion relation of the calibration frames taken before and after the science exposure was derived for each column and applied to the science frame, again separately for each column. The FWHM of the calibration lines was used as spectral resolution of the system (cf. Table 2). After rebinning the whole frame to constant wavelength steps the sky background for each exposure was fitted on both sides of the object's spectrum, using interactively defined sky regions. Before fitting the sky a median filter (3 pixels in spatial direction) was applied to erase cosmic events. The spatial profile of the sky background was fitted with a second order polynomial and we assumed that the spectral lines were parallel to the rows of the CCD. Finally the spectra were

Table 2. Observational parameters for M 15. We always used gratings with 72 Å/mm.

Date	channel	CCD	pixel size $[\mu\mathrm{m}^2]$	no. of pixels	conv. factor $[\mathrm{e}^-/\mathrm{count}]$	read-out noise $[\mathrm{e}^-]$
1989/06/12-15	B	RCA SID 006 EX	15×15	656×1024	3.7	36
1990/08/06-10	B	RCA SID 006 EX	15×15	656×1024	3.7	36
1991/07/20-25	B	RCA SID 006 EX	15×15	656×1024	3.7	36
1992/08/05-10	B	GEC P88231 S	22.5×22.5	768×1155	12	5
	R	RCA SID 006 EX	15×15	656×1024	3.7	36

Date	Channel/ Mode	Slit width $[{}'']$	Binning		Wavelength range [Å]	wavelength calibration		
			spatial	dispersion		number of lines used	r.m.s. error [Å]	resolution [Å]
1989/06/12-15	B/med	2.1	2	1	3870 – 5000	30	0.2	3.6
1990/08/06-10	B/med	2.1	2	1	3860 – 5000	30	0.2	3.6
1991/07/20-25	B/med	2.1	1	1	3850 – 5030	30	0.2	3.9
1992/08/05-10	B/low	3.6	1	2	3400 – 5300	35	0.6	5.7
	R/low	3.6	1	3	5000 – 6100	13	0.6	4.6
	R/med	2.1	1	1	3950 – 5070	40	0.2	3.7

extracted using the MIDAS implementation of Horne's Algorithm (Horne 1986) and co-added for each object. The resulting spectra (corrected for radial velocity shifts) are plotted in Fig. 7.

Observations obtained in 1992

In 1992 we obtained low resolution spectra (3400 – 6100 Å) to derive temperatures and medium resolved spectra as in the years before to determine surface gravities (see Table 2).

The dark currents obtained for the *low resolution* observing mode were 5.9±1.6 counts/hr/pixel for the GEC chip used in the blue channel and 17±2.6 counts/hr/pixel for the RCA chip used in the red channel (binned pixels in both cases). For both chips the dark current was corrected as described above. During observations we took care to orientate the slit along the direction of the atmospheric dispersion in order not to lose any light. Sky flats were taken during dusk to correct for the illumination. High exposure level (dome) flats were averaged to correct for the pixel-to-pixel variation as before, but we took out the dome illumination pattern, which was determined by averaging the mean dome flat along the dispersion direction and smoothing the result. In the same way we determined the illumination pattern of the sky flats. Finally we divided the mean dome flat by the dome illumination and multiplied it with the sky illumination frame. The spectral intensity profile was taken out by averaging along the spatial axis, smoothing the result and dividing the flat through it. In the red channel we performed the column correction as described above (the CCD in the blue channel did not show any column structure).

Wavelength calibration, sky subtraction, extraction of the object spectra and correction for atmospheric extinction were performed in the same way as for the older data, with the exception that we used a constant for the spatial profile of the sky background, which was possible due to the illumination correction. We took special care at the step of the flux calibration to achieve a good fit and therefore used a spline instead of a polynomial to fit the response curve. Finally the spectra were also corrected for interstellar extinction, using $E_{B-V} = 0.10$ (see also Sect. 3.2.3) and the reddening law of Savage & Mathis (1979). To reduce the noise the spectra were rebinned to a step size of 10 Å. The results are plotted in Fig 8. The spikes in the low resolution spectra are cosmic events that were not corrected during the extraction process. Note that there seems to be an indication of a G-band in the low-resolution spectrum of B 208, that is not seen in the medium resolution spectrum. This spectrum was taken with rather bad seeing ($2'' - 3''$) so probably there is some stray light from a red star

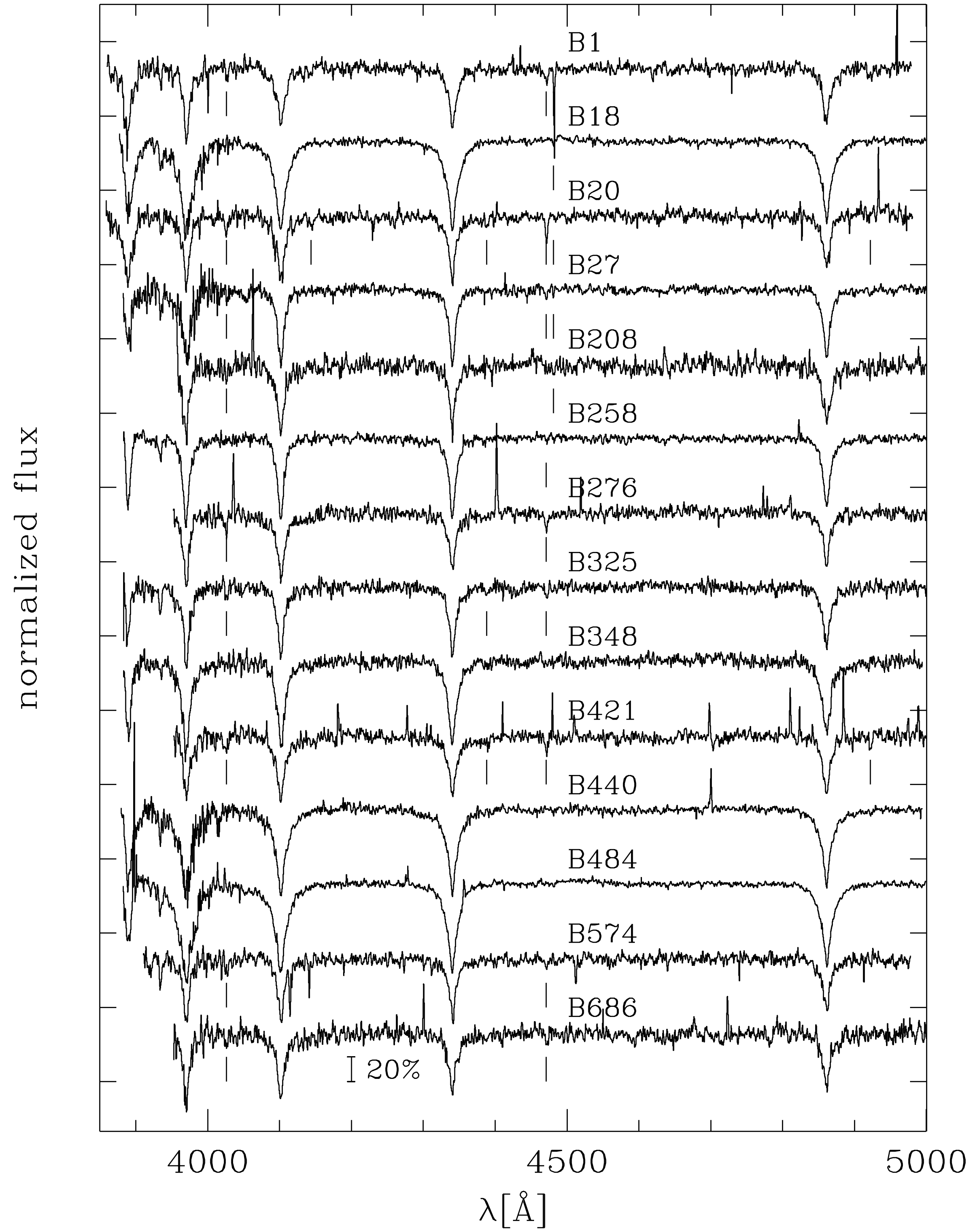

Fig. 7. Normalized medium resolution spectra. We did not correct any cosmic events besides using the optimal extraction of Horne (1986). The He I lines λλ 4026 Å, 4144 Å, 4388 Å, 4471 Å, 4922 Å and the Mg II line 4481 Å are marked (if visible in the spectrum). All spectra show the absorption of interstellar Ca II (except those of 1992, where this line lies outside the covered wavelength range).

(B 214), which is about 1 mag brighter and 4.″7 away. The spectrum of B 276 is rather flat compared to the other spectra. Studying the observing log it turned out that after adjusting the slit orientation

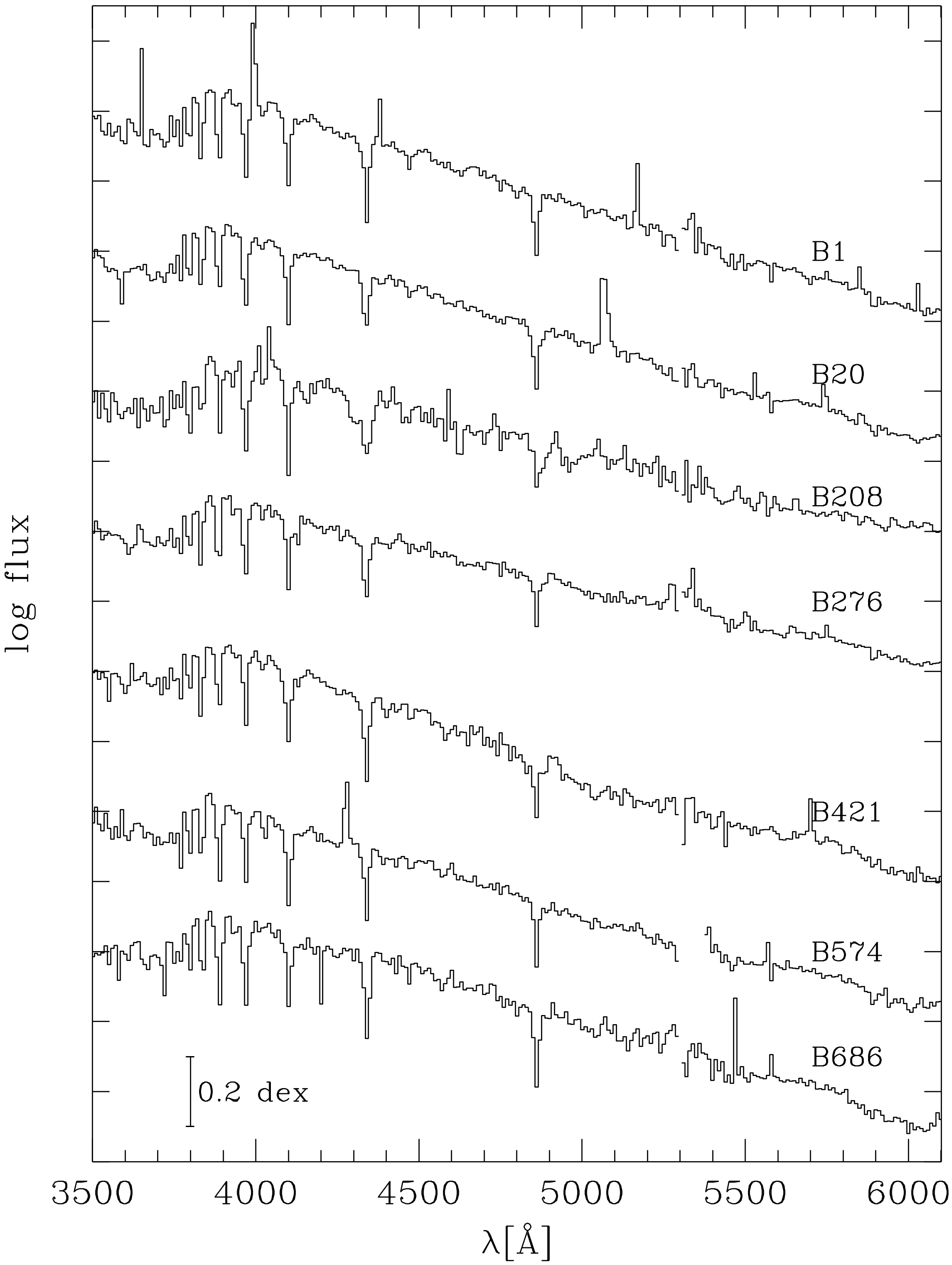

Fig. 8. Low resolution spectra used for the determination of $T_{\rm eff}$. We did not correct any cosmic events besides using Horne's (1986) algorithm. The gaps in the spectra mark the transition region from the blue to the red channel at about 5300 Å, where the flux distribution may be distorted by edge effects.

for atmospheric dispersion the spectrograph had not been clamped again. Thus it could have moved during the observation thereby leading to some loss of light that may be wavelength dependent.

For the **medium resolution spectra** we used only the red channel and employed a mirror instead of the beam splitter, thereby collecting all light in the red channel. Due to the optics we could use

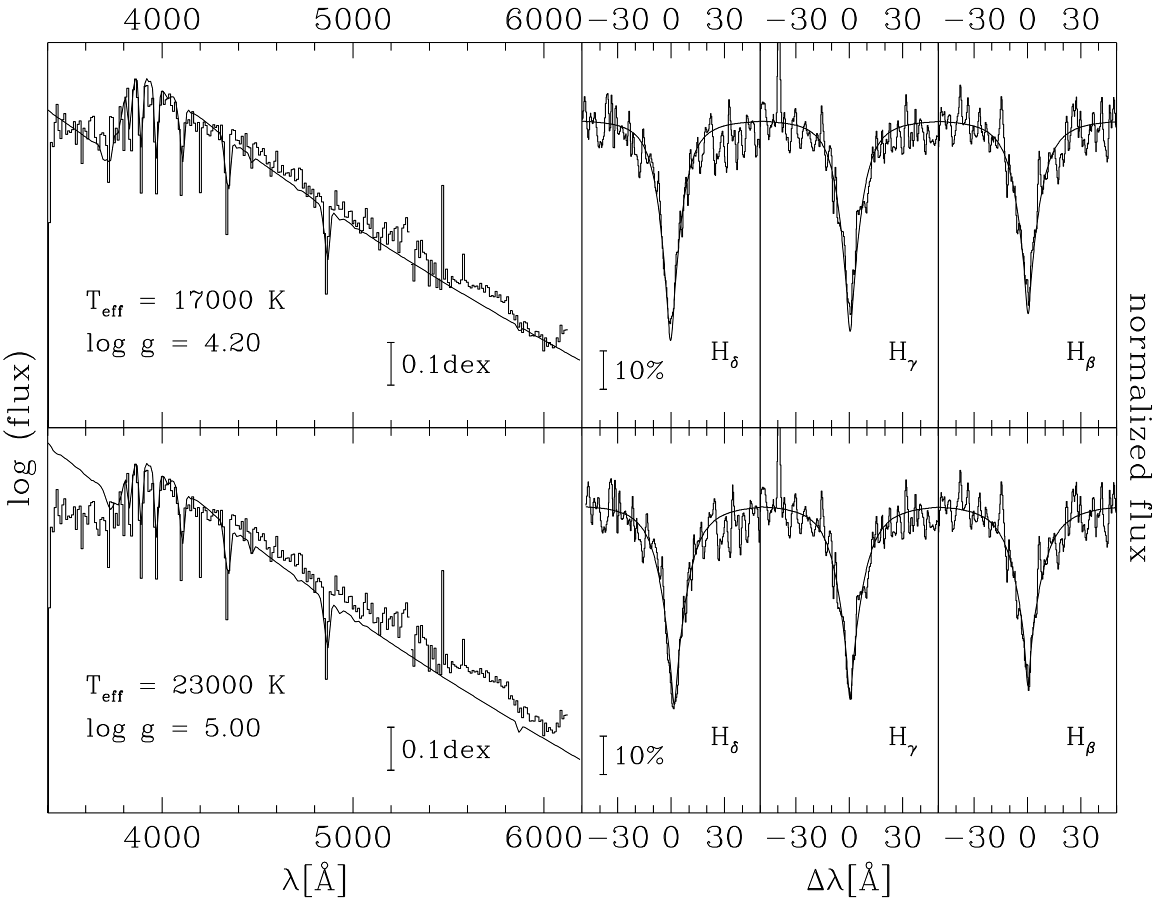

Fig. 9. The low resolution (**left panels**) and medium resolution (**right panels**) spectra of B 686 in M 15 and the fitted model spectra:
T_{eff} obtained solely from the low resolution spectrum (**upper panels**)
T_{eff} obtained solely from the line profile fits (**lower panels**)

only the range redwards of about 4000 Å. Here we used the RCA chip and did not bin. For this mode we obtained a mean dark current of 4.5±0.7 counts/hr/pixel which we did not correct due to its smallness. These data were reduced in the same way as the blue channel data from 1989 – 1991, except that we fitted the spatial profile of the sky with a constant. The resulting spectra are plotted in Fig. 7.

3.2.2 Atmospheric Parameters

To determine effective temperatures and surface gravities of our stars we used the fully line-blanketed ATLAS9 LTE model atmospheres of Kurucz (1992) for [M/H] = −2.0. This metallicity corresponds rather well to the metallicity of M 15 (−2.17, Djorgovski 1993). To derive the effective temperature we used only the low resolution spectra (see Fig. 9, upper left panel) that had been corrected for interstellar extinction as described above. For the temperature derived that way we then determined the value of $\log g$ from the best fit of the Balmer lines in the medium resolution spectra. This method is similar to the one we used for the field sdB stars (Moehler et al. 1990b), except that there we used photometric data (mainly Strömgren photometry) while we now use spectrophotometric data to measure the Balmer jump.

In one case (B 276) we saw a significant red excess although the fit with T_{eff} = 18,000 K represents the Balmer jump quite well. As already mentioned above we probably lost some light due to slit rotation during the exposure of this spectrum. The light losses were probably highest in the UV which leads to a relative flattening of the spectrum. Lowering the effective temperature in order to fit the red continuum would not only lead to contradictions with the observed Balmer jump but also with the fits obtained from the intermediate resolution spectra. As the light loss should not vary significantly across the Balmer jump we used as $T_{\rm eff}$ that of the model which fitted the Balmer jump best. Anyway, all results obtained for this star should be treated with some caution. Additionally we found some red excess in the low resolution spectrum of B 208 as well as an indication of a G band, which is probably due to stray light from a nearby red star (B 214, see above). Fitting only the Balmer jump and ignoring the red excess leads to atmospheric parameters consistent with those obtained from the medium resolution spectra (where no G band is seen). It is not possible to fit the Balmer jump and the continuum simultaneously with one Kurucz model.

After deriving the effective temperatures this way from the low resolution spectra we fitted the medium resolution spectra, interpolating along $\log g$ in steps of 0.1 and keeping the temperature fixed to the value found before. For that purpose the flux-calibrated intermediate resolution spectra were corrected for velocity shifts, then coadded and normalized by eye. Using the Doppler shifts of the Balmer lines we derived the radial velocities. The heliocentric[9] velocities derived from those shifts are given in Table 1 and we estimate their error (from the r.m.s. scatter of velocities derived from individual lines) to be about ±30 km/s.

In order to allow a comparison between model spectra and observed data we convolved the theoretical line profiles to the resolution of the observed spectra, which had been derived from the FWHM of the calibration lines. This was normally no problem as the seeing during our observations usually was around $2''$ (and thus well represented by a $2''$ slit width) with one exception: During the night in 1992 when we observed B 276, B 421, and B 686 the seeing was considerably better ($\approx 1''$) and we derived the resolution of these spectra for the determination of the atmospheric parameters using the seeing value of this night. Using the $2''$ resolution in this case would lead to too low values for $\log g$. To find the best fitting value of $\log g$ we computed for each of the blue Balmer lines (H_β, H_γ, H_δ – there were no theoretical line profiles available for the higher lines at that time and they were very noisy anyway) the squared difference between the observed spectrum and the theoretical line profile within ± 40 Å around the line center. We used the sum of these differences as estimator for the quality of the fit (see Fig. 9, right panel).

In order to test the reliability of our results we determined the effective temperature of BD+33°2642 by fitting the low resolution spectrum we had observed for this star. We found that the best fit was achieved for $T_{\rm eff}$ = 21,000 K and $\log g$ between 3 and 3.5. Using the intermediate resolution spectra we obtained the best fit at $T_{\rm eff}$ = 21,000 K for $\log g = 2.9$. These results correspond extremely well to those of Napiwotzki et al. (1994), who found $T_{\rm eff}$ = 21,000 K and $\log g = 3.0$.

The results for the programme stars obtained this way are summarized in Table 3a and plotted in Fig. 10a (left panel). As can be seen all stars have effective temperatures below about 20,000 K and therefore are hot HB (*not* EHB) stars according to their atmospheric parameters (independently of their position in the colour-magnitude diagram).

For some stars no low resolution spectra are available but only *UBV* photometry by Buonanno et al. (1983a). In these cases we have chosen the reddening-free Q index as temperature indicator by comparing it to the theoretical values of Kurucz (1992), thereby defining one curve in the $T_{\rm eff}$–$\log g$ plane. The Balmer line profile fits provide another curve when we use the fits with minimal errors (see Moehler & Heber 1998 and de Boer et al. 1995 for examples of this method). The error in $T_{\rm eff}$ of these results is probably somewhat larger because the Q index is less sensitive to $T_{\rm eff}$ than spectrophotometric data. Due to the temperature range involved, however, Q is still a rather good indicator for $T_{\rm eff}$, becoming rather insensitive for $T_{\rm eff} \geq$ 25,000 K (cf. Moehler et al. 1990b). In addition, Durrell & Harris (1993) find that the photographic photometry and their own CCD photometry give

---

[9] Moehler et al. (1995a) erroneously cite those velocities as corrected to local standard of rest.

similar values for stars in both samples. We assume that using this method we get an error in $\log T_{\rm eff}$ of about 0.04 dex (corresponding to ±1100 K at $T_{\rm eff}$ = 12,000 K). For $\log g$ we assume the error to be 0.2 dex. Three stars (B 18, B 440, and B 484) turned out to lie below 8500 K. In this region the Balmer lines depend stronger on $T_{\rm eff}$ than on $\log g$. Here we used the Balmer lines to estimate the temperature and the Q value to derive $\log g$. The results for these three objects are assigned a larger error in $\log g$ (0.3 dex) than the stars for which we derived $\log g$ from the Balmer line profiles. The results are listed in Table 3d and plotted in Fig. 10c (left panel).

We checked the $T_{\rm eff}$ values predicted by the Q-value also for the stars where low resolution spectra were available. For three objects (B 1, B 20, B 208) the $T_{\rm eff}$ values derived this way were much higher (4000 – 8000 K) than those derived from the spectrophotometric analyses. For B 574, B 421, and B 276 the differences were below 1000 K.

In order to check for systematic errors introduced by our method of analysis we determined $T_{\rm eff}$ and $\log g$ in a second run solely from the Balmer lines. This method has been widely used in the analysis of white dwarfs (e.g. Daou et al. 1990) and has also been applied to sdB analyses by Saffer et al. (1994). We then used as atmospheric parameters those values that yield the smallest residual, although this minimum normally was a rather shallow one (probably due to the lack of the higher Balmer lines, which constrain the fit). For the resulting fits to the line profiles and the low resolution spectrum of B 686 see Fig. 9 (lower panels). Note, however, that the low resolution spectra can in most cases **not** be fitted with the physical parameters obtained this way. The results are listed in Table 3b and plotted in Fig. 10b (left panel). Some stars now lie between 20,000 K and 25,000 K which is the transition region between hot HB and EHB stars. But also here several stars from the region below the gap show temperatures below 20,000 K.

As a compromise we decided to derive the atmospheric parameters iteratively: At first we determined the squared differences for the Balmer lines (as described above) using the grid provided by Kurucz with steps in $\log g$ of 0.5 dex (steps in $T_{\rm eff}$ were 1000 K for $T_{\rm eff}$ between 13,000 K and 30,000 K, 500 K for $T_{\rm eff}$ between 10,000 K and 13,000 K, and 250 K for $T_{\rm eff}$ below 10,000 K). Taking the five smallest values gave us a range of effective temperature and surface gravity. Taking the ($T_{\rm eff}$, $\log g$) combinations found by the method described above we tried to fit the Balmer jump and the continuum of the low resolution spectra. Thereby we defined the effective temperature of the star as these observations are sensitive mainly to $T_{\rm eff}$ (for temperatures above 10,000 K) and much less to $\log g$.

While the solutions obtained from the medium resolution spectra extend to higher $T_{\rm eff}$ (and $\log g$) than those obtained from the low resolution spectra, we could in most cases achieve a good fit for the low resolution data with a $T_{\rm eff}$, $\log g$-combination within the range derived from the best fits of the medium resolved data. Only in one case (B 276) the two regions were apart by about 4000 K (see also above). Here we kept the temperature obtained from fitting only the Balmer jump region of the low resolution spectrum. After deriving the effective temperature this way from the low resolution spectra we fitted the medium resolution spectra again, now interpolating along $\log g$ in steps of 0.1 and keeping the temperature fixed to the value found before. As we used already a combination of photometric and spectroscopic data for those stars which do not have any low resolution data we keep these results.

We assume that using this method we get an error in $\log T_{\rm eff}$ of about 0.03 dex (corresponding to ± 1300 K at $T_{\rm eff}$ = 18,000 K). For $\log g$ we assume the error to be 0.2 dex. The results are given in Table 3c and plotted in Fig. 10c (left panel). The gap in the CMD is marked in the $T_{\rm eff}$–$\log g$ diagram by a short-dashed line (Fig. 10a – c, left panels). Other gaps on the hotter part of the HB are due to observational selection effects. All stars below the gap are displaced from the zero-age HB towards lower gravities, in some cases even beyond the terminal-age HB (helium exhaustion in the core).

Table 3. Atmospheric parameters and masses for stars in M 15. The numbers of the stars refer to Buonanno et al. (1983a) and Battistini et al. (1985).

number	(a)			(b)			(c)		
	$T_{\rm eff}$ [K]	$\log g$ [cm/s^2]	M [M$_\odot$]	$T_{\rm eff}$ [K]	$\log g$ [cm/s^2]	M [M$_\odot$]	$T_{\rm eff}$ [K]	$\log g$ [cm/s^2]	M [M$_\odot$]
1	18000	4.10	0.29	22000	4.70	0.59	19000	4.30	0.30
20	18000	4.40	0.45	20000	4.60	0.61	18500	4.40	0.43
208	16000	4.10	0.21	17000	4.20	0.24	17000	4.20	0.24
276	18000	4.20	0.14	24000	5.00	0.55	18000	4.20	0.14
421	19000	4.50	0.26	20000	4.60	0.30	19000	4.50	0.26
574	19000	4.40	0.38	23000	4.90	0.88	20000	4.60	0.56
686	17000	4.20	0.19	23000	5.00	0.65	18000	4.30	0.19
number				(b)			(d)		
				$T_{\rm eff}$ [K]	$\log g$ [cm/s^2]	M [M$_\odot$]	$T_{\rm eff}$ [K]	$\log g$ [cm/s^2]	M [M$_\odot$]
18				8000	3.30	0.84	8000	3.50	1.34
27				12000	3.40	0.25	12500	3.50	0.29
258				11000	3.30	0.26	11500	3.50	0.39
325				15000	3.80	0.37	18000	4.30	0.88
348				12000	4.20	1.52	11500	4.00	1.02
440				7750	3.70	3.21	7750	3.00	0.63
484				8000	3.20	0.73	8000	3.00	0.44

(a) $T_{\rm eff}$ only from continuum, $\log g$ from Balmer lines
(b) parameters only from Balmer lines
(c) parameters from combination of continuum and Balmer lines
(d) parameters from combination of Q index and Balmer lines

3.2.3 Interstellar reddening

Using $T_{\rm eff}$ and $\log g$ we can determine $(B-V)_0$ from Kurucz (1992) and thus derive E_{B-V} from our data. We get a value of $0^{\rm m}.12 \pm 0^{\rm m}.02$ (r.m.s. error). Most stars have an individual reddening within 3σ of this value. The exceptions are B 18 and B 484 with too small values ($E_{B-V} = 0^{\rm m}.0$ and $0^{\rm m}.02$, resp.), and B 325, which has a reddening of $0^{\rm m}.28$. We assume that this may be due to some (physical or optical) companion, which reddens and increases the flux and thus renders the Q-value invalid (because the definition of Q attributes all reddening to interstellar extinction). The other possibility would be that there is some error in its colours (cf. Sect. 3.2.5). The values derived for B 325, esp. the mass, in any case will not be reliable.

Our value for E_{B-V} is somewhat larger than the one listed in the compilation of Pryor & Meylan (1993, see also the discussion by de Boer 1985). Their reddening, however, is lower than any other value obtained for M 15 and in contradiction with the results of Durrell & Harris (1993, $0^{\rm m}.10$) and Buonanno et al. (1985, $0^{\rm m}.10$, see also discussion there). We therefore decided to keep $E_{B-V} = 0^{\rm m}.10$ for all further computations.

3.2.4 Evolutionary Status

The derived $T_{\rm eff}$ and $\log g$ are plotted in Fig. 10a–c (left panels) and compared to the prediction of stellar evolution theory, i.e. the position of the ZAHB for a helium abundance on the main sequence of $Y_{MS} = 0.246$ and [Fe/H] = -2.26 (Dorman et al. 1991) as well as the position of the terminal age HB (TAHB, core helium exhaustion). These represent HB calculations *"based on input parameters which have been carefully derived from representative red giant branch precursors"* (Dorman 1992b). The position of the TAHB has been estimated from Fig. 3a of Dorman et al. (1993). All stars tend to lie above the ZAHB and even slightly above the TAHB irrespective of the method of analysis used.

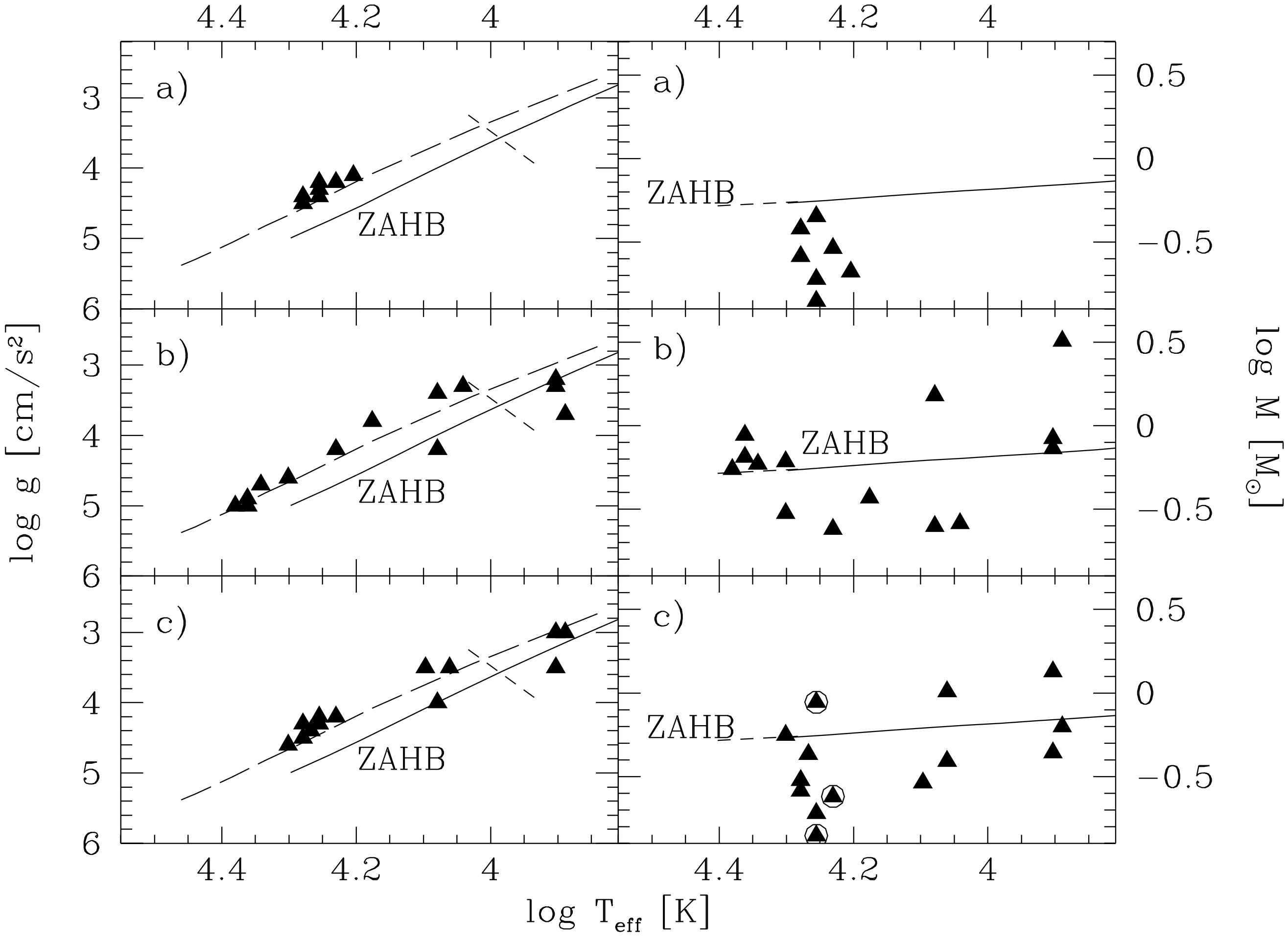

Fig. 10. $\log T_{\rm eff}$–$\log g$ (**left panels**) and $\log T_{\rm eff}$–log M (**right panels**) plots of the stars analysed in M 15. The solid line always represents a ZAHB model taken from Dorman et al. (1991) with [Fe/H] = −2.26 ($Y_{\rm MS} = 0.246$, [O/Fe] = 0.75).

a) $T_{\rm eff}$ only from low resolution spectra, $\log g$ from Balmer lines

b) $T_{\rm eff}$, $\log g$ from Balmer lines only

c) $T_{\rm eff}$, $\log g$ from combination of low resolution spectra (resp. Q index) and Balmer lines

Left panel The long dashed line marks the position of the HB at the time of helium exhaustion in the core (TAHB). The short dashed line depicts the gap seen along the HB in the CMD.

Right panel The short dashed line represents an extension of the ZAHB towards higher temperatures taken from Sweigart (1987) for $Y_{\rm MS} = 0.20$ and [M/H] = −2.3. The stars marked in panel **c)** are B 208, B 325, and B 276, for which the masses should be treated with great caution (see text).

This phenomenon is already known from field HBB and sdB stars (Schmidt et al. 1992, Moehler et al. 1990b, but see also Saffer et al. 1994, 1997 for different results).

In Fig. 11 we compare the positions of the programme stars in the ($\log T_{\rm eff}$, M_V)-diagram to the location of the HB, where the absolute magnitudes are calculated from the measured apparent magnitudes and the distance modulus ($(m - M)_V = 15\overset{\rm m}{.}43$). Again the programme stars tend to lie above the theoretical ZAHB taken from Dorman et al. (1991) but below or close to the TAHB, which has been estimated from Fig. 3a of Dorman et al. (1993) (except B 325, which is not very trustworthy anyway, as discussed in Sect. 3.2.2).

The observed positions of the hot HB stars in the $\log g$–$T_{\rm eff}$ diagram could be fitted by models having a larger helium abundance (see Figure 2 of Dorman et al. 1993), i.e. $Y_{HB} > 0.25$ and/or increased CNO abundances (see Dorman 1992a). Note that this does not imply that the primordial

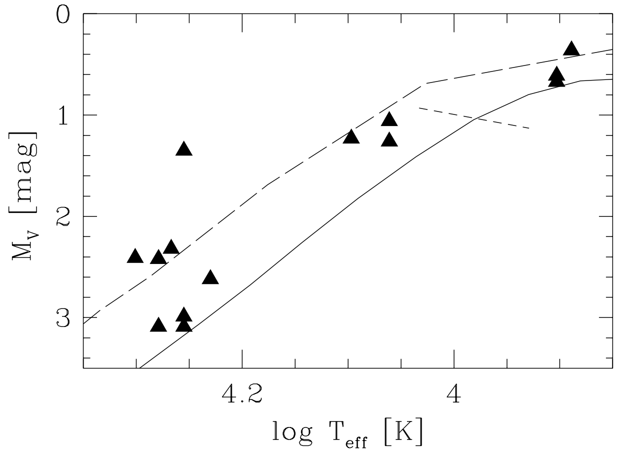

Fig. 11. $T_{\rm eff}$–M_V plot of the stars analysed in M 15. The solid line represents a ZAHB model taken from Dorman et al. (1991) for [Fe/H] = −2.26 (Y_{MS} = 0.246, and [O/Fe] = 0.75). The long dashed line marks the position of the HB at the time of helium exhaustion in the core. The short dashed line depicts the gap along the HB. M_V was derived using $(m-M)_V = 15\overset{\rm m}{.}43$.

helium abundance Y_{MS} had been that large. However, an increased helium abundance for the HB stars of M 15 appears to be at variance with the analysis of the HB morphology by Dorman et al. (1991), who concluded that the envelope helium abundance of the horizontal branch stars (including RR Lyrae stars) is in the range $0.21 < Y < 0.25$.

3.2.5 Determination of the stellar masses

Knowing the surface gravities and the effective temperatures of the stars we can determine the visual brightness at the surface of the star using model atmospheres (Kurucz 1992) and, combining it with the measured apparent visual brightness, the angular diameter of the star. As we also know the distances of the stars we then can derive the physical diameter of the star and from that deduce its mass:

$$\log\,({\rm M/M_\odot}) = const. + \log\ g + 0.4 \cdot ((m-M)_V - V + V_{th})$$

with the theoretical brightness at the stellar surface V_{th} as given by Kurucz 1992. The apparent visual magnitudes of the stars are taken from the photographic photometry of Buonanno et al. (1983a) and Battistini et al. (1985). The errors of the masses we derive can be divided into two groups: individual errors, affecting the mass of each star in a statistical way, and systematic errors, which have the same influence on all measurements. To the individual errors contribute the errors in $T_{\rm eff}$ and $\log g$ (and the uncertainty in the theoretical brightness that is introduced this way) and the error in the measured V brightness, which we assume to be $0\overset{\rm m}{.}1$. Together this translates into uncertainties of the masses of about 50% for hot stars ($T_{\rm eff}$ above 10,000 K) and 80% for cool stars ($T_{\rm eff}$ below 10,000 K). Assuming errors of $0\overset{\rm m}{.}1$ for the true distance moduli $(m-M)_0$ and $0\overset{\rm m}{.}05$ for E_{B-V} we get a systematic uncertainty of about 10% that would shift all masses in the same direction. The distance modulus taken for M 15 can be found in Table 8, but for the reddening we used $0\overset{\rm m}{.}10$ instead of $0\overset{\rm m}{.}05$ as given there (see also Sect. 3.2.3). The resulting masses are listed in Table 3a–d and plotted in Fig. 10a–c (right panels).

Results from three methods

The masses we get when we derive $T_{\rm eff}$ only from the Balmer jump are rather low. Comparing them in Fig. 10a (right panel) to a theoretical zero age HB (ZAHB) taken from Dorman et al. (1991) shows that the derived masses are well below the theoretically expected values for all stars.

Fitting only the Balmer lines results in rather low masses for $T_{\rm eff}$ between 10,000 and 19,000 K (except for B 348). For higher temperatures the masses are more consistent with the ZAHB than before (see Fig. 10b, right panel), for lower ones we have a big scatter. Within the lower temperature range the derivation of both parameters from the line profiles only should be treated with great caution anyway, as the line profiles here are mainly sensitive to $T_{\rm eff}$ and hardly to $\log g$.

The "compromise" method also yields "compromise" masses that are in most cases rather low (cf. Fig. 10c, right panel). For the three stars above the gap (B 18, B 440, B 484) the masses show again a large scatter with a (not very meaningful) mean value of $(0.80 \pm 0.40)\,{\rm M}_\odot$ (r.m.s. error), somewhat above the value predicted by stellar evolution theory. Taking into account the fact that the determination of the atmospheric parameters for these three stars is less accurate than for the hotter ones we consider this result reasonable. B 208, B 276, and B 325 are marked with circles in Fig. 10c (right panel) because we do not trust these mass determinations. Therefore they are also not used in the further discussions. The mean mass of the remaining eight stars below the gap is $0.43 \pm 0.24\,{\rm M}_\odot$(r.m.s. error).

3.2.6 Possible Errors

As the masses and surface gravities obtained for the stars below the gap are quite improbable we checked our analysis for any possible systematic effects. Some assumption used for the calculations of Kurucz model atmospheres may not be appropriate for the analysis of the stars discussed here. We want to discuss some conceivable possibilities here, i.e. variations of helium and metal abundances, vertical stratification of the He/H ratio, and stellar rotation.

(i) Most HBB and sdB stars in the field are known to be helium poor which is generally believed to be caused by diffusion. The assumption of a solar helium abundance for the BHB and blue tail stars in M 15 stars is therefore probably invalid. To check the effect of low helium abundances we fitted the low resolution spectra using models with a helium abundance of 1/10 solar value. The results were the same as for the models with solar helium abundance, which means that any differences in the flux distributions are too small to be recognized with the resolution and S/N of our data (see also Theissen et al. 1995).

(ii) Diffusion might also lead to peculiar abundance patterns such as observed in the Cp stars, because radiative levitation might push up some elements into the atmospheres whereas others (like He) might move down due to gravitational settling. Line blanketing effects of enhanced metals may change the atmospheric structure. As a crude test of this hypothesis we fitted our data with models for metallicities of −3.0 and 0.0 (i.e. solar). For the solar metallicity $T_{\rm eff}$ derived from the Balmer lines decreased by about 2000 K, $\log g$ by about 0.1 dex[10]. The temperature obtained from the low resolution spectra alone, however, decreased only by some 500 K. For a given $T_{\rm eff}$ $\log g$ is about 0.1 dex higher for $[{\rm M/H}] = 0$ than for $[{\rm M/H}] = -2.0$. For the compromise solution we got $T_{\rm eff}$ 500–1000 K lower and $\log g$ 0–0.05 dex higher than for $[{\rm M/H}] = -2.0$. For metallicity −3.0 neither $T_{\rm eff}$ nor $\log g$ derived from the Balmer lines changed. Only the temperature obtained from the low resolution spectra increased by about 500 K. For a given $T_{\rm eff}$ $\log g$ stayed the same as for metallicity −2.0. The compromise method resulted in $T_{\rm eff}$ about 500 K and $\log g$ about 0.05 dex higher than before. The masses derived from the compromise results differed by about 10% from those given in Table 3c. As such a large increase in line blanketing (as simulated by using solar metallicity model atmospheres) was deemed unlikely we ruled out metallicity variations as reason for our discrepancies (but see Sect. 4.4.2 for a more recent view of this topic). Also the fact that we could fit the low resolution spectra quite well with the metal-poor model atmospheres was considered an argument against this hypothesis. Note that unresolved metal line blends to the strategic Balmer lines (which we do not account for) would result in even lowering $\log g$ when taken into account.

---

[10] This is consistent with the findings of Leone & Manfrè (1997) that Balmer-line gravities can be underestimated by 0.25 dex if a solar metal abundance is assumed for metal-rich helium-weak stars.

(iii) Another effect of diffusion might be that the atmospheres could be stratified in helium content, i.e. that the helium abundance is increasing with depth. Such an effect has been predicted for white dwarf atmospheres (see Jordan & Koester 1986). But only for very few white dwarfs observational evidence for stratification has been found up to now. Farthmann et al. (1994) found evidence for vertical helium stratification in the atmosphere of the helium-weak main-sequence star HD 49333. Helium stratification, however, could affect the predicted Balmer jump significantly only if the transition from low to high He abundance occurs at an optical depth intermediate between the formation depths of the Paschen and the Balmer continua. Such a fine tuning is highly unlikely to occur.

(iv) Rapid rotation of the stars would also effect the gravity determination. Neglecting it results in too low gravities. This effect, however, becomes significant only if the rotation velocity exceeds about half of the break-up velocity. However, measured rotation velocities for hot HB stars are very small (Peterson 1994, Peterson et al. 1995b, Behr et al. 1999b) so that this possibility can be ruled out as well.

If we assume that there is no error in our analysis the remaining possibility would be an error in the photometric data, much larger than the one we assumed. To check this we computed the mean ratio between our masses and the values predicted by theoretical ZAHB's. For this computation we left out the masses of B 208, B 276, and B 325, which we think to be less reliable than the others. The mass ratios of the remaining eleven stars were averaged with their inverse relative errors as weight, which led us to a mean ratio of 0.79 (taking all stars results in the same value). This result would imply that either the individual brightnesses or the distance modulus are wrong by about $-0\overset{\rm m}{.}26$, which is quite high. Such an error in $(m-M)_V$ would correspond to a distance error of about 13%. This would, however, result in lowering M_V and thus shift the stars of M 15 above the TAHB in Fig. 11. As M 15 is a rather well studied cluster we thought that this was not very likely (see, however, Sect. 4.3 for a more recent view on this topic). Concerning the individual brightnesses one should recall that Durrell & Harris (1993) find that their results are quite consistent with those of Buonanno et al. (1983a).

3.3 NGC 6752

3.3.1 Observations and Data Reduction

We selected 17 blue stars from Buonanno et al. (1986) for follow-up spectroscopy. These stars are marked in Fig. 12 with squares. Open asterisks in this figure mark the stars discussed by Heber et al. (1986). Nine stars lie below the gap in the CMD ($V > 17\overset{\rm m}{.}0$), five stars are in the gap region ($16\overset{\rm m}{.}0 \leq V \leq 17\overset{\rm m}{.}0$) and three stars are above the gap ($V < 16\overset{\rm m}{.}0$), two of which have very blue colours. All optical spectra were obtained at telescopes of the ESO La Silla observatory using focal reducers. For calibration purposes we always observed 10 bias frames each night and 5-10 flat-fields with a mean exposure level of about 10,000 counts each. We obtained low resolution spectrophotometric data with large slit widths to analyse the flux distribution and medium resolution spectra to measure Balmer line profiles and helium line equivalent widths. The atmospheric extinction was corrected using the data of Tüg (1977) and the data for the flux standard stars were taken from Hamuy et al. (1992).

In 1992 we used EFOSC1 at the 3.6m telescope with a seeing between $1\overset{\prime\prime}{.}5$ and $2''$. Details of the setup are given in Table 4. Since the RCA chip showed some column structure we took flat-fields using U and B filters to achieve mean count levels between 5 and 10,000 counts to allow a correction of the column structure. As flux standard star we observed Feige 110. During these observations the slit angle was kept at its default east-west orientation.

In 1993 we observed with EMMI at the NTT, using the two-channel mode for the low resolution spectrophotometric observations to get a longer wavelength base. Seeing values for these observations varied between $0\overset{\prime\prime}{.}8$ and $1\overset{\prime\prime}{.}5$. Since no EMMI grism allows observations below 3600 Å (necessary to

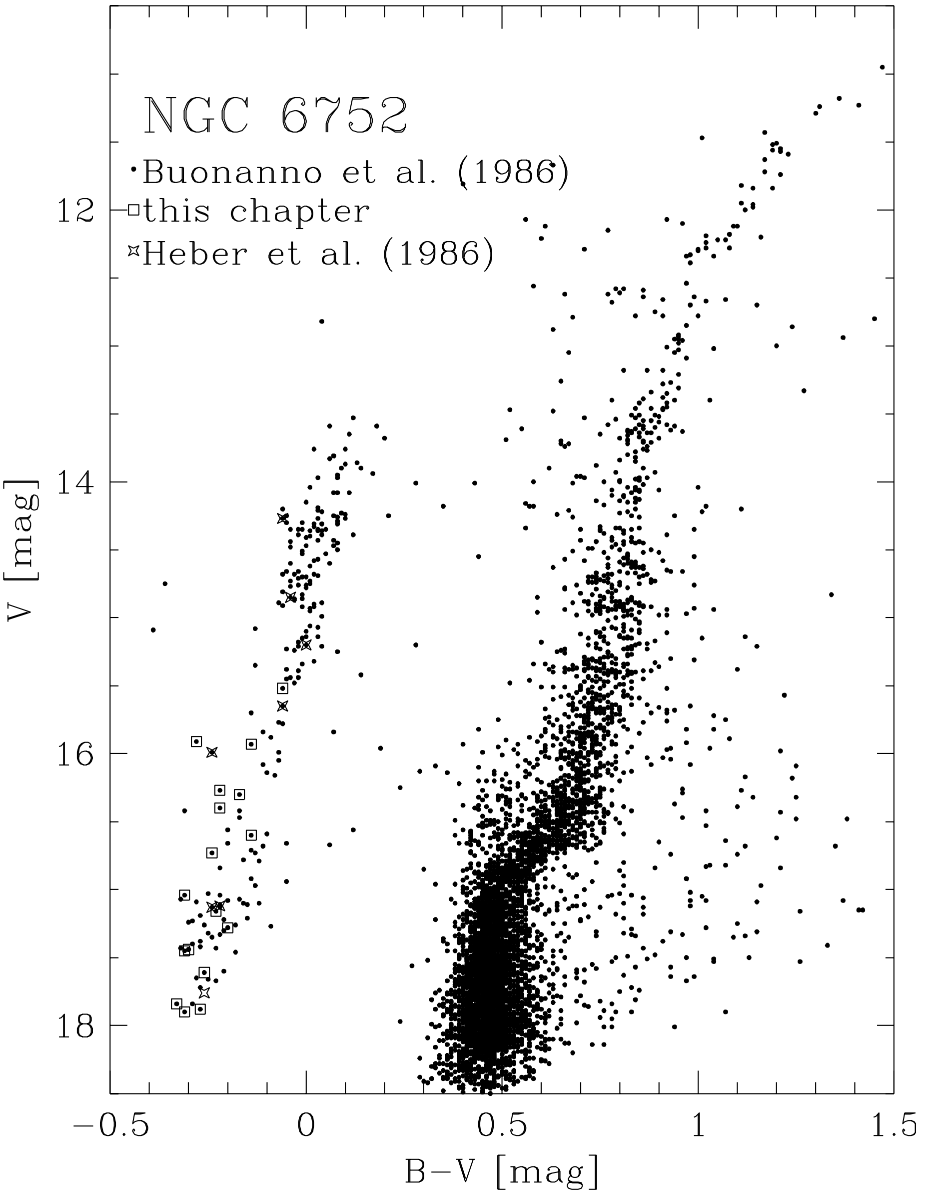

Fig. 12. The colour-magnitude diagram of NGC 6752 (Buonanno et al. 1986). Stars analysed in this chapter are marked by open squares, open asterisks mark the objects discussed by Heber et al. (1986). The star 3-118 of Heber et al. is not in the Buonanno data.

measure the Balmer jump) we used a grating in the blue channel and reduced the dispersion by binning along the dispersion axis by a factor of 3. For the intermediate resolution spectra we used only the blue channel and did not bin. The slit was kept at its default east-west orientation (= 0 °) except for the spectrophotometric observations of B 2395 (75 °), B 4009 (75 °), and B 4548 (85 °). Positive angles mean anti-clockwise rotation. Since we used a narrow slit for the medium resolution observations and did not try to align the slit along the parallactic angle (to correct for atmospheric dispersion) there are some slit losses at the blue end of the medium resolution spectra. As flux standard stars we used LTT 6248, LTT 9491, and Feige 110.

In 1995 we used EFOSC2 at the 2.2m MPI/ESO telescope to re-observe the low-resolution spectrophotometric data obtained with EMMI (see Sect. 3.3.1).We only used the low resolution setup and had seeing values between 1″ and 1.″5. Unfortunately the two nights we had were not really photometric. As we had observed the standard stars quite frequently we could, however, check the photometric

Table 4. Observational parameters for NGC 6752

Instrument/ Mode	Date	Telescope	CCD	pixel size [μm^2]	no. of pixels	conv. factor [e$^-$/count]	read-out noise [e$^-$]
EFOSC1	1992/07/04-07	3.6m	RCA # 8	15×15	656×1024	2.1	33
EMMI/B	1993/07/23-26	NTT	Tek # 31	24×24	1024×1024	3.4	5.7
EMMI/R			FA # 34	15×15	2048×2048	1.5	6.6
EFOSC2	1995/06/26-28	2.2m MPI/ESO	Th # 19	19×19	1024×1024	2.1	4.3

Instrument/ Mode	Slit width [″]	Grism/ Grating	Dispersion [Å/mm]	Wavelength range [Å]	wavelength calibration number of lines used	r.m.s. error [Å]	reso- lution [Å]
EFOSC1/low	5.0	UV300	210	3200 – 6400	11	0.5	12
EFOSC1/med	0.75	B150	120	3800 – 5600	12	0.3	4.6
EMMI/DIMD B	5.0	# 4	72	3400 – 5300	7	0.8	10
EMMI/BLMD B	1.0	# 4	72	3200 – 5100	15	0.3	5.7
EMMI/DIMD R	5.0	# 13	224	4000 – 8500	14	0.5	10
EFOSC2	5.0	# 1	442	1000 – 9400 (nominal)			
				3400 – 9400 (used)	16	1.7	47

conditions from the response curves. As flux standard stars we used EG 274 and Feige 110. During these observations we did not rotate the slit, but kept it at its default east-west orientation.

Reduction of EFOSC1 and EMMI data

We always averaged bias and flat-field frames for each night separately, since there were small variations in the bias frames (up to a few counts/pixel) and also a slight variation in the fringe patterns of the flat fields from one night to the next (below 5%). The dark currents were determined from several long dark frames and turned out to be negligible in all cases. To correct the electronic offset we scaled the bias frames by the mean overscan value of the science frame. To take the spectral signature of the flat field lamp out of the averaged flat field frames we fitted a 5$^{\rm th}$ (7$^{\rm th}$) order polynomial to the blue (red) channel EMMI data. The EFOSC1 flat fields could not be fitted well enough by polynomials. We therefore averaged the mean flat-field of each night along the spatial axis, smoothed it heavily to erase all small scale structure and divided the original mean flat by the smoothed average. For the EFOSC1 data we also had to correct column structure. This correction was performed as described in Sect. 3.2.1.

All spectra were wavelength calibrated, sky subtracted and extracted as described in Sect. 3.2.1. The flat field correction and wavelength calibration turned out to be good enough that a linear (EFOSC1) or constant (EMMI) fit to the spatial distribution of the sky light allowed to subtract the sky background at the object's position with sufficient accuracy. This means in our case that we do not see any absorption lines caused by the predominantly red stars of the clusters or by moon light and that the night sky emission lines in the red part of the spectra could be corrected down to a level of a few percent of the stellar continuum.

Finally the spectra were corrected for atmospheric extinction and response curves were derived from the spectra of the flux standard stars. Normally the response curves were fitted by a 3$^{\rm rd}$ order spline, except the red EMMI data, for which we used a 6$^{\rm th}$ order polynomial. We took special care to correctly fit the response curves for the low resolution data in the region of the Balmer jump, since we will use this feature for the determination of the effective temperatures of the stars.

Comparing the EFOSC1 and EMMI low resolution data for the stars observed during both runs showed that the EFOSC1 data have significantly less UV flux blueward of the Balmer jump than

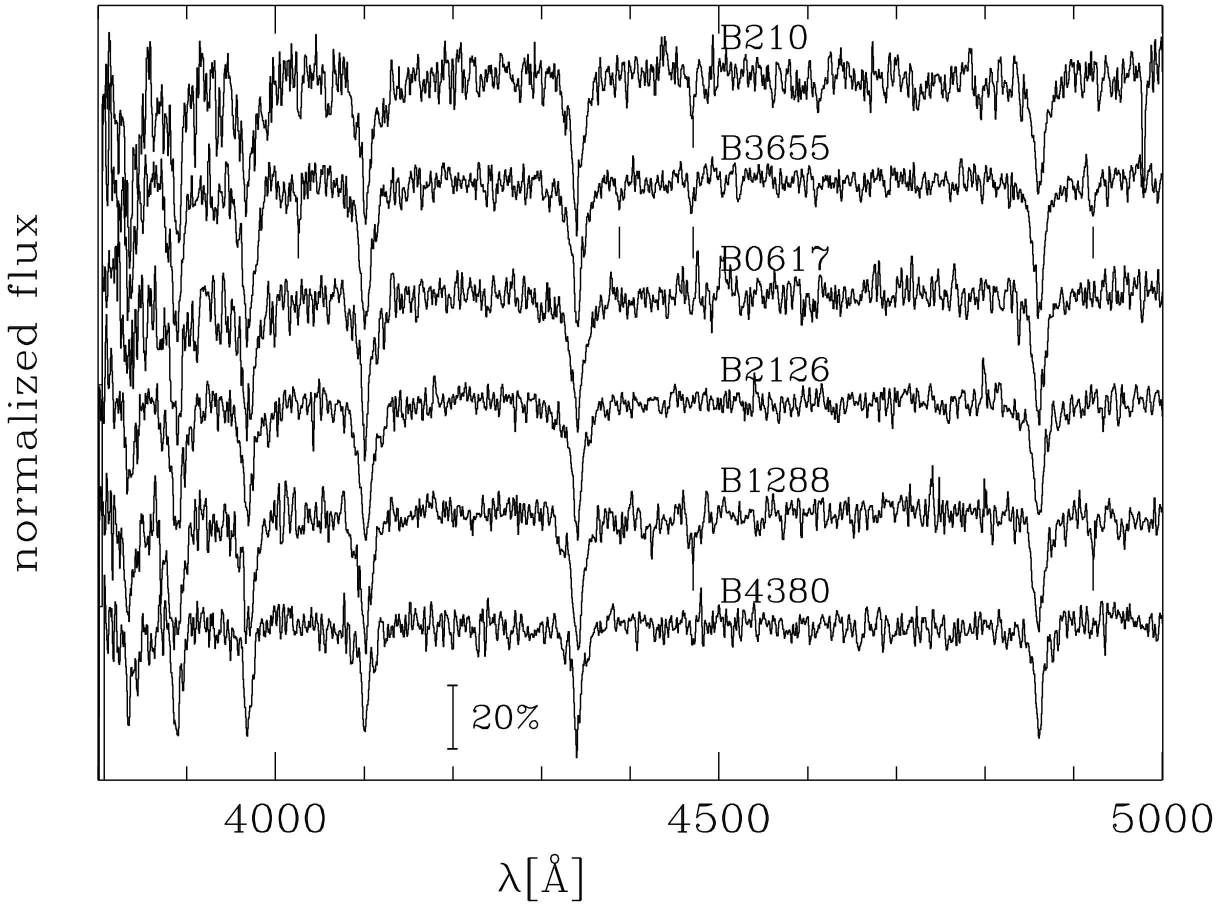

Fig. 13. Normalized medium resolution EFOSC1 spectra. The part shortward of 3900 Å was normalized by taking the highest flux point as continuum value. The spectra are sorted along decreasing Balmer line depths. The He I lines λλ 4026 Å, 4144 Å, 4388 Å, 4471 Å, 4922 Å and the Mg II line 4481 Å are marked (if visible in the spectrum).

the EMMI data. Since both sets of spectra could be fitted with Kurucz (1992) model spectra (but yielded temperatures different by up to 10,000 K) we could not decide which data set was the correct one and whether one or even both data sets were hampered by instrumental effects that were not removed by the described reduction. We discussed these problems extensively with people at ESO and finally decided to repeat the spectrophotometric observations with a third instrument (which decision resulted in the 1995 observations with EFOSC2).

The medium resolution spectra observed in 1992 and 1993 are plotted in Figs. 13 and 14. Besides the Balmer lines, He I lines can easily be identified in the spectra of several of the programme stars. In addition He II 4686Å is visible in B 852, which therefore has to be classified as spectral type sdOB according to the scheme of Baschek & Norris (1975). It is also worthwhile to note that weak Mg II 4481 Å absorption is detected in B 1509 and B 3975.

We also used the medium resolution data to derive radial velocities, which are listed in Table 5 (corrected to heliocentric system). The error of the velocities (as estimated from the scatter of the velocities derived from individual lines) is about 40 km/sec. Within error limits most of the radial velocities agree with the cluster velocity (−32.1 km/s, Pryor & Meylan 1993).

Reduction of EFOSC2 data

For the EFOSC2 data we averaged the bias and flat field frames over both nights of the run, as they showed no deviations above the 1% level. The bias correction was performed as described in

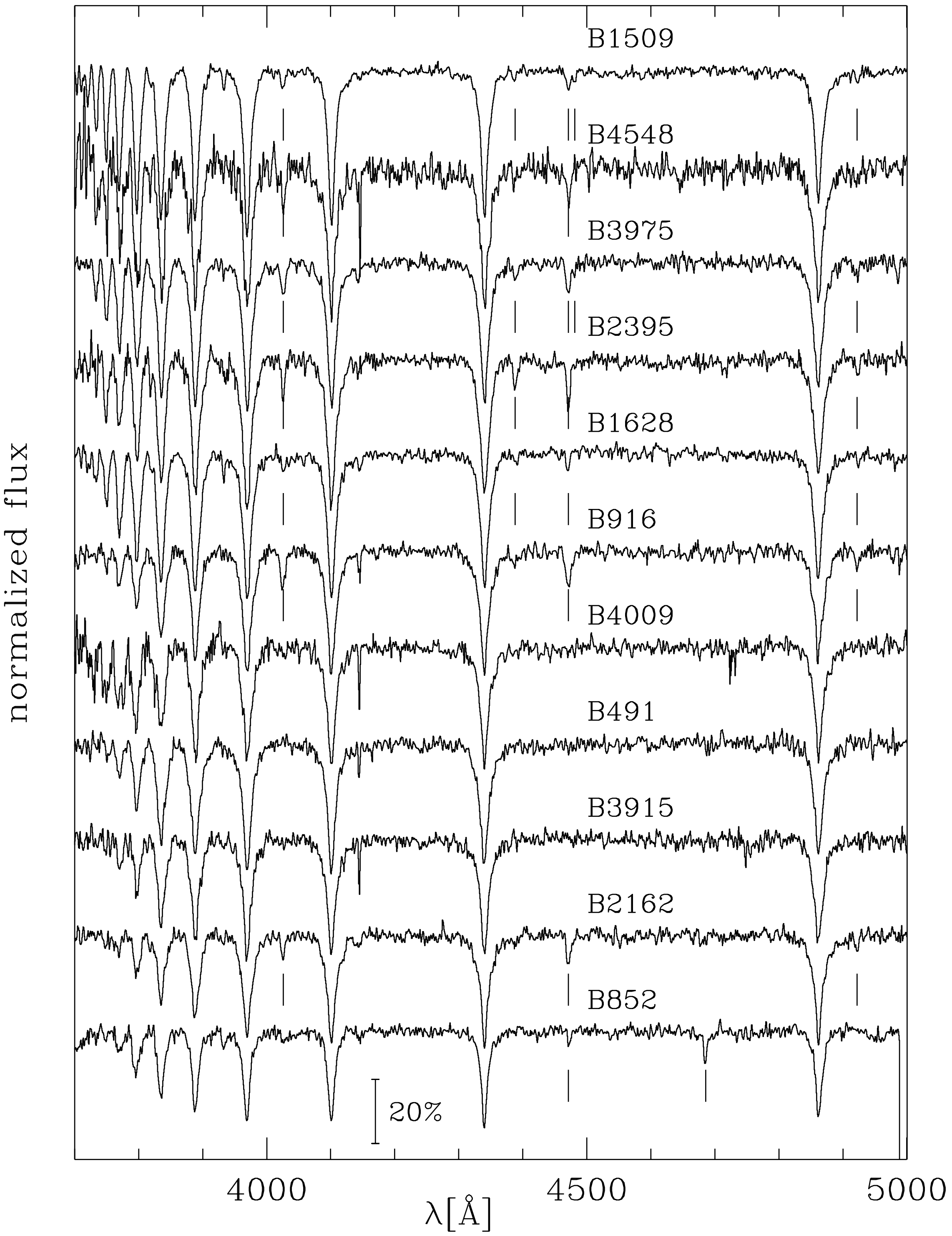

Fig. 14. Normalized medium resolution EMMI spectra. The part shortward of 3900 Å was normalized by taking the highest flux point as continuum value. The spectra are sorted along decreasing Balmer line depths. The He I lines λλ 4026 Å, 4144 Å, 4388 Å, 4471 Å, 4922 Å, He II 4686 Å, and the Mg II line 4481 Å are marked (if visible in the spectrum)

Sect. 3.2.1 and we did not correct for dark current. The normalization of the flat-field was somewhat difficult: We fitted a 7^{th} order polynomial to the flux distribution of the averaged flat fields, which did not fit well enough the UV/blue part. We therefore averaged and smoothed the flat as described for the EFOSC1 data and merged the UV/blue part of the smoothed averaged flat and the red part of the fit at a position where the two overlapped and had a similar slope. This merged frame was smoothed again before correcting the flat.

For the wavelength calibration we again used a $3^{\rm rd}$ order polynomial to fit the dispersion relation. However, while the wavelength calibration frames showed maximum deviations of 4 Å when rebinned using this dispersion relation, the science frames exhibited systematic shifts to the red in the order of 30 – 40 Å. The only difference between the two types of frames (beside the illumination) was the slit width, which was $1''$ for the calibration frames and $5''$ for the science frames. A possible explanation of this effect could lie with the fact that the polynomial fits normally used for wavelength calibrations are only an approximation to the true shape of the dispersion relation, which is described correctly by trigonometric functions (Strocke 1967, Bahner 1967). Tests performed by Rosa & Hopp (1995, priv. comm.) showed, however, that fits using such trigonometric functions are extremely unstable unless a very good guess of the true relation is already available. We therefore decided to correct the offsets by applying a mean shift of 36 Å to the blue.

Sky subtraction, extraction of the spectra, correction of atmospheric extinction, and flux calibration were performed as described in Sect. 3.2.1, using a constant for the spatial profile of the sky background and a spline fit for the response curve. As mentioned above we could judge the photometric quality of the observations from the response curves. We used only those response curves that yielded the maximum response since those should result from observations taken with minimum obscurations. Several object spectra calibrated with these response curves showed an offset from the B and V magnitudes taken from Buonanno et al. (1986), being about 0.2 mag too faint (indicating loss of light probably due to weather conditions). Although there was hardly any wavelength dependency of this offset visible we could not be sure that the absorption was truly grey. We therefore decided not to use these data for determinations of the effective temperatures because we could not rely on the continuum slope. They are marked in Table 5 by $\otimes$.

Comparison of the optical spectrophotometric data

Comparing the data for the three runs showed that the EMMI and the EFOSC2 data agreed rather well when a correction for the much lower resolution of the EFOSC2 data is applied (necessary to allow comparison of the Balmer jump region). This leads to the assumption that there is some problem with the UV response of the EFOSC1 that is not corrected by flux calibration. An additional reason could lie with the extraordinarily high extinction observed at La Silla in the years 1991 and 1992 (Burki et al. 1995). We therefore ignore all low resolution data obtained with EFOSC1 for the further analysis. As a consequence 5 (B 210, B 852, B 1509, B 1628, B 4380) out of 17 programme stars lack reliable spectrophotometric data. For an additional star (B 3915) we do not have any low resolution data at all.

IUE data

In addition to the observations described above low resolution vacuum UV spectra observed with the International Ultraviolet Explorer (IUE) are available from the archive for the stars B 491, B 916, B 4009, and B 4548. In addition to the standard reduction and calibration the correction for the new white dwarf flux scale as described by Bohlin et al. (1990) and Bohlin (1996) was performed. We also recalibrated the old IUE data used in Heber et al. (1986).

3.3.2 Model atmospheres

Effective temperatures, gravities, and helium abundances were derived using line blanketed LTE model atmospheres. Kurucz (1992) ATLAS9 models ($\log g$ = 5.0, solar He abundance) for [M/H] = −1.5 (closest to the cluster's metallicity, [Fe/H] = −1.54, Djorgovski 1993) were used to fit the energy

Table 5. Coordinates, observing runs, and heliocentric radial velocities for the stars in NGC 6752. The star numbers refer to Buonanno et al. (1986). For stars marked with * IUE SWP data are available. l (m) stands for low (medium) resolution spectra. × marks spectra observed with the respective setup, ⊗ marks low-resolution spectra obtained under non-photometric conditions. $v_{\rm rad,hel}$ is the heliocentric velocity as derived from the medium resolution spectra discussed here.

Star	α_{2000}	δ_{2000}	1992		1993		1995	$v_{\rm rad,hel}$
			l	m	l	m	l	[km/s]
B 210	$19^{\rm h}11^{\rm m}49\overset{\rm s}{.}4$	$-60^\circ05'24''$	×	×				−13
B 491*	$19^{\rm h}11^{\rm m}37\overset{\rm s}{.}7$	$-60^\circ03'11''$			×	×	×	+7
B 617	$19^{\rm h}11^{\rm m}33\overset{\rm s}{.}5$	$-60^\circ01'26''$	×	×	×		⊗	−28
B 852	$19^{\rm h}11^{\rm m}28\overset{\rm s}{.}5$	$-60^\circ00'33''$	×			×		0
B 916*	$19^{\rm h}11^{\rm m}27\overset{\rm s}{.}3$	$-60^\circ03'51''$			×	×	⊗	+12
B 1288	$19^{\rm h}11^{\rm m}20\overset{\rm s}{.}1$	$-60^\circ03'45''$	×	×	×		×	−27
B 1509	$19^{\rm h}11^{\rm m}15\overset{\rm s}{.}0$	$-59^\circ54'31''$	×	×		×		−33
B 1628	$19^{\rm h}11^{\rm m}11\overset{\rm s}{.}7$	$-59^\circ59'36''$	×			×		−21
B 2126	$19^{\rm h}11^{\rm m}03\overset{\rm s}{.}0$	$-59^\circ52'32''$	×	×	×			−25
B 2162	$19^{\rm h}11^{\rm m}01\overset{\rm s}{.}9$	$-60^\circ03'02''$			×	×	⊗	−36
B 2395	$19^{\rm h}10^{\rm m}57\overset{\rm s}{.}3$	$-60^\circ03'32''$			×	×	×	−52
B 3655	$19^{\rm h}10^{\rm m}30\overset{\rm s}{.}2$	$-59^\circ57'27''$	×	×	×			−19
B 3915	$19^{\rm h}10^{\rm m}24\overset{\rm s}{.}2$	$-59^\circ54'22''$				×		−9
B 3975	$19^{\rm h}10^{\rm m}22\overset{\rm s}{.}7$	$-60^\circ03'01''$			×	×		+18
B 4009*	$19^{\rm h}10^{\rm m}22\overset{\rm s}{.}2$	$-60^\circ07'47''$			×	×		−56
B 4380	$19^{\rm h}10^{\rm m}15\overset{\rm s}{.}0$	$-60^\circ01'10''$	×	×				−30
B 4548*	$19^{\rm h}10^{\rm m}10\overset{\rm s}{.}9$	$-59^\circ51'31''$			×	×	⊗	−65

distributions of the spectrophotometric data. To correct for interstellar reddening we applied the reddening law of Savage & Mathis (1979) and used an E_{B-V} of $0\overset{\rm m}{.}05$.

We expected some stars to have $\log g$ above 5 (typical for field sdB stars) and most of the stars to show helium depletion. Therefore we used ATLAS9 model atmospheres (Kurucz 1992) to calculate model spectra with an updated version of the code of Heber (1983), using ATLAS6 opacity distribution functions (ODF), [M/H] = −2.0, and a helium abundance of $\log \frac{N_{He}}{N_H} = -2$. These models were used to analyse the hydrogen and helium line spectra in order to account for the appropriate gravities and helium abundances. As these models were computed for [M/H] = −2.0 (instead of −1.5) and sub-solar helium abundance we fitted the Kurucz hydrogen line profiles for $T_{\rm eff}$ = 22,000 K and $\log g = 5.0$ by Heber models of [M/H] = −2.0. The use of different generations of ODF's (ATLAS9 versus ATLAS6) and different helium abundances turned out to be negligibly small, both for $T_{\rm eff}$ and $\log g$. Hence, the following procedure was applied: The Balmer lines H_β, H_γ, and H_δ were fitted using Heber's models. At the final parameters ($T_{\rm eff}$, $\log g$) curves of growths for the He I lines 4026, 4121, 4388, 4471, and 4921 Å were constructed to determine the helium abundances from equivalent widths of these lines.

In order to allow a consistent treatment of the results of Heber et al. (1986), which were obtained with solar metallicity models, we checked the effect of the metallicity on $T_{\rm eff}$ and $\log g$ by fitting solar metallicity models with the [M/H]= −2.0 models we used now. We found out that the solar metallicity models yield effective temperatures about 1000 K lower than the metal poor models, but essentially the same $\log g$ values. We therefore increased the $T_{\rm eff}$ values of Heber et al. (1986) by 1000 K to account for the lower cluster metallicity and kept the $\log g$ values.

In the case of B 852 LTE models were found to be inappropriate due to its high effective temperature (see Napiwotzki, 1997). We used Napiwotzki's NLTE models (see Sect. 6.2.1), which do not include metal line blanketing. Therefore the temperature scale differs slightly from the metal line blanketed scale of Kurucz and Heber models. No attempt was made to adjust the derived temperature .

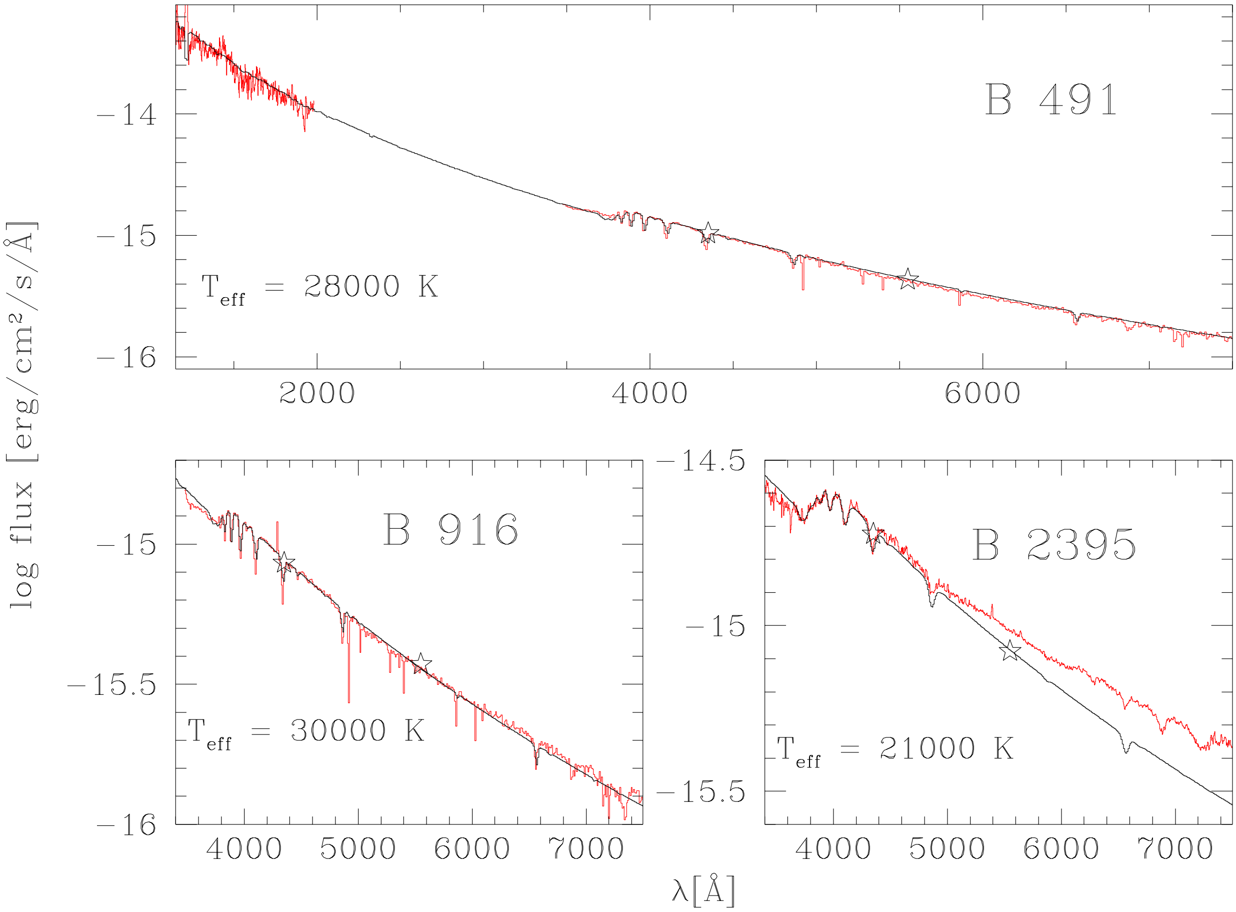

Fig. 15. Fits to low resolution data of B 491, B 916, and B 2395 (dark grey lines). The models (black lines) are ATLAS9 (Kurucz 1992) models of metallicity −1.5, all for $\log g = 5.0$. The asterisks mark the B and V fluxes derived from Buonanno et al. (1986) using the conversion factors given by Heber et al. (1984). The photometric fluxes as well as the observed spectra were dereddened using the reddening law of Savage & Mathis (1979). The fit to the low resolution spectrum of B 2395 clearly shows the red excess discussed on page 36f.

3.3.3 Atmospheric parameters

Effective Temperatures from IUE data

For the four stars which have vacuum UV spectra observed with IUE we tried to simultaneously fit the continuum data (IUE spectra, BV photometry, continuum of the low resolution optical spectra) and the Balmer jump (cf. Fig 15).

The same data have already been analysed by Cacciari et al. (1995) by calibrating UV-(1300 Å−1800 Å) and UV-visual (1800 Å−V) colours in terms of $T_{\rm eff}$ and $\log g$ using Kurucz model atmospheres. In all cases our effective temperatures were lower than the ones given by Cacciari et al. (1995). This can be traced back to the use of different IUE flux calibrations. We used the most recent calibration of Bohlin (1996), yielding a flux at 1800 Å that is lower than the one of Cacciari et al. (1995) by 10%, thereby changing the (18-V) colour by 10%, which translates in a decrease of the effective temperature exactly as found when comparing our results to those of Cacciari et al. Overall, the corrections achieved by applying the curve of Bohlin (1996) were considerably smaller than those resulting from the correction curve used by Cacciari et al.

In view of this flux calibration problem, we also went back to the IUE data for the stars analysed by Heber et al. (1986). We recalibrated the IUE spectra and fitted them together with the optical photometric data as described above. The new temperatures were always within 1000 K of the old values and no systematic trend showed up. We therefore decided to keep the old values and only adjust them for metallicity effects (see above).

Effective temperatures from optical data only

The simultaneous fitting of the spectrophotometric data (Balmer jump and continuum) and the B and V magnitudes worked well (cf. Fig. 15) in all cases except four: B 1628, B 2395, B 3655, and B 2126. B 1628 shows a strong red excess when compared to the B and V magnitudes and to the model fitting of the Balmer jump; the observed spectrum was also significantly brighter than the B and V magnitudes. The low resolution spectra of the stars B 2395 (cf. Fig. 15) and B 3655 both show a moderate red excess when compared to the model fitting the Balmer jump, which also reproduces the B and V magnitudes. In the case of B 2126 the optical spectrum agrees well with BV photometry, but both show a small red excess when compared to the model fitting the Balmer jump.

Cautioned by these findings we searched all stars for red neighbours. For this purpose we used the photometry of NGC 6752 by Buonanno et al. (1986), and extracted for each of our targets all stars within a radius of $20''$ (down to the limiting magnitude of $B \approx 18^{\mathrm{m}}\!.5$). We then estimated the straylight provided by these stars assuming that the seeing at larger distances is best described by a Lorentz profile and scaling the intensities with the V fluxes. We used $1''\!.5$ as “intrinsic seeing” for all observations (which overestimates some of the observed seeing values) and took into account the elongation caused by atmospheric dispersion. Under these assumptions we got stray light levels of more than 3% in V for the following objects: B 617, B 1288, B 1628, B 2162, B 2395, and B 3655. As expected we found the largest values for B 1628, B 2395, and B 3655, which were observed at relatively large zenith distances and have very bright neighbours. For those objects where the neighbour did not lie in the slit the observed stray light levels are lower than the calculated ones by a factor of 1.5 to 2. The calculated excesses for B 1288 and B 617 are about 7% and cannot be measured in our spectrophotometric data. Hence we can explain the above mentioned red excesses as being caused by stray light from nearby stars (except B 2126). At the same time we estimate the accuracy of our spectrophotometric calibration to be about 7%.

Since the Balmer lines (H_β, H_γ, H_δ) are diagnostic tools we also checked the stray light level in the medium resolved spectra. We used the same assumptions as above, but scaled the intensities with the B magnitudes. This results in straylight levels of at most 5% for B 617, B 1288, B 1509, B 1628, B 2162, B 2395, and B 3655. As the Balmer lines of cool stars are much weaker than those of our programme stars stray light from a cool companion will mainly affect the continuum. In order to estimate the effect of any additional continuum on the physical parameters we subtracted 5% of the continuum from the spectrum of B 2395, renormalized the spectrum and derived $T_{\rm eff}$ and $\log g$ again by fitting only the Balmer line profiles. It turned out that the best fit yielded an effective temperature of 1000 K less than before and the surface gravity remained the same.

Surface gravities from Balmer line profiles

We finally used as effective temperature the mean value of all available determinations, assessing the IUE temperatures double weight because of the superior sensitivity of UV data to $T_{\rm eff}$. Besides the internal errors quoted above we also have to account for systematic errors caused by the imperfections of models and data. These are estimated from the differences between various $T_{\rm eff}$ determinations for the same object to be about 7% in $T_{\rm eff}$ (cf. Table 6).

At the given final temperature we take that value of $\log g$ as surface gravity that yields the smallest errors for the Balmer line fits at this temperature. An error in $T_{\rm eff}$ of 7% translates into an error in $\log g$, which we estimated for the three groups of stars mentioned in Table 6: 0.1 dex for stars above the gap ($<T_{\rm eff}> = 15{,}000$ K); 0.15 dex for stars in the gap region ($<T_{\rm eff}> = 22{,}000$ K) and 0.2 dex for stars below the gap ($< T_{\rm eff}> = 29{,}000$ K). Added to these errors in $\log g$ are the internal errors

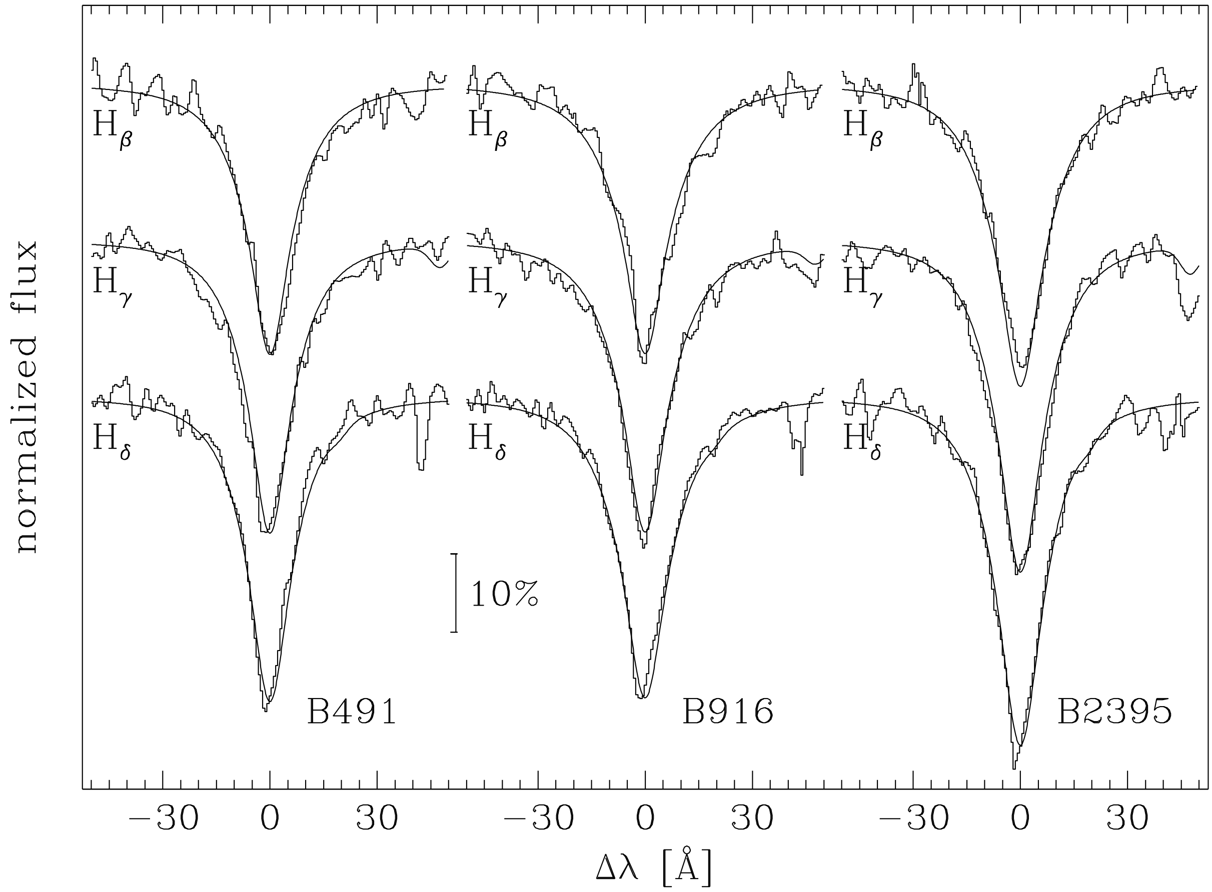

Fig. 16. Fits to medium resolution data of B 491, B 916, and B 2395. The models are those of Heber (1983) for those parameters which best fitted the Balmer lines:
B 491: $T_{\mathrm{eff}} = 28{,}000$ K, $\log g = 5.2$
B 916: $T_{\mathrm{eff}} = 30{,}000$ K, $\log g = 5.6$
B 2395: $T_{\mathrm{eff}} = 22{,}000$ K, $\log g = 5.0$

given by Saffer's fitting routine (see next paragraph). For the data given by Heber et al. (1986) we used the mean of the errors for the 1992 and 1993 data. This results in the following errors in $\log g$: stars above the gap (1992: 0.196; 1993: 0.115); stars in the gap region (1992: 0.225; 1993: 0.160); stars below the gap (1992: 0.261; 1993: 0.208).

Effective temperatures and surface gravities from Balmer line profiles

To check the validity of the effective temperatures obtained from the low resolution data we also determined T_{eff} and $\log g$ simultaneously by fitting the line profiles of H_β, H_γ, and H_δ. In most cases where low and intermediate resolution spectra are available the effective temperatures derived from both agree within the error limits (cf. Fig. 16 and Table 6). In one case (B 617) however, we find an effective temperature from the low resolution data of about 33,000 K, while the line profiles yield 25,000 K. Since this star is in colour and brightness comparable to B 1288 and B 2162, we assumed that the higher temperature is the valid one. The systematic offset between T_{eff} derived from low resolution data and from the Balmer line profiles reported in Sect. 3.2.2 for the stars in M 15 could not be verified with these data.

In order to get an estimate for the internal errors of the physical parameters derived from fitting the Balmer lines we used the independent line fitting code of Saffer (Saffer et al. 1994) to verify our results. It turned out that we got the same values for spectra with good S/N. For the spectra of 1992, which are considerably more noisy than the ones from 1993, we got systematically lower temperatures

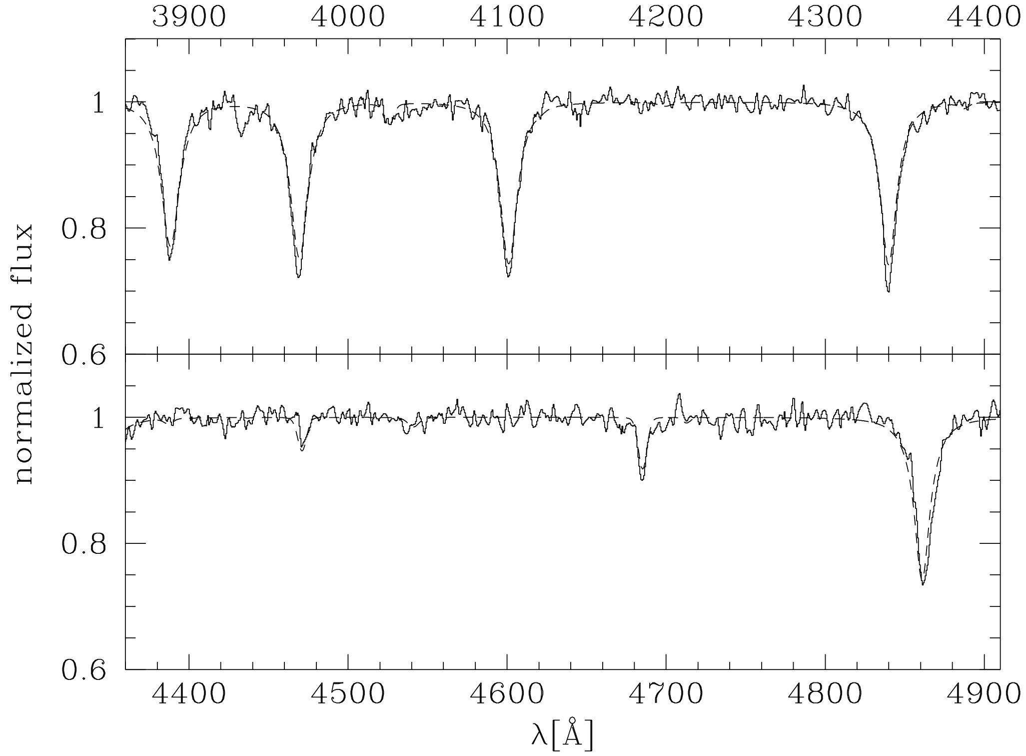

Fig. 17. Fit to medium resolution data of the sdOB star B 852. Overplotted is a Non-LTE model spectrum computed by R. Napiwotzki (priv. comm.) for a metal-free stellar atmosphere with a 0.1 solar helium abundance.

with Saffer's routine than from our line profile fits (using the same set of models). Since we could not reconcile the spectrophotometric data with the temperatures found by Saffer's routine we decided to keep our values. The mean internal error in $T_{\rm eff}$ provided by Saffer's fits are 1370 K (1992) and 460 K (1993); the mean internal error in $\log g$ is 0.17 dex (1992) and 0.06 dex (1993). Absolute visual magnitudes were derived from the apparent magnitude and the distance modulus ($(m-M)_V = 13\overset{\rm m}{.}24$, Djorgovski 1993). Note that the reddening free distance modulus of $13\overset{\rm m}{.}12$ of Djorgovski agrees within the error limits with the new distance modulus $(m-M)_0 = 13\overset{\rm m}{.}05$ derived by Renzini et al. (1996) from the white dwarf sequence. The results are listed in Table 6.

The case of B 852

B 852 is the only star in our sample which shows the He II 4686 Å line. Comparing its strength to that of the He I 4471 Å line suggests a temperature exceeding 35,000 K. At such high temperature deviations from LTE become important even for the relatively large gravities of hot subdwarf stars as demonstrated by Napiwotzki (1997). Therefore we used his NLTE models (see Sect. 6.2.1) to derive $T_{\rm eff}$, $\log g$, and helium abundance from H_β, H_γ, H_δ, He II 4686 Å and He I 4471 Å, the latter line ratio being a very sensitive $T_{\rm eff}$ indicator. The best fit is shown in Fig. 17. The depth of the observed Balmer line profile cores cannot be reproduced by the NLTE models, which we attribute to the lack of metal line blanketing. The helium lines are not affected by this effect and are reproduced very well. We therefore use the best fit values of $T_{\rm eff} = 40{,}000$ K, $\log g = 5.2$ and $\log \frac{N_{He}}{N_H} = -2.0$ as atmospheric parameters for B 852.

3.3.4 Helium abundances

From the medium resolution spectra we could also determine the helium abundances of the stars (if helium lines are seen) or at least upper limits. The measured equivalent widths of the He I lines are

Table 6. Physical parameters and masses for the stars in NGC 6752. The star numbers and $V, B-V$ data are taken from Buonanno et al. (1986), except for 3-118, whose data were obtained from Caloi et al. (1986). $T_{\rm eff,\mathit{UV}}$ is the effective temperature derived from IUE data, $T_{\rm eff,\mathit{opt.}}$ is the one from optical spectrophotometry and $T_{\rm eff,\mathit{opt.}}$ results from line profile fits. $T_{\rm eff,\mathit{final}}$ is the finally adopted effective temperature, which was used to derive the final $\log g$ and the mass. $(m-M)_V = 13.24$ was used to determine M_V.

Star	V	$B-V$	$T_{\rm eff,\mathit{UV}}$ [K]	$T_{\rm eff,\mathit{opt.}}$ [K]	$T_{\rm eff,\mathit{lines}}$ [K]	$T_{\rm eff,\mathit{final}}$ [K]	$\log g$ [cm/s^2]	M [M$_\odot$]	M_V
stars above the gap region									
B 577[1]	$14\overset{\rm m}{.}85$	$-0\overset{\rm m}{.}04$				13700[1]	3.9[1]	0.43	$+1\overset{\rm m}{.}61$
B 1509	$15\overset{\rm m}{.}52$	$-0\overset{\rm m}{.}06$			17000	17000	4.1	0.26	$+2\overset{\rm m}{.}28$
B 2454[1]	$14\overset{\rm m}{.}27$	$-0\overset{\rm m}{.}06$				10700[1]	3.5[1]	0.45	$+1\overset{\rm m}{.}03$
B 4104[1]	$15\overset{\rm m}{.}20$	$+0\overset{\rm m}{.}00$				17000[1]	4.0[1]	0.27	$+1\overset{\rm m}{.}96$
B 4719[1]	$15\overset{\rm m}{.}65$	$-0\overset{\rm m}{.}06$				16000[1]	4.0[1]	0.20	$+2\overset{\rm m}{.}41$
Stars in the gap region									
B 1628	$16\overset{\rm m}{.}30$	$-0\overset{\rm m}{.}17$			21000	21000	4.7	0.35	$+3\overset{\rm m}{.}06$
B 2395	$16\overset{\rm m}{.}73$	$-0\overset{\rm m}{.}24$		21000	22000	21500	5.0	0.46	$+3\overset{\rm m}{.}49$
B 3655	$16\overset{\rm m}{.}40$	$-0\overset{\rm m}{.}22$		24000	22000	23000	5.1	0.70	$+3\overset{\rm m}{.}16$
B 3975	$16\overset{\rm m}{.}27$	$-0\overset{\rm m}{.}22$		21000	21000	21000	4.8	0.46	$+3\overset{\rm m}{.}03$
B 4548	$16\overset{\rm m}{.}60$	$-0\overset{\rm m}{.}14$	22000	23000	23000	22500	5.2	0.75	$+3\overset{\rm m}{.}36$
stars below the gap region									
B 210	$17\overset{\rm m}{.}04$	$-0\overset{\rm m}{.}31$			27000	27000	5.6	0.94	$+3\overset{\rm m}{.}80$
B 331[1]	$17\overset{\rm m}{.}12$	$-0\overset{\rm m}{.}22$				26000[1]	5.6[1]	0.93	$+3\overset{\rm m}{.}88$
B 491	$17\overset{\rm m}{.}45$	$-0\overset{\rm m}{.}31$	28000	30000	28000	28500	5.3	0.29	$+4\overset{\rm m}{.}21$
B 617[2]	$17\overset{\rm m}{.}84$	$-0\overset{\rm m}{.}33$		33000	26000	33000	6.1	0.98	$+4\overset{\rm m}{.}60$
B 763[1]	$17\overset{\rm m}{.}13$	$-0\overset{\rm m}{.}24$				27000[1]	5.5[1]	0.68	$+3\overset{\rm m}{.}89$
B 916	$17\overset{\rm m}{.}61$	$-0\overset{\rm m}{.}26$	27000	30000	30000	28500	5.4	0.32	$+4\overset{\rm m}{.}37$
B 1288	$17\overset{\rm m}{.}90$	$-0\overset{\rm m}{.}31$		29000	27000	28000	5.5	0.31	$+4\overset{\rm m}{.}66$
B 2126	$17\overset{\rm m}{.}28$	$-0\overset{\rm m}{.}20$		31000	28000	29500	5.7	0.79	$+4\overset{\rm m}{.}04$
B 2162	$17\overset{\rm m}{.}88$	$-0\overset{\rm m}{.}27$		35000	32000	33500	5.9	0.57	$+4\overset{\rm m}{.}64$
B 3915	$17\overset{\rm m}{.}16$	$-0\overset{\rm m}{.}23$			31000	31000	5.5	0.47	$+3\overset{\rm m}{.}92$
B 4009	$17\overset{\rm m}{.}44$	$-0\overset{\rm m}{.}30$	33000	29000	31000	31500	5.7	0.61	$+4\overset{\rm m}{.}20$
3-118[1]	$17\overset{\rm m}{.}76$	$-0\overset{\rm m}{.}26$				24500[1]	5.2[1]	0.23	$+4\overset{\rm m}{.}52$
Post-EHB stars									
B 852	$15\overset{\rm m}{.}91$	$-0\overset{\rm m}{.}28$			39000	39000	5.2	0.53	$+2\overset{\rm m}{.}67$
B 1754[1]	$15\overset{\rm m}{.}99$	$-0\overset{\rm m}{.}24$				40000[1]	5.0[1]	0.29[3]	$+2\overset{\rm m}{.}75$
B 4380	$15\overset{\rm m}{.}93$	$-0\overset{\rm m}{.}14$			32000	32000	5.3	0.93	$+2\overset{\rm m}{.}69$

[1] Data from Heber et al. (1986), adjusted to the Kurucz temperature scale.

[2] Since B 617 lies close to B 1288 and B 2162 in the CMD we believed that the higher temperature was the correct one (see text). It was not taken into account for the mass distribution.

[3] Note that the mass value for B 1754 given by Cacciari et al. (1995) results from an incorrect bolometric correction (Cacciari, priv. comm.)

given in Table 7. Using the physical parameters listed in Table 6 we derived helium abundances. The spectra observed in 1992 were rather noisy and therefore equivalent widths of less than 0.35 Å could not be measured. The data taken in 1993 are of much better quality and allow equivalent widths as low as 0.15 Å to be measured. We take these values (0.35 Å resp. 0.15 Å) as upper limits if we cannot detect a helium line in a spectrum and derive an upper limit for the helium abundance from the absence of He I 4471 Å, the helium line predicted to be strongest in the observed wavelength range. This upper limit was determined for each object individually. All stars are helium deficient with respect to the sun by factors ranging from 3 to more than 100 and no trends with $T_{\rm eff}$ or $\log g$ are apparent, similarly to the field sdBs (as demonstrated by Schulz et al. 1991). The strong He I lines reported by Crocker et

Table 7. The equivalent widths of the He I lines as measured from the medium resolution spectra and the corresponding helium abundances (in particle numbers) for the stars in NGC 6752.

Name	year	4026 Å [Å]	4120 Å [Å]	4144 Å [Å]	4388 Å [Å]	4471 Å [Å]	4921 Å [Å]	log $\frac{N_{He}}{N_H}$
B 210	1992	0.75	–	–	–	1.06	–	-2.0
B 491	1992	–	–	–	–	–	–	< -3.2
B 617	1992	–	–	–	–	–	–	< -2.4
B 852[1]	1993	–	–	–	–	0.26	–	-2.0
B 916	1993	0.90	0.07	0.30	–	1.40	0.40	-1.8
B 1288	1992	–	–	–	–	1.57	1.00	-1.5
B 1509[2]	1993	0.46	–	0.12*	–	0.45	0.18*	-2.2
B 1628	1993	0.28	0.14	0.26	0.22*	0.38	0.31	-2.4
B 2126	1992	–	–	–	–	–	–	< -3.0
B 2162	1993	0.49	–	–	–	0.80	0.45	-1.8
B 2395	1993	0.79	–	–	0.73	0.90	0.35	-1.9
B 3655	1992	0.80	–	–	–	0.74	0.95	-1.8
B 3915	1993	–	–	–	–	–	–	< -3.0
B 3975[3]	1993	0.73	–	0.22	0.27	0.94	0.19*	-2.2
B 4009	1993	–	–	–	–	–	–	< -3.1
B 4380	1992	–	–	–	–	0.38:	–	-2.3
B 4548	1993	0.87	0.36:	0.97:	–	0.95	–	-1.9

[1] B 852 shows also He II at 4686 Å (W_λ = 0.8 Å)
[2] B 1509 (1993) shows also Mg II 4481 Å (W_λ = 0.23 Å)
[3] B 3975 shows also Mg II 4481 Å (W_λ = 0.26 Å) and He I 4168 Å(W_λ = 0.13: Å)
: equivalent width has a large error due to a rather noisy spectrum
$*$ equivalent width is at or below the level of the measuring error

al. (1986) for two blue HB stars in NGC 6752 (B4104, B4548) are not confirmed in later observations by Lambert et al. (1992) nor by our own observations.

3.3.5 Masses

Knowing $T_{\rm eff}$, $\log g$, and the distances of the stars we can derive the masses as described in Sect. 3.2.5. The results are listed in Table 6 and plotted in Fig. 18. In addition to the error in $\log g$ errors in the absolute magnitude and the theoretical brightness at the stellar surface also enter the final error in log M. We assume an error in the absolute brightness of $0\overset{\mathrm{m}}{.}1$ for stars with $V \leq 17\overset{\mathrm{m}}{.}0$ and $0\overset{\mathrm{m}}{.}13$ for fainter stars. The error in the theoretical V brightness is dominated by the errors in $T_{\rm eff}$ and amounts to $0\overset{\mathrm{m}}{.}12$ (stars above the gap), $0\overset{\mathrm{m}}{.}13$ (stars in the gap region), and $0\overset{\mathrm{m}}{.}14$ (stars below the gap). Altogether this leads to the following errors in log M: stars above the gap (1992: 0.210; 1993: 0.137), stars in the gap region (1992: 0.238; 1993: 0.178), stars below the gap (1992: 0.275; 1993: 0.225). To determine the mean mass of the sdBs (this section and Heber et al. 1986) we took all stars with $T_{\rm eff} > 20000$ K, excluding B 617 (due to the strange offset between temperatures from continuum and from line profiles) and the post-EHB stars B 852, B 1754, B 4380 (see Sect. 3.3.6) resulting in a total of 16 stars. We then calculated the weighted mean of the logarithmic masses for these stars (the weights being derived from the inverse errors). The mean logarithmic mass for these stars then was -0.300 ($\hat{=}0.50\ M_\odot$). The logarithmic standard deviation is 0.043 dex and the expected mean logarithmic error as derived from the observational errors was 0.054 dex. The mean mass therefore agrees extremely well with the value of 0.488 $M_\odot$ predicted by canonical HB theory for these stars (Dorman et al., 1993) and the standard deviation is less than expected. If we omit the stars observed in 1992 (due to their higher errors) we get a mean logarithmic mass for the remaining 12 stars of -0.327 ($\hat{=}0.47\ M_\odot$) in very good agreement with theoretical predictions. There was no significant difference

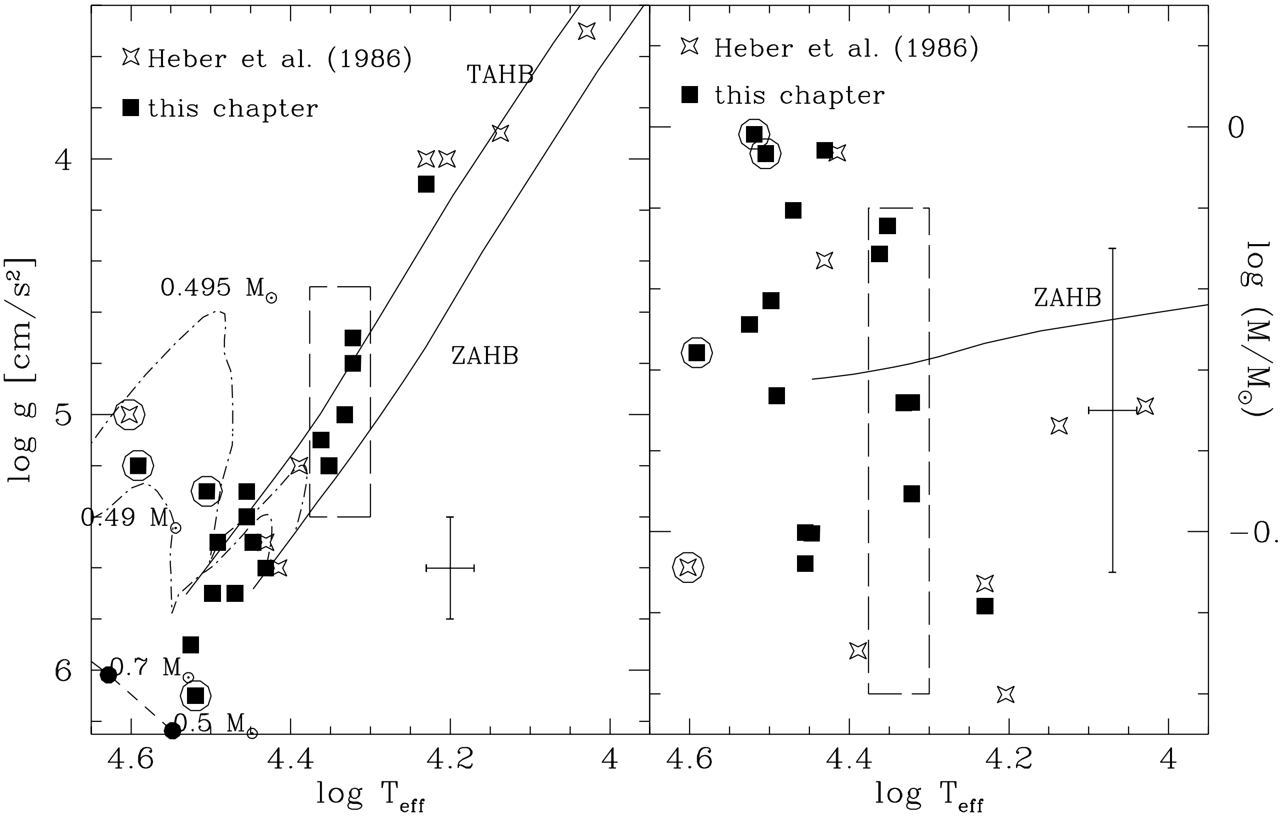

Fig. 18. The resulting physical parameters (**left panel**) and masses (**right panel**) for the stars in NGC 6752 (listed in Table 6) compared to theoretical predictions. The solid lines are the Zero Age HB and Terminal Age HB (core helium exhaustion, left panel only) for [Fe/H] = −1.48 of Dorman et al. (1993). The long dashed rectangle marks the gap region seen in the CMD by Buonanno et al. (1986). The short dashed line gives the position of the helium main sequence (Paczynski 1971). The dashed-dotted lines give post-EHB evolutionary tracks by Dorman et al. (1993), labeled with the total mass of the star. The crosses are error bars and the circles mark those stars that were not used to derive the mean sdB mass (B 617, B 852, B 1754, B 4380, see text for details).

between the mean mass for the eleven stars below the gap (<log M> = −0.306; <M> = 0.49 M$_\odot$) and the five stars inside the gap region (<log M> = −0.289; <M> = 0.51 M$_\odot$), again pointing towards their nature being identical. The five stars above the gap (V <16$^{\mathrm{m}}$.0, T_{eff} < 20,000 K) have a mean logarithmic mass of −0.518 ($\hat{=}$0.30 M$_\odot$) with a logarithmic standard deviation of 0.059 (compared to an expected error of 0.073). Canonical theory would predict for these stars a mean logarithmic mass of −0.256 ($\hat{=}$0.55 M$_\odot$) with a scatter of 0.018 dex.

3.3.6 Evolutionary status

The results are compared in Fig. 18 to the predictions of stellar evolution theory (Dorman et al. 1993). The bulk of the stars hotter than 20,000 K lies inside the theoretically predicted region (within the error bars), except three (B 852, B 1754, and B 4380). The latter three stars have about the same V magnitude (V = 15$^{\mathrm{m}}$.91–15$^{\mathrm{m}}$.99) and lie above the gap in the CMD, albeit far to the blue edge of the HB in this part. They are probably in a post-EHB stage of evolution (cf. Fig. 18, left panel), as already argued by Heber et al. (1986) in the case of B 1754, and will evolve directly towards the white dwarf cooling sequence. The distribution of stars in the (T_{eff}, M_V) diagram (Fig. 19) is consistent with that in the (T_{eff}, log g)-plane (Fig. 18, left panel) indicating that the stars above 20,000 K (except

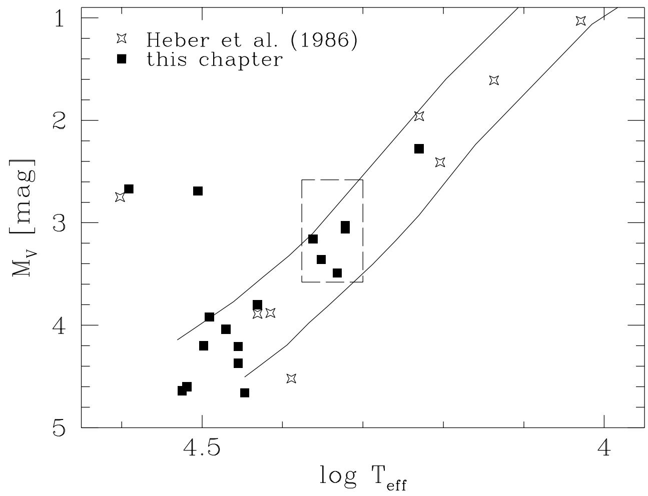

Fig. 19. The absolute V magnitudes and effective temperatures of the stars in NGC 6752 (cf. Table 6) compared to theoretical tracks by Dorman et al. (1993, details see Fig. 18). The three stars with $M_V \approx 2\overset{m}{.}7$ are UV bright stars (see Chapter 6) evolving from the EHB towards the white dwarf domain. The long dashed line marks the gap region seen in the CMD by Buonanno et al. (1986).

the three mentioned above) are bona fide EHB stars. The twelve stars below the gap ($V > 17\overset{m}{.}0$) have a mean absolute magnitude of $M_V = 4\overset{m}{.}2 \pm 0\overset{m}{.}3$ in excellent agreement with the mean absolute magnitude of south galactic pole sdBs, $M_V = 4\overset{m}{.}2 \pm 0\overset{m}{.}7$ (Heber, 1986). The five stars in the gap region ($16\overset{m}{.}0 \leq V \leq 17\overset{m}{.}0$) have $T_{\rm eff} > 20{,}000$ K, $\log g$ near 5 and subsolar helium abundances. Therefore they show the same characteristics as the field sdB stars and have to be classified as EHB stars (like the stars below the gap). However, they are somewhat more luminous ($M_V = 3\overset{m}{.}2 \pm 0\overset{m}{.}2$) than the stars below the gap in NGC 6752 and the field sdB's.

3.3.7 Discussion

Combining our results with those of Heber et al. (1986) we have carried out spectroscopic analyses of 25 blue stars in NGC 6752. We studied stars both brighter and fainter then the gap region ($16\overset{m}{.}0 \leq V \leq 17\overset{m}{.}0$) and also five stars within this gap region. The results can be summarized as follows:

(i) All stars are helium deficient and no trends of the helium abundance with atmospheric parameters become apparent.
(ii) All stars within or below the gap region lie on or close to the extreme horizontal branch, except three which have already evolved off the EHB towards the white dwarf cooling sequence.
(iii) The stars fainter than the gap ($V > 17\overset{m}{.}0$) are very similar to the field population of sdB stars. Their mean mass is consistent with the canonical value of half a solar mass.
(iv) The stars inside the gap region ($16\overset{m}{.}0 \leq V \leq 17\overset{m}{.}0$) are sdB stars too, although more luminous by one magnitude than the average field sdB's (which is, however, a difference of less than 1.5σ with regard to the uncertainty of $0\overset{m}{.}7$ of the field stars' absolute magnitude). Their mean mass is also consistent with the canonical mass.
(v) The stars brighter than the HB gap have significantly lower gravities than predicted by theory. Their masses are also significantly lower than predicted by evolutionary calculations.
(vi) The standard deviations of the mean logarithmic masses for all groups of stars are lower than expected from the observational errors.

From these results we conclude:

(i) The helium deficiency found in all stars is indicative for diffusion, i.e. gravitational settling of helium, as is the case for the field sdB and HBB stars.

(ii) The increased sample size allows a more meaningful determination of the mean mass of the stars below the gap than previous work did. The average mass determined here is in good agreement with the value predicted by canonical EHB theory. In addition, the standard deviation is smaller than the mean error derived from the observational errors. We take this as a verification that sdB stars indeed show a very narrow mass distribution, which is in full agreement with their status as EHB stars with a very thin hydrogen layer, produced by the same processes that produce hot HB stars. This finding, however, does not explain the gap that separates HBB from sdB stars in NGC 6752 (and also in M 15, Durrell & Harris 1993, Moehler et al. 1997). The mean mass and the width of the mass distribution is consistent with the single star evolutionary scenario or the Mengel et al. binary evolution scenario (No. 2 in Sect. 3.1) for the origin of EHB stars, but can hardly be explained within the framework of the common-envelope binary scenario (1) and the merger scenario (3) listed in Sect. 3.1, since both scenarios would predict a broader mass distribution with a mean mass below 0.5 $M_{\odot}$.

(iii) The low masses as well as the low surface gravities that we find for the HBB stars in M 15 and NGC 6752 remain a puzzle.

(iv) Further insight into the nature of hot HB and EHB stars may come from their radial distribution. We therefore investigated the radial distribution of all stars in Buonanno et al. (1986) that are fainter than $V = 13\overset{\rm m}{.}4$ and bluer than $B - V = -0\overset{\rm m}{.}2$. This sample, consisting of 214 stars, was divided into two groups: hot HB stars with $V < 16$ (142), and EHB stars with $V \geq 16$ (70), which combines all sdB stars. We then counted the stars in radial bins of $50''$ and normalized the numbers to the total numbers of stars in each group as well as to the area covered by each bin. The resulting radial distributions show no significant difference, supporting a similar evolutionary history and mass distribution, in contrast to the situation described above. One should keep in mind, however, that all stars observed by Buonanno et al. (1986) lie well outside the core of NGC 6752.

While the idea that there is something wrong with the model atmospheres, leading to too low values of $\log g$ for the temperature range between 10,000 K and 20,000 K sounds rather intriguing and would also explain the loci of the HBB stars in the $\log T_{\rm eff}$, $\log g$-diagram (cf. Fig. 20), it could not explain the findings of de Boer et al. (1995), where the physical parameters of the HBB/HBA stars agree very well with theoretical expectations, but result nevertheless in too low masses. The remaining possibility, i.e. that the HBB/HBA masses *are* indeed that low puts severe problems to stellar evolutionary models, since up to now no scenario is known to produce stars in that temperature range with masses of about 0.3 $M_{\odot}$.

3.4 Results from other analyses by end of 1998

In view of these results it seemed advisable to compare them to results obtained by other groups. Unfortunately we found only two publications where the results are given in sufficient detail to allow a direct comparison to our own results: The paper by Crocker et al. (1988) and the work by de Boer et al. (1995). Crocker et al. deal with five globular clusters, namely M 3, M 5, M 15, M 92, and NGC 288 (of which M 5 does not show any gap along the BHB/BT). They use ATLAS6 (Kurucz 1979) model atmospheres for their analyses. They obtain $T_{\rm eff}$ by fitting the continuum ($\lambda\lambda$ 3450–3700 Å, 4000–5100 Å) in their spectrophotometric data and employ a χ^2 test to find the best fit. In addition they use the star's position along the observed HB to obtain another estimate of its temperature and finally average both values for $T_{\rm eff}$. They determine $\log g$ from fits to H_{β} to H_{δ}, again using a χ^2 test to determine the best fit. In addition they correct their results for the subsolar helium abundance normally present in HBB stars. As they do not identify their targets in M 15 we cannot directly compare our results to theirs. De Boer et al. performed spectroscopic analyses and mass determinations for the

Table 8. Cluster parameters taken from Djorgovski (1993) and Pryor & Meylan (1993). Given are the reddening free distance modulus $(m-M)_0$, the reddening E_{B-V}, metallicity [Fe/H], velocity dispersion σ_0, and central density ρ_0. The last column gives the absolute magnitude of the gap along the HB, as estimated by Moehler et al. (1994).

Cluster	$(m-M)_0$	E_{B-V}	[Fe/H]	σ_0 [km/s]	log (ρ_0) [$M_\odot$/pc^3]	$M_{V,gap}$
M 3	$15\overset{\mathrm{m}}{.}02$	$0\overset{\mathrm{m}}{.}01$	−1.66	5.6	3.5	–
M 5	$14\overset{\mathrm{m}}{.}40$	$0\overset{\mathrm{m}}{.}03$	−1.40	5.7	4.0	–
M 15	$15\overset{\mathrm{m}}{.}11$	$0\overset{\mathrm{m}}{.}05$	−2.17	12.0	6.2	$+1\overset{\mathrm{m}}{.}0$
M 92	$14\overset{\mathrm{m}}{.}37$	$0\overset{\mathrm{m}}{.}02$	−2.24	5.9	4.4	$+1\overset{\mathrm{m}}{.}0$
NGC 288	$14\overset{\mathrm{m}}{.}62$	$0\overset{\mathrm{m}}{.}03$	−1.40	2.9	2.1	$+1\overset{\mathrm{m}}{.}4$
NGC 6397	$11\overset{\mathrm{m}}{.}71$	$0\overset{\mathrm{m}}{.}18$	−1.91	4.5	5.3	–
NGC 6752	$13\overset{\mathrm{m}}{.}12$	$0\overset{\mathrm{m}}{.}04$	−1.54	4.5	5.2	$+3\overset{\mathrm{m}}{.}1$

BHB stars in NGC 6397 (which does not show any gap or blue tail) using intermediate resolution spectra, Strömgren photometry, and IUE spectra.

In Fig. 20 the results from Sects. 3.2.2 (M 15) and 3.3.2 (NGC 6752) together with physical parameters of HB stars analysed by Crocker et al. (1988; M 3, M 5, M 92, NGC 288), de Boer et al. (1995; NGC 6397), and Moehler et al. (1997, sdB's in M 15) are compared to evolutionary tracks. The zero-age HB (ZAHB) marks the position where the HB stars have settled down and started to quietly burn helium in their cores. The terminal-age HB (TAHB) is defined by helium exhaustion in the core of the HB star. The distribution of stars belonging to an individual cluster is hard to judge in this plot but it is obvious that for temperatures between 11,000 K and 20,000 K the observed positions in the $(\log g,\, T_{\rm eff})$-diagram fall mostly above the ZAHB and in some cases even above the TAHB. An indication of a low-temperature gap can be seen at $\log T_{\rm eff} \approx 4.0 \ldots 4.1$ ($T_{\rm eff} \approx$10,000 K ...12,600 K). The gaps seen in the CMD of NGC 6752 and in the M 15 data of Durrell & Harris 1993 (from which the two hottest stars in M 15 were selected) are found to separate hot HB from EHB stars. In all other clusters the stars above and below the gaps are hot horizontal branch stars cooler than 20,000 K and the gaps along their horizontal branches vanish in the $T_{\rm eff}$-$\log g$ diagram. Thus most of the gaps seen along the horizontal branches of metal-poor globular clusters are due to statistical fluctuations as suggested by Catelan et al. (1998).

Independent of the occurrence of any gaps along the blue HB/blue tail stars with temperatures between 11,000 ($\log T_{\rm eff}$ = 4.04) and 20,000 K ($\log T_{\rm eff}$ = 4.30) show lower gravities than expected from canonical scenarios, whereas stars outside this temperature range are well described by canonical HB and EHB evolutionary tracks.

Using the atmospheric parameters plotted in Fig. 20, the photometric papers cited by Crocker et al. (1988) for the apparent visual magnitudes, and the distance moduli and reddenings listed in Table 8[11], we derived the masses of the blue stars in M 3, M 5, M 92, and NGC 288 in the same way as described in Sect. 3.2.5. Note that Crocker et al. derived masses by making reference to theoretical predictions and their results therefore differ from ours (see Moehler et al. 1994 for details). For the stars in NGC 6397 we used the results provided by de Boer et al. (1995). The results are plotted in Fig. 21:

While the stars in M 3, M 5, and NGC 6752 have mean masses consistent with the canonical values (see Table 11, page 61) the HBB stars in all other clusters show masses that are significantly lower than predicted by canonical HB evolution – even for temperatures cooler than 11,000 K where we saw no deviation in surface gravity from the canonical tracks. The fact that the stars in three of

---

[11] $(m-M)_V$ from Harris (1996) agree with those from Djorgovski (1993) to within $0\overset{\mathrm{m}}{.}1$, except for M 92, where Harris' value is larger by $0\overset{\mathrm{m}}{.}20$ than that of Djorgovski. This difference would increase the masses of the stars in M 92 by 20%.

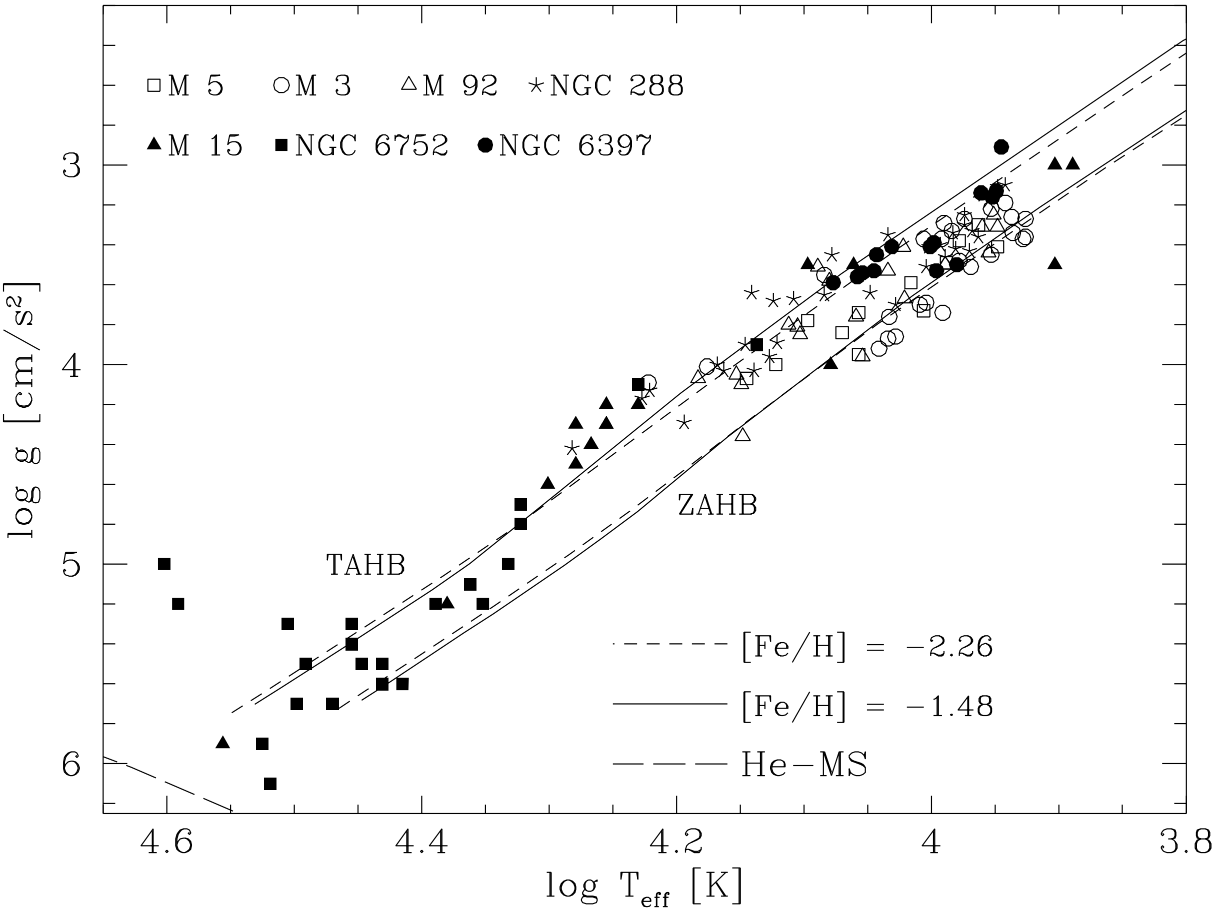

Fig. 20. The results of Sects. 3.2.2 (M 15), 3.3.2 (NGC 6752), Crocker et al. (1988; M 3, M 5, M 92, NGC 288), de Boer et al. (1995; NGC 6397) and Moehler et al. (1997, sdB's in M 15) compared to evolutionary tracks from Dorman et al. (1993). ZAHB and TAHB stand for zero-age and terminal-age HB (see page 44 and Appendix A for details). Also given is the position of the helium main-sequence (Paczynski 1971).

the clusters (M 3, M 5, and NGC 6752) show "normal" mass values makes errors in the analyses an unlikely cause for the problem (for a more detailed discussion see Sects 3.2.5, 3.3.5, and de Boer et al. 1995). Scenarios like the merging of two helium-core white dwarfs (Iben & Tutukov 1984) or the stripping of red giant cores (Iben & Tutukov 1993, Tuchman 1985) produce stars that are either too hot (merger) or too short-lived (stripped core) to reproduce our results.

Additional evidence for a mismatch between theoretical predictions and observational results for hot HB stars can be found in the literature:

- ⋆ Graham & Doremus (1966) already mentioned that the comparison of $(c_1)_0$ vs. $(b-y)_0$ for 50 blue HB stars in NGC 6397 to models from Mihalas (1966) indicated low surface gravities and a mean of mass of $0.3\,M_\odot$ ($0.4\,M_\odot$) for solar (negligible) helium abundance, assuming $(m-M)_0 = 12\overset{m}{.}0$ and $E_{B-V} = 0\overset{m}{.}16$. *"It is clear that the accurate fixing of this parameter* [log g] *is of the greatest importance for fixing limits to the masses of the horizontal branch stars since there seems no other way, at present, of determining them more directly."*
- ⋆ Crocker (1991) finds from the analysis of newer spectra for BHB stars in M 3 and M 13 that the M 3 stars cooler than $\log T_{\rm eff} = 4.05$ ($\hat{=}$11,200 K) stay very close to the ZAHB (the one star at $T_{\rm eff} \approx$ 12,500 K shows lower $\log g$). The M 13 stars cooler than $\log T_{\rm eff} = 4.05$ stay mostly close to the ZAHB, but the majority of stars in that cluster is hotter and shows lower $\log g$.

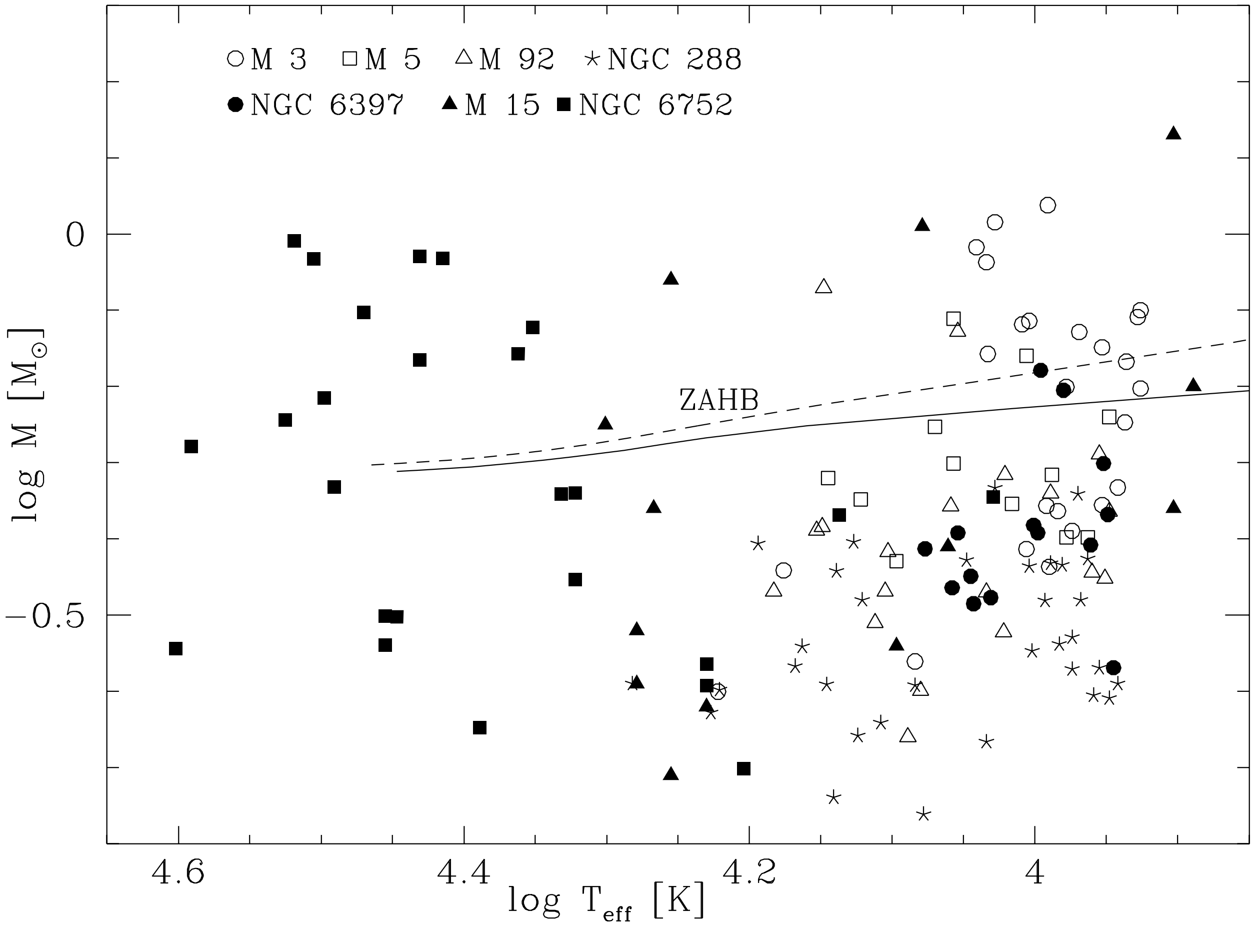

Fig. 21. The masses of the stars derived with the distances listed by Djorgovski (1993) compared to evolutionary calculations from Dorman et al. (1993). The solid line gives the ZAHB for [Fe/H] = −1.48, the dashed line marks the ZAHB for [Fe/H] = −2.26.

- ⋆ Altner & Matilsky (1993) find that their IUE spectra of M 79 are best fit by hot HB stars with 12,000 K $\leq T_{\rm eff} \leq$ 14,000 K and $\log g$ (derived from the luminosity and an assumed mass of 0.52 M$_\odot$) between 3.3 and 3.7 (lower than expected for ZAHB stars). Models with solar or slightly super-solar metallicities provide better fits to the data than the low-metallicity ones.
- ⋆ Saffer et al. (1997) find that field HBB stars show a larger scatter away from the ZAHB in $T_{\rm eff}$, $\log g$ than sdB stars.
- ⋆ Parise et al. (1998) compare UIT photometry of M 13 to evolutionary tracks using $(m-M)_0 = 14\overset{\rm m}{.}38$ and find a lack of stars close to the ZAHB at $-3\overset{\rm m}{.}3 < (m_{1620} - V) < -2\overset{\rm m}{.}1$. This colour (temperature) range might coincide with the low $\log g$ range observed in other clusters. Enhanced luminosities in this temperature range would be consistent with deep He mixing.
- ⋆ The HUT spectra of M 79 (Dixon et al. 1996) suggest lower than expected gravities for blue HB stars (but see Vink et al. 1999 who do not need lower than expected surface gravities to fit the same data). Hill et al. (1996) find from UIT photometry of M 79, whose optical colour-magnitude diagram is similar to that of M 13, that in the m_{152} vs. $m_{152} - m_{249}$ diagram stars bluer than $m_{152} - m_{249} = -0\overset{\rm m}{.}2$ lie above the ZAHB, whereas cooler stars scatter around the ZAHB.
- ⋆ Whitney et al. (1998) use UIT observations of the hot stars in ω Cen to claim that the extreme HB stars – which agree with theoretical expectations in our results – have lower than expected luminosities, i.e. higher than expected gravities. In addition they find a considerable number of stars above the ZAHB.

- ⋆ Landsman et al. (1996) on the other hand find good agreement between UIT photometry of blue stars in NGC 6752 and a standard ZAHB (in position and HB luminosity width) for $(m-M)_0 = 13\overset{\mathrm{m}}{.}05$ and $E_{B-V} = 0\overset{\mathrm{m}}{.}05$. Only 4 post-EHB stars can be identified, while 11 would be expected.

There is obviously considerable evidence that blue HB and blue tail stars, when analysed with standard model atmospheres, cannot be reconciled with the predictions of canonical stellar evolution.

Chapter 4

Horizontal Branch Stars in Metal-Poor Globular Clusters – A Solution?

The problems discussed in Chapter 3 can be summarized as follows:

- ⋆ HBB stars in metal-poor globular clusters with 11,000 K$\leq T_{\rm eff} \leq$20,000 K show lower gravities than expected from canonical HB evolution.
- ⋆ sdB stars ($T_{\rm eff}$ >20,000 K) and cooler HBB/HBA stars ($T_{\rm eff}$ <11,000 K) show surface gravities that agree well with theoretical predictions.
- ⋆ HBB/HBA stars ($T_{\rm eff} \leq$ 20,000 K) have mean masses lower than the canonical HB masses by about a factor of 2.
- ⋆ sdB stars show a mean mass of about 0.5 $M_\odot$, in good agreement with the EHB mass predicted by canonical theory.

One should note that the "low gravities" may as well be "high temperatures" – we do not know a priori which parameter is the real culprit. For sake of brevity we will, however, continue to refer to the low gravities as the main problem. Three possible solutions to this dilemma will be discussed in detail below, but are summarized shortly here:

- ⋆ **Helium mixing** means the dredge-up of helium-enriched material from the inner regions of a red giant to its surface. Such helium-enriched red giant stars evolve to higher luminosities and therefore lose more mass than their canonical counterparts. The resulting HB stars have less massive hydrogen envelopes and are thus hotter than in the canonical case. In addition the higher helium abundance in the hydrogen envelopes of the HB stars increases the efficiency of the hydrogen shell burning and thereby leads to higher luminosities at a given effective temperature. This increase in luminosity leads to lower gravities for helium mixed HB stars than predicted by canonical evolution and could thus explain the low gravities observed for hot HB stars. The luminosities/gravities of EHB stars are not affected, as their hydrogen shells are inert. The observational evidence for helium mixing and the theoretical scenarios to explain it are described in detail in Sect. 4.1 below.
- ⋆ **Radiative levitation** of heavy elements by diffusion can enrich the atmospheres of hot HB stars and thereby change the temperature structure of the stellar atmosphere. If enriched stellar atmospheres are analysed with metal-poor model atmospheres the surface gravities can be significantly underestimated. The helium abundances derived for HBB and sdB stars in globular clusters and in the field strongly suggest the presence of diffusion in their atmospheres. If this scenario holds true the low surface gravities would be an artifact of the use of metal-poor model atmospheres for enriched HB star atmospheres. Observational evidence and the scenario of Grundahl et al. (1999), who suggest radiative levitation as cause for the low surface gravities, are discussed extensively in Sect. 4.2

- ⋆ **Distances** to globular clusters affect the mass determinations. New results from HIPPARCOS parallaxes suggest that the distance scale to globular clusters may be longer than previously thought. Such an increase in distance would alleviate the problem of the low masses found for hot HB stars in some globular clusters (assuming that the "low gravities" are correct). The various distance determinations for globular clusters using HIPPARCOS parallaxes of local subdwarfs are described in Sect 4.3.

4.1 Helium mixing in red giants

Sweigart (1997a, 1997b) studies the influence of He mixing (mixing deep enough to access He enriched regions within a red giant's envelope) on the descendants of the red giants. The theoretical calculations assume that the mixing extends down into the H-burning shell. The mixing depth is specified by the parameter ΔX_{mix} which measures the difference in hydrogen abundance between the envelope and the innermost point reached by the mixing currents. Increasing ΔX_{mix} thus means an increase in the helium abundance of the material accessed by the mixing. All material above this innermost point is mixed up and consequently diluted into the envelope, whereas the material below is added to the He core. Mixing is assumed to commence after the H-burning shell passed the discontinuity in molecular weight μ created by the deepest extent of the convection zone on the base of the red giant branch (see below). Some results of the calculations which are important for the discussion in this work are summarized here (for more details and results affecting RR Lyrae stars and sdO's see Sweigart 1997b):

He mixing causes little change in the red giant branch (RGB) morphology, but increases the luminosity of the RGB tip and thus the mass loss on the RGB. Horizontal branch stars descending from He mixed red giants will thus have a lower envelope mass and a higher envelope He abundance than canonical HB stars. As the effective temperature of HB stars increases with decreasing envelope mass the mixed HB stars will be hotter. The increased mean molecular weight in the mixed envelope results in higher efficiency of the energy production in the H-burning shell, thereby increasing the luminosity. Higher luminosities lead to lower surface gravities and can thus explain the low surface gravities found for HBB stars (Chapter 3). The gravities/luminosities of extreme HB stars above 20,000 K would not be affected by He mixing (in agreement with the findings described in Section 3.3) as the H-shells are inactive in these stars.

Various degrees of mixing within one cluster (triggered, e.g., by varying rotation rates among the cluster stars) would result in different amounts of He enrichment, with the hottest HB stars being most enriched and the coolest HB stars least. A threshold for the mixing might therefore result in bimodal horizontal branches. If He mixing is indeed related to stellar rotation clusters with identical metallicities but different rotation rates may have different HB morphologies (see also Norris 1987, Peterson et al. 1995b). Density may affect the rotation rates via close encounters and thereby be related to HB morphology (Fusi Pecci et al. 1993, Buonanno et al. 1997).

Unfortunately helium enrichment can be verified directly neither in red giants/cool HB stars (too cool) nor in hot HB stars (diffusion, see Sect. 4.2). So while the above scenario sounds quite intriguing we should verify if there is at least indirect evidence for helium mixing in globular cluster red giant stars. With this goal in mind we discuss below the **observational evidence** for abundance variations in globular cluster red giants and their relation to possible mixing processes. It will be shown that not all abundance variations explained by mixing necessarily enrich the envelope of the red giant in helium.

Traditionally globular clusters have been thought to be mono-metallic systems, i.e. all stars within one cluster are supposed to have been born with the same content of elements. While this is still true for most globular clusters with respect to heavy elements (except ω Cen, M 22, and possibly M 15, M 4; see Suntzeff 1993 for an overview) the red giant stars in globular clusters exhibit a wide range of light element abundance variations (see Table 9). For more information on the observational part of these abundance variations and possible explanations the reader is referred to the reviews of Freeman & Norris (1981), Smith (1987), Kraft (1994), Shetrone (1996a, 1996b) and da Costa (1997). It was realized early on that at least some of the abundance variations could be explained if nuclearly processed material were dredged up to the surface.

Some abundance variations in the atmospheres of red giant stars are already expected from **canonical stellar evolution**: While a star evolves from the main sequence to the base of the red giant branch a convective envelope develops, which reaches from the surface to increasing depths. When the base of this envelope reaches deep enough into the stellar interior to access material polluted by the previous central H-burning it dredges up processed material and at the same time transports fresh hydrogen down. This is the so-called **first dredge-up** predicted by standard stellar evolution, which leads to a decrease in the surface abundance of ^{12}C and an increase of ^{14}N and ^{13}C. The approach of the H-burning shell as it burns outward causes the convective envelope to retreat, thereby decreasing its size and mass. At the deepest point reached by the envelope convection zone a discontinuity in molecular weight μ between H-rich envelope material (low μ) and H-poor processed material (high μ) is created. When the H-burning shell passes this discontinuity on its way outward the energy production (and thus the luminosity) decreases due to the reduced molecular weight. This results in a "bump" in the luminosity function of red giants. While the first dredge-up could qualitatively explain the C depletions, CN variations, N enrichments, C-N anticorrelations and the low ^{12}C/^{13}C ratios seen in red giants in globular clusters, its effect is not strong enough to agree quantitatively with the observations (e.g. Charbonnel 1994). In addition the first dredge-up is supposed to happen at the base of the red giant branch only – any progressive abundance variations (like a decrease in ^{12}C abundance along the RGB, see Table 9) cannot be explained by first dredge-up. Extra mixing is necessary for which the mixing currents have to access regions close to the H-burning shell.

Sweigart & Mengel (1979) proposed a scenario in which meridional circulation in rotating red giants would create circulation currents within the radiative zone between the H-burning shell and the convective envelope. Such currents could change the CNO abundance at the base of the convective envelope (and thus at the surface as well) if

1. The radiative zone between the H-burning shell and the convective envelope does not have a significant gradient in molecular weight μ.
2. The temperature at the base of the region reached by the circulation currents is high enough to allow at least CN processing.

Both conditions are *not* fulfilled before the H-burning shell reaches the discontinuity at the point of the deepest extent of the convective envelope during the subgiant phase. Within the H-shell a μ gradient exists which increases as the actual H-burning shell region is approached and which will stop the circulation current at a certain depth.

The temperature increases when approaching the H-burning shell from the stellar surface. First the initial reactions of the **CN-cycle** $^{12}C(p,\gamma)^{13}N(\beta^{+}\nu)^{13}C(p,\gamma)^{14}N$ become possible (C-shell), which leave a C-depleted, N-enriched zone behind. Further inward the temperature becomes high enough for the initial reactions of the **ON-cycle** $^{16}O(p,\gamma)^{17}F(\beta^{+}\nu)^{17}O(p,\alpha)^{14}N$ (O-shell), which deplete O and further enrich N. For metal poor stars the C- and O-shells are well enough separated from the H-burning shell region that their μ gradients stay negligible.

An increase in metallicity raises the CNO abundances in the H-burning shell region and thereby increases the efficiency of nuclear reactions. At a given luminosity the temperature in the H-burning shell region thus decreases with increasing metallicity and the temperatures necessary for CN/ON cycles are reached closer to the H-burning shell region. The higher μ gradient present there may prevent the circulation currents from reaching the O-shell (the C-shell is always well separated from the H-burning shell region). Also the masses of the C- resp. O-depleted regions decrease with increasing metallicity. With increasing metallicity the access to ON processed material becomes therefore restricted to progressively stronger mixing currents, i.e. faster rotating stars. Thus deep mixing would

Table 9. Examples for abundance variations in globular cluster red giant stars (ω Cen and M 22 are excluded from this discussion due to their known variations of heavy elements).

globular cluster	reference
	decreasing ^{12}C abundance along the red giant branch
M 92	Bell et al. (1979), Langer et al. (1986)
NGC 6397	Bell et al. (1979, 1992), Briley et al. (1990)
M 3, M 13	Suntzeff (1981)
M 15	Trefzger et al. (1983)
NGC 6752	Bell et al. (1984), Suntzeff & Smith (1991)
M 4	Suntzeff & Smith (1991)
M 55	Pilachowski et al. (1984)
	CN-variations
47 Tuc	Dickens et al. (1979), Smith & Norris (1982b, main sequence stars) Suntzeff & Smith (1991, main sequence stars)
NGC 6752	Norris et al. (1981), Suntzeff & Smith (1991, main sequence stars)
M 5	Suntzeff & Smith (1991, subgiants)
M 4	Ivans et al. (1999)
M 3	Suntzeff (1981), Norris & Smith (1984)
M 13	Suntzeff (1981)
M 71	Smith & Norris (1982)
M 92	Carbon et al. (1982)
M 15	Trefzger et al. (1983)
	N enrichment
47 Tuc	Dickens et al. (1979), da Costa & Demarque (1982, main sequence stars), Brown et al. (1990)
M 13	Suntzeff (1981)
NGC 6752	Bell et al. (1984)
M 15, M 92	Sneden et al. (1991)
M 4	Brown et al. (1990), Ivans et al. (1999)
	C-N anticorrelations
NGC 6752	Norris (1981), Norris et al. (1981, 1984), Suntzeff & Smith (1991, main sequence stars)
47 Tuc	Norris (1981), Norris & Freeman (1982, HB stars), Norris et al. (1984), Brown et al. (1990) Cannon et al. (1998, main sequence)
M 4	Norris (1981), Suntzeff & Smith (1991), Brown et al. (1990), Ivans et al. (1999)
M 3	Suntzeff (1981), Norris & Smith (1984)
M 13	Suntzeff (1981)
M 5	Smith & Norris (1983), Smith et al. (1997)
M 71	Smith & Norris (1982), Cohen (1999, main sequence)
	O depletion
M 15, M 92	Sneden et al. (1991)
M 3	Kraft et al. (1992, 1999)
M 13	Kraft et al. (1992)
M 4	Drake et al. (1992), Ivans et al. (1999)
M 55	Pilachowski et al. (1984)
	O-Na anticorrelation
M 5	Sneden et al. (1992), Shetrone (1996a)
M 3	Kraft et al. (1993)
M 13	Kraft et al. (1993), Briley & Smith (1993), Kraft et al. (1997), Shetrone (1996a)
M 15	Sneden et al. (1997)
M 92, M 5	Shetrone (1996a)
NGC 3201	Gonzalez & Wallerstein (1998)
M 4	Ivans et al. (1999)

be consistent with the *smaller range of abundance variations seen in metal-rich globular* clusters like M 71 and 47 Tuc.

Table 9. cont'd. Examples for abundance variations in globular cluster red giant stars (ω Cen and M 22 are excluded from this discussion due to their known variations of heavy elements).

globular cluster	reference
	Na variations
M 13	Peterson (1980), Shetrone (1996a)
NGC 6752	Cottrell & da Costa (1981), Smith & Norris (1982b)
47 Tuc	Cottrell & da Costa (1981), Smith & Norris (1982b), Brown & Wallerstein (1992)
M 4	Brown & Wallerstein (1992), Drake et al. (1992) Ivans et al. (1999)
M 71	Smith & Norris (1982), Shetrone (1996a)
M 3	Kraft et al. (1999)
M 92, M 5	Shetrone (1996a)
NGC 3201	Gonzalez & Wallerstein (1998)
	Al enrichment
NGC 6752	Cottrell & da Costa (1981), Norris et al. (1981), Norris & Smith (1983a), Shetrone (1997)
M 3	Norris & Smith (1983a, 1984), Kraft et al. (1999)
NGC 3201	Norris & Smith (1983a)
M 4	Brown & Wallerstein (1992), Drake et al. (1992), Wallerstein et al. (1987), Ivans et al. (1999)
47 Tuc	Brown & Wallerstein (1992)
M 13	Shetrone (1996a), Kraft et al. (1997)
M 5, M 92	Shetrone (1996a)
M 15	Sneden et al. (1997)
NGC 6397	Lambert et al. (1992)
NGC 2298	McWilliam et al. (1992)
NGC 3201	Gonzalez & Wallerstein (1998)
	Heavy element abundances (constant unless noted otherwise)
NGC 6752	Mg, Si, Ca, Fe, Ba (Cottrell & da Costa 1981); Ca, Fe (Bell et al. 1984)
M 3	Si, Ca, Ti, Fe, Ni, Sc, V (Kraft et al. 1993); Y, Ba, Ce, Nd (Armosky et al. 1994); Ca, Ti, Fe, Ni, Sc, V, Ba, Eu (Kraft et al. 1999)
M 10	Si, Ca, Ti, Ni, Sc, V (Kraft et al. 1995)
M 13	Si, Ca, Ti, Fe, Ni, Sc, V (Kraft et al. 1993); Y, Ba, Ce, Nd (Armosky et al. 1994); Eu (Shetrone 1996a)
M 15	Y, Ba, Ce, Nd (Armosky et al. 1994); large star-to-star variations in Ba, Eu (Shetrone 1996b)
M 5, M 92	Y, Ba, Ce, Nd (Armosky et al. 1994); Eu (Shetrone 1996a)
M 71	Eu (Shetrone 1996a)
NGC 7006	Mg, Si, Ca, Ti, Fe, Ni, V, Eu (Kraft et al. 1998)
47 Tuc	Ca (Cannon et al. 1998)
M 4	Fe, Sc, Ti, V, Ni, Eu, Ba, La (Ivans et al. 1999)

One should keep in mind, however, that the above described scenario rests on the following assumptions:

1. The interior of a main-sequence star rotates even though the convective envelope has spun down.
2. A star retains its angular momentum into the RGB phase.
3. The approximation used for the circulation velocity is correct to order of magnitude.
4. The circulation pattern efficiently mixes the radiative zone.

The fact that the mixing cannot start before the H-burning shell crosses the μ discontinuity restricts it to red giants brighter than the red giant "bump" mentioned above. Abundance changes below this luminosity as observed in M 92 (Langer et al. 1986) and M 13 (Kraft et al. 1997) that exceed the predictions of first dredge-up cannot be explained by this scenario (see also Denissenkov et al. 1998).

While the two scenarios described above (canonical first dredge-up and the Sweigart & Mengel mixing scenario) can at least qualitatively explain most of the CNO and Na/O variations seen in globular cluster red giants, none of them enriches the red giant's envelope with helium. This is mainly due to the fact that the CN and ON cycles (that are supposedly responsible for these abundance variations) can be active at quite some distance from the actual H-burning (He-producing shell).

The **Al variations** observed in red giants in globular cluster, however, can only be explained by deep mixing if the mixing extends to much hotter regions than the C- and/or O-shells. This was one of the reasons why variations in Al abundance were long taken as evidence for primordial variations, as there was no way known to achieve the temperatures necessary for the production of Al in low mass red giants. The problems of reconciling the various abundance measurements for O, Mg, Na, and Al with current nuclear reaction rates and our ideas about stellar structure and evolution are discussed extensively by Denissenkov & Denissenkova (1990), Langer et al. (1993, 1997), Langer & Hoffman (1995), Shetrone (1996a, 1996b, 1997), Cavallo et al. (1998), and Denissenkov et al. (1998).

In summary (and strongly simplified) it turns out that temperatures of $6.7 \ldots 7.8 \cdot 10^7$K are necessary to reproduce the observed Mg and Al abundances (Langer et al. 1997, Denissenkov et al. 1998). The maximum temperature reached in a steadily burning H-shell in a moderately metal-poor star is, however, only $5.5 \cdot 10^7$K (even lower in fainter, less evolved models). One possible solution would be an unstable H-shell that burns intermittedly at higher temperatures[12]. Of special interest for helium mixing is the fact that the largest ^{27}Al production (from ^{24}Mg) takes place well inside the H shell, where hydrogen is strongly depleted and helium highly enriched. Thus any mixing that dredges up Al will also dredge up helium. **Fujimoto et al. (1999)** have suggested the following scenario not only for the production of Al in a low-mass red giant, but also for its transport (and that of helium) to the surface of the star:

They emphasize that mixing not only carries processed material to the surface, but in turn also brings H-rich matter down. If meridional circulation is invoked to explain the CNO anomalies the necessary rotation rates of the O-shell will create differential rotation in the H-burning shell. The differential rotation can result in hydrodynamical instabilities that lead to mixing between the base of the H-burning shell and the outer region of the He core. Already small amounts of hydrogen mixed down to the helium core can trigger an H shell flash. Once the shell flash ignites convection starts, reaching from the H-burning shell into the H-rich outer layers. Hydrogen is thereby added to the shell flash zone, further fueling the flash and thereby extending the flash convection zone.

During the peak of the flash material within the flash's convection zone undergoes proton capture at high temperatures (which allows the production of, e.g., Al). The nuclear products are then spread over the whole flash convection zone, possibly even beyond the region of the former quiescent H burning (this region is now inactive due to the expansion of the lower layers caused by the shell flash). After the peak of the flash the burning shell expands greatly, thereby cooling and diminishing the burning rate sufficiently to sustain stable H-burning. At the same time the flash convection zone retreats and finally disappears. Afterwards the surface convection zone deepens and may reach farther down than during previous quiescent H-burning, as the luminosity in the equilibrium phase immediately following the flash is larger than that before the flash. For sufficiently strong flashes the surface convection zone can therefore reach regions previously occupied by the flash convection zone and dredge up processed material (Hollowell et al. 1990).

After the flash/dredge up the angular momentum distribution shows a discontinuity at the innermost point reached by surface convection. The next flash will likely be triggered when the H-burning shell crosses this discontinuity. Note, however, that this mechanism of deep mixing will work only as long as the rotation rate of the core differs from that of the matter incorporated during quiescent H-burning.

As the mixing requires the presence of surface convection it should start only after the electron degenerate core is formed and surface convection is active. If the hydrodynamical instabilities supporting the mixing are indeed caused by the transport of angular momentum from the convective

---

[12] Cavallo et al. (1998) object that this solution would increase the luminosity of the [Fe/H] = −1.67 model at the RGB tip by 1.6 dex which is inconsistent with photometric observations.

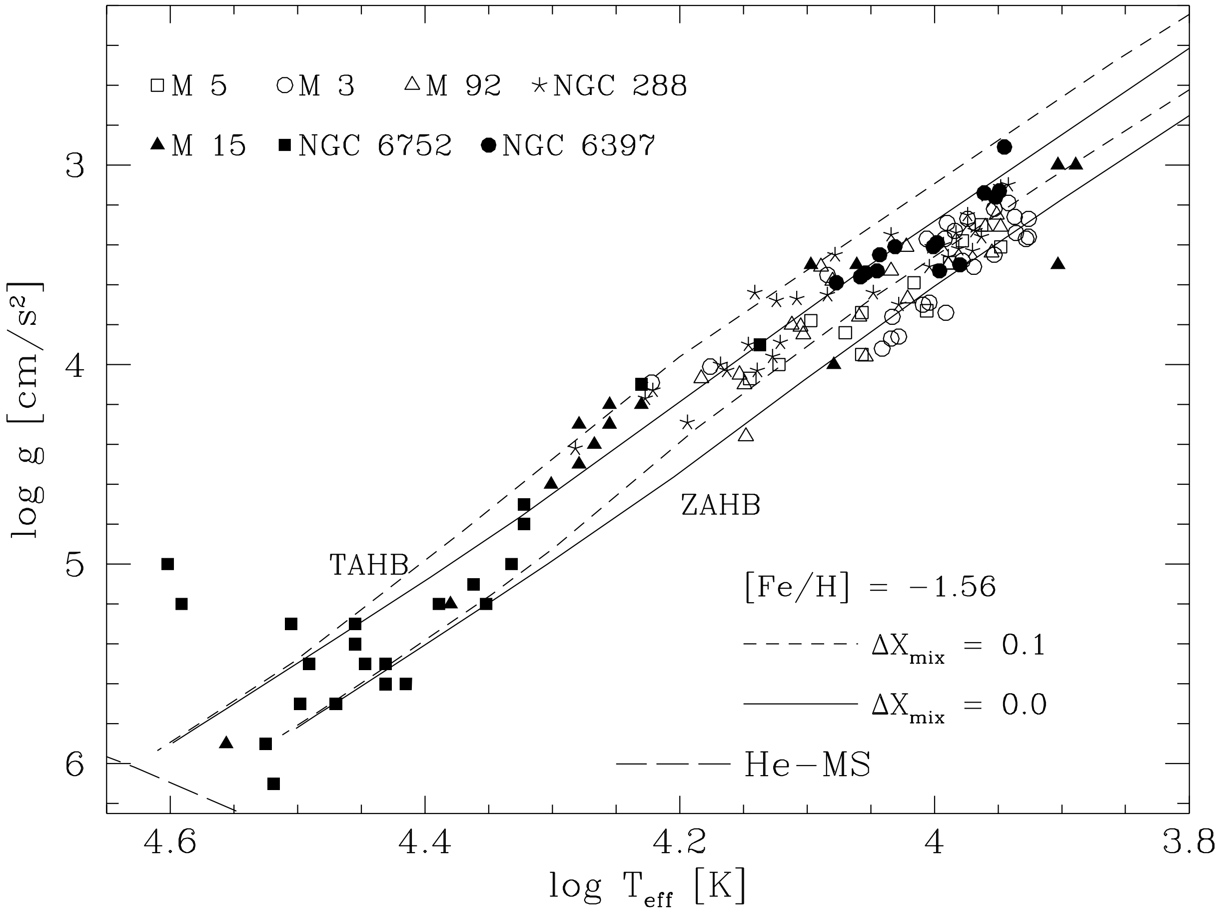

Fig. 22. The results from Fig. 20 compared to evolutionary tracks that take into account the effects of helium mixing (Sweigart 1997b). ΔX_{mix} gives the amount of He mixing with 0 indicating an unmixed track (for details see text and Sweigart 1997b). Also given is the position of the helium main-sequence (Paczynski 1971).

envelope down to the H-burning shell, flash mixing probably starts when the H-burning shell crosses the discontinuity in μ and angular momentum created by the deepest previous extent of the surface convection zone, i.e. early on the RGB and not on the main sequence. Differentially rotating stars will evolve slower up the RGB, because every shell flash decreases the mass of the He core by the amount of matter mixed outwards. The instabilities may be triggered by close encounters, which might spin up the red giant (see also Buonanno et al. 1985, Norris 1987). This scenario would also explain the lack of abundance anomalies among field stars, which lack this spin-up mechanism.

While the evidence for helium-mixing is still controversial we want to emphasize that the atmospheric parameters of most HB stars hotter than 11,000 K are well described by tracks that assume moderate helium mixing (see Fig. 22). The cooler stars are better explained by canonical evolution. There is, however, no a priori reason why all RGB stars within one cluster should experience the same degree of mixing. Since helium mixing leads to hotter and brighter blue HB stars it is possible that cool blue HB stars result from unmixed RGB stars. As already mentioned it is unfortunately not possible to determine the envelope helium abundance of a blue HB star because almost all of these stars are helium-deficient due to diffusion (Heber 1987).

4.2 Diffusion and abundance anomalies in blue HB stars

The abundance distribution within a stellar atmosphere influences the line profiles and the flux distribution (see Appendix C). A deviation in atmospheric abundances of HB stars from the cluster metallicity due to diffusion would thus affect the line profiles and flux distribution. Model atmospheres calculated for the cluster metallicity may then yield wrong results for effective temperatures and surface gravities when compared to observed spectra of HB stars.

It has been realized early on that the blue HB and blue tail stars in globular clusters show weaker helium lines than field main sequence B stars of similar temperatures (NGC 6397, Searle & Rodgers 1966; M 5, M 13, M 92, Greenstein & Münch 1966; M 13, M 15, M 92, Sargent 1967). Greenstein et al. (1967) already suggested diffusion as explanation for the He deficiency indicated by weak He lines in globular cluster and field HBB stars.

Michaud et al. (1983) performed the first theoretical study of diffusion effects in hot horizontal branch stars. Using the evolutionary tracks of Sweigart & Gross (1976) they selected combinations of temperature, gravity and mass appropriate for metal poor ([M/H] = -2) stars on the ZAHB. They assumed a helium abundance on the main sequence $Y_{\rm MS}$ of 0.2. For the metal-poor models it is found that *"in most of each envelope, the radiative acceleration on all elements* (i.e. C, N, O, Ca, Fe) *is much larger than gravity which is not the case in main-sequence stars."* The elements are thus pushed towards the surface of the star.

Turbulence affects the different elements to varying extent, but generally reduces the overabundances. Ca, Fe should be less affected by turbulence than CNO, i.e. should show larger overabundances in presence of turbulence. Models without turbulence and/or mass loss, which may reduce the effects of diffusion, predict stronger He depletions than are observed[13].

The extent of the predicted abundance variations varies with effective temperature, from none for HB stars cooler than about 5800 ± 500K (due to the very long diffusion timescales) to 2 – 4 dex in the hotter stars (the hottest model has $T_{\rm eff}$ = 20,700 K). RR Lyrae stars have temperatures between 6,000 K and 7,600 K and their Ca abundance could thus be affected by diffusion (which could play a rôle for the metallicity determination of field RR Lyrae stars). Due to the lower gravities (compared to main sequence stars) of the two cooler models (6300 K and 8400 K) one would expect them to have mass loss at least of the order found for Fm and Am stars, which would reduce overabundances by at least 1 dex. It is unclear whether radiative acceleration decreases fast enough towards the upper atmosphere to keep the levitated elements bound to the star. The overabundances in the two hottest models (12,500 K and 20,700 K) are limited to 3 dex for relatively abundant elements by the saturation of lines. Less abundant elements like P, Eu, Ga could show much larger overabundances before their lines saturate (up to 5 dex for original values of [M/H] = -2).

Further observations of blue HB stars in globular clusters support the idea of diffusion being active above a certain temperature:

Glaspey et al. (1985) find no evidence for super-solar iron abundance from spectra of 4 BHB stars in NGC 6397 ($T_{\rm eff} \approx$ 10,300 K ... 12,000 K).

Glaspey et al. (1989) determine abundances from high-resolution spectra for two stars in NGC 6752, using temperatures and surface gravities from Heber et al. (1986). The cooler star (CL1007, $T_{\rm eff}$ = 10,000 K) shows a higher rotational velocity ($v \sin i = 30 \pm 10$km/s) than the hotter star (CL1083, $T_{\rm eff}$ = 16,000 K; $v \sin i < 15$km/s). For CL1007 they find values for [(Mg,Si,Fe)/H] that agree with the metallicity of NGC 6752. CL1083, however, shows He depletion ($\log \frac{N_{He}}{N_H} = -1.74$) and a *super-solar* iron abundance of [Fe/H] $\approx +0.4$ (relative to a solar iron abundance of $\log \epsilon_{\rm Fe} = 7.46$). [(Mg,Si)/H] again agree with the cluster metallicity.

---

[13] Michaud (1982) and Charbonneau & Michaud (1988) showed that meridional circulation can prevent gravitational settling and that the limiting rotational velocity decreases with decreasing $\log g$.

Lambert et al. (1992) analyse high resolution spectra of two BHB stars in M 4 (4408, 4632) and one in NGC 6397 (48), finding $v \sin i = 12$km/s for M4-4408, ≤ 6km/s for the other two stars, and $T_{\rm eff} = 8600$ K – 9000 K. The abundances of the stars are found to be in good agreement with those known from red giants in the clusters, ruling out diffusion effects for these cool stars and any additional mixing between the tip of the red giant branch and the horizontal branch.

Altner & Matilsky (1993) find that their IUE spectra of M 79 are best fit by hot HB stars with 12,000 K $\leq T_{\rm eff} \leq$ 14,000 K and $\log g$ between 3.3 and 3.7 (lower than expected for ZAHB stars). Models with solar or slightly super-solar metallicities provide better fits to their data than the low-metallicity ones. This is in agreement with **Huenemoerder et al. (1984)** who found for *field* HBA stars that the metal-poor models were too bright below 1600Å and that Population I and Population II stars have indistinguishable UV colours above 10,000 K.

Cohen & McCarthy (1997) obtain abundances and rotational velocities of 5 cool (7300 – 9400 K) BHB stars in M 92. They find $v \sin i = 15 \ldots 43 km/s$ without any correlation with $T_{\rm eff}$ and abundances for the four cooler (7325 K – 7550 K) stars that agree with those derived for red giants in M 92.

The analyses of 13 HBB/HBA stars in M 13 by **Behr et al. (1999a)** show strong abundance anomalies above ≈11,000 – 12,000 K: strong enrichment of Fe, Ti, P, Cr; moderate enrichment of Ca, Si; possibly moderate CNO enrichment; strong He depletion; no change in Mg. The abundance anomalies are consistent with diffusion as described by Michaud et al. (1983) as well as with the observations of Glaspey et al. (1989) for NGC 6752.

Behr et al. (1999b) determine rotational velocities of 13 HBB/HBA stars with 7000 K $< T_{\rm eff} <$ 20,000 K in M 13. For stars above 10,000 K $v \sin i \leq 10$km/s (10 stars) whereas the cooler stars show velocities between 15 and 35 km/s (3 stars). The cooler stars show a similar velocity distribution as the one obtained by Peterson et al. (1995b) and the four stars common to both samples yield consistent values. The change in rotational velocity appears to be quite sudden and seems to coincide roughly with the temperature at which abundance anomalies start to show.

All this evidence supports the recent suggestion of **Grundahl et al. (1999)** that the onset of diffusion in stellar atmospheres may play a rôle in explaining the jump along the HB towards brighter u magnitudes at effective temperatures of about 11,500 K (see Fig. 23, which is an excerpt of Fig. 1 of Grundahl et al. 1999). This jump towards brighter magnitudes in $u, u - y$ is seen in all CMD's of globular clusters that have Strömgren photometry of sufficient quality. The observed HB stars return to the theoretical ZAHB at temperatures between 15,000 K and 20,000 K (see Fig. 1 of Grundahl et al. 1999).

The effective temperature of the jump is roughly the same for all clusters, irrespective of metallicity, central density, concentration or mixing evidence (meaning that the mass of the HB stars corresponding to the jump varies with metallicity). The jump temperature coincides with the apparent gap in $T_{\rm eff}$, $\log g$ found from spectroscopic analyses of HBB stars (cf. Fig. 20), which is also found at the same temperature for very different clusters. The u jump and the $\log g$ jump are even connected on a star-by-star basis. The constancy of $T_{\rm eff(u-jump)}$ among very different clusters makes helium mixing an unlikely explanation for the u-jump. The fact that the low $\log g$ values are seen among field HBB stars (e.g. Saffer et al. 1997), whereas field RGB stars do not show evidence for helium mixing argues against helium mixing as cause for the $\log g$ jump.

Radiative levitation of heavy elements decreases the far-UV flux and by backwarming increases the flux in u. Grundahl et al. (1999) show that the use of metal-rich atmospheres improves the agreement between observed data and theoretical ZAHB in the UV-CMD at all effective temperatures, but it worsens the agreement between theory and observation for hotter stars in the Strömgren CMD of NGC 6752 (see Fig. 8 of Grundahl et al. 1999). Thus diffusion may either not be as important in the hotter stars or the effects may be diminished by a weak stellar wind (invoked to explain the presence of He in sdB stars). An enrichment to [Fe/H] = +0.5, however, is necessary to achieve good fits with scaled-solar ATLAS9 Kurucz model atmospheres ($\log \epsilon_{Fe,\odot} = 7.60$).

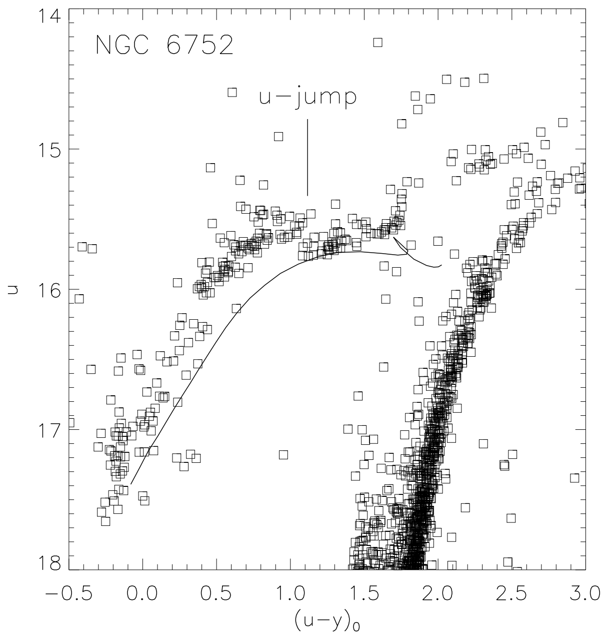

Fig. 23. $u, (u-y)_0$ CMD of NGC 6752 (Grundahl et al. 1999, their Fig. 1). The ZAHB plotted here is taken from VandenBerg et al. (2000). The $(u-y)_0$ colour of $\approx +0.4$ at which the stars return to the ZAHB corresponds to an effective temperature of $\approx 15,000$K.

The scenario proposed by Caloi (1999) to explain gaps at $(B-V)_0 \approx 0$ (see Sect. 3.1) is not directly related to the u-jump discussed here as $(B-V)_0 \approx 0$ corresponds to an effective temperature of about 9000 K. This cooler gap also is not seen in every cluster (which would be expected if it were due to an atmospheric phenomenon). The gap at $T_{\rm eff} \approx 13{,}000$ K seen in the $c_1, b-y$ diagram of field horizontal branch stars (Newell & Graham 1976) may be related to the u jump discussed by Grundahl et al. (1999) as the c_1 index contains u.

While we had discussed abundance anomalies caused by diffusion as possible cause for the offset from the ZAHB found for the blue HB stars in M 15 (see Sect. 3.2.6) we failed to recognize that the *combined* effect of metal-rich model atmospheres on $T_{\rm eff}$ *and* $\log g$ would move the stars considerably closer to the ZAHB. Solar metallicity, however, does not seem metal-rich enough to solve the low $\log g$ problem: Crocker et al. (1988) used solar-metallicity ATLAS6 model atmospheres for stars hotter than 10,000 K and their results show the low $\log g$ problem very clearly.

4.3 Distances to Globular Clusters

There have been indications that differences between RR Lyrae stars in the field and in globular clusters could result in an underestimate of the distances to globular clusters: **Cacciari & Bruzzi (1993)** found from analyses of type-c RR Lyrae stars in several Oosterhoff type I and II globular clusters that the zero-point for the cluster stars may be $0\overset{m}{.}2$ – $0\overset{m}{.}3$ brighter than that obtained from Baade-Wesselink analyses of field RR Lyrae stars. **Storm et al. (1994)** got a similar result from Baade-Wesselink analyses of RR Lyrae stars in M 92, but not in M 5. They cautioned that RR Lyrae stars in clusters with few such stars are probably evolved stars on their way from the BHB to the AGB and thus brighter than unevolved "original" RR Lyrae stars. On the theoretical side **Caloi et al. (1997)** reported that new HB models are more luminous (at low metallicities) by about $0\overset{m}{.}15$ than older versions (at the colour of the RR Lyrae strip). As HIPPARCOS results for metal-poor field subdwarfs became available several authors determined the distances to globular clusters by fitting their main sequence with the local subdwarfs. Below the work of Reid (1997, 1998), Gratton et al.

(1997) and Pont et al. (1998) are briefly described – the reader is referred to the original papers for more details. The results of the papers are summarized in Table 10.

Reid (1997) used a sample of 15 metal-poor ($-2.18 <$ [Fe/H] < -1.28) subdwarfs with Hipparcos parallaxes π with errors $d\pi/\pi \leq 0.12$, four of which are suspected binaries and one of which is a confirmed binary. He supplemented this sample with three stars that have high-precision ground-based parallaxes. Comparing Hipparcos subdwarfs with [Fe/H] ≈ -1.5 to those with [Fe/H] < -2 shows little difference between their M_V at a given $(B-V)_0$, much less than predicted from theoretical isochrones. The observed very metal-poor subdwarfs are thus brighter than predicted. Due to the small measurement errors of the Hipparcos parallaxes the corrections for Lutz-Kelker bias[14] (Lutz & Kelker 1973) are below $0\overset{\mathrm{m}}{.}13$.

The local calibrating subdwarfs are selected according to the metallicity of the globular cluster, for which the Zinn-West metallicity scale (Zinn & West 1984) is used. Within one metallicity range the calibration stars were not adjusted in $(B-V)$ for the metallicity differences between them and the globular cluster, which may lead to an overestimate of the distance modulus by $\leq 0\overset{\mathrm{m}}{.}1$. Changes of $\pm 0\overset{\mathrm{m}}{.}02$ in E_{B-V} result in changes of $\pm 0\overset{\mathrm{m}}{.}1$ in the distance modulus. Excluding binaries, possibly evolved stars with $M_V < 5\overset{\mathrm{m}}{.}5$ and/or slightly more metal-rich calibrating stars affects the distance moduli at the $\pm 0\overset{\mathrm{m}}{.}05$ level only. The distances to the metal-poor clusters M 15, M 68, M 30, M 92 and to M 13 derived here are significantly larger than previous determinations, whereas M 5 and NGC 6752 are scarcely affected. The longer distances lead to younger ages (11-13 Gyrs), but the isochrones cannot fit the main sequence and the RGB simultaneously (see also Harris et al. 1997). The younger ages, however, agree better with ages derived from the Hubble constant.

Gratton et al. (1997) start with a sample of 13 Hipparcos stars with errors $d\pi/\pi < 0.12$ and $-1.92 \leq$ [Fe/H] ≤ -0.4 (only 6 stars with [Fe/H] < -1). Monte Carlo simulations indicate Lutz-Kelker like corrections of $-0\overset{\mathrm{m}}{.}002$ for the complete sample, which are neglected. They enlarge their sample with 6 stars from Reid (1997, all with [Fe/H] < -1.2) and 9 additional Hipparcos stars from published lists. For these additional stars the Lutz-Kelker corrections are applied. Abundances for 2/3 of the program stars are obtained from high-dispersion spectroscopy analysed in the same way as the data of Carretta & Gratton (1997). Of the 28 stars with Hipparcos parallaxes selected in the beginning 13 fulfil the criteria for main sequence fitting (single, $M_V > 5\overset{\mathrm{m}}{.}5$).

The stars within one metallicity bin were corrected in $B-V$ to one common metallicity. Only clusters with $E_{B-V} < 0\overset{\mathrm{m}}{.}05$ are considered (47 Tuc, M 5, M 13, M 30, M 68, M 92, NGC 288, NGC 362, NGC 6752) and the abundance scale of Carretta & Gratton (1997) is used which yields abundances higher by 0.2–0.3 dex than those of Zinn & West (1984) for intermediate metallicity clusters. Including or correcting for possible undetected binaries in the local subdwarf sample would reduce the distance moduli by $\leq 0\overset{\mathrm{m}}{.}02$. Comparing the distances to those of Reid (1997) shows a mean offset of $-0\overset{\mathrm{m}}{.}08 \pm 0\overset{\mathrm{m}}{.}04$ with Reid's distance moduli being larger. However, the three metal-poor clusters alone (for which only 2 resp. 3 subdwarfs were used in contrast to Reid's 8) have an average offset of $-0\overset{\mathrm{m}}{.}17 \pm 0\overset{\mathrm{m}}{.}03$, whereas M 5, M 13, and NGC 6752 have an offset of $+0\overset{\mathrm{m}}{.}02 \pm 0\overset{\mathrm{m}}{.}09$. Gratton et al. also find younger ages for the globular cluster resulting from the longer distances and the new metallicities for cluster and field stars.

Pont et al. (1998) start with a sample of 330 Hipparcos subdwarfs (mostly F stars at or near the turnoff) and 216 Hipparcos stars below the Hyades main sequence with $d\pi/\pi < 0.2$. Metallicities and radial velocities were obtained from *Coravel* measurements for most stars. From Monte-Carlo simulations a bias working opposite the Lutz-Kelker bias is detected and corrected. Known and suspected binaries are corrected by a constant offset in M_V.

---

[14] Selecting stars by a lower limit to the parallax (i.e. upper limit to the distance) will bias the mean distance to smaller values: Errors will result in a scattering of stars across the distance limit, but more stars lie outside the distance limit than inside. Thus there will be more stars with too low distances than stars with too high distances and the mean distance (and thereby the mean absolute brightness) will be underestimated.

For the fit to M92's main sequence 17 subdwarfs (including binaries and evolved stars) with $-2.6 <$ [Fe/H] < -1.8 are used (corrected for the various biases). The use of evolved stars implicitly assumes that the field subdwarfs have a similar age as the globular cluster. The authors argue that the evolved metal-poor ([Fe/H] < -1.8) field stars show a turnoff colour at least as red as the one of M 92 and should therefore be at least as old. Depending on the selected sub-samples (only unevolved stars, with/without binaries etc.) $(m-M)_V$ for M 92 varies between $14\overset{\mathrm{m}}{.}64$ and $14\overset{\mathrm{m}}{.}76$ with $14\overset{\mathrm{m}}{.}67\pm0\overset{\mathrm{m}}{.}08$ being adopted as final result. This distance together with isochrone fits leads to an age of $\approx$ 13-14 Gyrs.

The distance is much smaller than those derived by Reid (1997, $14\overset{\mathrm{m}}{.}99$) and Gratton et al. (1997, $14\overset{\mathrm{m}}{.}80$). Using only unevolved stars, omitting binary corrections and applying the corrections for Lutz-Kelker bias only would result in $(m-M)_V = 14\overset{\mathrm{m}}{.}91$ in good agreement with Reid (1997) and Gratton et al. (1997). Pont et al. (1998) argue that the long distance to M 92 would put the cluster main sequence close to that of the more metal-rich field subdwarfs in contrast to the prediction of stellar evolution that the main sequence for [Fe/H] $= -2.2$ is $0\overset{\mathrm{m}}{.}2$–$0\overset{\mathrm{m}}{.}3$ fainter (at a given $(B-V)_0$) than that for [Fe/H] $= -1.5$ (which is supported by the field subdwarfs used in this paper, but not by Reid 1997).

Reid (1998) performed a new distance determination using a sample of 91 HIPPARCOS stars with $d\pi/\pi < 0.15$ and $V < 10\overset{\mathrm{m}}{.}5$. Monte Carlo simulations taking into account the limit in V and the $d\pi - \pi$ correlation show that for $V < 11\overset{\mathrm{m}}{.}0$ and $d\pi/\pi < 0.15$ M_V is underestimated by at most $0\overset{\mathrm{m}}{.}15$. Metallicities are taken from Gratton et al. (1997) for the field stars and Carretta & Gratton (1997) for the globular clusters. Reid cautions against the use of subgiants for distance determinations because solar-metallicity main sequence stars occupy a similar region in $M_V, B-V$ as metal-poor subgiants. The unevolved stars with $-2 <$ [Fe/H] < -1 of the sample used in this paper can be described by one common main sequence (in contradiction to Pont et al. 1998).

Stars with $M_V \geq 4\overset{\mathrm{m}}{.}75$ (excluding subgiants, although some stars may already evolve away from the main sequence) are used for the main sequence fitting. The subdwarfs are colour-shifted to a common metallicity. Distance moduli derived with and without Lutz-Kelker corrections differ only on the $0\overset{\mathrm{m}}{.}01$ level. As only 2 stars in the current sample have [Fe/H] < -1.7 the metal-poor clusters are not discussed here. Among the intermediate metallicity clusters the distance moduli for M 5, M 13 and NGC 6752 are very similar to those of Reid (1997) and Gratton et al. (1997), which is not surprising as the subdwarf samples have large overlaps. $M_V(RR) = 0.79 + 0.17$[Fe/H] results for the globular cluster stars ($0\overset{\mathrm{m}}{.}3$ brighter than obtained from field RR Lyrae stars), which might be understood from He mixing.

Reid & Gizis (1998) use a sample of M-subdwarfs (selected by proper motion, [Fe/H] < -1.5) with $d\pi/\pi < 0.1$ to determine the distance to NGC 6397 from main sequence fitting. They adopt $E_{B-V} = 0\overset{\mathrm{m}}{.}18$ and obtain $(m-M)_0 = 12\overset{\mathrm{m}}{.}13$. Extending the distance determination (via relative offsets) to M 92, M 68, M 3, M 13 yields a $M_V(RR)$ vs. [Fe/H] relation in good agreement with Caloi et al.'s (1997) most recent HB models.

From the above description it is obvious that the question of the distance scale for globular clusters is far from answered and that the various biases and their treatment strongly influence the results. The discussion by **Carretta et al. (1999)** of biases affecting the main sequence fitting of globular clusters by local field subdwarfs is very enlightening and highly recommended. They argue that total effect of various biases yields an uncertainty of at least $\pm0\overset{\mathrm{m}}{.}12$ for the resulting distance moduli and thus neither the long nor the short distance scale can currently be ruled out. Unfortunately the only distance determination from a white dwarf sequence (which avoids several of the problems of subdwarf fitting) has been performed for NGC 6752 (Renzini et al. 1996), for which all distance determinations yield rather similar results (see Chapter 8 for more information on white dwarfs in globular clusters).

The differences between the brightness of **RR Lyrae stars in the field and globular clusters** prompted several investigations:

Table 10. HIPPARCOS based distance moduli for globular clusters compared to older values. The data are taken from Zinn & West (1984, ZW84), Carretta & Gratton (1997, CG97), Djorgovski (1993, D93), Reid (1997, R97; 1998, R98), Gratton et al. (1997, G97), Reid & Gizis (1998, NGC 6397), Renzini et al. (1996, NGC 6752/white dwarfs), and Pont et al. (1998, M 92).

Cluster	[Fe/H]		$(m-M)_0/E_{B-V}$(number of local subdwarfs)				
	ZW84	CG97	D93	R97	R98	G97*	other
47 Tuc	-0.71	-0.67	$13^{\rm m}.31/0^{\rm m}.04$		$13^{\rm m}.56/0^{\rm m}.04$ (9)	$13^{\rm m}.46/0^{\rm m}.055$ (8)	
M 71	-0.58	-0.70	$12^{\rm m}.96/0^{\rm m}.28$		$13^{\rm m}.19/0^{\rm m}.28$ (9)		
NGC 288	-1.40	-1.05	$14^{\rm m}.62/0^{\rm m}.03$		$15^{\rm m}.00/0^{\rm m}.01$ (9)	$14^{\rm m}.85/0^{\rm m}.033$ (6)	
M 5	-1.40	-1.10	$14^{\rm m}.40/0^{\rm m}.03$	$14^{\rm m}.45/0^{\rm m}.03$ (8)	$14^{\rm m}.52/0^{\rm m}.02$ (9)	$14^{\rm m}.51/0^{\rm m}.035$ (7)	
NGC 362	-1.28	-1.12	$14^{\rm m}.67/0^{\rm m}.04$			$14^{\rm m}.88/0^{\rm m}.056$ (6)	
M 13	-1.65	-1.41	$14^{\rm m}.29/0^{\rm m}.02$	$14^{\rm m}.48/0^{\rm m}.02$ (10)	$14^{\rm m}.45/0^{\rm m}.02$ (9)	$14^{\rm m}.41/0^{\rm m}.02$ (9)	
NGC 6752	-1.54	-1.43	$13^{\rm m}.12/0^{\rm m}.04$	$13^{\rm m}.17/0^{\rm m}.02$ (10)	$13^{\rm m}.17/0^{\rm m}.04$ (12)	$13^{\rm m}.23/0^{\rm m}.035$ (9)	$13^{\rm m}.05/0^{\rm m}.04$
NGC 6397	-1.91	-1.82	$11^{\rm m}.71/0^{\rm m}.18$		$12^{\rm m}.24/0^{\rm m}.19$ (8)		$12^{\rm m}.13/0^{\rm m}.18$ (15)
M 30	-2.13	-1.88	$14^{\rm m}.35/0^{\rm m}.05$	$14^{\rm m}.95/0^{\rm m}.05$ (9)		$14^{\rm m}.84/0^{\rm m}.039$ (3)	
M 68	-2.09	-1.95	$14^{\rm m}.84/0^{\rm m}.05$	$15^{\rm m}.29/0^{\rm m}.05$ (9)		$15^{\rm m}.20/0^{\rm m}.040$ (2)	
M 15	-2.15	-2.12	$15^{\rm m}.11/0^{\rm m}.05$	$15^{\rm m}.38/0^{\rm m}.09$ (9)			
M 92	-2.24	-2.15	$14^{\rm m}.38/0^{\rm m}.02$	$14^{\rm m}.93/0^{\rm m}.02$ (9)		$14^{\rm m}.74/0^{\rm m}.025$ (2)	$14^{\rm m}.61/0^{\rm m}.02$ (17)

* Moehler (1999) erroneously gave $(m-M)_V$ instead of $(m-M)_0$.

Gratton (1998) analyses a sample of 20 field HB stars with $V < 9^{\rm m}.0$ and 2 fainter ones with HIPPARCOS parallaxes for mean M_V. To avoid Lutz-Kelker bias the parallaxes rather than absolute magnitudes are averaged. Analysing the metallicity ranges separately leads to $M_V(RR) = (0.22 \pm 0.22)$[Fe/H]$+(0.99 \pm 0.11)$ in consistency with independent determinations for field RR Lyrae stars, but considerably fainter than HIPPARCOS based calibrations for cluster RR Lyrae stars. The cluster calibration might be affected if the abundance scales for field stars (derived from dwarfs) and globular clusters (derived from red giants) were systematically different. Real differences between field and cluster RR Lyrae stars might result from helium mixing in globular cluster stars. The RR Lyrae stars in the LMC seem to agree better with the field stars than with the globular cluster stars.

In contrast **Groenewegen & Salaris (1999)** analyse field RR Lyrae stars with HIPPARCOS parallaxes and find $M_V(RR) = 0.18$[Fe/H]$+(0.77\pm0.26)$ in good agreement with the distance scale for globular clusters derived by Gratton et al. (1997).

Catelan (1998) finds that metal-poor ([Fe/H]< -1) field RR Lyrae stars with HIPPARCOS parallaxes show the same period-temperature relation as globular cluster RR Lyrae stars in the same metallicity range, arguing against luminosity differences between the two samples.

De Boer et al. (1997) report that HIPPARCOS parallaxes for field HBA stars still yield masses significantly below the canonical mass expected for these objects (mean mass of $0.38\,{\rm M}_\odot$ for five stars vs. $0.55\,{\rm M}_\odot$). They suggest problems with theoretical Balmer lines resulting in too low values of $\log g$ as likely cause for the discrepancy. One should note, however, that $T_{\rm eff}$ and $\log g$ for the HBA stars were mostly derived from spectrophotometry and not from line profile analyses. In any case the temperature range of these HBA stars ($7500\,{\rm K} < T_{\rm eff} < 9000\,{\rm K}$) makes any analysis for physical parameters a tricky business.

On the theoretical side **Salaris & Weiss (1998)** find that the $M_V(RR)$ vs. [Fe/H] relation of Gratton et al. (1997) for globular cluster stars agrees well with their theoretical relation. Also **Cassisi et al. (1999)** argue that BVI magnitudes from theoretical tracks of Cassisi et al. (1998) show good agreement with $M_V(RR)$ vs. [Fe/H] as given by Gratton et al. (1997). The new models of **D'Antona et al. (1997)** for globular cluster stars (better convection treatment and updated input physics) agree with the long distance scale and younger cluster ages, although some problems with the RGB colour remain.

Table 11. The average ratio of calculated mass (as described in Sect. 3.2.5) to the mass on the ZAHB (for the respective temperature) of HB stars in globular clusters plotted in Figs. 21 and 24. The distance moduli were taken from Djorgovski (1993, D93) and Reid (1997, 1998, R).

Cluster	[Fe/H]		$<\frac{M}{M_{ZAHB}}>_{D93}$	$<\frac{M}{M_{ZAHB}}>_{R}$
	ZW84	CG97		
NGC 288	−1.40	−1.05	0.52±0.12	0.69±0.16
M 5	−1.40	−1.10	0.87±0.21	0.95±0.22
M 3	−1.66	−1.34	0.97±0.40	–
NGC 6752	−1.54	−1.43	1.04±0.52	1.10±0.55
NGC 6397	−1.91	−1.82	0.62±0.16	0.78±0.20
M 15	−2.15	−2.12	0.81±0.49	1.10±0.67
M 92	−2.24	−2.15	0.66±0.25	1.10±0.42

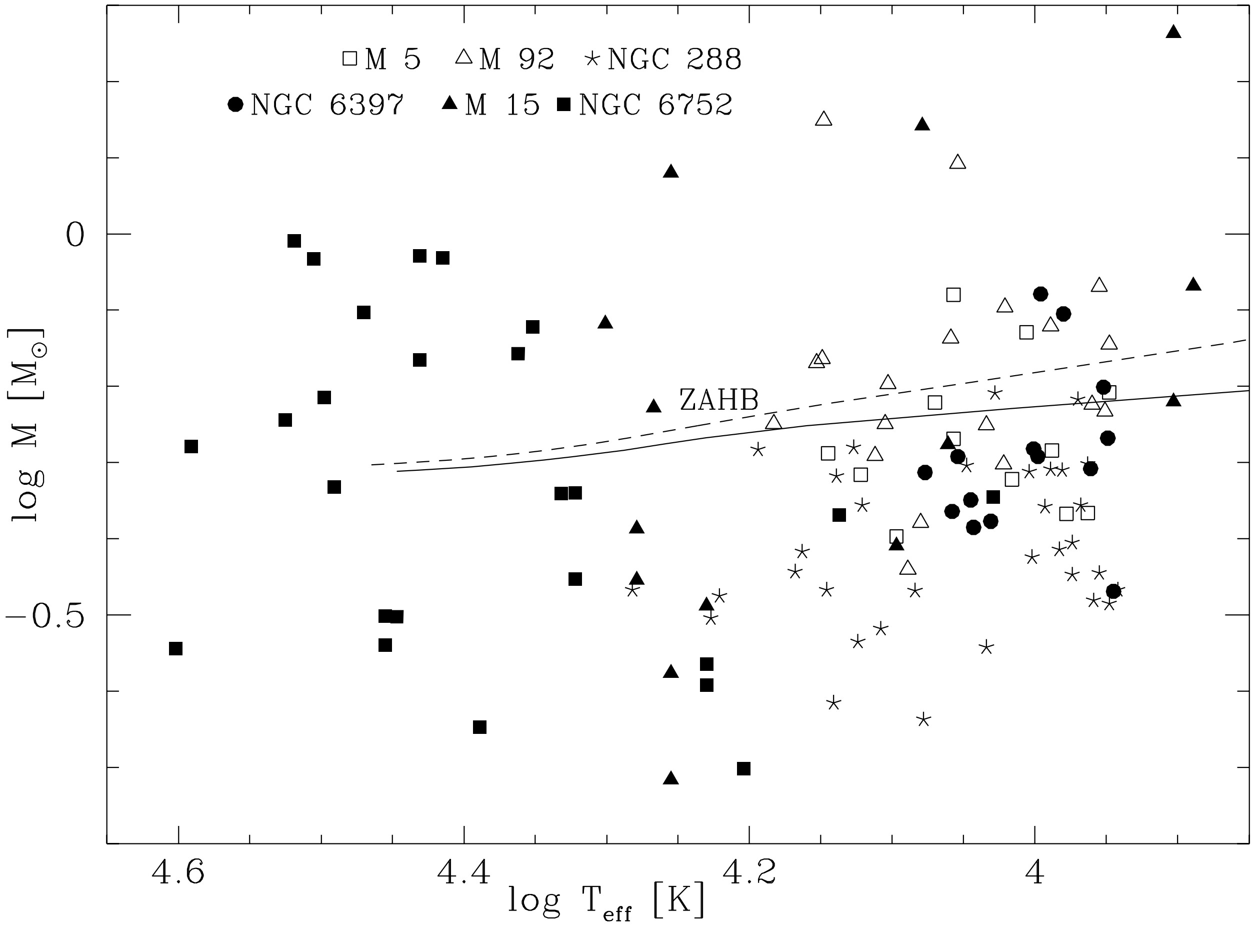

Fig. 24. The masses of the stars derived with the new distances listed by Reid (1997, 1998, no new distance estimate available for M 3) compared to evolutionary tracks from Dorman et al. (1993). The solid line gives the ZAHB for [Fe/H] = −1.48, the dashed line marks the ZAHB for [Fe/H] = −2.26 (Dorman et al. 1993).

It is interesting to note that for M 5 and NGC 6752 (where the masses of the hot HB/EHB stars almost agree with the canonical expectations) the new distances are close to the old ones, whereas for the metal poor clusters M 15, M 92, and NGC 6397 the new distance moduli are $0^{\text{m}}\!.3$ – $0^{\text{m}}\!.6$ larger than the old ones, thereby greatly reducing the mass discrepancies (see also Heber et al. 1997). The resulting new masses are plotted in Fig. 24 and in Table 11 we list the average ratio between the mass calculated for an HB star (Sect. 3.3.5) and the supposed ZAHB mass for its temperature (from Dorman et al. 1993). It can be seen that in all cases (except NGC 6752) the agreement between expected and calculated mass improves with the new distance moduli, although the masses in NGC 288 remain significantly too low. From our observations we therefore favour the longer distance scale for globular clusters.

4.4 Hot HB stars in NGC6752

As we know that the sdB stars observed and analysed in NGC 6752 show surface gravities and masses in good agreement with canonical theory (Sect. 3.3) *and* that the distance modulus of NGC 6752 is rather constant among the different distance determinations (see Table 10) we decided that spectroscopic analyses of HBB stars in NGC 6752 would offer a perfect test case: If the HBB stars analysed there show low surface gravities and canonical masses, then the combination of deep mixing and the long distance scale (for the other globular clusters) could solve the problems discussed in Chapter 3. If the HBB stars show low surface gravities and low masses, diffusion may indeed play a rôle when analysing these stars for effective temperature and surface gravity. Then the low surface gravities found for HBB stars could be artifacts from the use of inappropriate model atmospheres for the analyses.

4.4.1 New Observations and their reduction

We selected our targets from the photographic photometry of Buonanno et al. (1986, see Table 12 and Fig. 25). For our observations we used the ESO 1.52m telescope with the Boller & Chivens spectrograph and CCD # 39 (2048 × 2048 pixels, $(15\,\mu\mathrm{m})^2$ pixel size, read-out noise 5.4 e^-, conversion factor 1.2 e^-/count). We used grating # 33 (65 Å/mm) to cover a wavelength of 3300 Å – 5300 Å. Combined with a slit width of $2''$ we thus achieved a spectral resolution of 2.6 Å. The spectra were obtained on July 22-25, 1998. For calibration purposes we observed each night ten bias frames and ten dome flat-fields with a mean exposure level of about 10,000 counts each. Before and after each science observation we took HeAr spectra for wavelength calibration purposes. We observed dark frames of 3600 and 1800 sec duration to measure the dark current of the CCD. As flux standard stars we used LTT 7987 and EG 274.

We first averaged the bias and flat field frames separately for each night. As we could not detect any significant change in the mean bias level we computed the median of the bias frames of the four nights and found that the bias level showed a gradient across the image, increasing from the lower left corner to the upper right corner by about 1%. We fitted the bias with a linear approximation along both axes and used this fit as bias for the further reduction. As no overscan was recorded we could not adjust the bias level. Bias frames taken during the night, however, revealed no significant change in the mean bias level. The mean dark current determined from long dark frames showed no structure and turned out to be negligible (3 ± 3 e^-/hr/pixel).

We normalized the flat fields as described in Sect. 3.3.1 (EFOSC1 data). The normalized flat fields of the first three night were combined. For the fourth night we used only the flat field obtained during that night as we detected a slight variation in the fringe patterns of the flat fields from the first three nights compared to that of the fourth (below 5%). The spectra were wavelength calibrated, sky subtracted (with a linear fit to spatial distribution of the sky background), extracted and corrected for atmospheric extinction as described in Sect. 3.2.1. The data for the flux standard stars were taken from Hamuy et al. (1992) and the response curves were fitted by splines.

We also analyse data that were obtained as backup targets at the NTT during observing runs dedicated to other programs. The observational set-up and the data reduction were identical to those described in Chapter 5.

Table 12. Coordinates, photometry, and heliocentric radial velocities for the new target stars in NGC 6752. The numbers refer to Buonanno et al. (1986) and "acc." refers to targets that happened to be in the slit by accident. For the NTT spectra obtained in 1998 no radial velocities could be determined due to problems with the wavelength calibration (see Sect. 5.1).

star	α_{2000}	δ_{2000}	V	$B-V$	$v_{\mathrm{rad,hel}}$ [km/s]	acc.
		ESO 1.52m (1998)				
B652	$19^{\mathrm{h}}11^{\mathrm{m}}32\overset{\mathrm{s}}{.}6$	$-59^{\circ}57'41''$	$14\overset{\mathrm{m}}{.}70$	$-0\overset{\mathrm{m}}{.}01$	−51	
B1132	$19^{\mathrm{h}}11^{\mathrm{m}}23\overset{\mathrm{s}}{.}5$	$-59^{\circ}58'14''$	$15\overset{\mathrm{m}}{.}34$	$-0\overset{\mathrm{m}}{.}01$	−53	
B1152	$19^{\mathrm{h}}11^{\mathrm{m}}23\overset{\mathrm{s}}{.}1$	$-59^{\circ}59'27''$	$15\overset{\mathrm{m}}{.}21$	$-0\overset{\mathrm{m}}{.}02$	−54	
B1157	$19^{\mathrm{h}}11^{\mathrm{m}}23\overset{\mathrm{s}}{.}1$	$-59^{\circ}56'36''$	$15\overset{\mathrm{m}}{.}07$	$+0\overset{\mathrm{m}}{.}03$	−41	
B1738	$19^{\mathrm{h}}11^{\mathrm{m}}09\overset{\mathrm{s}}{.}7$	$-60^{\circ}03'54''$	$15\overset{\mathrm{m}}{.}48$	$-0\overset{\mathrm{m}}{.}03$	−40	
B2735	$19^{\mathrm{h}}10^{\mathrm{m}}49\overset{\mathrm{s}}{.}5$	$-60^{\circ}04'05''$	$14\overset{\mathrm{m}}{.}43$	$+0\overset{\mathrm{m}}{.}03$	−66	
B3253	$19^{\mathrm{h}}10^{\mathrm{m}}38\overset{\mathrm{s}}{.}3$	$-59^{\circ}51'38''$	$14\overset{\mathrm{m}}{.}47$	$+0\overset{\mathrm{m}}{.}00$	−49	
B3348	$19^{\mathrm{h}}10^{\mathrm{m}}36\overset{\mathrm{s}}{.}3$	$-60^{\circ}00'15''$	$14\overset{\mathrm{m}}{.}27$	$+0\overset{\mathrm{m}}{.}03$	−27	×
B3408	$19^{\mathrm{h}}10^{\mathrm{m}}35\overset{\mathrm{s}}{.}4$	$-60^{\circ}00'19''$	$15\overset{\mathrm{m}}{.}14$	$+0\overset{\mathrm{m}}{.}00$	−73	×
B3410	$19^{\mathrm{h}}10^{\mathrm{m}}35\overset{\mathrm{s}}{.}3$	$-60^{\circ}00'47''$	$15\overset{\mathrm{m}}{.}32$	$+0\overset{\mathrm{m}}{.}02$	−30	
B3424	$19^{\mathrm{h}}10^{\mathrm{m}}35\overset{\mathrm{s}}{.}1$	$-60^{\circ}02'13''$	$15\overset{\mathrm{m}}{.}23$	$-0\overset{\mathrm{m}}{.}05$	−51	
B3450	$19^{\mathrm{h}}10^{\mathrm{m}}34\overset{\mathrm{s}}{.}6$	$-60^{\circ}00'17''$	$14\overset{\mathrm{m}}{.}81$	$-0\overset{\mathrm{m}}{.}06$	−39	
B3461	$19^{\mathrm{h}}10^{\mathrm{m}}34\overset{\mathrm{s}}{.}3$	$-60^{\circ}01'50''$	$14\overset{\mathrm{m}}{.}87$	$-0\overset{\mathrm{m}}{.}03$	−41	
B3655	$19^{\mathrm{h}}10^{\mathrm{m}}30\overset{\mathrm{s}}{.}2$	$-59^{\circ}57'27''$	$15\overset{\mathrm{m}}{.}08$	$-0\overset{\mathrm{m}}{.}22$	−29	×
B3736	$19^{\mathrm{h}}10^{\mathrm{m}}28\overset{\mathrm{s}}{.}3$	$-60^{\circ}00'48''$	$14\overset{\mathrm{m}}{.}47$	$+0\overset{\mathrm{m}}{.}07$	−57	×
B4172	$19^{\mathrm{h}}10^{\mathrm{m}}19\overset{\mathrm{s}}{.}1$	$-59^{\circ}57'26''$	$14\overset{\mathrm{m}}{.}48$	$-0\overset{\mathrm{m}}{.}04$	−50	
B4424	$19^{\mathrm{h}}10^{\mathrm{m}}14\overset{\mathrm{s}}{.}2$	$-59^{\circ}55'23''$	$14\overset{\mathrm{m}}{.}70$	$+0\overset{\mathrm{m}}{.}00$	−55	
B4551	$19^{\mathrm{h}}10^{\mathrm{m}}10\overset{\mathrm{s}}{.}9$	$-60^{\circ}03'50''$	$14\overset{\mathrm{m}}{.}93$	$+0\overset{\mathrm{m}}{.}01$	−55	
B4822	$19^{\mathrm{h}}10^{\mathrm{m}}01\overset{\mathrm{s}}{.}9$	$-60^{\circ}01'12''$	$15\overset{\mathrm{m}}{.}06$	$+0\overset{\mathrm{m}}{.}01$	−30	
B4951	$19^{\mathrm{h}}09^{\mathrm{m}}55\overset{\mathrm{s}}{.}0$	$-60^{\circ}01'25''$	$15\overset{\mathrm{m}}{.}38$	$-0\overset{\mathrm{m}}{.}05$	−36	
		ESO NTT (1997, see Sect. 5.2)				
B944	$19^{\mathrm{h}}11^{\mathrm{m}}26\overset{\mathrm{s}}{.}7$	$-59^{\circ}56'03''$	$14\overset{\mathrm{m}}{.}58$	$+0\overset{\mathrm{m}}{.}02$	+72	×
B1391	$19^{\mathrm{h}}11^{\mathrm{m}}11\overset{\mathrm{s}}{.}8$	$-59^{\circ}55'35''$	$15\overset{\mathrm{m}}{.}84$	$-0\overset{\mathrm{m}}{.}11$	−32	
B1780	$19^{\mathrm{h}}11^{\mathrm{m}}09\overset{\mathrm{s}}{.}0$	$-59^{\circ}52'06''$	$15\overset{\mathrm{m}}{.}77$	$-0\overset{\mathrm{m}}{.}07$	−32	
B2099	$19^{\mathrm{h}}11^{\mathrm{m}}03\overset{\mathrm{s}}{.}3$	$-59^{\circ}55'39''$	$15\overset{\mathrm{m}}{.}88$	$-0\overset{\mathrm{m}}{.}09$	−38	
		ESO NTT (1998, see Sect. 5.1)				
B2697	$19^{\mathrm{h}}10^{\mathrm{m}}50\overset{\mathrm{s}}{.}3$	$-60^{\circ}01'21''$	$14\overset{\mathrm{m}}{.}29$	$+0\overset{\mathrm{m}}{.}08$	–	×
B2698	$19^{\mathrm{h}}10^{\mathrm{m}}50\overset{\mathrm{s}}{.}3$	$-60^{\circ}02'34''$	$15\overset{\mathrm{m}}{.}08$	$-0\overset{\mathrm{m}}{.}13$	–	
B2747	$19^{\mathrm{h}}10^{\mathrm{m}}49\overset{\mathrm{s}}{.}1$	$-59^{\circ}52'55''$	$15\overset{\mathrm{m}}{.}99$	$-0\overset{\mathrm{m}}{.}07$	–	
B2932	$19^{\mathrm{h}}10^{\mathrm{m}}44\overset{\mathrm{s}}{.}9$	$-59^{\circ}51'48''$	$16\overset{\mathrm{m}}{.}08$	$-0\overset{\mathrm{m}}{.}11$	–	
B3006	$19^{\mathrm{h}}10^{\mathrm{m}}43\overset{\mathrm{s}}{.}4$	$-59^{\circ}56'56''$	$16\overset{\mathrm{m}}{.}14$	$-0\overset{\mathrm{m}}{.}10$	–	
B3094	$19^{\mathrm{h}}10^{\mathrm{m}}41\overset{\mathrm{s}}{.}5$	$-60^{\circ}02'51''$	$14\overset{\mathrm{m}}{.}19$	$+0\overset{\mathrm{m}}{.}03$	–	×
B3140	$19^{\mathrm{h}}10^{\mathrm{m}}40\overset{\mathrm{s}}{.}7$	$-59^{\circ}51'55''$	$13\overset{\mathrm{m}}{.}97$	$+0\overset{\mathrm{m}}{.}08$	–	×
B3253	$19^{\mathrm{h}}10^{\mathrm{m}}38\overset{\mathrm{s}}{.}3$	$-59^{\circ}51'38''$	$14\overset{\mathrm{m}}{.}47$	$+0\overset{\mathrm{m}}{.}00$	–	
B3699	$19^{\mathrm{h}}10^{\mathrm{m}}29\overset{\mathrm{s}}{.}3$	$-59^{\circ}58'11''$	$16\overset{\mathrm{m}}{.}05$	$-0\overset{\mathrm{m}}{.}07$	–	

4.4.2 New Atmospheric Parameters

To derive effective temperatures, surface gravities, and helium abundances we fitted the observed Balmer and helium lines with stellar model atmospheres. Beforehand we corrected the spectra for radial velocity shifts, derived from the positions of the Balmer lines. The resulting heliocentric velocities are listed in Table 12. The error of the velocities (as estimated from the scatter of the velocities derived from individual lines) is about 40 km/s. The spectra were then normalized by eye and are plotted in Figs. 26 and 27.

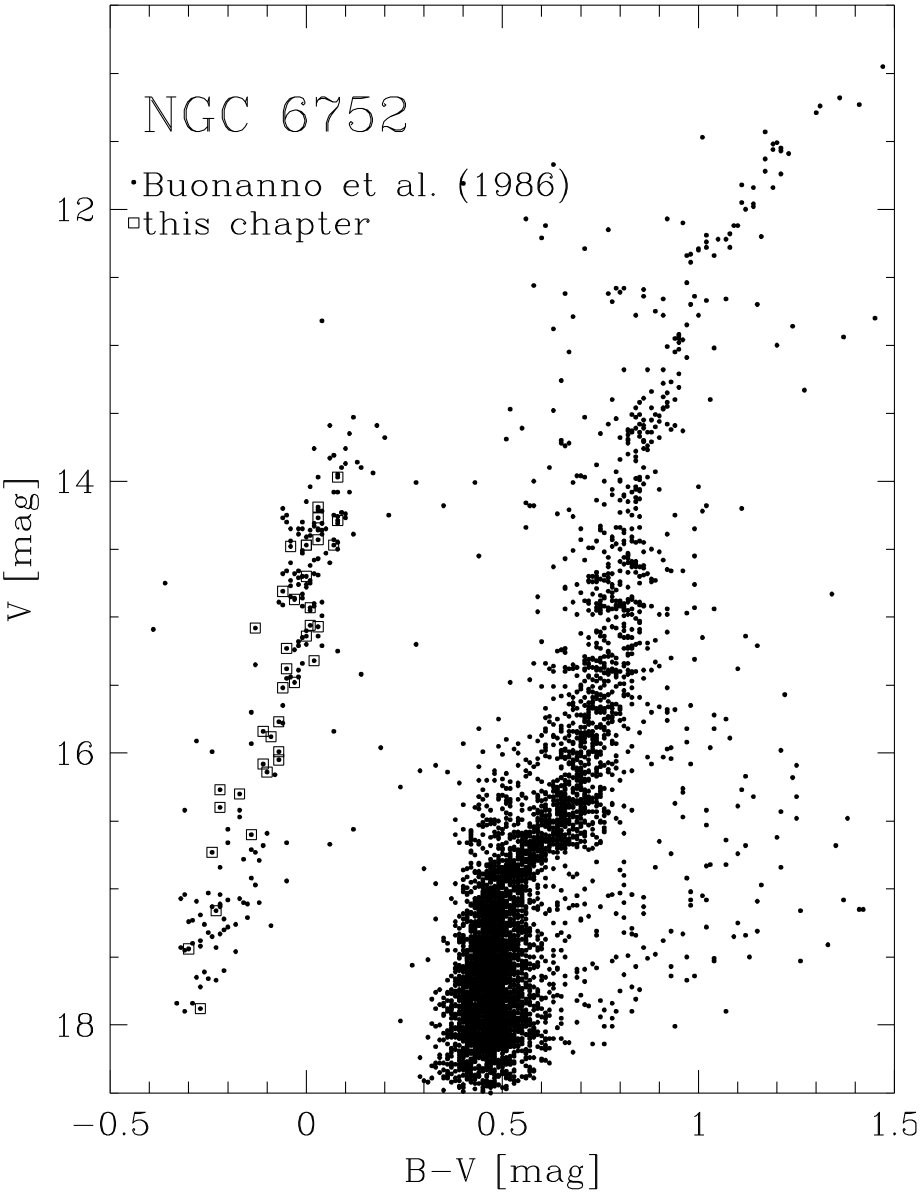

Fig. 25. The colour-magnitude diagram of NGC 6752 (Buonanno et al. 1986). Stars analysed in this chapter are marked by open squares.

To establish the best fit we used the routines developed by Bergeron et al. (1992) and Saffer et al. (1994), which employ a χ^2 test. The σ necessary for the calculation of χ^2 is estimated from the noise in the continuum regions of the spectra. In addition the fit program normalizes model spectra *and* observed spectra using the same points for the continuum definition. The values for $T_{\rm eff}$ and $\log g$ will be used to derive masses for the stars as described in Sect. 3.2.5. We will use $(m-M)_0 = 13.17$ and $E_{B-V} = 0.04$ for the calculation of the masses. These are mean values derived from the determinations of Renzini et al. (1996), Reid (1997, 1998), and Gratton et al. (1997). The errors in log M are estimated to be about the same as obtained for the 1993 data in Sect. 3.3.5: 0.15 dex for stars above the gap, 0.17 dex for stars within the gap region and 0.22 dex for stars below the gap.

Using ATLAS9 and LINFOR we computed a grid of theoretical spectra covering the range 10,000 K $\leq T_{\rm eff} \leq$ 35,000 K, $2.5 \leq \log g \leq 6.0$, $-3.0 \leq \log \frac{N_{He}}{N_H} \leq -1.0$, at a metallicity of [M/H] = −1.5. In Table 13 we list the results obtained from fitting the Balmer lines H_β to H_{10} (excluding H_ϵ to avoid the Ca II H line) and the He I lines 4026 Å, 4388 Å, 4471 Å, and 4921 Å. The errors given are r.m.s.

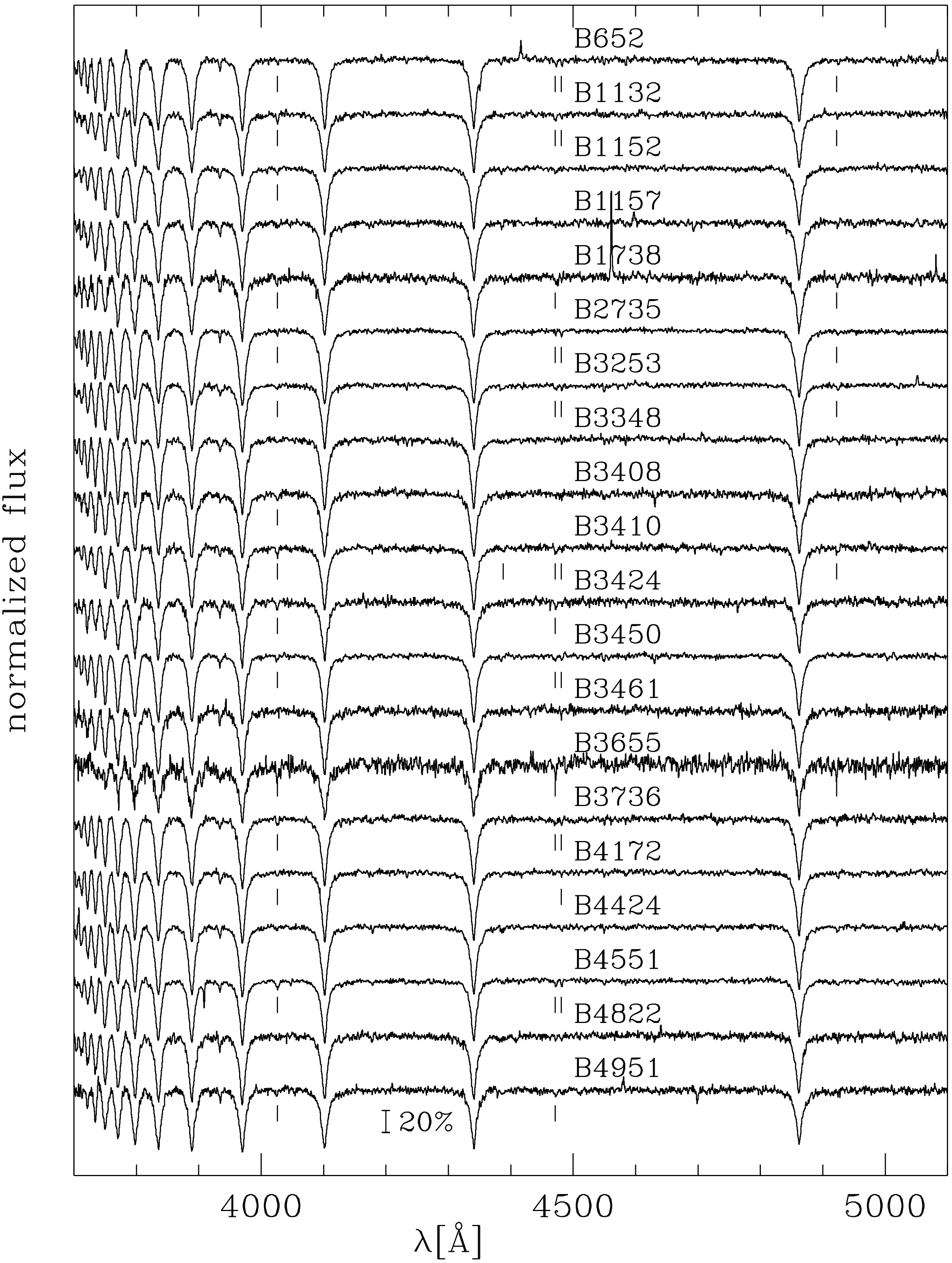

Fig. 26. Normalized spectra for the programme stars that were observed at the ESO 1.52m telescope. The part shortward of 3900 Å was normalized by taking the highest flux point as continuum value. The He I lines λλ 4026 Å, 4144 Å, 4388 Å, 4471 Å, 4922 Å and the Mg II line 4481 Å are marked (if visible in the spectrum).

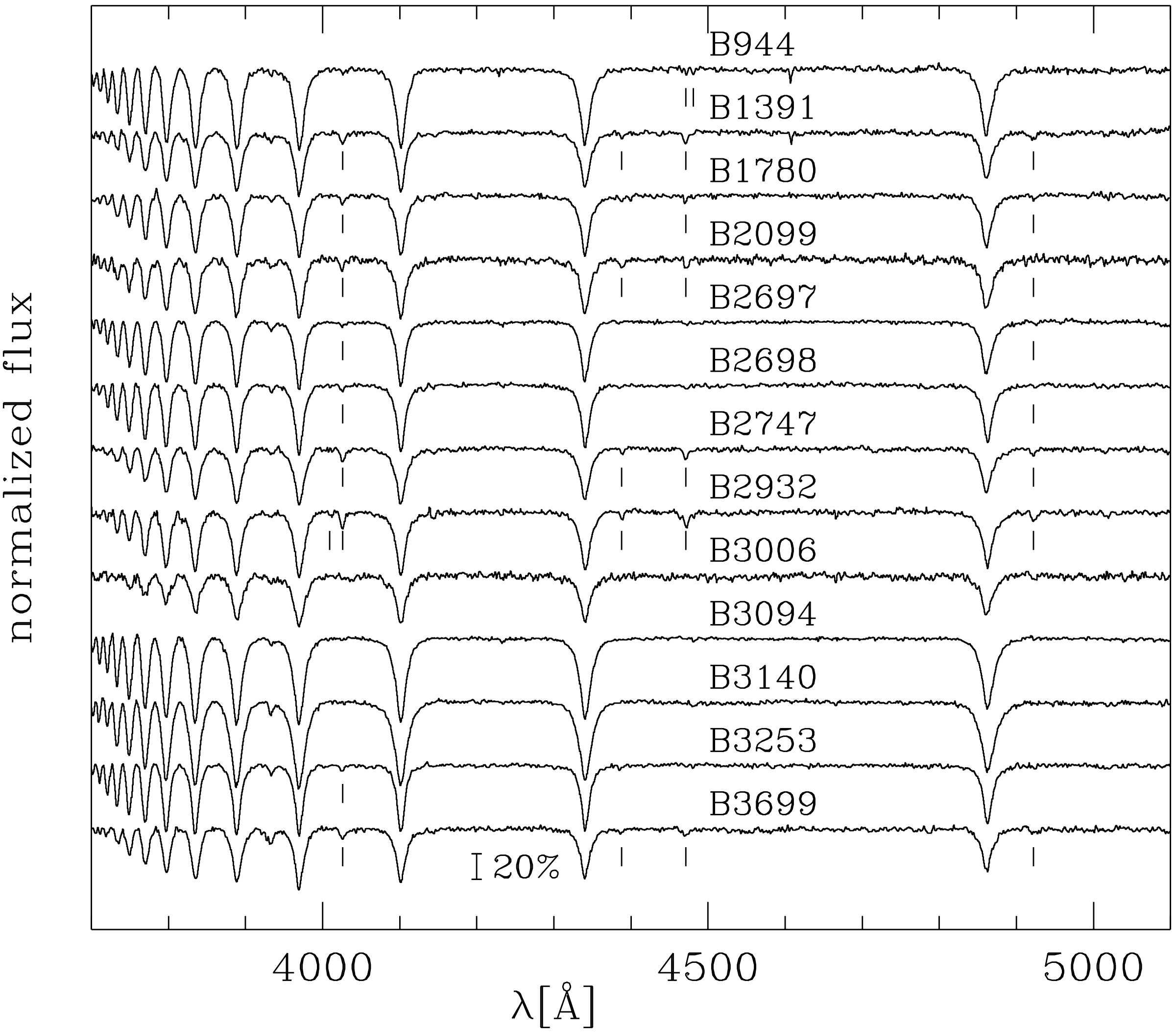

Fig. 27. Normalized spectra for the programme stars that were observed at the NTT during 1997 and 1998. The part shortward of 3900 Å was normalized by taking the highest flux point as continuum value. The He I lines λλ 4026 AA, 4144 Å, 4388 Å, 4471 Å, 4922 Å and the Mg II line 4481 Å are marked (if visible in the spectrum).

errors as derived from the fit (adjusted as described in Sect. 5.1.2, where also a more detailed discussion of these errors is given). The true errors are likely to be larger, about 10% in $T_{\rm eff}$ and 0.15 dex in $\log g$ (cf. Sect. 3.3.2). A representative error bar is shown in Fig. 28. To increase our data sample we reanalysed the NTT spectra described and analysed in Sect. 3.3. We did not reanalyse the EFOSC1 data published in that section as they are of worse quality. We find that the atmospheric parameters determined by line profile fitting on average agree rather well with those determined in Sect. 3.3.2. Fig. 28 (top panel) shows that the HBB stars in NGC 6752 show the same effect as seen in other globular clusters, namely an offset from the ZAHB towards lower $\log g$. The helium-mixed track offers a better description for the stars hotter than 11,200 K ($\log T_{\rm eff} \geq 4.05$) than the canonical track.

The masses derived from the analysis using metal-poor model atmospheres are plotted in Fig. 29 (top panel). The sdB stars hotter than 20,000 K ($\log T_{\rm eff} = 4.3$) scatter around the ZAHB. The stars below 16,000 K ($\log T_{\rm eff} = 4.2$) lie mainly below the ZAHB. Even stronger deviations towards low masses are found between 16,000 K and 20,000 K. To quantify the offsets we compare the masses of the stars to those they would have on the helium-mixed ZAHB at the same $T_{\rm eff}$. Excluding stars below

Table 13. Physical parameters, helium abundances, and masses for the target stars in NGC 6752 as derived using metal-poor model atmospheres. Also given is the reduced χ^2 from the line profile fits.

Star	χ^2	$T_{\rm eff}$ [K]	$\log g$ [cm/s^2]	$\log\frac{N_{He}}{N_H}$	M [M$_\odot$]
ESO 1.52m telescope observations in 1998					
652	2.50	12500±310	3.86±0.09	−2.00±0.35	0.55
1132	1.75	17300±520	4.31±0.09	−2.46±0.16	0.50
1152	2.25	15700±360	4.19±0.05	−2.57±0.17	0.50
1157	1.91	15800±460	4.14±0.09	−2.89±0.31	0.50
1738	1.59	16700±700	4.15±0.12	−2.24±0.28	0.32
2735	3.21	11100±260	3.78±0.12	−1.14±0.36	0.73
3253	3.02	13700±390	3.80±0.09	−2.41±0.29	0.50
3348	2.49	12000±270	3.73±0.07	−2.18±0.38	0.65
3408	1.61	14600±400	4.21±0.09	−2.40±0.36	0.63
3410	1.77	15500±460	4.14±0.09	−2.22±0.19	0.41
3424	1.04	17900±570	4.23±0.09	−2.60±0.21	0.44
3450	1.52	13200±290	3.84±0.07	−2.05±0.24	0.43
3461	1.39	15200±500	4.18±0.09	≤ −3	0.70
3655	1.14	25800±1300	5.15±0.16	−2.32±0.24	0.68
3736	2.69	13400±370	3.91±0.09	−1.84±0.17	0.67
4172	2.03	12200±260	3.68±0.07	−2.24±0.54	0.46
4424	2.05	13000±290	3.99±0.07	−2.36±0.38	0.69
4551	4.80	15400±530	3.96±0.09	−2.21±0.24	0.39
4822	1.29	13900±450	3.91±0.09	−2.24±0.28	0.37
4951	1.85	17300±580	4.38±0.09	−2.63±0.22	0.56
ESO NTT observations in 1997					
944	1.68	11100±230	3.70±0.10	−0.84±0.31	0.52
1391	1.95	19700±570	4.49±0.09	−2.04±0.10	0.39
1780	2.28	18000±580	4.40±0.09	−2.31±0.14	0.39
2099	2.79	20000±820	4.61±0.12	−2.38±0.22	0.48
ESO NTT observations in 1998					
2697	3.79	15700±400	4.08±0.07	−2.36±0.17	0.91
2698	5.97	15400±610	4.11±0.10	−2.07±0.28	0.49
2747	3.25	22700±650	4.85±0.09	−2.16±0.10	0.61
2932	3.16	18600±700	4.63±0.12	−1.57±0.12	0.47
3006	1.91	30000±640	5.19±0.09	≤ −3	0.71
3094	9.21	10400±120	3.81±0.17	−1.83±1.35	1.09
3140[1]	9.40	8000±100	2.84±0.14	−1.00±0.00	0.28
3253	5.86	13700±470	3.75±0.10	−1.85±0.31	0.45
3699	3.43	22900±990	4.64±0.12	−2.29±0.10	0.35
ESO NTT observations in 1993					
491	2.12	29000±520	5.41±0.07	≤ −3	0.38
916	2.38	30200±430	5.61±0.07	−1.71±0.05	0.48
1509	3.24	17400±630	4.10±0.10	−2.17±0.16	0.26
1628	3.29	21800±590	4.83±0.09	−2.53±0.12	0.47
2162	3.24	33400±390	5.78±0.07	−1.94±0.09	0.45
2395	2.61	22200±690	5.10±0.09	−1.78±0.07	0.57
3915	2.11	31300±510	5.55±0.09	≤ −3	0.59
3975	3.08	21700±460	4.97±0.07	−2.04±0.10	0.67
4009	3.35	30700±920	5.61±0.12	≤ −3	0.54
4548	3.79	22000±1380	5.11±0.19	−2.02±0.16	0.67

[1] This star is omitted from further analysis as it lies in a temperature range that is difficult to analyse and not of great interest for our discussion.

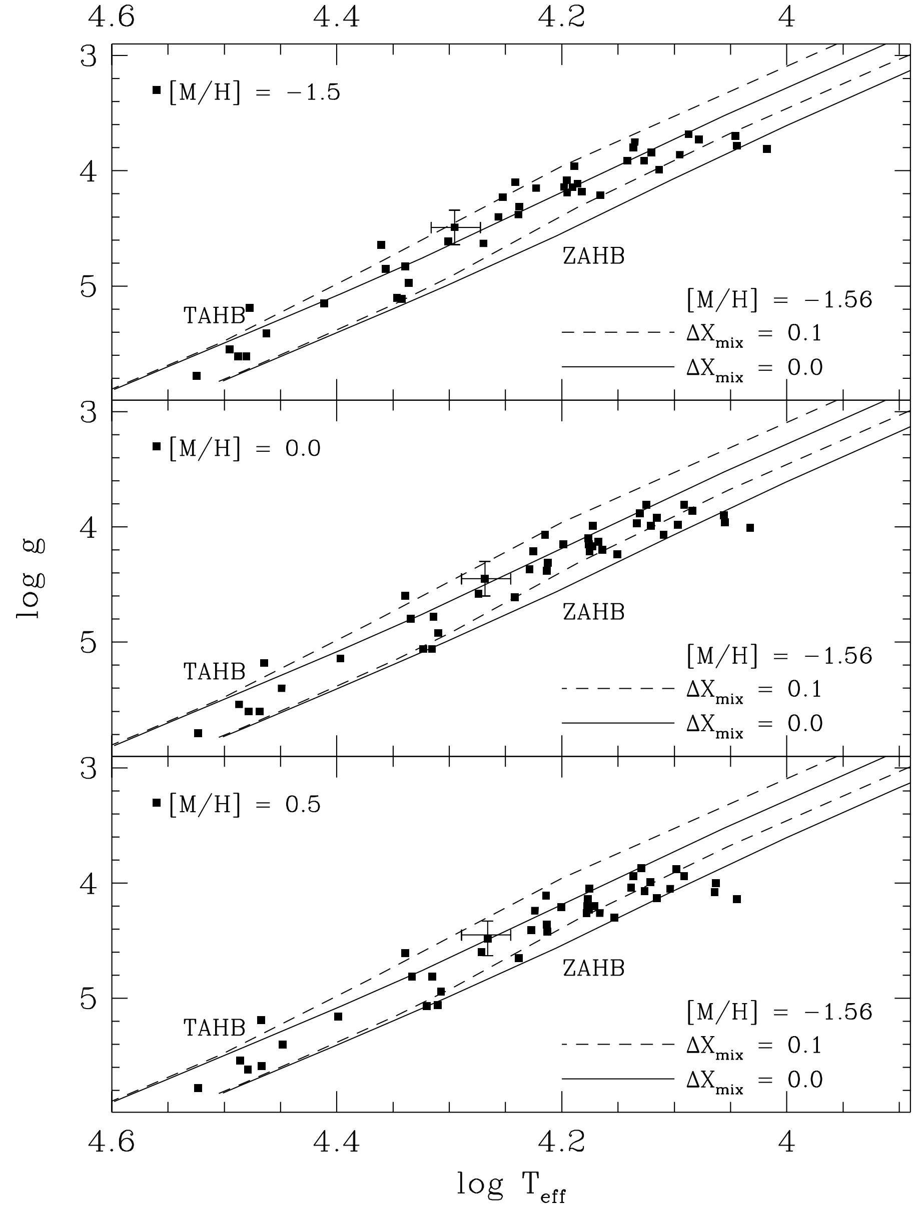

Fig. 28. Temperatures and gravities of the programme stars in NGC 6752. **top panel**: determined using model atmospheres with cluster metallicity ([M/H] = −1.5), **central panel**: adopting a solar metallicity ([M/H] = 0) for the model atmospheres, **bottom panel**: adopting a super-solar metallicity ([M/H] = +0.5) for the model atmospheres. For more details see text. The dashed resp. solid lines mark evolutionary tracks from Sweigart (1997b) for metallicity [M/H] = −1.56 (with and without mixing, respectively; see Sect. 4.1 and Fig. 22 for more details). Representative error bars are plotted.

11,500 K we find a mean $< \frac{M}{M_{\rm ZAHB}} > = 0.88^{+0.23}_{-0.18}$ ($T_{\rm eff} < 16{,}000$ K, 17 stars), $0.73^{+0.19}_{-0.17}$ (16,000 K $\leq T_{\rm eff} \leq 20{,}000$ K, 9 stars), $0.97^{+0.24}_{-0.20}$ ($T_{\rm eff} > 20{,}000$ K, 13 stars). The cited errors are r.m.s. errors. So the cooler HBB stars and the sdB stars agree with theoretical predictions for helium mixing, but not the hot HBB stars.

4.4.3 Iron abundances

Prompted by the suggestion of Grundahl et al. (1999) that radiative levitation of metals may enrich the atmospheres of HBB stars (see Sect. 4.2) we started to look for any evidence of iron absorption

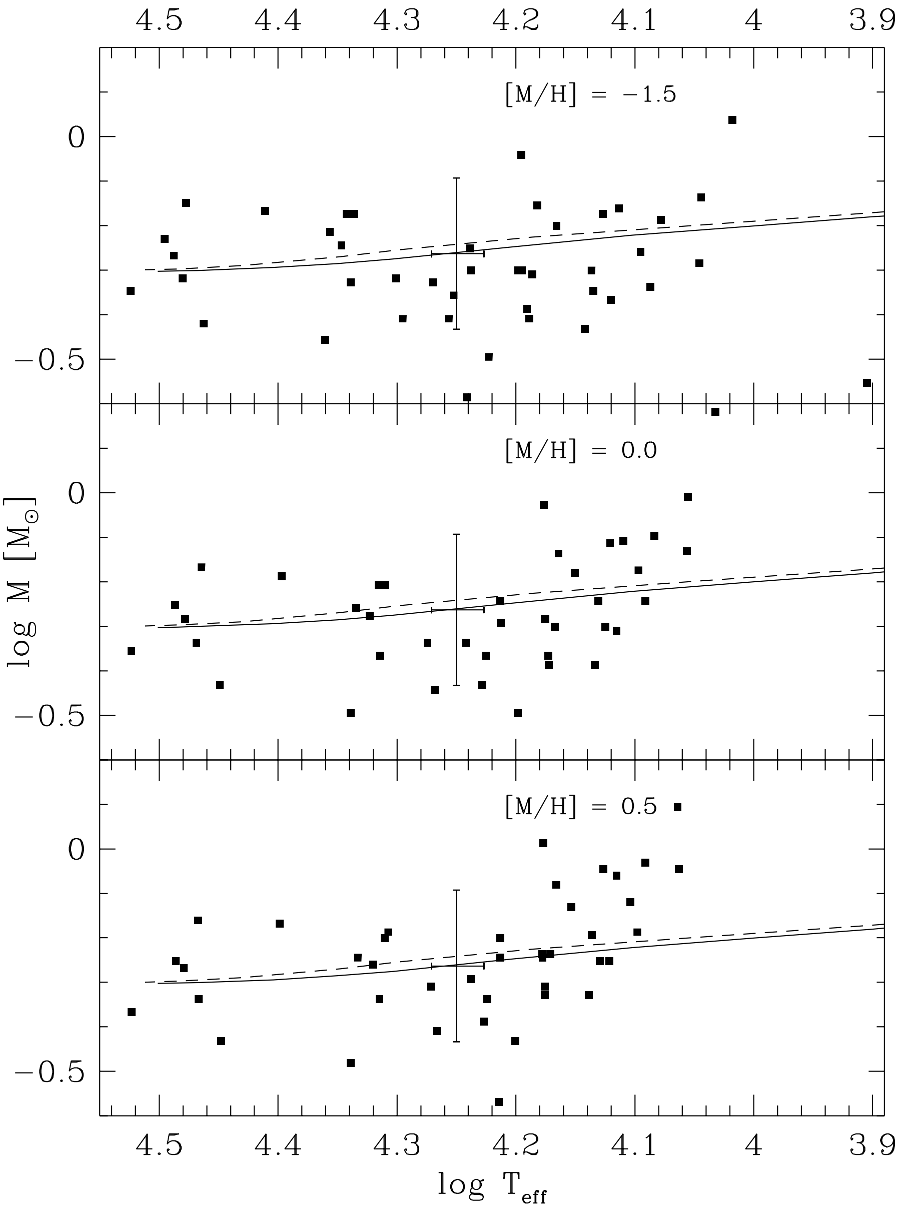

Fig. 29. Temperatures and masses of the programme stars in NGC 6752. **top panel**: determined using model atmospheres with cluster metallicity ([M/H] = −1.5), **central panel**: adopting a solar metallicity ([M/H] = 0) for the model atmospheres **bottom panel**: adopting a super–solar metallicity ([M/H] = +0.5) for the model atmospheres. For more details see text. The dashed resp. solid lines mark evolutionary tracks from Sweigart (1999) for metallicity [M/H] = −1.56 (with and without mixing, respectively, see Sect. 4.1 and Fig. 22 for more details).

lines in the ESO 1.52m spectra (the NTT data have a too low resolution). Indeed we did find Fe II absorption lines in almost all spectra (for examples see Fig. 30). A first check indicated that the iron abundance was about solar whereas the magnesium abundance was close to the mean cluster abundance. As iron is very important for the temperature stratification of stellar atmospheres we tried to take the increased iron abundance into account by computing model atmospheres for [M/H] = 0. We now repeated the fit to derive $T_{\rm eff}$, $\log g$, and $\log \frac{N_{He}}{N_H}$ with these enriched model atmospheres. The results are listed in Table 14 and plotted in Figs. 28 and 29 (central panels).

From Fig. 28 (central panel) it is clear that the use of solar-metallicity model atmospheres moves most stars closer to the canonical zero-age horizontal branch (ZAHB) due to combination of lower $T_{\rm eff}$

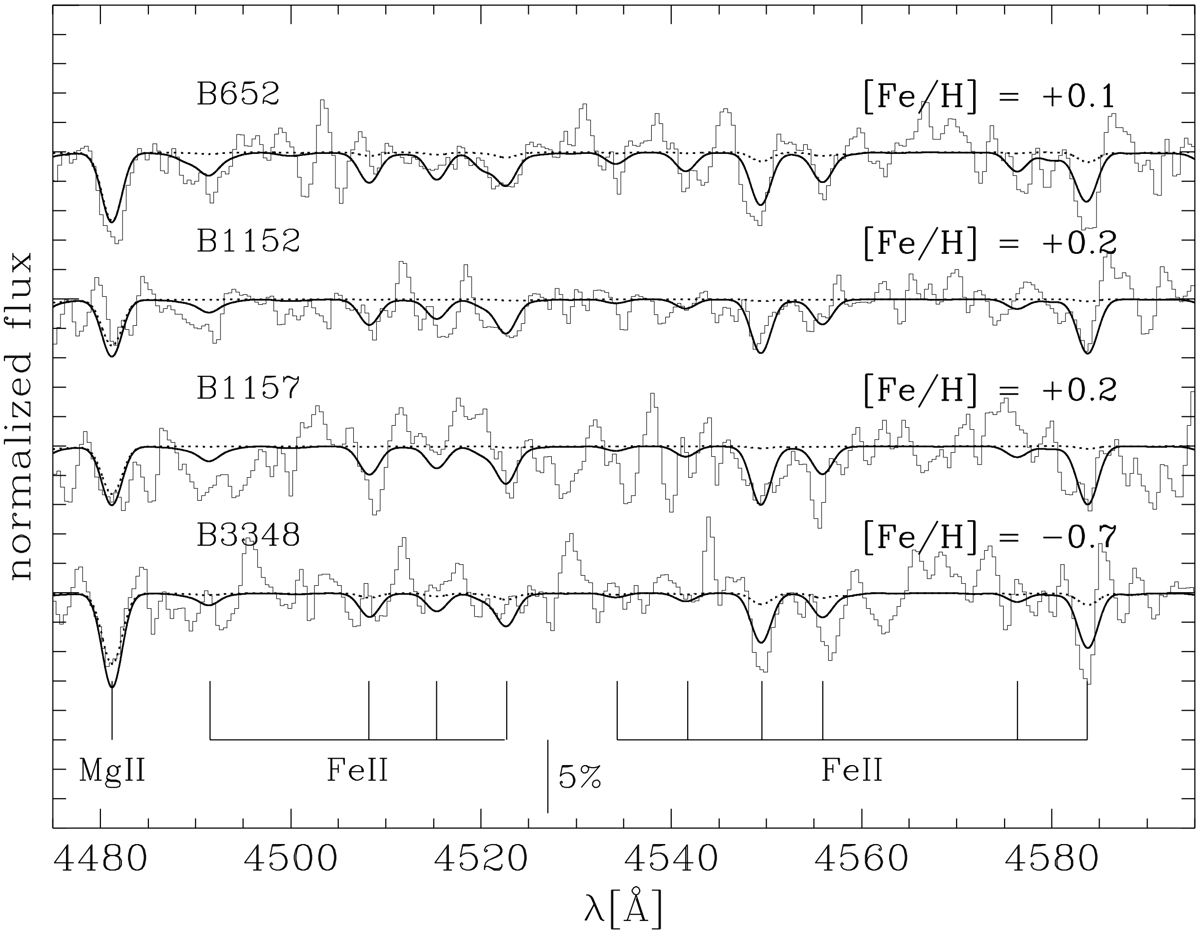

Fig. 30. The iron and magnesium lines as seen in the spectra of some of the stars in NGC 6752. The solid line marks a model spectrum for which we used a solar metallicity model atmosphere but adjusted all metals except iron to [M/H] = −1.5 for the spectrum synthesis. The iron abundance was then adjusted to the noted values to reproduce the marked Fe II lines. The dashed line marks a model spectrum calculated from a metal-poor model atmosphere for which we used the cluster metal abundance for all metals for the line formation. Effective temperature and surface gravity for both models are those plotted in Fig. 28, central and top panel, respectively. The temperatures of the stars range from 12,000 K (B3348) to 16,000 K (B1152). Obviously iron is strongly enriched whereas magnesium is consistent with the mean cluster abundance.

and/or higher $\log g$. The three stars between 10,000 K and 12,000 K, however, fall *below* the canonical ZAHB when fitted with enriched model atmospheres. This is plausible as the radiative levitation is supposed to start around 11,500 K (Grundahl et al. 1999) and the cooler stars therefore should have metal-poor atmospheres (see also Fig. 31 where the coolest analysed star shows no evidence of iron enrichment, in agreement with the results of Glaspey et al. 1989). Now the stars below 15,500 K (which interestingly is roughly the temperature at which the stars in NGC 6752 return to the ZAHB in Fig. 1 of Grundahl et al., see also Fig. 23, page 57) scatter around the helium-mixed ZAHB or between the canonical ZAHB and TAHB (terminal-age HB) – depending on personal preference. The stars between 15,500 K and 19,000 K, however, still show offsets that are better fit by helium-mixed tracks. For the sdB stars not much is changed. The masses seen in Fig. 29 show a similar effect – below 15,300 K and above 20,000 K they basically scatter around the helium-mixed ZAHB ($< \frac{M}{M_{\rm ZAHB}} > = 0.96^{+0.27}_{-0.21}$ [17 stars] resp. $0.96^{+0.25}_{-0.19}$ [13 stars]), but the stars in between these two groups still show $< \frac{M}{M_{\rm ZAHB}} > = 0.70^{+0.20}_{-0.16}$ (9 stars). As the stars become cooler when analysed with more metal-rich atmospheres the temperature boundaries were shifted to include the same stars as for the comparison made above.

Table 14. Physical parameters, helium abundances, and masses for the target stars in NGC 6752 as derived using solar metallicity model atmospheres. Also given is the reduced χ^2 from the line profile fits.

Star	χ^2	$T_{\rm eff}$ [K]	$\log g$ [cm/s^2]	$\log \frac{N_{He}}{N_H}$	M [M$_\odot$]
ESO 1.52m telescope observations in 1998					
652	2.50	12500±230	3.98±0.07	−2.19±0.36	0.67
1132	1.74	16300±460	4.31±0.07	−2.45±0.16	0.51
1152	2.21	15000±290	4.21±0.05	−2.58±0.17	0.52
1157	1.92	15000±360	4.15±0.07	−2.89±0.31	0.52
1738	1.59	15800±580	4.15±0.10	−2.23±0.28	0.32
2735	3.26	11400±170	3.96±0.07	−1.51±0.28	0.98
3253	2.99	13500±310	3.88±0.07	−2.57±0.28	0.57
3348	2.46	12100±220	3.86±0.07	−2.44±0.38	0.80
3408	1.62	14100±330	4.24±0.07	−2.47±0.36	0.66
3410	1.74	14900±370	4.17±0.07	−2.25±0.19	0.43
3424	1.04	16800±510	4.21±0.09	−2.58±0.22	0.43
3450	1.52	13000±210	3.92±0.05	−2.22±0.24	0.49
3461	1.38	14600±400	4.20±0.09	≤ −3	0.73
3655	1.14	24900±1250	5.14±0.16	−2.32±0.24	0.65
3736	2.68	13200±270	3.99±0.07	−1.98±0.17	0.77
4172	2.02	12300±200	3.81±0.05	−2.49±0.55	0.57
4424	2.04	12900±210	4.07±0.05	−2.58±0.40	0.78
4551	4.77	14900±410	3.99±0.09	−2.26±0.24	0.41
4822	1.29	13600±350	3.97±0.09	−2.37±0.28	0.41
4951	1.84	16300±520	4.38±0.09	−2.61±0.22	0.57
ESO NTT observations in 1997					
944	1.72	11400±190	3.90±0.09	−1.27±0.22	0.74
1391	1.93	18500±570	4.45±0.09	−2.02±0.10	0.36
1780	2.27	16900±530	4.37±0.09	−2.28±0.14	0.37
2099	2.79	18800±790	4.58±0.10	−2.36±0.22	0.46
ESO NTT observations in 1998					
2697	3.92	15000±360	4.10±0.07	−2.39±0.17	0.94
2698	5.92	14700±490	4.13±0.10	−2.10±0.26	0.50
2747	3.18	21600±700	4.80±0.09	−2.16±0.10	0.55
2932	3.14	17500±600	4.61±0.10	−1.54±0.10	0.46
3006	1.91	29100±740	5.18±0.09	≤ −3	0.68
3094	9.29	10800±310	4.01±0.14	−2.33±1.97	1.52
3253	5.79	13300±370	3.81±0.09	−1.95±0.31	0.50
3699	3.39	21800±1050	4.60±0.12	−2.30±0.10	0.32
ESO NTT observations in 1993					
491	2.12	28100±540	5.40±0.07	≤ −3	0.37
916	2.39	29400±480	5.60±0.07	−1.70±0.05	0.46
1509	3.21	16400±510	4.07±0.09	−2.15±0.16	0.24
1628	3.31	20600±620	4.78±0.09	−2.52±0.12	0.43
2162	3.18	33400±460	5.79±0.07	−1.92±0.09	0.44
2395	2.60	21000±750	5.06±0.10	−1.78±0.09	0.53
3915	2.11	30700±620	5.54±0.09	≤ −3	0.56
3975	3.09	20400±520	4.92±0.07	−2.02±0.12	0.62
4009	3.35	30100±1120	5.60±0.14	≤ −3	0.52
4548	3.79	20700±1490	5.06±0.19	−2.00±0.17	0.62

To verify our crude estimate of roughly solar iron abundance we tried to determine the actual iron abundance in the stars by fitting the iron lines marked in Fig. 30. For each star that has been observed at the ESO 1.52m telescope we computed a solar metallicity model spectrum with $T_{\rm eff}$, $\log g$

Table 15. Iron abundances derived for those HBB stars that were observed with the ESO 1.52m telescope (except B 3655, which has a too noisy spectrum). $\log\epsilon_{\rm Fe}$ gives the number abundance of iron with $\log\epsilon_{\rm Fe} = \log(Fe/H) + 12$ ($\log\epsilon_{\rm Fe,\odot} = 7.46$). The physical parameters are taken from Table 14.

Star	$T_{\rm eff}$ [K]	$\log g$ [cm/s^2]	$\log\frac{N_{He}}{N_H}$	$\log\epsilon_{\rm Fe}$	[Fe/H]
652	12500	3.98	-2.19	7.56	$+0.1$
1132	16300	4.31	-2.45	7.98	$+0.5$
1152	15000	4.21	-2.58	7.61	$+0.2$
1157	15000	4.15	-2.89	7.63	$+0.2$
1738	15800	4.15	-2.23	7.62	$+0.2$
2735	11400	3.96	-1.51	<5.90	<-1.6
3253	13500	3.88	-2.57	8.30	$+0.8$
3348	12100	3.86	-2.44	7.25	-0.2
3408	14100	4.24	-2.47	7.61	$+0.2$
3410	14900	4.17	-2.25	8.01	$+0.6$
3424	16800	4.21	-2.58	7.37	-0.1
3450	13000	3.92	-2.22	7.08	-0.4
3461	14600	4.20	≤ -3	7.72	$+0.3$
3736	13200	3.99	-1.98	7.72	$+0.3$
4172	12300	3.81	-2.49	7.28	-0.2
4424	12900	4.07	-2.58	8.09	$+0.6$
4551	14900	3.99	-2.26	6.79	-0.9
4822	13600	3.97	-2.37	7.31	-0.2
4951	16300	4.38	-2.61	7.61	$+0.2$

as given in Table 14 and $\log\frac{N_{He}}{N_H} = -2$. One should note here that there is a discrepancy between Kurucz' [Fe/H] = 0 ($\log\epsilon_{\rm Fe} = 7.60$, Anders & Grevesse 1989) and our [Fe/H] = 0 ($\log\epsilon_{\rm Fe} = 7.46$). We thus use slightly different iron abundances for the temperature stratification (Kurucz) and the line formation. The fit of the iron lines was started with a solar iron abundance of $\log\epsilon_{\rm Fe} = 7.46$ and the iron abundance was varied until χ^2 achieved a minimum (for more details see Sect. 7.3). As the radiative levitation is due to diffusion processes (which is also indicated by the helium deficiency found in these stars) the atmospheres have to be very stable . We therefore kept the microturbulent velocity ξ at 0km/s – the listed iron abundances are thus upper limits. The mean iron abundance turns out to be [Fe/H] $\approx +0.1$ dex ($\log\epsilon_{Fe} = 7.59$) for stars hotter than about 11,500 K – in good agreement with the findings of Behr et al. (1999a) for HBB/HBA stars in M 13 and Glaspey et al. (1989) for two HBB stars in NGC 6752. While this is an enhancement by about a factor of 50 the resulting mean iron abundance still is too low by about a factor of 3 compared to the iron abundance required to explain the Strömgren u-jump discussed by Grundahl et al. (1999, $\log\epsilon_{Fe} = 8.1$).

We repeated the Balmer line profile fits by increasing the metal abundance of the model atmospheres to [M/H]=+0.5 (see Figs. 28 and 29, bottom panels, and Table 16), which did not change the resulting values for $T_{\rm eff}$ and $\log g$ significantly. Especially the "deviant" stars (now between 15,500 K and 19,000 K) stay away from the canonical ZAHB (although their masses increased a bit). For the masses we get (below 15,300 K, between 15,500 K and 19,000 K, above 20,000 K) ($<\frac{M}{M_{\rm ZAHB}}> = 1.09^{+0.31}_{-0.24}$ (17 stars), $0.76^{+0.23}_{-0.17}$ (9 stars), $0.99^{+0.25}_{-0.21}$ (13 stars) respectively. Thus the problem of the hot HBB stars (15,500 K$\leq T_{\rm eff} \leq$19,000 K) cannot be completely solved by the scaled-solar metal-rich atmospheres used here.

4.4.4 Discussion

We could verify the results of Behr et al. (1999a) that the atmospheres of HBB stars with $T_{\rm eff} >$ 11,500 K are enriched in iron ([Fe/H] $\approx +0.1$) whereas magnesium is consistent with the cluster metallicity.

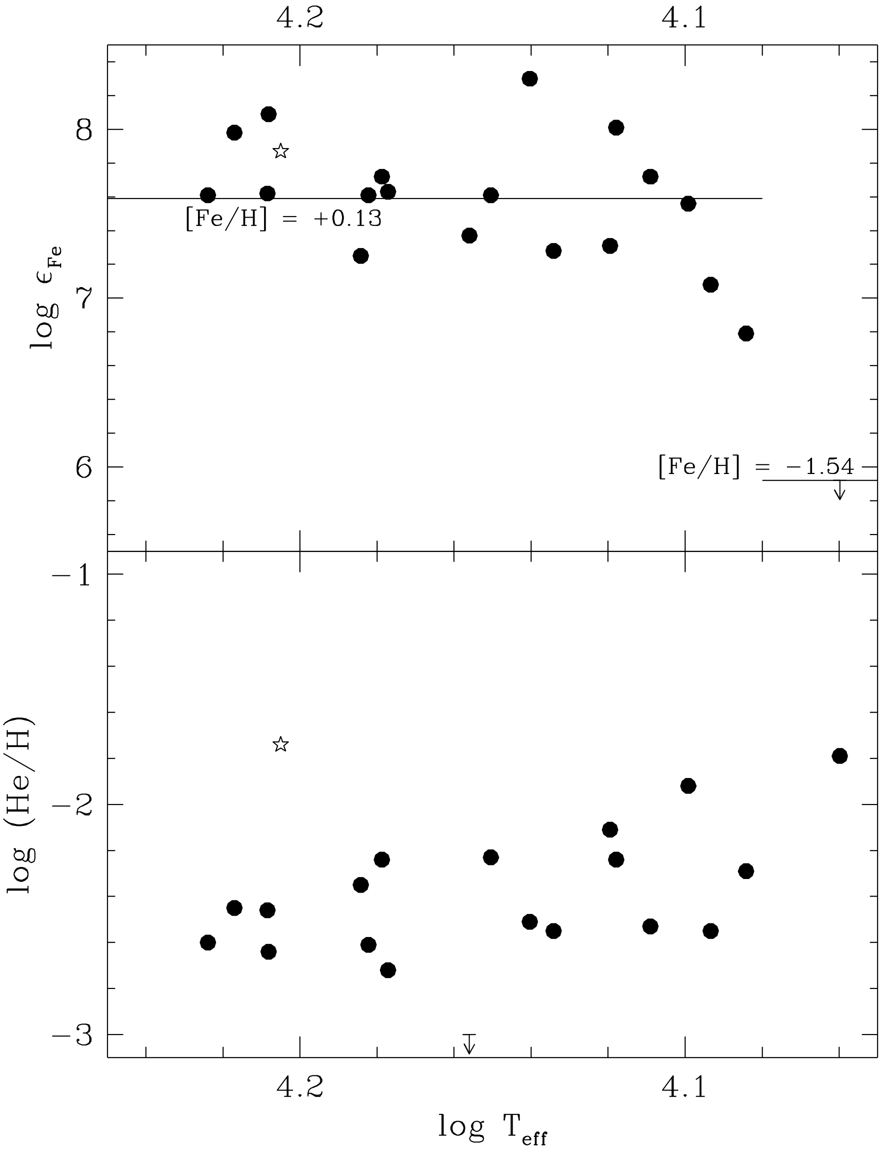

Fig. 31. The iron and helium abundances for the stars observed with ESO 1.52m telescope. Iron was not detected in the coolest star and is plotted as an upper limit. The trend to lower helium abundances for higher temperatures agrees with the findings of Behr et al. (1999). Iron is obviously enhanced to roughly solar abundances. The mean iron abundance as derived from our spectra ([Fe/H] = +0.13) and the cluster abundance ([Fe/H] = −1.54) are marked. The asterisk marks the result of Glaspey et al. (1989) for the hotter of their two HBB stars in NGC 6752.

Using model atmospheres that try to take into account this enrichment in iron (and presumably other heavy elements) reconciles the atmospheric parameters of stars with 11,500 K $\leq T_{\rm eff} <$ 15,500 K with canonical expectations. Also the masses derived from these analyses are in good agreement with canonical predictions. However, we found that even with metal-rich ([M/H] = +0.5) model atmospheres the atmospheric parameters of the hot HBB stars (15,500 K $< T_{\rm eff} <$ 19,000 K) in NGC 6752 cannot be reconciled with the canonical ZAHB (and also their masses are slightly too low). In addition the masses for the stars below 15,500 K are now slightly too high (the EHB stars are hardly affected at all by changes in the metallicity of the model atmospheres). As Michaud et al. (1983) noted diffusion will not necessarily enhance all heavy elements by the same amount and the effects of diffusion vary with effective temperature. Elements that were originally very rare may be enhanced even stronger than iron (see also Behr et al. 1999a, where P and Cr are enhanced to [M/H] $\geq$ +1). The question

Table 16. Physical parameters, helium abundances, and masses for the target stars in NGC 6752 as derived using metal-rich model atmospheres. Also given is the reduced χ^2 from the line profile fits.

Star	χ^2	$T_{\rm eff}$ [K]	$\log g$ [cm/s^2]	$\log \frac{N_{He}}{N_H}$	M [M$_\odot$]
ESO 1.52m telescope observations in 1998					
652	2.51	12700±220	4.05±0.07	−2.40±0.36	0.76
1132	1.74	16300±430	4.36±0.07	−2.55±0.14	0.57
1152	2.20	15100±290	4.26±0.05	−2.71±0.16	0.58
1157	1.92	15100±370	4.20±0.07	−2.98±0.26	0.57
1738	1.59	15900±540	4.21±0.10	−2.37±0.26	0.37
2735	3.31	11600±180	4.08±0.07	−1.74±0.24	1.24
3253	2.98	13700±300	3.94±0.07	−2.76±0.24	0.64
3348	2.46	12300±210	3.94±0.07	−2.65±0.36	0.93
3408	1.63	14200±310	4.30±0.07	−2.64±0.35	0.74
3410	1.73	15000±350	4.23±0.07	−2.40±0.19	0.49
3424	1.04	16700±490	4.24±0.09	−2.66±0.21	0.46
3450	1.53	13200±200	3.99±0.05	−2.45±0.26	0.56
3461	1.38	14700±380	4.26±0.09	≤ -3	0.83
3655	1.13	25000±1170	5.16±0.16	−2.31±0.24	0.68
3736	2.68	13400±260	4.07±0.07	−2.17±0.17	0.90
4172	2.03	12500±200	3.88±0.05	−2.70±0.50	0.65
4424	2.04	13000±210	4.13±0.05	−2.79±0.35	0.87
4551	4.77	15000±400	4.05±0.09	−2.43±0.24	0.47
4822	1.30	13800±340	4.04±0.09	−2.59±0.28	0.47
4951	1.85	16300±480	4.42±0.09	−2.72±0.21	0.63
ESO NTT observations in 1997					
944	1.74	11600±180	4.00±0.07	−1.52±0.19	0.90
1391	1.94	18400±580	4.48±0.09	−2.08±0.10	0.39
1780	2.27	16900±500	4.41±0.09	−2.37±0.12	0.41
2099	2.79	18700±810	4.60±0.10	−2.41±0.22	0.49
ESO NTT observations in 1998					
2697	4.02	15000±330	4.14±0.07	−2.52±0.17	1.03
2698	5.93	14800±490	4.20±0.10	−2.25±0.28	0.58
2747	3.25	21500±830	4.81±0.09	−2.17±0.10	0.57
2932	3.13	17300±570	4.65±0.10	−1.61±0.10	0.51
3006	1.84	29300±590	5.19±0.07	≤ -3	0.69
3094	9.33	11100±290	4.14±0.10	−2.54±1.97	1.94
3253	5.77	13500±350	3.87±0.09	−2.12±0.31	0.56
3699	3.50	21800±1030	4.61±0.12	−2.31±0.10	0.33
ESO NTT observations in 1993					
491	2.12	28000±520	5.40±0.07	≤ -3	0.37
916	2.38	29300±460	5.59±0.05	−1.70±0.05	0.46
1509	3.21	16400±500	4.11±0.09	−2.25±0.16	0.27
1628	3.29	20700±720	4.81±0.09	−2.55±0.12	0.46
2162	3.13	33400±500	5.78±0.07	−1.91±0.09	0.43
2395	2.62	20900±810	5.07±0.09	−1.80±0.09	0.55
3915	2.12	30600±580	5.54±0.07	≤ -3	0.56
3975	3.11	20300±580	4.94±0.07	−2.06±0.12	0.65
4009	3.35	30100±1040	5.62±0.12	≤ -3	0.54
4548	3.79	20400±1590	5.06±0.19	−2.03±0.17	0.63

of whether diffusion is *the* (one and only) solution to the "low gravity" problem cannot be answered without detailed abundance analyses to determine the actual abundances and model atmospheres that allow to use non scaled-solar abundances (like ATLAS12). We can, however, state that those model atmospheres, which reproduce the u-jump discussed by Grundahl et al. (1999) cannot completely reconcile the atmospheric parameters of hot HB stars with canonical theory. Model atmospheres with abundance distributions that may solve the discrepancy between theoretically predicted and observed atmospheric parameters of hot HB stars may then, in turn, not reproduce the Strömgren u jump. It is intriguing that the temperature, at which the stars in $u, u - y$ seem to return to the ZAHB is roughly the same at which they start to deviate again from the canonical ZAHB when analysed with metal-rich atmospheres.

The stars between 15,500 K and 20,000 K (when analysed with metal-rich atmospheres) are currently best fit by a moderately mixed ZAHB. However, the fact that their masses are too low cautions against identifying He mixing as the only cause for these low gravities - because in this case the luminosities of the stars would be increased and canonical masses would result.

Cool blue HB stars are not affected by diffusion and their surface gravities mostly agree with canonical HB evolution. To obtain canonical masses for those stars in the clusters studied so far the long distance scale is better suited than the short one.

Chapter 5

Horizontal Branch Stars in Metal-Rich Globular Clusters

So far we have dealt with blue HB and blue tail stars in metal-poor ([Fe/H] < -1) globular clusters. As mentioned in Chapter 1 (see also Appendix A) the HB morphology correlates with metallicity, i.e. metal-rich stars will populate mainly the cool regions of the HB because for a given mass of the hydrogen envelope the resulting temperature decreases with increasing metallicity. The detection of sdB/sdO candidates in the metal-rich open clusters NGC 188 ([Fe/H] ≈ 0) and NGC 6791 ([Fe/H] $\approx +0.5$) by UIT (Landsman et al. 1998) and the spectroscopic verification of the sdB stars in NGC 6791 by Liebert et al. (1994) proves that at least EHB stars can be produced in metal-rich systems as well (see also D'Cruz et al. 1996 for theoretical scenarios).

UV observations of elliptical galaxies, which are in general even more metal-rich than metal-rich globular clusters (based on the strength of Mg_2 index) showed that such old, metal-rich systems contain hot stars (Burstein et al. 1988). Stellar evolution models yield a maximum lifetime UV output for EHB stars with envelope masses $M_{env} \leq 0.02\,M_\odot$(see also Greggio & Renzini 1990), while post-AGB stars do not live long enough at high temperatures to play a significant rôle for the UV flux. The fraction of EHB stars required to reproduce the observed UV excess is consistent with the number of hot subdwarfs observed in the disk of the Milky Way. Further evidence in support of hot subdwarfs as cause for the UV excess in elliptical galaxies is provided by Brown et al. (1997): Their analysis of Hopkins Ultraviolet Telescope *HUT* spectra of 6 elliptical and S0 galaxies shows that models with super-solar metal and helium abundances provide the best fit to the flux distribution of the observed spectra and that EHB stars are required in all fits. Most absorption line features (of C, N, Si), however, are consistent with [M/H] $= -1$, in contrast to the energy distribution. This may be due to diffusion in the atmospheres of the sdB stars (see Sect. 4.2).

Dorman et al. (1995) present a thorough discussion of the observational evidence for UV excess in elliptical galaxies and compare the galaxy data to those obtained for globular clusters. Comparing the UV-visual colour $(15 - V)_0$ for galaxies and globular clusters to the Mg_2 metallicity index (see Fig. 32, 15 being the observed brightness at 1500 Å) they find that while the globular clusters and the galaxies occupy distinct ranges in Mg_2 they overlap in $(15 - V)_0$ with the globular clusters being bluer on average. The region between globular clusters and galaxies in Mg_2 is occupied by the metal-rich globular clusters discussed here (47 Tuc, NGC 6388, NGC 6441)[15], and the small elliptical galaxy M 32. The discovery of hot stars in the metal-rich globular clusters occupying the transition region (in Mg_2) between globular clusters and elliptical galaxies is thus of special interest as analyses of these stars may provide additional information to understand the nature of the UV excess in elliptical galaxies:

---

[15] There are no measurements of $(15 - V)_0$ for NGC 362.

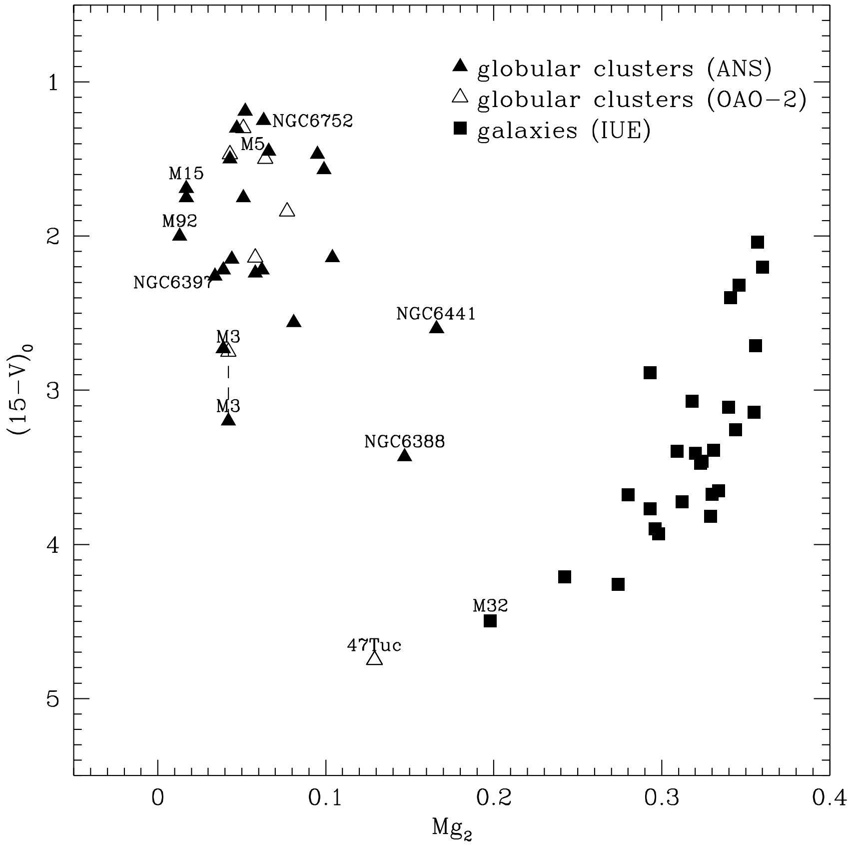

Fig. 32. UV-visual colour $(15 - V)_0$ vs. metallicity index Mg$_2$ for globular clusters and elliptical galaxies (Dorman et al. 1995, 15 being the brightness at 1500 Å). The metal-poor clusters discussed so far and the metal-rich clusters of this chapter are marked. Obviously three of the metal-rich cluster discussed here (47 Tuc, NGC 6388, NGC 6441) lie in between metal-poor globular clusters and elliptical galaxies in this diagram.

Rich et al. (1993) analysed IUE spectra of the cores of 11 disk globular clusters (including NGC 6388, NGC 6441, 47 Tuc). NGC 6441 shows a rise in UV flux towards shorter wavelengths (similar to elliptical galaxies), NGC 6388 shows a flat UV spectrum, and 47 Tuc does not show any evidence for stars hotter than blue stragglers (within the IUE aperture). They find that the UV spectra within the IUE aperture in combination with the fuel consumption theorem make blue HB/post-HB stars the most likely sources for the UV flux in NGC 6388/NGC 6441, respectively. The ratio L_{UV}/L_{total} of NGC 6441 agrees very well with those seen in elliptical galaxies, whereas that of NGC 6388 is one order of magnitude lower.

Some years later Rich et al. (1997) discovered the first well populated blue tails in metal-rich globular clusters from WFPC2 photometry of the cores of NGC 6388 and NGC 6441 (see Fig. 33). Most surprisingly, the HB stars at the top of the blue HB tail are roughly 0.5 mag brighter in V than the red HB "clump," which itself is strongly sloped as well. Differential reddening alone cannot be the cause of these sloped HB's (Piotto et al. 1997, Sweigart & Catelan 1998, Layden et al. 1999). WFPC2 photometry of the core of 47 Tuc obtained within the same program does not show any evidence for a blue HB or a blue tail nor any slope along its red HB. Layden et al. (1999) verify the slope of the blue HB and red clump in NGC 6441 that has been reported for by Rich et al. (1997).

O'Connell et al. (1997) detected about 20 hot stars on the UIT FUV image of 47 Tuc. Identifying those stars with blue HB stars would be consistent with the number of post-HB stars seen in 47 Tuc. They suggest that the hot stars in 47 Tuc are probably identical to those producing the UV upturn in elliptical galaxies, but are too few to produce a significant UV upturn in 47 Tuc. As the UIT field is much larger than the IUE aperture the chance of finding hot stars is much higher and the difference in interpretation of UIT and IUE results can be understood if one assumes that none of the few hot stars in 47 Tuc happened to be inside the IUE aperture.

Finally, Dorman et al. (1997) find evidence for hot stars in NGC 362 from UIT observations. While this globular cluster is not metal-rich, its HB morphology is too red for its metallicity. Together with NGC 288, which has a predominantly blue HB at a similar metallicity, it forms a second-parameter pair of globular clusters (meaning that an additional parameter besides metallicity is necessary to explain the difference in HB morphology between these two clusters). If NGC 362 contained a significant number of blue HB stars the discrepancy in HB morphology between the two clusters may be reduced.

Both 47 Tuc and NGC 362 lie in the direction of the far outer halo of the Small Magellanic Cloud (SMC), but the radial distribution of the hot stars detected by UIT suggests that a majority of these hot stars are indeed globular cluster members. They should have the same age and metallicity as the majority red HB population in the clusters, and may thus provide important clues as to the other parameters that can yield hot HB stars in globular clusters and/or elliptical galaxies.

What are the possible origins for the hot stars in these four globular clusters and how can they be distinguished spectroscopically?

- ⋆ **High mass loss tail:** Dorman et al. (1997) and O'Connell et al. (1997) suggest that the hot stars in NGC 362 and 47 Tuc are simply the high mass-loss tail of the red HB distribution. In this case, the hot stars should have a *narrow range of luminosity and gravity*, which is derivable as an extension of the existing red HB. This explanation will most probably not work for NGC 6388 and NGC 6441 as the blue stars there are much more numerous. In addition increasing RGB mass loss moves an HB star blueward in the V, $B-V$ plane but does not increase its luminosity, so the sloped HB cannot be explained by increased mass loss.
- ⋆ **Rotation:** Rotation during the RGB phase can delay the helium flash, thereby increasing both the final helium-core mass and the amount of mass loss near the tip of the RGB. The net effect is to shift a star's HB location towards higher effective temperatures and luminosities, depending on the amount of rotation. This scenario predicts a sloped HB with the *shift towards higher luminosities (and hence lower gravities) increasing with effective temperature* (Rood & Crocker 1989).
- ⋆ **Helium mixing:** The helium mixing described in Sect. 4.1 could also produce hot HB stars in metal-rich globular clusters. In this scenario, the hot stars in 47 Tuc and NGC 362 might have arisen from stars that were rotating fast enough to cross a threshold needed for helium mixing. The blue stars will then be observed to have *lower gravities and higher luminosities* than in the high mass-loss scenario. To produce as many hot HB stars as observed in NGC 6388 and NGC 6441 the mixing has to be quite strong and very common. The resulting increase in luminosity and its dependance on effective temperature may explain the sloped blue HB's observed in these two clusters[16].
- ⋆ **Binary evolution**: Bailyn (1995) has reviewed the binary evolution scenarios which could yield luminous blue stars in globular clusters. He suggests that HB morphology could be a function of the dynamical history of the cluster, through its influence on the number and type of binary stars. A binary origin for the hot stars could be detected either directly through a composite or emission-line spectrum, or by the presence of a *wide spread in the derived gravities and luminosities.* Binary evolution could be a valid explanation for 47 Tuc and NGC 362 although it is puzzling that the center of 47 Tuc (where interactions should be most pronounced) does not show any evidence for hot stars. O'Connell et al. (1997), however, remark that the hot stars in 47 Tuc are certainly not more concentrated towards the cluster center than the V band light, arguing in favour of single-star evolution.

---

[16] Much less mixing is necessary to produce blue tails in metal-poor clusters and the effects on luminosity are thus much smaller than in the case of blue tails in metal-rich globular clusters. Therefore helium mixing is not expected to produce sloped horizontal branches in metal-poor globular clusters.

Table 17. Coordinates and photometric data for the target stars in NGC 6388 and NGC 6441 from Piotto (priv. comm.)

Cluster	Star	α_{2000}	δ_{2000}	V	$B-V$
NGC 6388	WF2–42	$17^{h}36^{m}21.^{s}4$	$-44^\circ42'56''$	$17.^{m}440$	$+0.^{m}334$
NGC 6388	WF3–14	$17^{h}36^{m}23.^{s}5$	$-44^\circ43'11''$	$16.^{m}914$	$+0.^{m}333$
NGC 6388	WF3–15	$17^{h}36^{m}24.^{s}1$	$-44^\circ43'15''$	$16.^{m}896$	$+0.^{m}432$
NGC 6388	WF4–20	$17^{h}36^{m}20.^{s}9$	$-44^\circ45'10''$	$17.^{m}183$	$+0.^{m}341$
NGC 6441	WF2–24	$17^{h}50^{m}08.^{s}5$	$-37^\circ04'09''$	$17.^{m}567$	$+0.^{m}386$
NGC 6441	WF3–16	$17^{h}50^{m}06.^{s}2$	$-37^\circ02'50''$	$17.^{m}683$	$+0.^{m}558$
NGC 6441	WF3–17	$17^{h}50^{m}04.^{s}5$	$-37^\circ02'20''$	$17.^{m}643$	$+0.^{m}499$

If collisional encounters created the HB stars in NGC 6388 and NGC 6441 one would expect to see about 75 in the WFPC2 photometry of 47 Tuc by Rich et al. (1997), judging from the collision rates calculated for the respective cluster cores. In addition the blue HB and blue tail stars should be more centrally concentrated than the RGB stars which is not the case in these HST data. One should note, however, that Layden et al. (1999) find a much less pronounced blue tail in the outer regions of NGC 6441 (where of course the contamination by the field bulge population is much stronger) and suggest that the blue HB stars are more centrally concentrated than the red clump stars. Binaries cannot explain the slope of the HB seen in NGC 6388 and NGC 6441.

In principle a high primordial helium abundance can also explain a sloped HB together with a blue tail: Red clump stars evolve along blue loops during most of their HB lifetime. For larger than "standard" helium abundances Y_{MS} on the main sequence, these loops become considerably longer, reaching higher effective temperatures and deviating more in luminosity from the zero-age HB (ZAHB). For sufficiently high $Y_{\rm MS}$ ($\gtrsim 0.4$) the HB will slope upward (Catelan & de Freitas Pacheco 1996), as observed in NGC 6388 and NGC 6441. However, this scenario also predicts a much larger value for the number ratio of HB to RGB stars than the value recently obtained by Layden et al. (1999) for NGC 6441. Thus a high primordial helium abundance seems unlikely to be the cause of the sloped HB's. The explanation cannot work for 47 Tuc or NGC 362 as it would predict much more hot HB stars than observed.

5.1 NGC 6388 and NGC 6441

We selected our targets from the WFPC2 images of Rich et al. (1997) which were convolved to a "seeing" of $1''$ in order to allow the selection of stars suitable for ground-based spectroscopic observations. We took spectra of four stars in NGC 6388 and three stars in NGC 6441 (see Table 17). Unfortunately, due to rather mediocre weather conditions we could not observe more stars during our observing run at the NTT (June 21–24, 1998).

We used only the blue channel of EMMI and obtained medium resolution spectra to measure Balmer line profiles and helium line equivalent widths. We used grating #4 (72 Å/mm) and a slit width of $1.''0$, keeping the slit at parallactic angle for all observations. Seeing values varied between $0.''8$ and $1.''5$. The CCD was a Tek 1024 × 1024 chip with $(24\,\mu\mathrm{m})^2$ pixels, a read-out-noise of 5.7 e^- and a conversion factor of 2.84 e^-/count.

For calibration purposes we observed each night ten bias frames and ten dome flat-fields with a mean exposure level of about 10,000 counts each. In the beginning of each night we took a long HeAr exposure for wavelength calibration. Due to the long exposure times for the Ar spectrum we only obtained He calibration spectra during the night (before and after each science observation) and determined the offsets relative to the HeAr spectrum (from which the dispersion relation was derived) by correlating the two spectra. For the second night (and part of the third night) we could not obtain

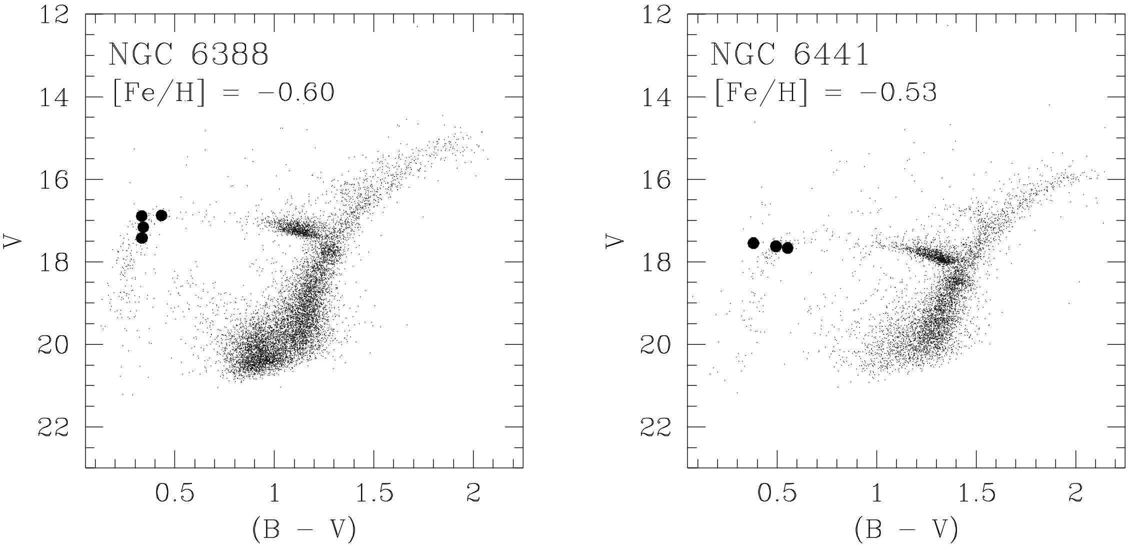

Fig. 33. Colour-magnitude diagrams of NGC 6388 and NGC 6441 from Rich et al. (1997). The stars discussed in this section are marked by big dots.

any wavelength calibration spectra due to technical problems. To correct any spectral distortions we used HeAr spectra from the first night for those data. The FWHM of the HeAr lines was measured to be 5.67±0.2 Å and was used as instrumental resolution. As flux standard stars we used LTT 7987 and EG 274.

We averaged the bias frames of the three nights and used their mean value instead of the whole frames as there was no spatial or temporal variation detectable. To correct the electronic offset we adjusted the mean bias by the difference between the mean overscan value of the science frame and that of the bias frame. The dark currents were determined from several long dark frames and turned out to be negligible (5.6±4.2 e^-/hr/pixel). The flat fields were averaged separately for each night, since we detected a slight variation in the fringe patterns of the flat fields from one night to the next (below 5%). They were then normalized as described in Sect. 3.3.1 for the EFOSC1 data.

For the wavelength calibration we fitted 3^{rd}-order polynomials to the dispersion relations of the HeAr spectra. They were adjusted for eventual offsets by cross-correlating them with the He spectra belonging to the science frame. The science spectra were then rebinned, sky subtracted (using a linear fit to the spatial distribution of the sky background), extracted and corrected for atmospheric extinction as described in Sect. 3.2.1. The data for the flux standard stars were taken from Hamuy et al. (1992) and the response curves were fitted by splines.

5.1.1 Atmospheric Parameters

To derive effective temperatures, surface gravities, and helium abundances we proceeded as described in Sect. 4.4.2. Beforehand we corrected the observed spectra for wavelength shifts introduced by radial velocities and the lack of appropriate wavelength calibration frames (see Sect. 5.1), as derived from the positions of the Balmer lines. The individual spectra for each star were then co-added and normalized by eye and are plotted in Fig. 34. For the normalization we assumed that the observed noise is mostly caused by photon noise. However, to account for the possibility of faint unresolved metal lines (keeping in mind that these are stars in metal-rich globular clusters) we tried to place the continuum line at the upper region of the scatter.

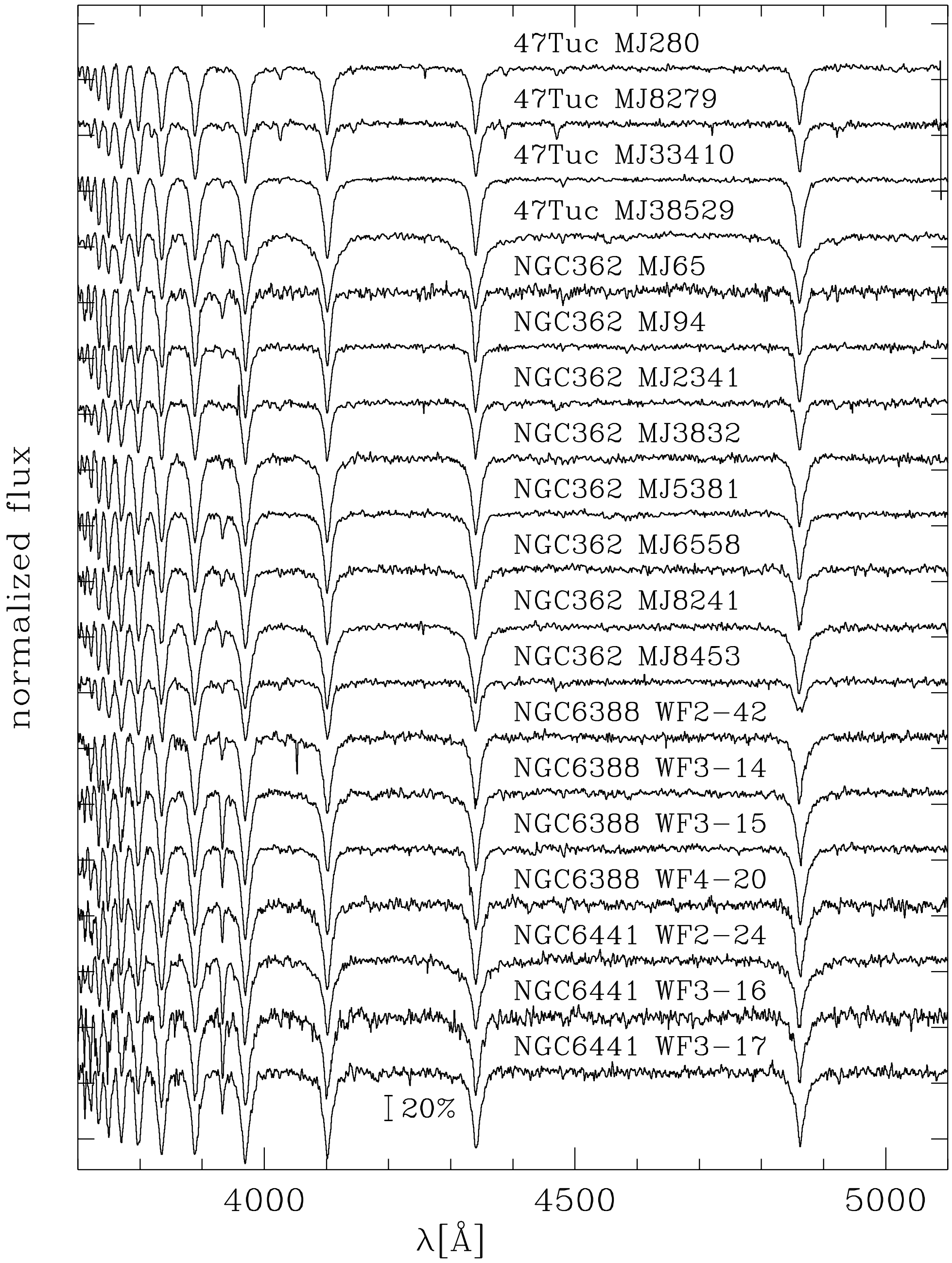

Fig. 34. Normalized spectra for the programme stars in 47 Tuc, NGC 362, NGC 6388, and NGC 6441. The part shortward of 3900 Å was normalized by taking the highest flux point as continuum value.

Using ATLAS9 and LINFOR we computed a grid of theoretical spectra covering the range 7500 K $\leq T_{\rm eff} \leq$ 20,000 K, $2.5 \leq \log g \leq 6.0$, $-3.0 \leq \log\frac{N_{He}}{N_H} \leq -1.0$, at metallicities of [M/H] = −0.75 and [M/H] = −0.50. To check the effects of metallicity we fitted the spectra at $\log\frac{N_{He}}{N_H} = -1.0$ using model spectra with [M/H] = −0.50 and [M/H] = −0.75. The fit results for the two metallicities were almost identical: $T_{\rm eff}$ and $\log g$, respectively, increased by at most 1% and 0.03 dex from [M/H] = −0.50 to −0.75 (except for NGC 6441 WF3-16, where $\Delta\,T_{\rm eff}$ and $\Delta\log g$ were 1.6% and 0.07 dex, respectively). All further analysis was therefore performed for a fixed metallicity of [M/H] = −0.50, which is close to the metallicities of the cluster (−0.60 and −0.53 for NGC 6388 and NGC 6441, respectively).

As none of the programme stars showed any He absorption lines we first fitted all spectra at two fixed helium abundances, $\log\frac{N_{He}}{N_H} = -1.0$ and -2.0, using the Balmer lines H_β to H_{10} (except H_ϵ to avoid contamination by the Ca II H line). When defining the fit regions we took care to extend them as far as possible while avoiding any predicted strong He I lines ($\lambda\lambda$ 4026 Å, 4388 Å, 4921 Å) which might be present at the noise level although undetected by eye. Such lines would distort the fit: Fitting regions of strong He I lines while keeping the helium abundance fixed will result in erroneous results for $T_{\rm eff}$ and $\log g$ if the helium abundance of the model atmospheres is not identical to that of the star. The results are listed in Table 18.

As the stars are rather cool it is not obvious from the spectra on which side of the Balmer maximum they lie. However, the strength of the Ca II K line can be used to distinguish between the "hot" and the "cool" solution: the observed equivalent width of this line has stellar and interstellar contributions. As the clusters are highly reddened – $E_{B-V}= 0\overset{\rm m}{.}34$ and $0\overset{\rm m}{.}42$ for NGC 6388 and NGC 6441, respectively (Djorgovski 1993; Harris 1996 gives $0\overset{\rm m}{.}40$ and $0\overset{\rm m}{.}44$, respectively) – *the observed equivalent width has to be significantly larger than the one predicted by the model atmosphere* for [M/H] = -0.5. In Table 18 we list the atmospheric parameters for all stars together with the measured and predicted equivalent widths for the Ca II K line. The comparison between observed and predicted values places all ambiguous stars on the *hot* side of the Balmer maximum.

For those stars that are hotter than 9,500 K we finally fitted the Balmer lines mentioned above together with those regions of the spectra where the He I lines $\lambda\lambda$ 4026 Å, 4388 Å, 4471 Å, and 4921 Å are expected. This way we want to put at least an upper limit to the He abundance even though no He lines are visible. As can be seen from Table 18 this upper limit tends to be subsolar for the hotter stars, in agreement with the results for HBB stars in metal-poor clusters (Behr et al. 1999a, see also Sect. 3.3.4 and 4.4.2).

5.1.2 Possible errors and discrepancies

1. **Error estimates:** The fit program gives r.m.s. errors derived from $\Delta\chi^2 = 2.71$ ($T_{\rm eff}$, $\log g$) resp. 3.53 ($T_{\rm eff}$, $\log g$, $\log \frac{N_{He}}{N_H}$). However, since χ^2 is not close to 1 these errors will most likely underestimate the true errors. As the errors causing the large χ^2 values are most probably systematic (see below) they are hard to quantify. We decided to get an estimate of their size by assuming that the large χ^2 is solely caused by noise. Increasing the noise parameter σ until $\chi^2 = 1$ then yields new formal errors for $\Delta\chi^2 = 2.71$ and 3.53, respectively, which are given in Table 18. These errors still underestimate the internal errors as we oversampled the spectra by a factor of 2.5 when rebinning to constant wavelength steps. Thus only 40% of the wavelength points used for the fit are truly independent. We correct this by applying a factor of $\sqrt{2.5} = 1.6$ to all error estimates (this has been done for the values given in Sect. 4.4.2 and 5.2.1 as well).
2. **Large χ^2:** As can be seen from Table 18 the reduced χ^2 is far from 1. We believe that these bad χ^2 values are due to the low resolution of the data (5.7 Å): At $T_{\rm eff}$ = 11,000 K and $\log g = 4$ the FWHM of the theoretical Balmer lines are around 12 Å. Thus the instrumental profile makes up a considerable part of the observed line profile. Therefore any deviations of the instrumental profile from a Gaussian (which is used to convolve the model spectra) will lead to a bad fit. Fortunately we could compare the effects for one hot HB star in NGC 6752, for which we have an NTT spectrum with the same setup as is used here and a spectrum from the ESO 1.52m telescope with a resolution of 2.6 Å (for details see Sect. 4.4.2). Performing a spectroscopic analysis as described above with model atmospheres of [M/H] = -1.5 we find the parameters listed in Table 13 (p. 67). While the reduced χ^2 values for both fits differ by a factor of 2 (5.9 vs. 3.1) the resulting effective temperatures and surface gravities are rather similar (13,700 K/3.75 vs. 13,700 K/3.80).
3. **Continuum placement:** Using the spectrum of NGC 6441 WF3–17 we checked the effects of a possible misplacement of the continuum: We now normalized the spectrum again, using only the uppermost resp. lowermost continuum points. This amounted to changes of -1% (upper continuum) resp. +3% (lower continuum) in the normalized continuum level. Temperature, gravity and χ^2 were

Table 18. Atmospheric parameters, reduced χ^2 values, and equivalent widths of the Ca II K line for the programme stars for an assumed [M/H] = −0.5. For stars hotter than 9,500 K the first row gives the atmospheric parameters obtained by fitting the Balmer lines and the spectral region of the strongest He I lines. For all stars the first two of the four rows at fixed helium abundance give the solutions on the hot side of the Balmer maximum for the cited helium abundances, while the last two rows give the solutions on the cool side of the Balmer maximum that were rejected because of the strength of the Ca II K line. The errors are r.m.s. errors adjusted for $\chi^2 > 1$ (see also Sect. 5.1.1). A colon marks extrapolated values.

Star	χ^2	T_{eff} [K]	δT_{eff} [K]	$\log g$ [cm s^{-2}]	$\delta \log g$ [cm s^{-2}]	$\log \frac{N_{He}}{N_H}$	$\delta \log \frac{N_{He}}{N_H}$	W_λ (Ca II K) obs. [Å]	model [Å]
NGC 6388 WF2–42	4.34	12130	590	4.14	0.19	≤ -2.0	0.6	1.2	0.1
	4.78	12090	500	4.03	0.14	−1.00			
	4.78	12140	510	4.15	0.14	−2.00			
	4.75	7010	110	1.9:	0.41	−1.00			6.5
	4.73	7060	80	2.1:	0.24	−2.00			
NGC 6388 WF3–14	4.12	12250	500	4.56	0.16	≤ -1.9	0.4	3.1	0.1
	3.86	12180	400	4.44	0.11	−1.00			
	3.85	12210	380	4.56	0.11	−2.00			
	3.82	7450	60	2.79	0.13	−1.00			4.2
	3.83	7450	60	2.87	0.11	−2.00			
NGC 6388 WF3–15	2.94	9080	940	3.13	0.54	−1.00		1.7	0.7
	2.94	9130	720	3.26	0.42	−2.00			
	2.94	9100	910	3.14	0.53	−1.00			
	2.94	9160	670	3.29	0.38	−2.00			
NGC 6388 WF4–20	2.18	9960	510	3.71	0.20	≤ -1.5	0.9	1.4	0.3
	1.82	9900	400	3.62	0.19	−1.00			
	1.83	9910	400	3.73	0.19	−2.00			
	1.79	8150	220	2.69	0.11	−1.00			2.5
	1.79	8130	210	2.77	0.10	−2.00			
NGC 6441 WF2–24	2.96	14360	670	5.2:	0.18	≤ -1.8	0.4	3.8	0.1
	3.20	14460	510	5.1:	0.13	−1.00			
	3.28	14400	560	5.2:	0.13	−2.00			
	1.99	7570	30	5.0:	0.18	−1.00			4.1
	2.01	7570	30	5.0:	0.18	−2.00			
NGC 6441 WF3–16	2.61	12710	770	4.65	0.22	≤ -1.8	0.4	3.8	0.1
	2.23	12630	580	4.53	0.16	−1.00			
	2.22	12630	580	4.63	0.16	−2.00			
	1.97	7360	60	3.14	0.24	−1.00			4.2
	1.97	7370	60	3.23	0.24	−2.00			
NGC 6441 WF3–17	2.55	10910	500	4.04	0.24	≤ -1.0	0.5	2.3	0.2
	2.44	10920	400	4.05	0.16	−1.00			
	2.44	10930	400	4.16	0.16	−2.00			
	2.38	7720	110	2.61	0.08	−1.00			3.7
	2.38	7720	110	2.71	0.08	−2.00			

only slightly affected by these changes: In both cases the temperature increased by about 50 K, $\log g$ by 0.03 dex, and χ^2 by about 0.04. The effect of a misplaced continuum is mostly erased

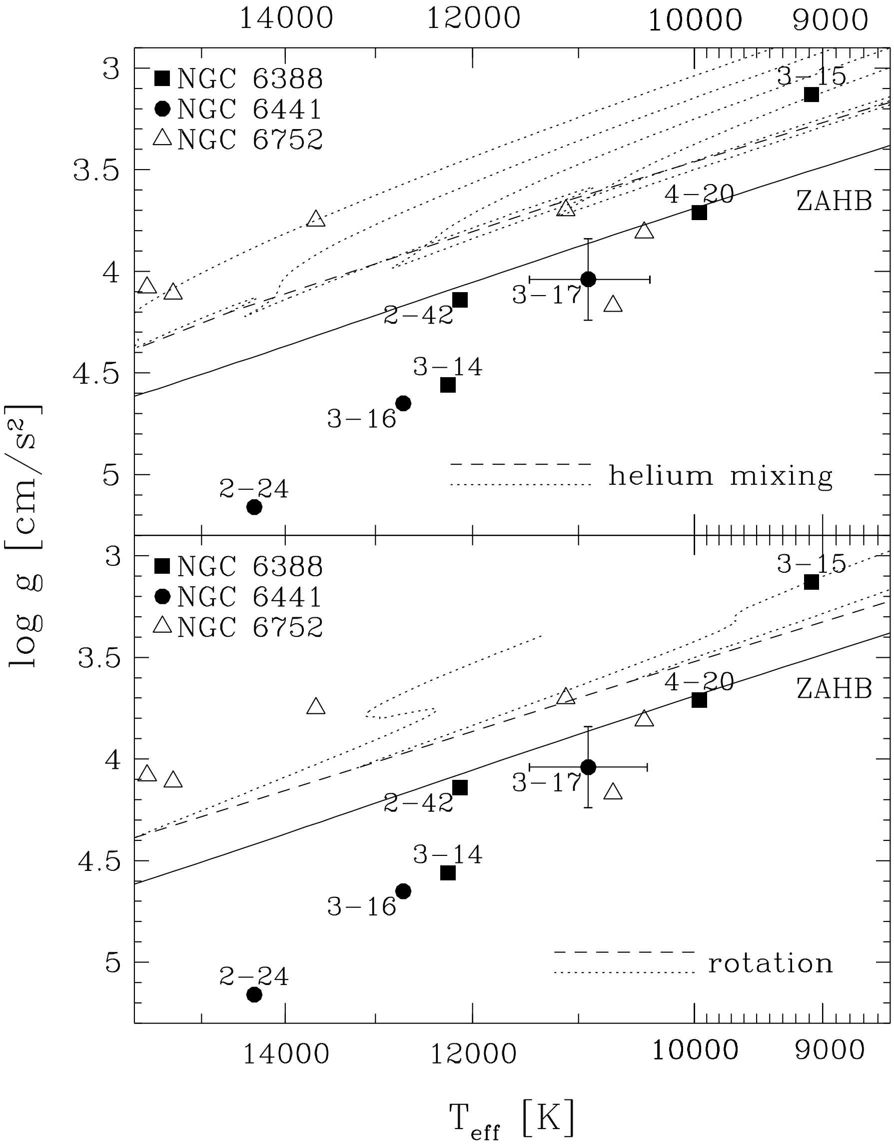

Fig. 35. Comparison of the measured gravities and temperatures for our programme stars in NGC 6388 and NGC 6441 against the HB models for [M/H] = −0.5 from Sweigart & Catelan (1999). The solid curve represents a canonical zero-age HB (ZAHB) for this metallicity. The ZAHB and evolutionary tracks for the sequences which reproduce the observed HB slope in these globular clusters are indicated by the dashed and dotted curves, respectively. The **upper panel** shows the helium-mixed tracks, the **lower panel** shows the rotation tracks. The numbers of the stars refer to Table 18. A representative error bar is plotted at the location of the star NGC 6441 WF3–17. In addition we show the positions of cool blue HB stars in NGC 6752, which were observed with the same instrumental setup (see Table 13, page 67) and have been analysed with the same model spectra as the stars in NGC 6388 and NGC 6441.

by the renormalization of observed *and* model spectrum before fitting, using the same continuum points for both.

The effective temperatures from Table 18 and the $B-V$ colours from Table 17 do not correlate well for the stars in NGC 6441. However, as the reddening towards both globular clusters is relatively large ($E_{B-V} \approx 0^{\rm m}\!.4$) and *may* vary by a few hundredths of a magnitude on small scales (especially in the case of NGC 6441; see Sect. 3.1 in Piotto et al. 1997; for a more general discussion see Heitsch & Richtler 1999), we do not put too much emphasis on this (apparent) inconsistency between spectroscopically derived temperatures and observed WFPC2 colours.

5.1.3 Discussion

The atmospheric parameters derived for our programme stars are compared in Fig. 35 to the canonical ZAHB and to the non-canonical tracks for [M/H] = −0.5 from Sweigart & Catelan (1998, 1999, helium-mixed resp. rotation, cf. page 78). Quite unexpectedly, the studied stars tend to lie preferentially *below* the canonical ZAHB[17]. This behaviour stands in marked contrast to the results for hot HB stars in more metal-poor globular clusters, where lower than canonical gravities are normally found (see Chapter 3). To verify that the high gravities are not due to problems with the low resolution of the data or with the model atmospheres used here, we also show results for cool HBB stars in NGC 6752 that were observed during the same run and reduced in the same way (Sect. 4.4.2, Table 13 – stars observed in 1998 were observed during the run reported here). It can be clearly seen that those stars follow the overall trend seen in NGC 6752 to show lower than expected surface gravities when fitted with the same model atmospheres as the stars in NGC 6388 and NGC 6441. If the high gravities found for the stars in NGC 6388 and NGC 6441 were caused by systematic errors in the data analysis or the model atmospheres the stars in NGC 6752 should exhibit the same effect.

Considering the estimated 1σ errors in $T_{\rm eff}$ and $\log g$ the positions of NGC 6388 WF2–42, WF3–14, WF4–20, and NGC 6441 WF3–17 are consistent with the canonical ZAHB within 2σ. NGC 6388 WF3–15 could be a hot post-HB star already on its way to the asymptotic giant branch – as we observed rather bright blue HB stars at the top of the blue tail in both clusters (see Fig. 33) we are biased towards stars evolving from the ZAHB towards higher luminosities. NGC 6441 WF3–16 lies marginally more than 2σ below the unmixed ZAHB, but has also the lowest S/N of all observed stars. NGC 6441 WF2–24 lies 0.7 dex in $\log g$ below the canonical ZAHB along the track of a 0.195 $M_\odot$ helium-core white dwarf (Driebe et al. 1998). In this case it would be a foreground object and most probably member of a binary system having undergone mass transfer, as the low mass single star precursors of helium-core white dwarfs evolve too slowly to reach this stage within a Hubble time. While helium-core white dwarfs evolve rather fast and the probability of finding one is therefore rather low, we could not find any other physical explanation for a star like NGC 6441 WF2–24. As we are not able to derive radial velocities (see Sect. 5.1) we cannot decide whether this star is a cluster member or not.

The derived gravities (except for NGC 6388 WF3–15) are *significantly* larger than those predicted by the non-canonical tracks that reproduce the upward sloping HB's in the colour-magnitude diagrams of NGC 6388 and NGC 6441 (see p. 78). The discrepancy would increase if the atmospheric abundances of the programme stars (and thereby their line profiles) were affected by the radiative levitation of metals (Grundahl et al. 1999): As shown in Sect. 4.4.2 accounting for this effect moves the parameters of blue HB stars in NGC 6752 to lower temperatures and/or higher gravities. However, the moderate resolution and S/N of the data discussed here do not allow abundances of the heavy elements to be estimated.

We do not have an explanation for this surprising result. All scenarios that could reproduce the sloped HB's (SC98, see page 78) predict anomalously low gravities for globular cluster HB stars within the temperature range of our programme stars. As far as we are aware, there are no alternative models capable of accounting for the sloped HB's seen in NGC 6388 and NGC 6441 without producing anomalously bright HB stars and hence low gravities. In fact, recent analyses of RR Lyrae variables in NGC 6388 and NGC 6441 (Layden et al. 1999, Pritzl et al. 1999) strongly indicate that the RR Lyrae stars of these globular clusters are substantially brighter than canonical models would predict. Thus we face a conundrum: the non-canonical models which explain the upward sloping HB's in these globular clusters are inconsistent with the derived temperatures and gravities of the hot HB stars.

---

[17] The difference between Fig. 35 here and Fig. 8 in Moehler (1999) results from using fitting ranges for the preliminary analysis of the line profiles that did not extend far enough to include the wings of the Balmer line profiles.

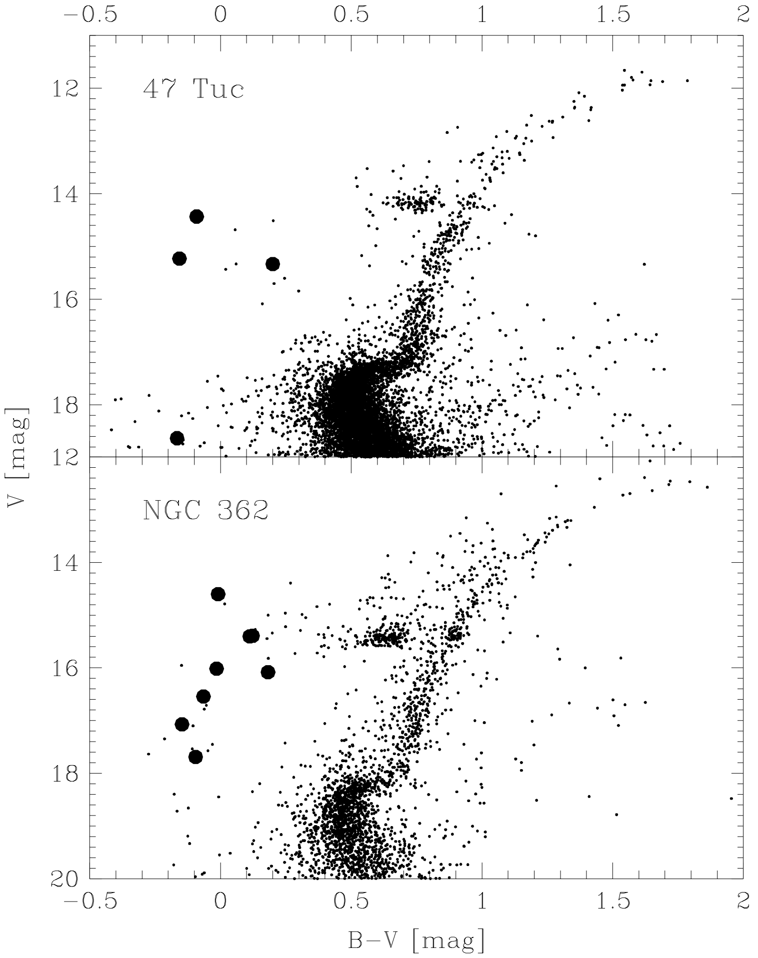

Fig. 36. The colour-magnitude diagrams for 47 Tuc (**upper panel**) and NGC 362 (**lower panel**) as observed by Montgomery & Janes (priv. comm.). The big dots mark the stars for which we took spectra.

5.2 47 Tuc and NGC 362

We selected a total of 12 blue stars in 47 Tuc and NGC 362 for follow-up spectroscopy. These stars are listed in Table 19 and marked in Fig. 36 with big dots. We observed with EMMI at the NTT on October 26 and 27, 1997. We obtained low resolution spectrophotometric data with large slit widths (5″) and medium resolution spectra with a 1″ slit. Seeing values for these observations varied between 0.″7 and 1.″3, but some clouds were present. The slit was kept at parallactic angle for all observations. We used grating #4 (72 Å/mm) and reduced the dispersion for the low resolution spectra by binning along the dispersion axis by a factor of 4. The CCD was a Tek 1024×1024 chip with $(24\mu\mathrm{m})^2$ pixels, a read-out-noise of 5.7 e^- and a conversion factor of 2.84 e^-/count. For calibration purposes we observed each night 10 bias frames and 10 dome flat-fields with a mean exposure level of about 10,000 counts each. In addition we obtained sky flat fields to correct for the slit illumination. As flux standard stars we used LTT 7987 and EG 21.

Bias and flat field correction were performed as described in Sect. 5.1 and we found a negligible dark current of 9.4±5.6 e^-/hr/pixel. The spectra were wavelength calibrated, sky subtracted (using a constant to fit the spatial distribution of the sky background), extracted, and corrected for atmospheric extinction as described in Sect. 3.2.1. The data for the flux standard stars were taken from Hamuy et al. (1992). The response curves were fitted by 8th order polynomials for the low and medium resolution spectra. We took special care to correctly fit the response curves for the low resolution data in the

Table 19. Coordinates, photometric data, heliocentric radial velocities (obtained from our spectra), and cluster membership information for the target stars in 47 Tuc and NGC 362. The numbers and the $B, B-V$ photometric data are from Montgomery & Janes (priv. comm.). m_{162} is the UIT magnitude at 1620 Å. The cluster membership is taken from Tucholke (1992a, 1992b)

Cluster	Star	α_{2000}	δ_{2000}	B	$B-V$	m_{162}	$m_{162}-V$	$\mathrm{v}_{\mathrm{rad,hel}}$ [km/s]	cluster member
47 Tuc	MJ280	$00^{\mathrm{h}}21^{\mathrm{m}}29.^{\mathrm{s}}35$	$-71^\circ58'14.''3$	$15.^{\mathrm{m}}07$	$-0.^{\mathrm{m}}16$	$13.^{\mathrm{m}}18$	$-2.^{\mathrm{m}}05$	-37	yes (T1948)
	MJ8279	$00^{\mathrm{h}}22^{\mathrm{m}}57.^{\mathrm{s}}71$	$-71^\circ57'56.''6$	$18.^{\mathrm{m}}47$	$-0.^{\mathrm{m}}17$	$15.^{\mathrm{m}}86$	$-2.^{\mathrm{m}}78$	$+161$	–
	MJ33410	$00^{\mathrm{h}}24^{\mathrm{m}}44.^{\mathrm{s}}79$	$-72^\circ09'33.''1$	$14.^{\mathrm{m}}34$	$-0.^{\mathrm{m}}09$	$13.^{\mathrm{m}}70$	$-0.^{\mathrm{m}}73$	-25	
	MJ38529	$00^{\mathrm{h}}25^{\mathrm{m}}33.^{\mathrm{s}}20$	$-72^\circ10'44.''3$	$15.^{\mathrm{m}}54$	$+0.^{\mathrm{m}}20$	$13.^{\mathrm{m}}82$	$-1.^{\mathrm{m}}51$	-46	yes (T300)
NGC 362	MJ65	$01^{\mathrm{h}}01^{\mathrm{m}}58.^{\mathrm{s}}4$	$-70^\circ50'28.''9$	$14.^{\mathrm{m}}59$	$-0.^{\mathrm{m}}01$	$14.^{\mathrm{m}}97$	$+0.^{\mathrm{m}}37$	$+120$	no (T15)
	MJ94	$01^{\mathrm{h}}03^{\mathrm{m}}18.^{\mathrm{s}}7$	$-70^\circ52'20.''9$	$16.^{\mathrm{m}}47$	$-0.^{\mathrm{m}}07$	$15.^{\mathrm{m}}04$	$-1.^{\mathrm{m}}50$	$+137$	no (T16)
	MJ2341	$01^{\mathrm{h}}03^{\mathrm{m}}11.^{\mathrm{s}}8$	$-70^\circ51'20.''8$	$17.^{\mathrm{m}}59$	$-0.^{\mathrm{m}}10$	$15.^{\mathrm{m}}29$	$-2.^{\mathrm{m}}40$	$+75$	–
	MJ3832	$01^{\mathrm{h}}03^{\mathrm{m}}04.^{\mathrm{s}}5$	$-70^\circ51'30.''5$	$15.^{\mathrm{m}}51$	$+0.^{\mathrm{m}}11$	$15.^{\mathrm{m}}19$	$-0.^{\mathrm{m}}21$	$+197$	–
	MJ5381	$01^{\mathrm{h}}04^{\mathrm{m}}17.^{\mathrm{s}}8$	$-70^\circ54'23.''8$	$16.^{\mathrm{m}}26$	$+0.^{\mathrm{m}}18$	$16.^{\mathrm{m}}38$	$+0.^{\mathrm{m}}30$	$+109$	no (T247)
	MJ6558	$01^{\mathrm{h}}03^{\mathrm{m}}16.^{\mathrm{s}}1$	$-70^\circ51'27.''1$	$16.^{\mathrm{m}}00$	$-0.^{\mathrm{m}}02$	$14.^{\mathrm{m}}66$	$-0.^{\mathrm{m}}36$	$+228$	no (T304)
	MJ8241	$01^{\mathrm{h}}03^{\mathrm{m}}25.^{\mathrm{s}}0$	$-70^\circ51'55.''2$	$15.^{\mathrm{m}}51$	$+0.^{\mathrm{m}}12$	$15.^{\mathrm{m}}74$	$+0.^{\mathrm{m}}35$	$+244$	–
	MJ8453	$01^{\mathrm{h}}02^{\mathrm{m}}00.^{\mathrm{s}}1$	$-70^\circ51'15.''0$	$16.^{\mathrm{m}}92$	$-0.^{\mathrm{m}}15$	$15.^{\mathrm{m}}90$	$-2.^{\mathrm{m}}17$	$+73$	no (T396)

region of the Balmer jump, since we planned to use this feature for the determination of the effective temperatures of the stars.

We also used the medium resolution data to derive radial velocities, which are listed in Table 19 (corrected to heliocentric system). The error of the velocities is about 30 km/sec (estimated from the r.m.s. scatter of the velocities derived from individual lines). The normalized and velocity-corrected spectra are plotted in Fig. 34 (p.81).

5.2.1 Atmospheric Parameters

T_{eff} derived from energy distributions

We searched all stars for red neighbours as described on page 36 using the photometry of 47 Tuc and NGC 362 (Montgomery & Janes, priv. comm.). With this procedure we get stray light levels of more than 3% in B only for MJ3832 (36%) in NGC 362. For those objects where the neighbour did not lie in the slit the observed stray light levels are lower than the calculated ones by a factor of 1.5 to 2.

We used line blanketed LTE model atmospheres of Kurucz (1992, ATLAS9) for a metallicity [M/H] = -1.0 to derive effective temperatures from the low resolution spectra. To correct for interstellar reddening we applied the reddening law of Savage & Mathis (1979) and used an E_{B-V} of $0.^{\mathrm{m}}04$ for both clusters. The simultaneous fitting of the spectrophotometric data (Balmer jump and continuum) was generally possible except for MJ 38529 in 47 Tuc and MJ6558 and MJ3832 in NGC 362. MJ3832 has a cool star close by (MJ3749, distance $3''$, $B = 14.^{\mathrm{m}}39$, $B-V = +1.^{\mathrm{m}}43$) which may contaminate the low resolution spectrum that was observed with a $5''$ slit (see above). MJ6558 was observed at rather high airmass (1.8) and MJ38529 may be a binary (see below). However, comparing our measured intensities to those derived from B and V magnitudes of the stars normally led to discrepancies of up to $0.^{\mathrm{m}}3$. In most of the cases the observed spectra were brighter than the corresponding photometric fluxes. This can be understood by the fact that there were some clouds present during the observations – if the flux standard stars were stronger affected than the targets the resulting flux calibration would yield too much flux for the targets stars. The slope as derived from $B-V$ was consistent with the slope of the spectrophotometric continuum in most cases except MJ38529 in 47 Tuc and MJ5381 in NGC 362 ($B-V$ being more positive than indicated by the spectrophotometric continuum). We found that the observed H_β line in the low resolution spectrum of NGC362-MJ8453 was significantly shallower than the theoretical one (see also below).

Line profile fits

To derive effective temperatures, surface gravities and helium abundances from line profile fits we proceeded as described in Sect. 4.4.2. If available the temperatures and gravities derived from the low resolution data were used as starting points for the line profile fits. Beforehand we corrected the spectra for radial velocity shifts, derived from the positions of the Balmer lines. The resulting heliocentric velocities are listed in Table 20, together with the physical parameters of the stars. Using ATLAS9 and LINFOR we computed a grid of theoretical spectra covering the ranges 8000 K$\leq T_{\rm eff} \leq$20,000 K, 2.5$\leq \log g \leq$6.0, and −2.0, −1.0 in $\log\frac{N_{He}}{N_H}$ at metallicities of −1 and −0.75. For the temperature range 6500 K to 9000 K we computed a grid of model spectra that also include all metal lines, using a scaled solar abundance of [M/H] = −1. We used this grid to fit the cooler stars (MJ3832 and MJ8241 in NGC 362) as for temperatures below 8000 K metal lines may become important for the fitting of the Balmer line profiles.

We fitted the Balmer lines from H_β to H_{12} (excluding H_ϵ because of the Ca II H line) and the He I lines λλ 4026 Å, 4388 Å, 4472 Å, 4713 Å, and 4922 Å (for $T_{\rm eff} \geq$ 10,500 K). For cooler stars we fitted only the Balmer lines for a fixed helium abundance of $\log\frac{N_{He}}{N_H} = -1$ (the helium abundance in these cooler stars should be close to solar as they should not be affected by diffusion). In the medium resolution spectrum of MJ8453 the observed H_β line is significantly less deep than the theoretical one and also H_γ shows some evidence for filling. We therefore excluded those two lines form the fit for this star. Several stars above 10,500 K do not show He I lines. We nevertheless fitted those regions of the spectra, where the He I lines are expected, to obtain an upper limit of the He abundance. To check for any effects of metallicity on the final results we fitted the spectra with models of [M/H] = −1.00 and [M/H] = −0.75. We found that in all cases except MJ3832 in NGC 362 the differences in effective temperature and surface gravity were below 1% resp. 0.05 dex (2% and 0.11 dex for MJ3832). As the difference are well below our expected errors we decided to use only the results for [M/H] = −1 for the further discussion, which lies between the metallicity for 47 Tuc ([M/H] ≈ −0.7) and that of NGC 362 ([M/H] ≈ −1.2).

Comparison of effective temperatures obtained with different methods

As can be seen from Table 20 the temperatures derived from the spectrophotometric data deviate from the ones derived from the Balmer lines, which may be an effect of strongly varying atmospheric extinction (as is already suggested by the discrepancies between spectrophotometric and photometric fluxes for the stars, see Sect. 5.2.1). Differences in the reddening and interstellar extinction law between galactic globular clusters and the SMC may affect the flux distribution of the stars, which are by default only corrected for the galactic extinction towards the respective cluster. Sasselov et al. (1997) report that the extinction law for the SMC is essentially the same as that for the Large Magellanic Cloud (LMC). We therefore dereddened the extinction corrected spectra once more, this time using $E_{B-V} = 0\overset{\rm m}{.}09$ and the reddening law towards the LMC (Howarth 1983) as implemented in MIDAS. The resulting differences between spectra with and without this additional reddening correction are too small to explain the temperature differences between the results from the low resolution data and the line profiles. We thus conclude that the most probable explanation for the discrepancies lies with the non-photometric observing conditions.

Masses

Knowing $T_{\rm eff}$, $\log g$, and the distances of the stars we can derive the masses as described in Sect. 3.2.5 and the results are listed in Table 20. We determine two masses for each star, one assuming that it is a cluster member and one assuming it belongs to the SMC. We use the following reddening-free

Table 20. Atmospheric parameters and masses for the programme stars as derived from low and medium resolution spectroscopic data. The surface gravities derived from the low resolution spectrophotometric data are rather uncertain. We also give the reduced χ^2 values from the line profile fits and the errors listed below are the r.m.s. errors of the fit routine adjusted as described in Sect. 5.1.2.

Cluster	Star	spectrophotometry		medium resolution data				Masses	
		$T_{\rm eff}$	$\log g$	χ^2	$T_{\rm eff}$	$\log g$	$\log \frac{N_{He}}{N_H}$	cluster	SMC
		[K]	[cm/s^2]		[K]	[cm/s^2]		[M$_\odot$]	[M$_\odot$]
47Tuc	MJ280	13500	4.0:	2.75	14500±290	4.21±0.08	−1.41±0.16	0.65	133
	MJ8279	18000	4.5:	1.96	18500±530	4.20±0.10	−1.56±0.11	0.02	3.8
	MJ33410	10000	3.5:	4.53	10400±210	3.53±0.11	−1.00	0.51	104
	MJ38529	8000[1]	3.0:	2.25	7950±20	5.21±0.05	−1.00	24	4900
		12500[2]	3.5:	7.85	14000±400	5.34±0.11	<−2	8.4	1700
NGC362	MJ65	8500	2.5:	2.03	9460±540	2.46±0.32	−1.00	0.16	9.5
	MJ94	11000	3.5:	3.53	11700±350	3.33±0.11	−1.93±0.35	0.13	7.6
	MJ2341	16000	4.5:	2.08	17400±500	3.97±0.10	−1.79±0.13	0.10	5.9
	MJ3832			2.64	8250±140	2.77±0.06	−1.00	0.23	13
	MJ5381	9000	3.0:	2.43	7780±100	2.14±0.05	−1.00	0.03	2.0
	MJ6558			3.06	12500±350	4.09±0.11	−1.61±0.40	1.08	62
	MJ8241	8500	3.5:	3.49	7980±50	3.06±0.06	−1.00	0.51	29
	MJ8453[3]	14000	4.0:	1.53	16600±560	4.11±0.11	−1.99±0.11	0.27	18

[1] fitting the continuum

[2] fitting the Balmer jump

[3] H_β, H_γ are not included in the fit of MJ8453

distance moduli $(m-M)_0$: $13\overset{\mathrm{m}}{.}31$ for 47 Tuc, $14\overset{\mathrm{m}}{.}67$ for NGC 362 (both from Djorgovski 1993; Harris 1996 gives $13\overset{\mathrm{m}}{.}25$ resp. $14\overset{\mathrm{m}}{.}65$), and $18\overset{\mathrm{m}}{.}91$ for the SMC (Sasselov et al. 1997). Using the HIPPARCOS based distance moduli to 47 Tuc and NGC 362 of $13\overset{\mathrm{m}}{.}51$ and $14\overset{\mathrm{m}}{.}88$ (see Table 10, page 60) would increase the masses by about 20% in both cases.

The errors given in Table 20 are the r.m.s. errors of the fits (see Sect. 5.1.2 for details). The real errors in $T_{\rm eff}$ and $\log g$ are estimated to be about 7% and 0.15 dex, respectively. In addition to the error in $\log g$ errors in the absolute magnitude and the theoretical brightness at the stellar surface also enter the final error in log M. We assume an error in the absolute brightness (combining errors in the photometric data and errors in the distance moduli and reddenings) of $0\overset{\mathrm{m}}{.}15$. The error in the theoretical V brightness is dominated by the errors in $T_{\rm eff}$. We estimate the total error in log M to be about 0.23 dex, corresponding to an error of 70% in mass (for a detailed discussion of error sources see Sect. 3.3.5).

5.2.2 Discussion

47 Tuc: As can be seen from Table 19 three of the four stars in 47 Tuc are probably members of the cluster. MJ8279 according to its radial velocity belongs to the SMC. The comparison of the spectroscopically derived mass (3.8 M$_\odot$) with the mass obtained from the evolutionary tracks (5 M$_\odot$) further supports its SMC membership. Of the remaining three stars MJ 38529 is very probably a binary: Its UV-visual colour suggests an effective temperature of 13,700 K, but $B-V$ is much too red for such a temperature (see also its position in Fig. 36 below the HB). The low resolution spectrum suggests effective temperatures of 12,500 K (Balmer jump only) resp. 8000 K (continuum only). The superposition of two different stellar spectra (with different Balmer lines) may explain the strange values obtained for $\log g$ from the Balmer line profiles.

MJ 280 is hot enough to be affected by diffusion processes. Fitting it with enriched model atmospheres described in Sect. 4.4.2 ([Fe/H] = +0.5) indeed yields $T_{\rm eff}$ = 14,200 K, $\log g$ = 4.29 and

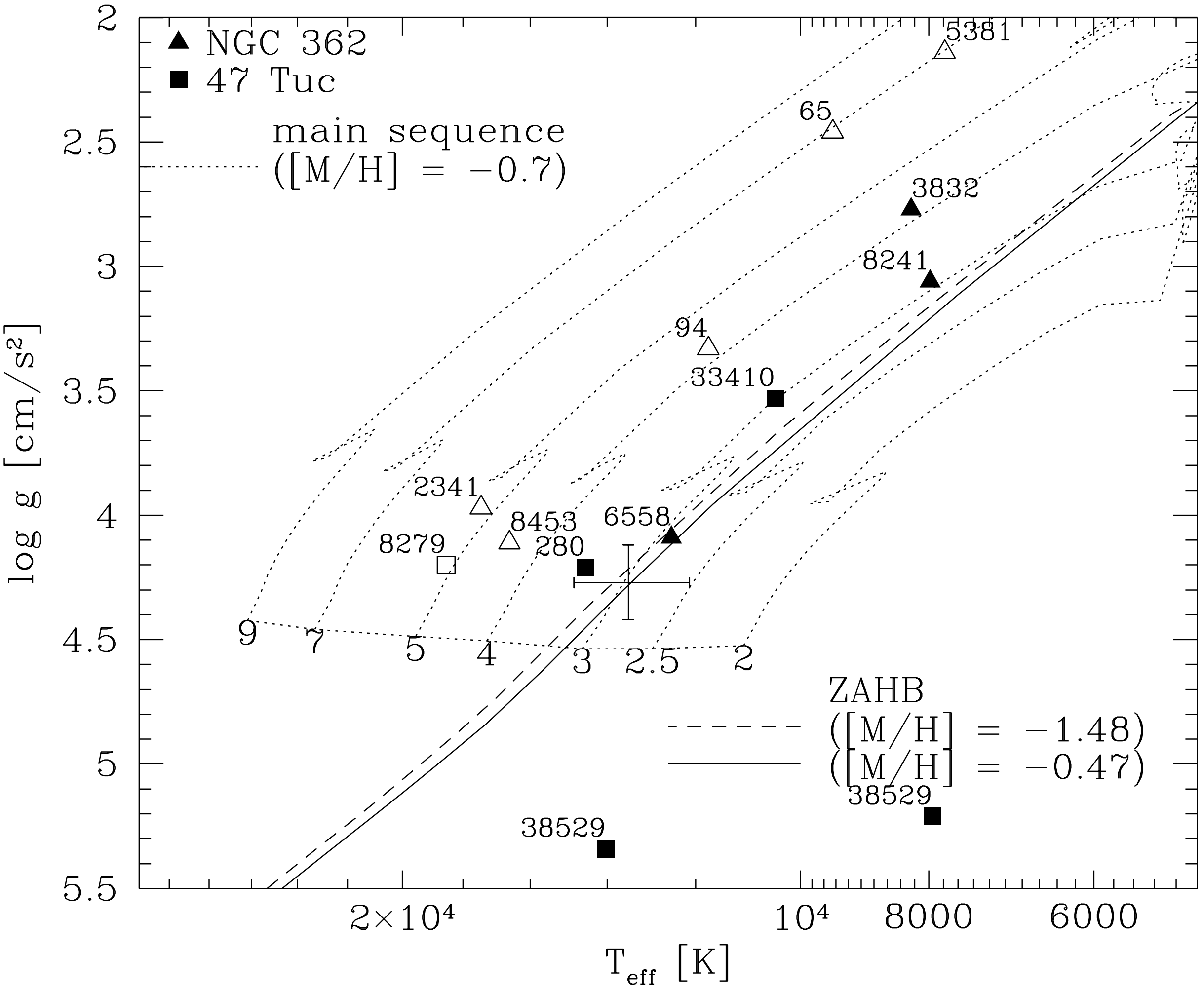

Fig. 37. The atmospheric parameters of the target stars in 47 Tuc and NGC 362 compared to zero-age horizontal branch models (Dorman et al. 1993) and main-sequence resp. post-main sequence models (Charbonnel et al. 1993). The suspected field/SMC stars are marked by open symbols.

$\log\frac{N_{He}}{N_H} = -1.63$, moving the star closer to the ZAHB. MJ 33410 finally is a normal cool HBB star. The masses of MJ 280 and MJ 33410 agree well with canonical predictions.

NGC 362: According to Table 19 three of the eight targets in NGC 362 are radial velocity members. MJ 6588 is not a proper motion member, but the error of its proper motion is rather large compared to the measurements of the other stars. MJ 6558 and MJ 8241 lie close to the canonical ZAHB, whereas MJ 3832 has evolved towards lower $\log g$. The mean mass of all three stars is $0.50^{+0.44}_{-0.23}\,M_\odot$ and thus also in good agreement with canonical HB theory.

Looking at Fig. 2 of Dorman et al. (1997) all stars that are not radial velocity members lie more than 3′ from the cluster center. Three stars may belong to the SMC according to their radial velocities: MJ 65, MJ 94, and MJ 5381. They lie, however, farther from the SMC main sequence in m_{162}, $m_{162}-V$ than MJ 2341 and MJ 8453. Comparing the spectroscopically determined masses to those derived from evolutionary sequences would put MJ 65 ($9.5\,M_\odot$ vs. $7\,M_\odot$), MJ 94 ($7.6\,M_\odot$ vs. $4\,M_\odot$), and MJ 2341 ($5.9\,M_\odot$ vs. $5\,M_\odot$) to the SMC. MJ 2341 could be a member of the halo of the SMC, which might explain its deviating radial velocity (see, e.g., Keenan 1992, 1997 for a discussion of main-sequence B stars in the halos of galaxies). While all three stars lie quite far away from the main sequence one should keep in mind that our selection is heavily biased towards evolved (= bright) hot SMC stars.

The evolutionary status of MJ 5381 is somewhat unclear: In the $m_{162}, m_{162} - V$ diagram of Dorman et al. (1997) it lies rather isolated – being fainter than the theoretical ZAHB for NGC 362, but much cooler than the SMC main sequence. The filled H_β line of MJ 8453 reminds us of the Be stars analysed by Mazzali et al. (1996), but it is considerably cooler than those objects. A spectrum of the H_α region of this star would be necessary to decide whether it indeed shows a Be-like spectrum.

5.3 Conclusions

The spectroscopic analyses of hot HB stars in metal-rich globular clusters has presented us with some interesting results: In 47 Tuc and NGC 362 at least some hot HB stars exist – and they look like textbook examples for hot HB stars in that they perfectly fit the expectations of canonical HB evolution. Thus the interpretation by O'Connell et al. (1997) and Dorman et al. (1997) that these stars probably result from a small percentage of red giants with unusually high mass loss is very plausible. Unfortunately – from our point of view – only a small part of the hot star candidates in NGC 362 turned out to be cluster members, which emphasizes the need for spectroscopic analyses to verify the evolutionary of stars in fields with high contamination from other stellar populations. The small number of blue HB stars in 47 Tuc agrees with the findings of Rich et al. (1993) that the cluster shows no evidence for hot stars within the IUE aperture used for their spectra. Also Rich et al. (1997) find no blue HB or blue tail stars in the core of 47 Tuc. This is also consistent with the more recent result of Rose & Deng (1999) that only about 7% of the mid-UV light of 47 Tuc comes from stars hotter than about 7,500 K (most of which are probably blue stragglers). Also Kaluzny et al. (1997) find only 2 candidates for blue tail stars in 47 Tuc (the fainter of which is very similar to the SMC star MJ8279).

The spectroscopic analyses of the hot HB stars in NGC 6388 and NGC 6441 show quite contradictory results: The surface gravities of most stars would agree with canonical HB evolution, putting them in a similar place as the hot HB stars in 47 Tuc and NGC 362. However, they tend to deviate towards higher surface gravities for higher effective temperatures – the opposite behaviour of what would be expected from the colour-magnitude diagrams, that show evidence for increasing brightness with increasing temperatures. We see currently no way out of this contradiction. Analyses of more, esp. hotter stars are necessary to decide whether this contradiction persists.

Chapter 6

UV Bright Stars in Globular Clusters

As mentioned in Chapter 1 UV bright stars have originally been defined as stars brighter than the horizontal branch and bluer than red giants (Zinn et al. 1972, see also Fig. 1, p. 5), that are brighter in U than any other cluster star. It has been realized early on that UV bright stars are descendants of HB stars: They either evolve away from the horizontal branch (towards the asymptotic giant branch or towards the white dwarf domain, depending on their envelope mass) and show up as "supra-HB" stars or they have already passed the AGB and evolve from there as post-AGB stars to the white dwarf region.

Zinn (1974) verified this evolutionary scenario using spectroscopic observations of 38 optically selected UV bright stars in 8 globular clusters. He found that different HB morphologies in globular clusters with similar ages and metallicities result in different UV bright star (UVBS) populations: The presence/absence of "supra-HB" stars was found to be correlated with the presence/absence of hot HB stars in M 13, M 15, and M 3, in agreement with the theoretical expectation that hot HB stars evolving away from the HB show up as "supra-HB" stars. The more luminous UVBS's in all three globular clusters are consistent with post-AGB tracks. Also the existence of a planetary nebula and the presence of red HB stars in M 15 (which is unusual for such a metal-poor globular cluster) are linked to each other: The red HB stars in M 15 have masses of $0.8-0.9\,\mathrm{M}_\odot$, which favour the creation of planetary nebulae relative to less massive HB stars. Schönberner (1983) discusses the theoretical evolution of post-AGB stars with special emphasis on the production of planetary nebulae: The $0.546\,\mathrm{M}_\odot$ model, which leaves the AGB before thermal pulses start (post-early AGB), evolves so slowly that its age at 30,000 K exceeds the age of the oldest known planetary nebulae. Thus the lower mass limit for central stars of planetary nebulae (CSPNe) is $0.55\,\mathrm{M}_\odot$.

The search for UV bright stars in globular clusters continued and Harris et al. (1983) list 29 globular clusters with 23 (11) UVBS's bluer than $(B-V)_0 = 0$ that are definite (probable) cluster members. Thus hot UVBS's are quite common among globular clusters and will contribute significantly to the integrated UV light of the clusters. De Boer (1985) uses IUE spectra of 10 hot UVBS's in 7 globular clusters to estimate the contribution of these stars to the integrated UV light of the respective globular clusters: hot post-AGB stars contribute less than 3% to the total cluster light at 3300Å, increasing to about 15% at 1500Å and further increasing towards even shorter wavelengths. De Boer (1987) gives a compilation of luminous hot UV bright stars ($M_V < 0$, $(B-V)_0 < 0.2$) in globular clusters, listing a total of 45 stars in 36 clusters (in some of the clusters no hot UVBS's have been found). About 1/3 of the stars lie along post-AGB tracks, 2/3 are less luminous and probably supra-HB stars.

Hot stars in these evolutionary stages do not necessarily fulfil the original definition of UV bright stars given above: As stars get hotter the maximum of their flux distribution moves to ever shorter wavelengths and especially the less luminous UV bright stars evolving away from the extreme HB can be quite faint at visual and near-UV wavelengths. The lists of hot UVBS's mentioned above are thus certainly incomplete as they are based on optical searches, which favour cool and/or luminous

UV bright stars. In addition optical searches are limited by selection effects due to crowding in the cluster cores. As hot UV bright stars shine up in far-UV images of globular clusters searches in that wavelength range should be much more efficient. The Ultraviolet Imaging Telescope (UIT, Stecher et al. 1997) was therefore used to obtain ultraviolet ($\sim$ 1620 Å) images of 14 globular clusters during the two flights of the *ASTRO* observatory in 1990 and 1995. The solar-blind detectors on UIT suppress the cool star population, which allows UV-bright stars to be detected into the cluster cores, and the $40'$ field of view of UIT is large enough to image the entire population of most of the observed clusters. Thus the UIT images provide a complete census of the hot UV-bright stars in the observed clusters, which is well suited to test post-HB and post-AGB evolutionary tracks.

Such a test is especially important as hot post-AGB stars probably make a significant (although not the dominant) contribution to the UV-upturn observed in elliptical galaxies (Dorman et al. 1995, Dorman 1997, Brown et al. 1997, see also page 76). However, a large uncertainty exists in modeling the contribution of hot post-AGB stars to the integrated spectrum of an old stellar population, due to the strong dependence of the post-AGB luminosity and lifetime on the core mass, which in turn depends on when the stars leave the AGB (Charlot et al. 1996). Also the previous mass loss on the red giant branch (RGB) plays an important rôle here, since it determines the fate of a star during and after the horizontal branch stage (see above). A further uncertainty arises because theoretical post-AGB tracks have been only minimally tested for old, low-mass stars. The need for further information on these evolutionary stages is illustrated by the results of Jacoby et al.'s (1997) search for planetary nebulae (PNe) in globular clusters. In their O III imaging survey of 133 globular clusters they found only four planetary nebulae, two of which were previously known (K648 in M 15 and IRAS 18333-2357 in M 22). They expected to find 16 planetary nebulae in their sample, on the basis of the planetary nebula luminosity function for metal-poor populations. The origin of this discrepancy is not yet understood, but we mention two possible contributing factors. First, the O III search of Jacoby et al. may have missed some old, faint planetary nebulae. Second, Jacoby et al. derive the number of expected PNe from the total cluster luminosity, assuming that all stars in a globular cluster will eventually go through the AGB phase. But in a cluster such as NGC 6752 about 30% of the HB population consist of EHB stars (with $T_{\rm eff} > 20{,}000$ K), which are predicted to evolve into white dwarfs without ever passing through the thermally pulsing AGB phase. While globular clusters with a populous EHB are expected to be deficient in post-AGB stars, they should show a substantial population of less luminous ($1.8 < \log \frac{L}{L_\odot} < 3$) UV-bright stars, which can be either post-EHB stars or post-early AGB stars, neither of which would produce a planetary nebula. The population of post-EHB stars is expected to be about 15–20 % of the population of EHB stars (Dorman et al. 1993). The post-early AGB population arises from hot HB stars with sufficient envelope mass to return to the AGB, but which peel off the AGB prior to the thermally pulsing phase (Dorman et al. 1993). The exact fraction of stars which follow such evolution will depend on the poorly known mass loss rates during the HB and early-AGB phases.

All this emphasizes the need for spectroscopic analyses of hot UV bright stars to compare their parameters to evolutionary calculations. Most analyses so far, however, have been limited to the use of IUE spectra. While IUE spectra allow a good determination of $T_{\rm eff}$ for hot stars they are not very suitable to determine $\log g$ (see Cacciari et al. 1995). We found analyses that also used hydrogen lines (Ly$_\alpha$ or Balmer lines, line profile fits or equivalent widths) only for seven hot UV bright stars (in some cases only the most recent analysis is given): M22 II-81 (Glaspey et al. 1985); NGC6712-C49 (Remillard et al. 1980, only lower limit for $T_{\rm eff}$); NGC 6397 ROB162 (Heber & Kudritzki 1986); NGC 1851 UV5, M 3 vZ1128 (Dixon et al. 1994); 47 Tuc BS (Dixon et al. 1995); M13 Barnard 29 (Conlon et al. 1994). We therefore began a programme to obtain spectra of all the UV-bright stars found on the UIT images, in order to derive effective temperatures and gravities for the complete sample, for comparison with evolutionary tracks. Several of the more luminous UV bright stars found on the UIT images, such as ROB 162 in NGC 6397, Barnard 29 in M 13, and vZ 1128 in M 3, were previously known and are well-studied (see above). Other UIT stars are too close to the cluster

Table 21. Coordinates, photometric data and observing parameters for the UV bright stars

Cluster	Star	α_{2000}	δ_{2000}	V	$B-V$	slit orientation	seeing [$''$]
NGC 2808	C2946[1]	$09^{\rm h}12^{\rm m}22\overset{\rm s}{.}36$	$-64^\circ52'37''3$	$17\overset{\rm m}{.}63$	$+0\overset{\rm m}{.}09$	EW/NS	1.0 – 1.9
	C2947[1]	$09^{\rm h}12^{\rm m}22\overset{\rm s}{.}86$	$-64^\circ52'36''7$	$17\overset{\rm m}{.}10$	$+0\overset{\rm m}{.}21$	EW/NS	1.0 – 1.9
	C4594[1]	$09^{\rm h}12^{\rm m}01\overset{\rm s}{.}98$	$-64^\circ47'35''1$	$16\overset{\rm m}{.}36$	$+0\overset{\rm m}{.}03$	NS	1.6 – 1.9
NGC 6121	Y453[2]	$16^{\rm h}23^{\rm m}22\overset{\rm s}{.}25$	$-26^\circ28'02''4$	$15\overset{\rm m}{.}86$	$+0\overset{\rm m}{.}00$	NS	1.0 – 1.4
NGC 6723	III-60[3]	$18^{\rm h}59^{\rm m}29\overset{\rm s}{.}0$	$-36^\circ40'49''0$	$15\overset{\rm m}{.}61$	$-0\overset{\rm m}{.}25$	NS	2.6 – 3.9
	IV-9[3]	$18^{\rm h}59^{\rm m}24\overset{\rm s}{.}1$	$-36^\circ37'56''0$	$14\overset{\rm m}{.}64$[4]	$-0\overset{\rm m}{.}17$[4]	EW	1.5 – 1.6
NGC 6752	B2004[5]	$19^{\rm h}11^{\rm m}04\overset{\rm s}{.}9$	$-59^\circ57'47''0$	$16\overset{\rm m}{.}42$	$-0\overset{\rm m}{.}31$	EW/NS	1.2 – 1.7

[1] Ferraro et al. (1990) (This photometry has been adjusted $0\overset{\rm m}{.}1$ fainter, as reported by Sosin et al., 1997a)

[2] Cudworth & Rees (1990)

[3] Menzies (1974)

[4] L.K. Fullton (priv. comm.)

[5] Buonanno et al. (1986)

cores for ground-based spectroscopy, and have been observed with STIS onboard HST (GO7436, PI Landsman). Here we report on spectroscopy of those UIT UV-bright stars accessible for ground-based observations from the southern hemisphere.

6.1 Observations and data reduction

In May 1996 we took medium resolution spectra of UV bright stars in southern globular clusters using EFOSC2 at the 2.2m MPI/ESO telescope (Table 21). We used grism #3 (100 Å/mm, 3800 – 5000 Å) and a slit width of $1''$, resulting in a resolution of 6.7 Å. The instrument was equipped with a Thompson CCD (1024×1024 pixels, $[19\mu{\rm m}]^2$ pixels, gain 2.1 e^-/count, read-out-noise 4.3 e^-). For calibration purposes we always observed 10 bias frames each night and 5-10 flat-fields with a mean exposure level of about 10,000 counts each. For observations longer than 30 minutes we took wavelength calibration frames before and after the object's observation. Since the Ar light is rather faint, we took HeAr frames at the beginning of the night and only He during the night. The seeing values and slit orientations are listed in Table 21.

We averaged the bias frames over all nights of the run, as they showed no deviations above the 1% level and corrected for bias as described in Sect. 3.2.1. We did not correct for dark current, which was less than 3 counts/hr/pixel and showed no discernible structure. The flat fields were averaged separately for each night and normalized as described in Sect. 3.3.1 for the EFOSC1 data. The flat fields showed night-to-night variations of less than 1% between the first and second night and again between the third and fourth night. We therefore averaged the flat-fields of the first and second night and those of the third and fourth night.

For the wavelength calibration we used a 3rd order polynomial to fit the dispersion relation for the HeAr frames. We used 15 lines, avoiding blended lines. The fits then yielded mean residuals of less than 0.2 Å. From the He frames obtained during the night we derived offsets relative to the HeAr frames by cross correlating the spectra, which were then used to adjust the zero-points of the dispersion relations.

The science spectra were rebinned, sky subtracted (using a constant to fit the spatial distribution of the sky background), extracted and corrected for atmospheric extinction as described in Sect. 3.2.1. The normalized and velocity-corrected spectra are plotted in Fig. 38.

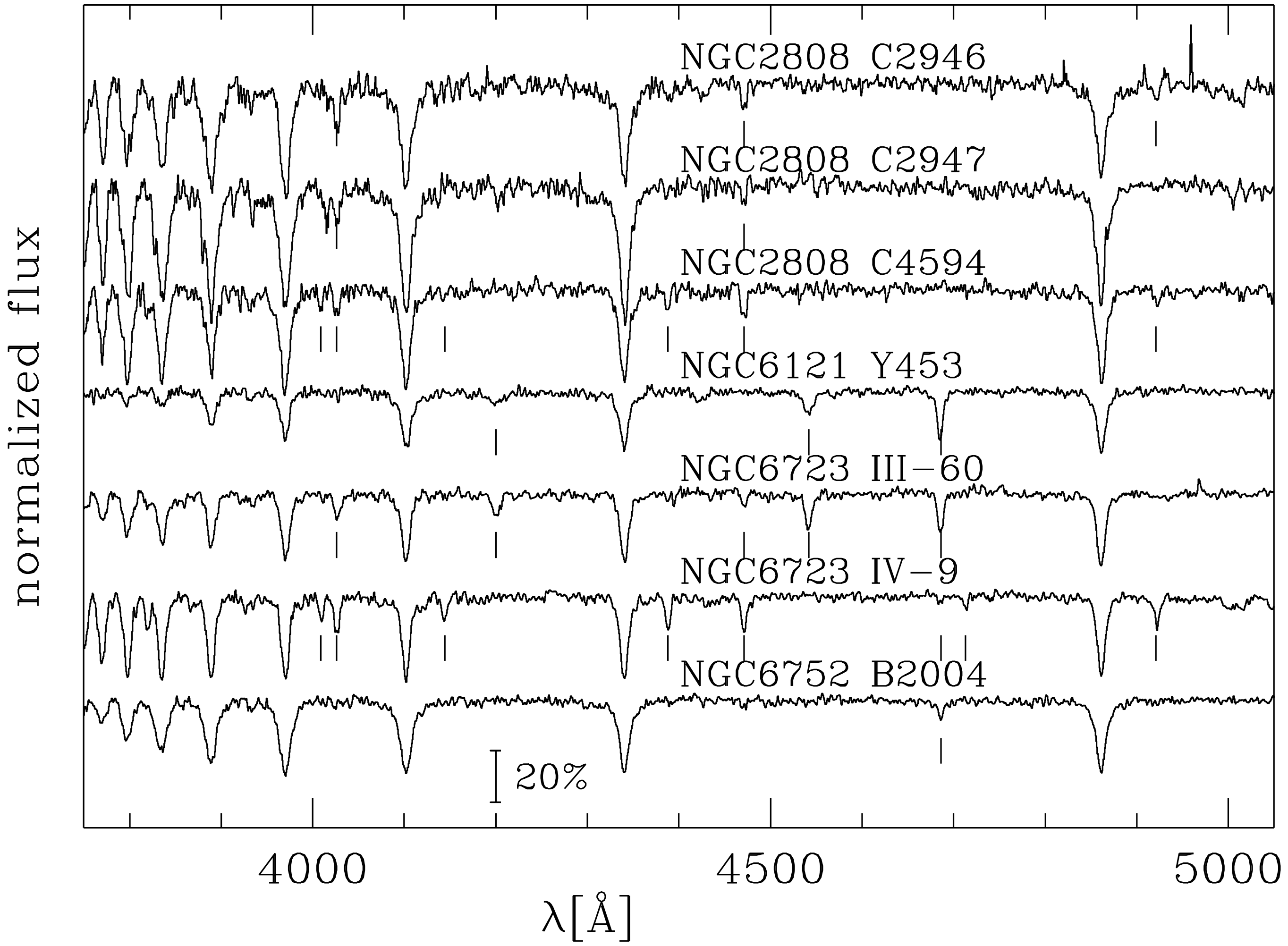

Fig. 38. The normalized spectra of the UV bright stars. The part shortward of 3900 Å was normalized by taking the highest flux point as continuum value. Lines of He I and He II are marked.

6.2 Atmospheric Parameters and Masses

To derive effective temperatures, surface gravities and helium abundances from the line profile we proceeded as described in Sect. 4.4.2. Beforehand we corrected the spectra for radial velocity shifts, derived from the positions of the Balmer and helium lines. The resulting heliocentric velocities are listed in Table 22, together with the physical parameters of the stars. The error of the velocities (as estimated from the scatter of the velocities derived from individual lines) is about 40 km/s. We obtained radial velocities for the clusters from the tabulation of Harris (1996), as Pryor & Meylan (1993) do not give radial velocities for NGC 2808 and NGC 6723.

6.2.1 Very hot UV bright stars

Those stars which show – besides Balmer lines – only He II lines in their spectra are classified as sdO stars (Y453 in NGC 6121 and B2004 in NGC 6752). III-60 in NGC 6723 shows He II and He I lines and is therefore classified as sdOB star. To analyse these stars correctly it is necessary to take non-LTE effects into account (Napiwotzki 1997). R. Napiwotzki therefore calculated NLTE model atmospheres with the code developed by Werner (1986). The basic assumptions are those of static, plane-parallel atmospheres in hydrostatic and radiative equilibrium. In contrast to the LTE atmospheres used to

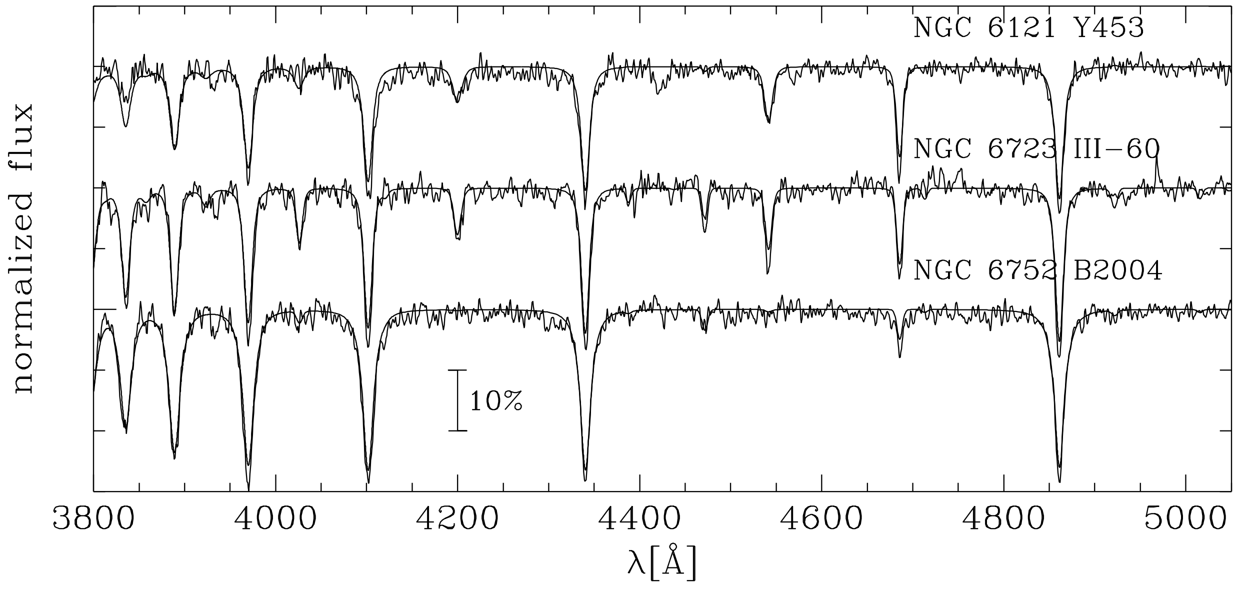

Fig. 39. The NLTE model atmosphere fits for the sdO and sdOB stars (see text for details).

analyse the cooler programme stars, the assumption of local thermal equilibrium (LTE) is relaxed and the detailed statistical equilibrium is solves instead. The accelerated lambda iteration (ALI) method is used to solve the non-linear system of equations as described in Werner (1986).

To keep the computational effort within reasonable limits the influence of heavy elements is neglected and a mixture of hydrogen and helium only is assumed. Elaborate hydrogen and helium model atoms were used for this purpose and pressure dissolution of the higher levels is included according the Hummer & Mihalas (1988) occupation probability formalism. Details are given in Napiwotzki (1997). Napiwotzki's NLTE model grid covers the temperature range $27,000 < T_{\rm eff} < 70,000$ K (stepsize increasing with $T_{\rm eff}$ from 2000 K to 5000 K) and gravity range $3.5 < \log g < 7.0$ (stepsize 0.25 dex) with the helium abundance varying from $\log\frac{N_{He}}{N_H} = -3.0$ to $+0.5$ in 0.5 dex steps. The fits for the parameters given in Table 22 are shown in Fig. 39.

6.2.2 Cooler UV bright stars

The remaining stars showed only Balmer and He I lines in their spectra. For these stars LTE model atmospheres are sufficient to derive physical parameters (Napiwotzki 1997). Using ATLAS9 and LINFOR we computed a grid of theoretical spectra covering the range 10,000 …27,500 K in $T_{\rm eff}$, 2.5 …5.0 in $\log g$ and −2.0 …−0.3 in $\log\frac{N_{He}}{N_H}$ at metallicities of −2 and −1.

We fitted the Balmer lines from H_β to H_{12} (excluding H_ϵ because of the interstellar Ca II H line) and (if present) the He I lines λλ 4026 Å, 4388 Å, 4472 Å, 4922 Å, and 5016 Å. Fitting the spectra of the three stars in NGC 2808 and IV-9 in NGC 6723 with models for both metallicities resulted in temperature differences of about 500 K (the temperature being higher for the lower metallicity). The surface gravities and helium abundances were not affected. We decided to keep the values determined for a metallicity of −1.0, since this value is closer to the actual metallicities of these two clusters. The results of the spectroscopic analyses are given in Table 22.

6.2.3 Luminosities and masses

To compute the luminosities, we obtained the cluster distances and reddenings from the May 1997 tabulation of Harris (1996, except for M 4, see below), which was also used for the radial velocities.

Table 22. Atmospheric parameters, heliocentric radial velocities, masses, and luminosities of the UV bright stars. The metallicities and radial velocities for the clusters were taken from Harris (1996, version of May 1997).

Cluster	[Fe/H]	$v_{\rm rad,hel}^{\rm cluster}$	Star	$T_{\rm eff}$	$\log g$	$\log \frac{N_{He}}{N_H}$	$v_{\rm rad,hel}$	M	status	$\log \frac{L}{L_\odot}$	
		[km/s]		[K]	[cm/s^2]		[km/s]	[M$_\odot$]		UV	opt.
NGC 2808	−1.37	+94	C2946	22700	4.48	−1.72	+93	0.46	pEHB		+1.99
			C2947	15100	3.82	−1.21	+134	0.32	pEHB		+1.78
			C4594	22700	4.06	−1.57	+89	0.55	pEHB	+2.44	+2.41
NGC 6121	−1.20	+70	Y453	58800	5.15	−0.98	+31	0.16	pEAGB	+2.61	+2.54
NGC 6723	−1.12	−95	III-60	40600	4.46	−1.03	−109	0.49	pEAGB	+2.92	+3.06
			IV-9	20600	3.34	−0.83	−52	0.29	pEAGB	+2.82	+2.79
NGC 6752	−1.55	−25	B2004	37000	5.25	−2.39	0	0.32	pEHB	+1.94	+1.94

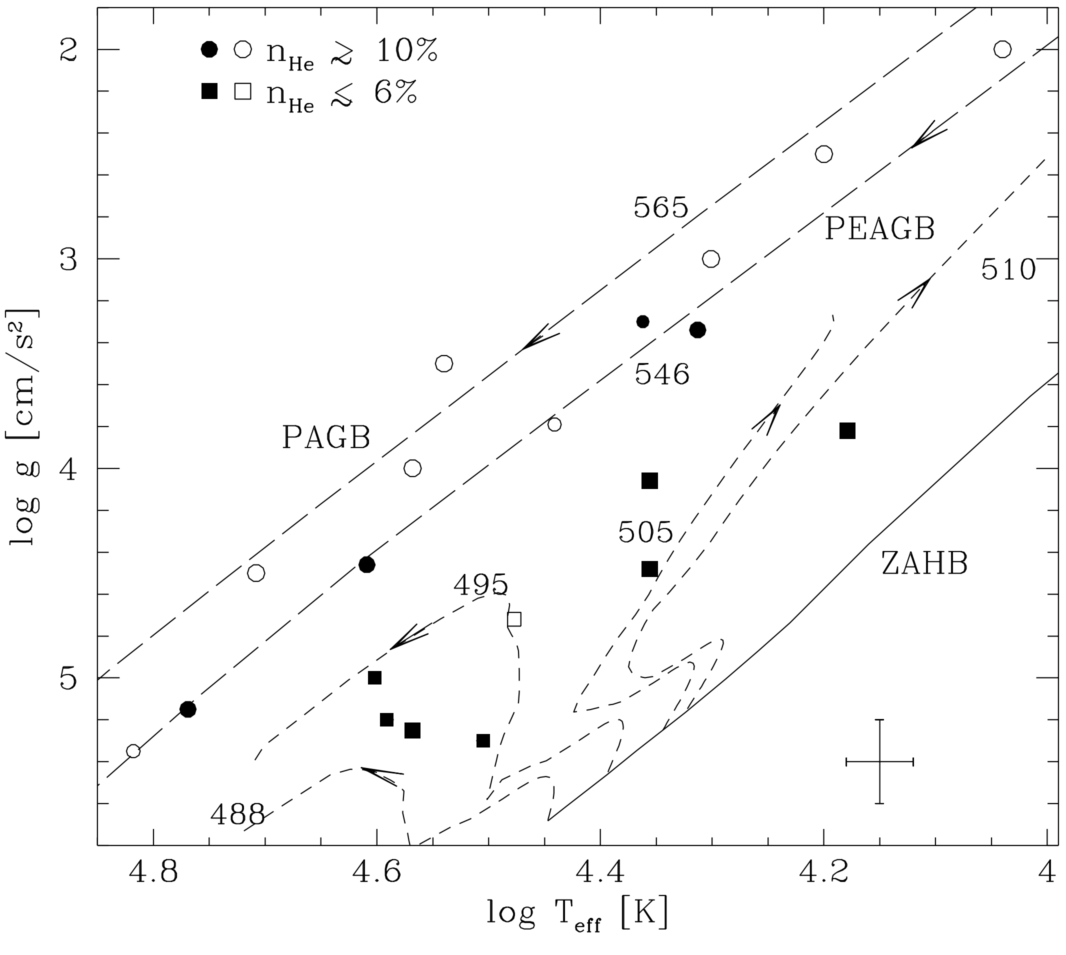

Fig. 40. The atmospheric parameters of hot UV bright stars compared to evolutionary tracks. The solid resp. short-dashed lines mark the ZAHB resp. post-HB evolutionary tracks for [Fe/H] = −1.48 (labeled with the total mass of the stars in units of 10^{-3} M$_\odot$, Dorman et al. 1993). The dashed lines give post-AGB (0.565 M$_\odot$) and post-early AGB (0.546 M$_\odot$) tracks from Schönberner (1983), also labeled with the mass of the stars in units of 10^{-3} M$_\odot$. The large filled symbols are from the analysis presented here, the small filled symbols are taken from Sect. 3.3 and Chapter 7. The large open symbols are taken from the literature (Conlon et al. 1994, Dixon et al. 1994, 1995, Glaspey et al. 1985, Heber & Kudritzki 1986, Heber et al. 1993). The small open symbols refer to preliminary results from STIS spectra of UVBS's (Landsman, priv. comm.).

The values of $(m-M)_V$, which enter into the mass and luminosity determination, differ little between Harris (1996) and Djorgovski (1993) for NGC 2808 (15.55 vs. 15.56), M 4 (12.78 vs. 12.75), and NGC 6723 (14.82 vs. 14.79). NGC 6752 shows the largest difference with 13.08 vs. 13.24, which would increase the resulting mass and luminosity by 16% if Djorgovski's values were used. The distance and reddening toward M 4 (d = 1.73 kpc, $E_{B-V} = 0.35$) is taken from the HST study of Richer et al. (1997). We also use the nonstandard value of 3.8 for R_V $[=\mathrm{A}_V/E_{B-V}]$ toward M 4, as suggested recently by several authors (Peterson et al. 1995a, Richer et al. 1997), along with the ISM parameterization of Cardelli et al. (1989).

Luminosities were determined by first using the distance and reddening to convert the V or UIT magnitude to an absolute magnitude, and then applying a bolometric correction using the $T_{\rm eff}$ derived from the model atmosphere fit. Because these hot stars have large bolometric corrections, the luminosities derived using the V magnitude are very sensitive to the value of $T_{\rm eff}$ (Δ log $L\sim$ 3Δlog$T_{\rm eff}$). The UIT magnitude has a much smaller bolometric correction, but typically has poorer photometric precision, and is more sensitive to reddening. Therefore, we have computed luminosities using both methods. As can be seen from Table 22 both values agree rather well, which supports the reliability of our analysis. The uncertainty in the derived luminosities ranges from 0.12 dex for the cooler stars, to 0.16 dex to NGC 6121-Y453, assuming uncertainties of $0^{\rm m}.1$ in V, $0^{\rm m}.15$ in the UIT flux, $0^{\rm m}.02$ in E_{B-V}, 0.035 dex in $T_{\rm eff}$, and 10% in the cluster distances.

Knowing effective temperatures, surface gravities and absolute magnitudes we can derive the masses of the stars as described in Sect. 3.2.5. Assuming errors of $0^{\rm m}.1$ and $0^{\rm m}.13$ in the observed and theoretical V magnitudes, respectively, $0^{\rm m}.1$ in $(m-M)_0$, and 0.15 dex in $\log g$ we arrive at an error for log M of 0.19 dex or about $^{+55\%}_{-35\%}$. For a detailed discussion of error sources see Sect. 3.3.5. The results are listed in Table 22.

6.3 Discussion

The derived effective temperatures and gravities of the target stars are plotted in Fig. 40, along with ZAHB and post-HB evolutionary tracks for [Fe/H] = −1.48 from Dorman et al. (1993), and post-AGB (0.565 $M_\odot$) and post-early AGB (0.546 $M_\odot$) tracks from Schönberner (1983). The stars NGC 6121-Y453, NGC 6723-III60, and NGC 6723-IV9 appear to fit the post-early AGB track, while the remaining four targets are consistent with post-EHB evolutionary tracks. In agreement with this scenario, the three post-early AGB stars have approximately solar helium abundances, while the post-EHB stars have subsolar helium abundances. The latter stars are direct descendants of EHB stars, which are known to show helium deficiencies (see Sects. 3.3.4), most likely due to diffusion processes. The post-early AGB stars, on the other hand, have evolved off the AGB, where the convective atmosphere is expected to eliminate any previous abundance anomalies caused by diffusion.

As expected, the two clusters with a populous EHB (NGC 2808 and NGC 6752) have post-EHB stars but no post-AGB stars. The clusters NGC 6723 and M 4, on the other hand, do not have an EHB population, although they do have stars blueward of the RR Lyrae gap (which are potential progenitors of post-early AGB stars). The lack of true post-AGB stars may be understood from the different lifetimes: The lifetime of Schönberner's post-early AGB track is about 10 times longer than his lowest mass post-AGB track. Thus, even if only a small fraction of stars follow post-early AGB tracks, those stars may be more numerous than true post-AGB stars. Due to their relatively long lifetime, post-early AGB stars are unlikely to be observed as central stars of planetary nebulae (CSPNe) since any nebulosity is probably dispersed before the central star is hot enough to ionize it. The predominance of post-early AGB stars is also consistent with the suggestion that the observed mass loss rates along the AGB may be higher than suggested by the Reimers mass-loss formula. Iben (1991) noted that low-mass stars may lose their envelopes and evolve blueward before thermal pulsing starts. Such stars correspond to the post-early AGB stars that we find. Additional detail on the individual stars is given below:

NGC 2808

All three stars in NGC 2808 analysed here are likely post-EHB stars. The best post-AGB candidate star on the UIT image of NGC 2808 is very close to the center and has recently been observed with STIS. A preliminary analysis yields $T_{\rm eff}$ = 27,600 K, $\log g$ = 3.8, and $\log \frac{N_{He}}{N_H} = -0.8$, which puts the star on a post-early AGB track in Fig. 40. Although C2946 and C2947 could be separated in the long-slit optical spectra, they are too close together to estimate individual UV fluxes from the UIT image, and thus there is no UV luminosity determination in Table 22. Due to the well-populated EHB of NGC 2808 (Sosin et al. 1997a) a large number of post-EHB stars are expected.

From their three-colour WFPC2 photometry of NGC 2808, Sosin et al. (1997a) find a larger distance modulus [$(\rm m\text{-}M)_0 = 15.25 - 15.40$] and lower reddening [$E_{B-V} = 0^{\rm m}\!.09 - 0^{\rm m}\!.16$] than the values listed by Djorgovski (1993; 14.82, $0^{\rm m}\!.24$) and Harris (1996; 14.84, $0^{\rm m}\!.23$). The use of the distance and reddening of Sosin et al. would yield masses about 20% larger, and luminosities about 0.05 dex larger than the values given in Table 22.

NGC 6121 (M 4)

Y453 is among the hottest globular cluster stars known so far. Only M 79 UIT1 is verified to be even hotter from an analysis of optical and UV STIS spectra (Landsman, priv. comm.) which yield $T_{\rm eff}$ = 64,700 K, $\log g$ = 5.4, and $\log \frac{N_{He}}{N_H} = -1.1$. These values place M 79 UIT1 on the same post-early AGB track in Fig. 40 as M 4 Y453. Other candidates for the hottest stars in globular clusters are three central stars of planetary nebulae (IRAS 18333-2357 in M 22, Harrington & Paltoglou 1993; JaFu1 in Pal 6 and JaFu2 in NGC 6441, Jacoby et al. 1997), which however lack model atmosphere analyses of their stellar spectra. Such a high effective temperature is not unexpected, since according to the Schönberner tracks, a post-AGB star will spend most of its lifetime at temperatures greater than 30,000 K. However, as pointed out by Renzini (1985), the large bolometric corrections of such hot stars in the visible have biased the discovery of post-AGB stars in favour of cooler stars.

In the $\log T_{\rm eff}$–$\log g$ plot Y453 fits well on the 0.546 $M_\odot$ post-early AGB track of Schönberner (1983). However, our derived luminosity ($\log \frac{L}{L_\odot} = 2.6$) is considerably lower than the Schönberner track at that $T_{\rm eff}$ and $\log g$, and the derived mass of 0.16 $M_\odot$ is astrophysically implausible (even considering our large error bars). In order to obtain a mass of 0.55 $M_\odot$, the value of $\log g$ would need to be 5.68 instead of 5.15, which is too large to be accommodated by the spectral fitting. Therefore we consider below some other possible sources of error:

- ⋆ *Line Blanketing:* The use of fully line-blanketed NLTE models for the analysis of Y453 might result in a somewhat lower temperature (0.05 dex) without any changes in surface gravity (Lanz et al. 1997; Haas 1997). Such a lower temperature would increase the derived mass by about 15%.
- ⋆ *Differential Reddening:* Cudworth & Rees (1990) find a gradient in the reddening that would increase the adopted reddening for Y453 ($0^{\rm m}\!.35$) by about $0^{\rm m}\!.015$. Lyons et al. (1995) report a patchiness in the reddening toward M 4 that is at least as significant as the gradient, and find a total range of $0^{\rm m}\!.16$ in E_{B-V}. An increase by such a large amount would still lead to a mass of only 0.3 $M_\odot$. Due to the non-standard reddening law toward M 4, the reddening correction for Y453 has a rather high uncertainty in any case.
- ⋆ *Distance:* The adopted distance (1.72 kpc) to M 4 is on the low side of the range of distance determinations but is supported by both a recent astrometric measurement (Rees 1996), and HST observations of the main-sequence (Richer et al. 1997). Use of the distances given by Djorgovski (1993, 2 kpc) or Harris (1996, 2.2 kpc) would give masses of 0.22 $M_\odot$ resp. 0.26 $M_\odot$.
- ⋆ *Photometry:* The only ground-based photometry of Y453 of which we are aware is the photographic photometry of Cudworth & Rees (1990), who also derive a 99% probability of cluster membership

from its proper motion. Y453 is among the faintest stars studied by Cudworth & Rees, so the photometric precision might be poorer than their quoted $0\overset{\mathrm{m}}{.}025$ (which corresponds to an error of 2% in M).

NGC 6723

The V and $B-V$ magnitudes in Table 21 for III-60 are from Menzies (1974) and we are not aware of any other photometry of this star. The tabulated photometry for IV-9 is from L.K. Fullton (1997, priv. comm.), who also gives $U-B=-0\overset{\mathrm{m}}{.}84$. Photometry for IV-9 was also obtained by Menzies (1974; $V=14\overset{\mathrm{m}}{.}86$, $B-V=-0\overset{\mathrm{m}}{.}25$), and Martins & Fraquelli (1987; $V=14\overset{\mathrm{m}}{.}69$, $B-V=-0\overset{\mathrm{m}}{.}142$). III-60 and IV-9 fit well on the 0.546 $M_\odot$ post-early AGB track (see above) of Schönberner, and also have luminosities ($\log\frac{L}{L_\odot}\sim 3.0$) consistent with being post-early AGB stars.

The spectrum of IV-9, however, was difficult to fit with any single model. As can be seen from Fig. 38 there is an absorption feature blueward of the He I line at 4713 Å, which matches the He II absorption line at 4686 Å in wavelength. The He II line strength and the Balmer line profiles can be reproduced by a model with $T_{\rm eff}=30{,}000$ K, $\log g=4.08$, and $\log\frac{N_{He}}{N_H}=-0.89$. However, this model is inconsistent with both the size of the Balmer jump and with the photometric indices (optical and UV) of this star. The photometric data indicate a temperature of 20,000 – 21,000 K instead. Excluding the absorption feature at 4686 Å from the fit results in a temperature of 20,700 K and a $\log g$ value of 3.34, in good agreement with the photometric temperature. The detection of metal lines (such as the O II absorption lines in BD+33°2642 discussed by Napiwotzki et al. 1994) could help to decide between the two temperatures. Simulations with theoretical spectra, however, show that due to the low resolution of our data we cannot expect to see any metal lines. Any decision will therefore have to await better data.

NGC 6752

B2004 was one of only four post-EHB candidate stars present in the UIT-optical colour-magnitude diagram of NGC 6752 reported by Landsman et al. (1996), and the position of B2004 in the $\log T_{\rm eff}$–$\log g$ plot (Fig. 40) is consistent with post-EHB tracks. Landsman et al. estimated $T_{\rm eff}=45{,}000$ K and $\log L=2.12$ for B2004 on the basis of IUE spectrophotometry. However, the IUE photometry of B2004 had large uncertainties due to the presence of the nearby ($2\overset{\prime\prime}{.}5$ distant) blue HB star B1995, and the $T_{\rm eff}$ (37,000 K) and luminosity ($\log\frac{L}{L_\odot}=1.94$) of B2004 derived here should be more accurate. Spectroscopic analyses of the other three post-EHB candidate stars (B852, B1754, and B4380) in NGC 6752 were presented in Sect. 3.3.2. The fifth UV bright star detected by UIT lies very close to the core (and therefore has no optical photometry) and has been observed with STIS recently. A preliminary analysis yields $T_{\rm eff}=30{,}000$ K, $\log g=4.7$, and $\log\frac{N_{He}}{N_H}=-1.9$, thus putting it on a post-EHB track in Fig. 40. The four previously known post-EHB stars in NGC 6752 occupy a fairly narrow range in temperature ($4.5<\log T_{\rm eff}<4.6$) and luminosity ($1.94<\log\frac{L}{L_\odot}<2.12$), and are separated by a large luminosity gap (0.5 dex) from stars on the populous EHB. As discussed by Landsman et al. (1996) these two characteristics would support the helium-mixed HB models of Sweigart (1997a, 1997b, see Sect. 4.1). A more definitive test of EHB evolutionary tracks will require a larger sample of post-EHB stars.

6.4 Conclusions

Among the seven UIT-selected UV-bright stars observed from the ground in four globular clusters, we find three post-early AGB stars and four post-EHB stars. The space-based STIS observations add two more post-early AGB stars and one more post-EHB star. Thus none of the stars newly discovered by UIT lies along a "true" post-AGB track, in contrast to hot UV bright stars previously known from optical searches. However, as mentioned in the beginning of this chapter, optical searches for hot UV bright stars will be biased towards the more luminous ones due to the large bolometric corrections for hot stars. The analysis of optically selected UV bright stars thus gives a wrong impression of the importance of the various evolutionary phases that contribute to the UV flux of old stellar populations.

The large number of post-early AGB and post-EHB stars among the hot UV bright stars studied here can be understood from evolutionary time scales and the HB morphology of the globular clusters observed: NGC 6752 shows only an almost vertical blue tail, which means that there is a lack of possible progenitors for post-AGB stars. In NGC 2808 the more luminous UV bright stars could not be observed from the ground due to their proximity to the cluster center. The faint blue tail stars of this cluster, on the other hand, provide plenty of progenitors for post-EHB stars. M 4 and NGC 6723 lack blue tails – it is therefore no surprise that we do not find any post-EHB stars in these two clusters. The blue HB stars found in both clusters are potential progenitors of post-early AGB stars.

We find that post-EHB stars have sub-solar helium abundances, similar to their progenitors, which are identified with subdwarf B stars known in the field of the Milky Way, while the post-early AGB stars show more or less solar helium abundances. This difference is not unexpected, because the diffusive processes at work on the HB are counteracted by convection and mass loss on the AGB and afterwards.

The present results suggest that post-early AGB stars might be more numerous than post-AGB stars in globular clusters with a blue HB. Theoretical simulations would be useful to determine whether the relative populations of post-AGB and post-early AGB stars can be accommodated using existing post-HB evolutionary tracks. For example, in the models of Dorman et al. (1993), post-early AGB stars arise only from HB stars within a narrow temperature range near log $T_{\rm eff}\sim$ 4.25. However, any additional mass-loss processes, either on the hot HB or during the early AGB, would extend the $T_{\rm eff}$ range of the progenitors of post-early AGB stars to cooler HB stars. Such processes would also reduce the number of PN candidates and thereby reduce the discrepancy between the predicted and observed number of PNe (Jacoby et al. 1997).

Chapter 7

Abundance Patterns of UV Bright Stars in Globular Clusters

As discussed in Chapter 6 the more luminous of the hot UV bright stars in globular clusters can be identified as stars on their way from the asymptotic giant branch to the white dwarf domain. (Sweigart et al. 1974, de Boer 1987). Up to now detailed abundance analyses of post-AGB stars have been performed mainly for field stars (McCausland et al. 1992, Napiwotzki et al. 1994, Moehler & Heber 1998), for which the population membership and the original abundance patterns are difficult to establish. The summarized result of these analyses is that the abundances of N, O, and Si are roughly 1/10 of the solar values, while Fe and C are closer to 1/100 solar. These abundances have led to a debate on whether low-mass AGB stars experience a third dredge-up or not. Third dredge-up describes the mixing of α-processed material to the surface of the star, that happens on the AGB when the convective envelope reaches extremely deep into the stellar interior. McCausland et al. (1992) argue that a comparison of the elemental abundances of field post-AGB stars to the upper limits for the iron abundance in these stars suggests enrichment of most elements heavier than oxygen (relative to iron), indicating the dredge-up of α-processed material. However, the strong C depletion argues against third dredge-up which should enhance carbon. Conlon (1994) on the other hand put more emphasis on the carbon deficiency of the hot field post-AGB stars and suggest that these stars leave the AGB before the thermal pulses start (i.e. they are post-early AGB stars). This would agree with standard stellar evolutionary theories (Renzini & Voli 1981, Vassiliadis & Wood 1993) which do not predict any dredge-up processes for the low-mass precursors of the C-poor post-AGB stars.

One should however keep in mind that cool ($T_{\rm eff}$ < 10,000 K) post-AGB stars are often C-rich and do show evidence for CNO enhancement (Luck 1993, Conlon 1994, Gonzalez & Wallerstein 1994). Also the planetary nebula Ps 1 in M 15 as well as the atmosphere of its central star K 648 are both strongly enriched in carbon when compared to the cluster carbon abundance[18] (Adams et al. 1984, Heber et al. 1993), pinpointing the dredge-up of α-processed material to the stellar surface and suggesting a possible connection between dredge-up and planetary nebula ejection (Sweigart 1998). This discrepancy may be solved by newer evolutionary calculations which are able to produce a third dredge-up also in low-mass AGB stars (Herwig et al. 1997).

Napiwotzki et al. (1994) discuss another possible explanation for the abundances of low-mass post-AGB stars: The photospheric abundances of the central star BD+33°2642 (and also of the objects analysed by McCausland et al. 1992 and Conlon 1994) can be understood as the results of gas-dust separation towards the end of the AGB phase, which leads to a depletion of certain elements. This

---

[18] A preliminary analysis of ZNG1 in M 5 also shows evidence for a third dredge-up, but no trace of a nebula (Heber & Napiwotzki 1997).

process has already been proposed by Bond (1991) for some cooler post-AGB stars with extreme metal deficiencies. Mathis & Lamers (1992) invoked two scenarios to produce these extreme iron deficiencies:

i) At the end of the AGB phase mass loss ceases rapidly and gas falls back onto the stellar surface while the dust particles are blown away by radiative pressure.
ii) The post-AGB star captured cleaned (= iron-deficient) gas from a moderately close companion during previous evolutionary stages.

A strong case for scenario (ii) was made by the detection of radial velocity variations (indicating binarity) in five (out of five investigated) extremely iron-poor post-AGB stars in the field of the Milky Way (van Winckel et al. 1995).

The single star scenario of Mathis & Lamers (1992) predicts the purified gas layer to be very thin. It is unclear if this thin purified layer can avoid mixing into the subphotospheric convection zone present in cool post-AGB stars. In any case, subsequent mass loss of the post-AGB stars should quickly (i.e. within a few hundred years) remove the purified layer. The detection of iron depletion in the low mass post-AGB star BD+33°2642 (with a post-AGB age of 6000^{+4000}_{-2000} years, Napiwotzki et al. 1994) shows that the purified gas layer must contain more mass if gas-dust separation should explain the observed abundance patterns. However, higher layer masses can only be produced if gas-dust separation is working continuously on the AGB, i.e. a large amount of gas is purified.

The hydrodynamic calculations of Bowen (1988) demonstrated that the excessively high mass loss rates observed in many AGB stars are driven by radiative pressure on dust grains forming in the extended atmospheres of these stars. In luminous (massive) AGB stars the densities in the dust formation layers are high and the coupling between gas and dust particles is very close. Thus the dust takes the gas away, too. In less luminous (low mass) AGB stars with lower mass loss rates the densities in the outer atmosphere are lower and the coupling between dust and gas is less tight, which results in considerably different drift velocities of gas and dust. Steffen et al. (1997) found velocity differences of typically a factor of two between both components in the case of low mass loss rates. Thus it seems plausible that the newly produced dust is driven away by radiative pressure, but is unable to carry away the gas component, which falls back to the stellar surface in the course of the pulsation cycle. One would therefore expect to find iron depletion preferentially in low mass post-AGB and post-early AGB stars, which – on the other hand – should not experience a third dredge-up.

A distinction between the third dredge-up and the gas-dust separation scenario is hampered by the fact that the original metallicities have to be known. Iron is one of the elements which are most sensitive to depletion. Thus the knowledge of its abundance in post-AGB or post-early AGB stars in globular clusters and a comparison with the known cluster metallicity should allow an unambiguous distinction between both scenarios (see also Conlon et al. 1994). Very few abundance analyses of post-AGB stars in globular clusters exist so far. Gonzalez & Wallerstein (1994) published an abundance analysis of cool post-AGB stars in ω Cen and Barnard 29 in M 13 has recently been analysed by Conlon et al. (1994) using optical high resolution spectra and by Dixon & Hurwitz (1998) using far-UV spectra:

Gonzalez & Wallerstein analyse 3 variable and 2 non-variable cool post-AGB stars in ω Cen with $5000\ K < T_{\rm eff} < 7000\ K$. Their results on CNO enrichment (seen only in the three brightest stars, which in addition show s-process enhancements) suggest that CNO enrichment seems to start between $\log L = 2.51$ and 2.74. All stars show [(Mg,Si,S,Ca,Ti)/Fe] $\geq$0.5 as usual for metal-poor stars. From the correlation between log (C+N+O) and [Fe/H] for stars in ω Cen they estimate a primordial value of [(C+N+O)/Fe] = 0.2. Relative to this primordial value the three brightest stars show CNO enhancements of $\approx$1 dex. This strong enrichment may be due (in part) to the small mass of the remaining H envelope – the same amount of polluting matter will create a larger enrichment in the thin H-envelope of a post-AGB star ($\approx$1 dex more) than in an AGB star, where it will be much more diluted. The N excess shows that the 3α-products C and O passed through an H-burning shell on their way outward (CN cycle). Very low Al abundances might indicate gas-dust separation.

Conlon et al. (1994) suggest the use of post-AGB stars in globular clusters to establish an abundance pattern and start with an abundance analysis of Barnard 29. They derive an effective temperature of 20,000 K and $\log g = 3.0$, together with solar helium abundance. These values yield a mass of $\approx 0.55\,M_\odot$ in agreement with the mass obtained from comparison to evolutionary tracks. Similar to the hot post-AGB stars in the field Barnard 29 shows strong C-depletion (upper limit of [C/H] < -1.8), N enrichment ([N/H] $= -0.75$) and [(Si,O,Mg)/H] ≈ -1.3 in agreement with the metallicity of M 13 ([Fe/H] ≈ -1.6). O, Mg, and Si show no evidence for α-processing. C depletion and N enhancement are consistent with first and second dredge-up of CN-processed material (see Sect. 4.1 and Appendix A for more details). The CNO pattern of Barnard 29 is thus consistent with that of red giants in M 13, arguing against third dredge-up. It seems that Barnard 29 left the AGB before third dredge-up occurred. This is consistent with the suggestion that the observed mass loss rates along the AGB are higher than suggested from the Reimers mass-loss formula. As mentioned before Iben (1991) noted that low-mass stars may lose their envelopes and evolve blueward before thermal pulsing starts, an idea which has been suggested by Landsman et al. (1992) to explain the origin of ROA 5701 and UIT-1 in ω Cen (see also the UV bright stars discussed in Chapter 6, esp. Fig. 40).

Unfortunately, for hot metal-poor stars iron is not accessible for a spectroscopic analysis from optical spectra due to the lack of lines in this wavelength region. Conlon et al. (1994) therefore give only an upper limit for the iron abundance of [Fe/H] < -0.8 which is insignificant for a cluster metallicity of ≈ -1.6. In the ultraviolet, however, a large number of spectral lines can be used. Thus the analysis of Dixon & Hurwitz (1998) could provide abundances for C, S, and Fe. The best fit to their high-resolution, far-UV spectrum of Barnard 29 is obtained for $T_{\rm eff} = 21{,}000$ K, $\log g = 3.0$, and [M/H] $= -2.5$. They derive abundances of [S/H] ≈ -1.9, [C/H] ≈ -2.4 and [Fe/H] ≈ -2.2 and suggest gas-dust separation as possible explanation. Abundances for He, N, O, Si are consistent with those given by Conlon et al. (1994).

In this chapter we use spectra obtained with the Goddard High Resolution Spectrograph (GHRS) of the Hubble Space Telescope to measure the iron abundance of ROA 5701 and Barnard 29.

7.1 Observations and data reduction

7.1.1 UV spectroscopy

The UV spectra of ROA 5701 and Barnard 29 were obtained with the Goddard High Resolution Spectrograph onboard the Hubble Space Telescope, using the G200M grating (1860 – 1906 Å, 0.07 Å resolution) and the large science aperture. The spectral region was chosen because the strongest Fe III absorption lines are expected there as judged from the high resolution IUE spectra of BD+33°2642 (Napiwotzki et al. 1994), which shows an optical spectrum similar to ROA 5701 and Barnard 29. The observing dates were August 3$^{\rm rd}$, 1996 for ROA 5701 and November 30$^{\rm th}$, 1996 for Barnard 29. We did not use the FP split option as we did not expect any lines strong enough to allow a correct alignment of the individual spectra by correlation.

After the standard pipeline reduction we co-added the flux of the individual spectra, which were on identical wavelength scales. The resulting spectra were converted to MIDAS bdf-format and interpolated to a step size of 0.02 Å. They were then corrected for Doppler shifts using the heliocentric radial velocities of the clusters (+232 km/sec, ω Cen; −246 km/sec, M 13) and the corrections for heliocentric velocities appropriate for the observation dates. To allow a better definition of the continuum we smoothed the spectra with a 3 pixel wide box average filter. The continuum was then defined by eye and we estimate that the error of the normalization lies between 5% and 10%.

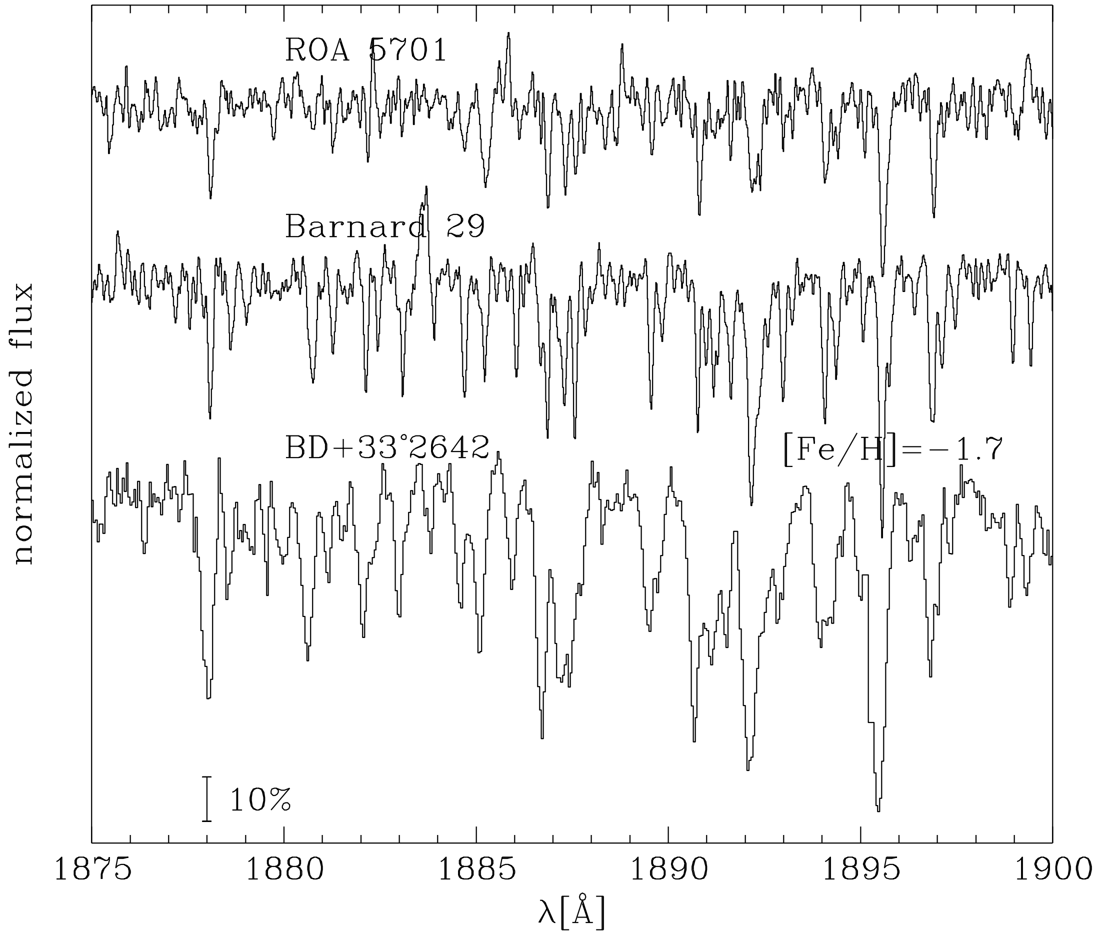

Fig. 41. The GHRS spectra of ROA 5701 and Barnard 29, compared to IUE high resolution spectra of BD+33°2642[1]. The GHRS data were smoothed by convolution with a Gaussian of 0.06 Å FWHM, which yields an effective resolution of 0.09 Å, similar to that of the IUE data (0.1 Å). We used a microturbulent velocity of 10 km/s to derive the abundance noted for BD+33°2642 from equivalent width measurements by Napiwotzki et al. (1994) .

Fig. 41 shows a section of the GHRS spectra of ROA 5701 and Barnard 29 compared to the IUE data of BD+33°2642[19], a field post-AGB star with $T_{\rm eff}$ and $\log g$ similar to ROA 5701 and Barnard 29. The iron abundance noted for BD+33°2642 in Fig. 41 was derived from equivalent width measurements (Napiwotzki et al. 1994) for a microturbulent velocity of 10 km/s (which is the value Conlon et al. 1994 derived for Barnard 29). The iron abundance of BD+33°2642 is comparable to that of red giants M 13 and ω Cen. The much weaker iron lines in the GHRS spectra therefore suggest that Barnard 29 and ROA 5701 show significant iron depletions.

7.1.2 Optical high resolution spectra

ROA 5701 was observed with the ESO CAssegrain echelle SPECtrograph (CASPEC) at the 3.6m telescope at La Silla, Chile, on May 24, 1988. The spectra were binned during read out in order to improve the S/N ratio. Reduction of the data proceeded in two steps: first the MIDAS echelle package (Ponz & Brinks 1986) was used for wavelength calibration and extraction of the echelle orders. The background correction and flat fielding were done separately using a computer program written by G.

---

[19] For this purpose the IUE spectra SWP04791, SWP37966, SWP43623, SWP45533 were calibrated with the NEWSIPS software and co-added.

Jonas (Kiel, see Heber et al. 1988). We then merged the orders of the CASPEC spectra and rebinned them to a common wavelength scale. The optical spectra have a resolution of 0.3 Å.

7.1.3 Equivalent widths

We always used the normalized spectra to measure equivalent widths. The measurement in the optical spectra was straightforward since the lines are isolated and well defined and the spectra have a good S/N. In the UV, however, the lines are more crowded and the S/N is lower. Therefore, three different methods were used: i) direct integration without any fit of the line shape using a global continuum (assuming that the overall continuum definition is more reliable than a local one due to the low S/N), ii) same as i), but for a local continuum, and iii) fitting Gaussians to the absorption line profiles (using a locally defined continuum). Method iii) could not be used for ROA 5701 because the lines were too weak.

The equivalent widths measured for a global continuum (which were used for the abundance determinations) were on average larger than those measured for a locally defined continuum. This offset leads to a difference in the mean iron abundance derived from the GHRS spectra of 0.08 dex for ROA 5701 and 0.03 dex for Barnard 29. For the CASPEC data the abundances derived for a global continuum are larger than those determined for a local continuum by 0.12 dex for O, 0.02 dex for N, and 0.14 dex for Si. As the CASPEC spectra showed small-scale continuum variations that are difficult to correct by a global continuum fit we decided to keep the abundances derived from the "local continuum" equivalent widths (in contrast to the GHRS data).

7.2 Atmospheric Parameters

Detailed analyses of optical spectra are available for Barnard 29 (Conlon et al. 1994), whereas only an estimate of the effective temperature from low resolution IUE spectra (Cacciari et al. 1984, $T_{\rm eff}$ = 24,000 K, $E_{B-V} \geq 0\overset{\rm m}{.}11$) exists for ROA 5701. Therefore we determined the photospheric parameters of ROA 5701 by analysing the optical CASPEC spectra together with optical photometry (Norris 1974) and low resolution IUE spectrophotometry (SWP07849, LWR06845).

To derive a first estimate of the temperature we dereddened the optical photometry and the IUE data, using the interstellar extinction law of Savage & Mathis (1979). The *UBV* magnitudes were converted into fluxes, using the conversion given by Heber et al. (1984). The data were then fitted with ATLAS9 (Kurucz 1992) models for [M/H] = −1.5. For a reddening of $0\overset{\rm m}{.}11$ (Norris 1974) resp. $0\overset{\rm m}{.}15$ (Djorgovski 1993) the best fits were achieved for effective temperatures of 22,000 K resp. 24,000 K. These results compare very well to those of Cacciari et al. (1984).

For the temperatures given above we fitted ATLAS9 model spectra with solar helium abundances and [M/H] = −1.5 to the Balmer lines and obtained the surface gravities from the best fit. To verify our results we also derived effective temperature, surface gravity, and helium abundances from the Balmer and He I line profiles only as described in Sect. 4.4.2. For this purpose we used the model spectra described in Sect. 6.2 ([M/H] = −1). The results of all procedures are listed in Table 23. It is clear that the agreement is rather good. For the further analysis we used the mean value of the results using IUE-based effective temperatures, i.e. an effective temperature of 23,000 K and a $\log g$ value of 3.3.

7.3 Abundance analysis

The determination of elemental abundances is interlocked with the microturbulent velocity ξ, which can be derived if a sufficient number of lines of one ion can be measured over a wide range of line strengths. In the optical O II lines are most suitable for this purpose as they are most frequent. For

Table 23. Atmospheric parameters of our programme stars.

Name	$T_{\rm eff}$ [K]	$\log g$	$\log \frac{N_{He}}{N_H}$	remarks
ROA 5701	22000	3.2	−1.00	E_{B-V}= $0^{\rm m}.11$, [M/H] = −1.5, fixed (solar) He abundance
	24000	3.4	−1.00	E_{B-V}= $0^{\rm m}.15$, [M/H] = −1.5, fixed (solar) He abundance
	24500	3.4	−0.98	Balmer and He I line profiles only, [M/H] = −1.0
Barnard 29	20000	3.0	−1.06	Conlon et al. 1994, [M/H] = −1.0

ROA 5701 we could measure equivalent widths of 22 O II lines, which yield a value of 20 km/s for ξ. Gies & Lambert (1992) note in their analysis of B-type supergiants that the high microturbulent velocities of about 20 km/s obtained from LTE analyses decrease to about 10 km/s if NLTE effects are taken into account. The microturbulent velocity of Barnard 29, ξ=10 km/s, has been determined by Conlon et al. (1994). If we exclude the blend at $\lambda\lambda$ 1892.3 Å from the line list the Fe III lines yield 10 km/s for ξ for Barnard 29. For ROA 5701 we derive a microturbulent velocity of 2–3 km/s from the measured Fe III lines (in contrast to the result from the optical O II lines). Determinations of ξ from model spectra to which noise was added show, however, that noise tends to increase the measured microturbulent velocity rather than decrease it. The low S/N of the GHRS data can thus not explain the low ξ found from the Fe III lines. We finally used the same value for ξ (10km/s) for ROA 5701 and Barnard 29, as both stars have rather similar atmospheric parameters.

Abundances have been derived using the classical curve-of-growth technique as well as a spectrum synthesis technique. In both cases we computed model atmospheres for the appropriate values of effective temperature, surface gravity, and cluster metallicity and used the LINFOR spectrum synthesis package for the further analysis. We calculated *curves of growth* for the elements of interest, from which abundances were derived. We took into account that in many cases more than one line contributed to the measured equivalent widths by treating those lines as blends in LINFOR. In addition we tried to avoid lines with significant contributions from other elements or ionization stages. In a second trial we fitted the *whole spectrum* at once. In this mode the LINFOR package tries to fit the line profiles of the metal lines using a χ^2 test by adjusting the abundance of the element(s) that are fitted. We used the same line lists as for the curve-of-growth analysis.

For the analysis of the CASPEC data of ROA 5701 we used atomic data for C II (Yan et al. 1987), N II (Becker & Butler 1989), O II (Bell et al. 1994) and Si III (Becker & Butler 1990). Table 24 lists the results for individual lines. For C II we could only derive an upper limit, assuming an equivalent width of 10 mÅ for the C II line at 4267 Å. The spectrum synthesis resulted in abundances higher than those from the classical curve-of-growth analysis by about 0.1 dex for N II, O II, and Si III (cf. Table 27). Part of this offset is due to the fact that the spectrum synthesis has to use a “global continuum” for its fit (see also page 106).

Our main aim is to determine the iron abundances of both stars from the Fe III lines in the UV. We used the atomic data given by Ekberg (1993). The measured equivalent widths and the resulting abundances for both stars are listed in Table 25. The spectrum synthesis yields iron abundances about 0.2 dex lower than those obtained from the equivalent widths.

Error estimates

The iron abundances derived for ROA 5701 and Barnard 29 from different equivalent width measurements differ by up to 0.1 dex and 0.05 dex, respectively. The effects of differences in effective temperature, surface gravity, and microturbulent velocity are given in Table 26. To check the effects of using different line lists we also derived abundances using the line lists of Kurucz (1991, priv. comm., observed lines only). The derived mean abundances differed by about 0.05 dex from those given in Table 27. The errors given in Table 27 include those of Table 26 plus 0.05 dex (to account for possible

Table 24. Equivalent widths and abundances for C II (upper limit only), N II, O II, and Si III as derived from the CASPEC spectra of ROA 5701. $\log\epsilon$ gives the number abundance of the respective element with $\log\epsilon = \log(X/H) + 12$. χ is the excitation potential of the lower level. gf is the product of statistical weight g and oscillator strength f of the line. The brackets mark blends.

Ion/ Multiplet	λ [Å]	χ [eV]	$\log gf$	W_λ [mÅ]	$\log\epsilon$
C II 6	4267.020	18.047	+0.559		
6	4267.270	18.047	+0.734	<10	<5.78
N II 12	3995.000	18.498	+0.225	38	6.79
15	4447.030[1]	20.411	+0.238	20	6.86
O II 17	3919.285	25.655	−0.247	36	8.29
10	4069.623	25.625	+0.157		
10	4069.886	25.632	+0.365	86	7.98
10	4075.862	25.658	+0.700	66	7.73
48	4089.285	28.699	+0.885	59	8.22
20	4119.216	25.842	+0.454	33	7.63
36	4189.600	28.354	−0.821		
36	4189.789	28.354	+0.723	35	7.99
59	4302.858	31.311	+0.092		
59	4303.070	31.311	−0.008		
2	4303.836	28.814	+0.660	37	8.17
2	4345.559	22.973	−0.330	36	7.80
2	4349.426	22.993	+0.085	54	7.62
2	4366.888	22.993	−0.319	38	7.82
5	4414.901	23.435	+0.211	71	7.79
5	4416.973	23.413	−0.041	54	7.86
32	4447.673[1]	28.354	−1.380		
32	4448.186[1]	28.354	+0.047	20	7.79
14	4590.972	25.655	+0.346	53	8.06
14	4595.960	25.655	−1.037		
14	4596.176	25.655	+0.196	41	8.03
1	4638.857	22.960	−0.307	41	7.90
1	4641.817	22.973	+0.084	78	7.91
1	4649.143	22.993	+0.343	112	7.93
1	4650.842	22.960	−0.331	45	7.97
1	4661.633	22.973	−0.249	61	8.08
1	4676.236	22.993	−0.359	41	7.96
35	4699.003	28.502	+0.429		
22	4699.220	26.219	+0.270	41	7.99
22	4705.350	26.242	+0.518	43	7.93
Si III 2	4552.620	19.018	+0.283	64	6.00
2	4567.820	19.018	+0.061	54	6.13
2	4574.760	19.018	−0.509	17	6.13

[1] blend of N II/O II (not used for the determination of ξ)

errors in the line lists) and 0.1 dex resp. 0.05 dex in the iron abundances derived from W_λ (to account for errors in the equivalent widths measurements).

The stars we analyse are in a temperature-gravity range where non-LTE effects start to play a rôle. Gies & Lambert (1992) and Kilian (1994) find that the non-LTE abundances of C, N, O, and Si for B-type main sequence and supergiant stars are on average about 0.1 – 0.2 dex lower than the corresponding LTE abundances. As the non-LTE corrections shift the abundances of all elements in the same direction the relative abundance trends should remain unchanged within our error bars.

Table 25. Equivalent widths and abundances as derived from the GHRS spectra of Barnard 29 and ROA 5701. We list the equivalent widths that were measured for a global continuum. Multiplet numbers are from Ekberg (1993). The brackets mark blends. See Table 24 for definitions of χ, $\log gf$, and $\log \epsilon$.

Ion/ Multiplet	λ [Å]	χ [eV]	$\log gf$	ROA 5701		Barnard 29	
				W_λ [mÅ]	$\log \epsilon$	W_λ [mÅ]	$\log \epsilon$
Fe III UV52	1866.315	7.869	−0.249	29	4.88		
UV52	1866.570	7.870	−0.770	25	5.33		
UV52	1869.837	7.870	−2.134				
	1869.844	7.870	−2.805				
	1869.927	11.578	+0.123			62	5.93
	1870.592	8.245	−1.665			6	5.58
	1871.336	10.332	−0.646				
	1871.446	10.332	−0.862	17	5.47		
	1872.211	11.144	+0.243	21	5.09	54	5.64
	1873.549	10.317	−0.737			14	5.64
UV62	1878.003	8.639	+0.312	50	4.80	54	4.87
	1878.547	8.238	−0.991			27	5.63
	1881.194	11.118	+0.225	15	4.94	30	5.27
UV62	1882.050	8.639	−0.082				
	1882.064	8.650	−1.339			39	5.03
UV62	1884.597	8.656	−0.257	26	5.05	60	5.51
UV96	1885.965	10.308	−0.083	12	4.94	34	5.45
	1886.609	8.656	−0.316				
UV52	1886.765	7.867	+0.336				
	1886.783	11.144	−1.870	34	4.31	81	4.78
UV53	1887.212	7.867	−0.068	37	4.82	69	5.21
	1887.472	7.870	−0.464				
UV52	1887.479	7.870	−1.541				
	1887.492	7.869	−0.286	25	4.61	53	4.99
	1887.751	14.170	+0.484				
	1887.752	7.870	−1.204	13	5.11	16	5.19
UV53	1889.463	7.870	−0.302				
	1889.471	7.870	−0.889	12	4.44	37	4.92
	1889.742	10.765	−0.141			22	5.39
UV52	1890.678	7.861	+0.504	40	4.29		
UV53	1890.882	7.870	−0.805				
	1890.882	10.368	−2.528			28	5.36
UV52	1892.151	7.867	−0.355				
UV96	1892.253	10.308	+0.140				
	1892.348	10.994	−0.409			197	6.08
	1892.882	7.869	−1.205				
UV96	1892.896	10.308	−0.047				
	1893.111	13.127	+0.116	28	5.10	42	5.27
	1893.309	10.368	−0.387			12	5.21
UV83	1893.988	9.899	+0.481	36	4.80	46	4.95
	1896.334	14.174	+0.279			13	5.63
	1896.741	10.225	−0.059				
UV83	1896.821	9.897	+0.514	51	4.84	105	5.44
	1897.385	9.899	−0.677			20	5.63
	1901.258	10.305	−0.691				
	1901.383	10.225	−0.517				
	1901.394	10.211	−0.073				
UV96	1901.549	10.368	−1.813	31	5.14	95	5.83

Table 25. cont'd Equivalent widths and abundances as derived from the GHRS spectra of Barnard 29 and ROA 5701. We list the equivalent widths that were measured for a global continuum. Multiplet numbers are from Ekberg (1993). See Table 24 for definitions of χ, $\log gf$, and $\log \epsilon$.

Ion/ Multiplet	λ [Å]	χ [eV]	$\log gf$	ROA 5701 W_λ [mÅ]	ROA 5701 $\log \epsilon$	Barnard 29 W_λ [mÅ]	Barnard 29 $\log \epsilon$
Fe III UV94	1902.098	10.308	+0.118			36	5.28
	1902.411	10.215	−0.051			44	5.54
	1902.910	10.895	+0.243			30	5.20
	1903.177	10.308	−1.003				
	1903.263	9.153	−0.547			49	5.70
	1904.265	13.581	+0.224				
	1904.384	13.127	−0.235				
	1904.412	8.656	−0.274			58	5.37

Table 26. Error estimates for abundances analysis results

Star	Ion	$\Delta \log \epsilon$ from W_λ			$\Delta \log \epsilon$ from spectrum synthesis		
		$\Delta T_{\rm eff} = \pm 1000$ K	$\Delta \log g = \pm 0.1$ dex	$\Delta \xi = \pm 5$ km/s	$\Delta T_{\rm eff} = \pm 1000$ K	$\Delta \log g = \pm 0.1$ dex	$\Delta \xi = \pm 5$ km/s
ROA 5701	C II	±0.08	∓0.03	∓0.01	±0.03	∓0.03	±0.05
	N II	±0.00	∓0.00	∓0.01	±0.02	∓0.01	∓0.01
	O II	∓0.12	±0.04	∓0.04	∓0.13	±0.01	∓0.02
	Si III	∓0.06	±0.03	∓0.02	∓0.07	±0.03	±0.01
	Fe III	±0.03	±0.02	∓0.01	∓0.04	±0.04	±0.02
Barnard 29	Fe III	∓0.04	±0.04	∓0.11	∓0.05	±0.04	∓0.08

Prompted by a remark from Dr. P. Dufton we investigated whether the low iron abundances that we derived from UV lines of Fe III might be due to systematic errors. For this check we obtained 6 high resolution UV spectra of the normal main sequence B star γ Peg from the IUE final archive, which we coadded in order to increase the S/N. As line blending and continuum placement lists pose much more severe problems for solar-metallicity B stars than for our (metal-poor) programme stars, we synthesized the spectral range in question using the entire Kurucz line list and varied the iron abundance. From the IUE data we get an iron abundance of $\log \epsilon_{Fe} = 6.95$[20]. This is at variance with the near solar value ($\log \epsilon_{Fe} = 7.56$, Pintado & Adelman 1993) derived from the analysis of optical Fe III lines for this star, which we confirm from ESO CASPEC spectra. A similar discrepancy has been found by Grigsby et al. (1996) for the normal main sequence B star ι Her, for which the iron abundance from ultraviolet Fe II and Fe III lines was found to be more than 0.47 dex below the near solar value obtained from the analysis of optical lines. Grigsby et al. argue that the lower iron abundance derived from the UV lines is the correct one, as the abundances for both ionization stages agree, whereas the previous optical analyses found differences between the two ionization stages of up to 1.0 dex.

In summary the UV spectral analysis of normal B stars is currently so severely hampered by line crowding and continuum definition problems that it is impossible to draw any clear cut conclusions on systematic abundance offsets for our metal-poor programme stars, which are much less affected by these problems. We therefore do not apply any offsets to the iron abundances derived from the GHRS spectra.

---

[20] An error of 5% in the continuum definition results in an error of 0.2 dex in the iron abundance.

Table 27. Abundances derived for ROA 5701 and Barnard 29.

ROA 5701					Barnard 29					remarks
$\log\epsilon_C$	$\log\epsilon_N$	$\log\epsilon_O$	$\log\epsilon_{Si}$	$\log\epsilon_{Fe}$	$\log\epsilon_C$	$\log\epsilon_N$	$\log\epsilon_O$	$\log\epsilon_{Si}$	$\log\epsilon_{Fe}$	
<5.78	6.83	7.93	6.08	4.89		7.30^1	7.60^1	6.30^1	5.38	W_λ
±0.10	±0.05	±0.14	±0.09	±0.12		$\pm0.11^1$	$\pm0.20^1$	$\pm0.27^1$	±0.14	
≤5.92	6.89	8.00	6.20	4.68	6.15^2				5.21	spectrum synthesis
±0.08	±0.06	±0.14	±0.09	±0.08	$\pm0.10^2$				±0.10	
8.58	8.05	8.93	7.55	7.50	8.58	8.05	8.93	7.55	7.50	solar values
[C/H]	[N/H]	[O/H]	[Si/H]	[Fe/H]	[C/H]	[N/H]	[O/H]	[Si/H]	[Fe/H]	
< −2.80	−1.22	−1.00	−1.47	−2.61		-0.75^1	-1.33^1	-1.25^1	−2.12	W_λ
≤ −2.66	−1.16	−0.93	−1.35	−2.82	-2.33^2				−2.29	spectrum synthesis

[1] Conlon et al. (1994)

[2] Dixon & Hurwitz (1998)

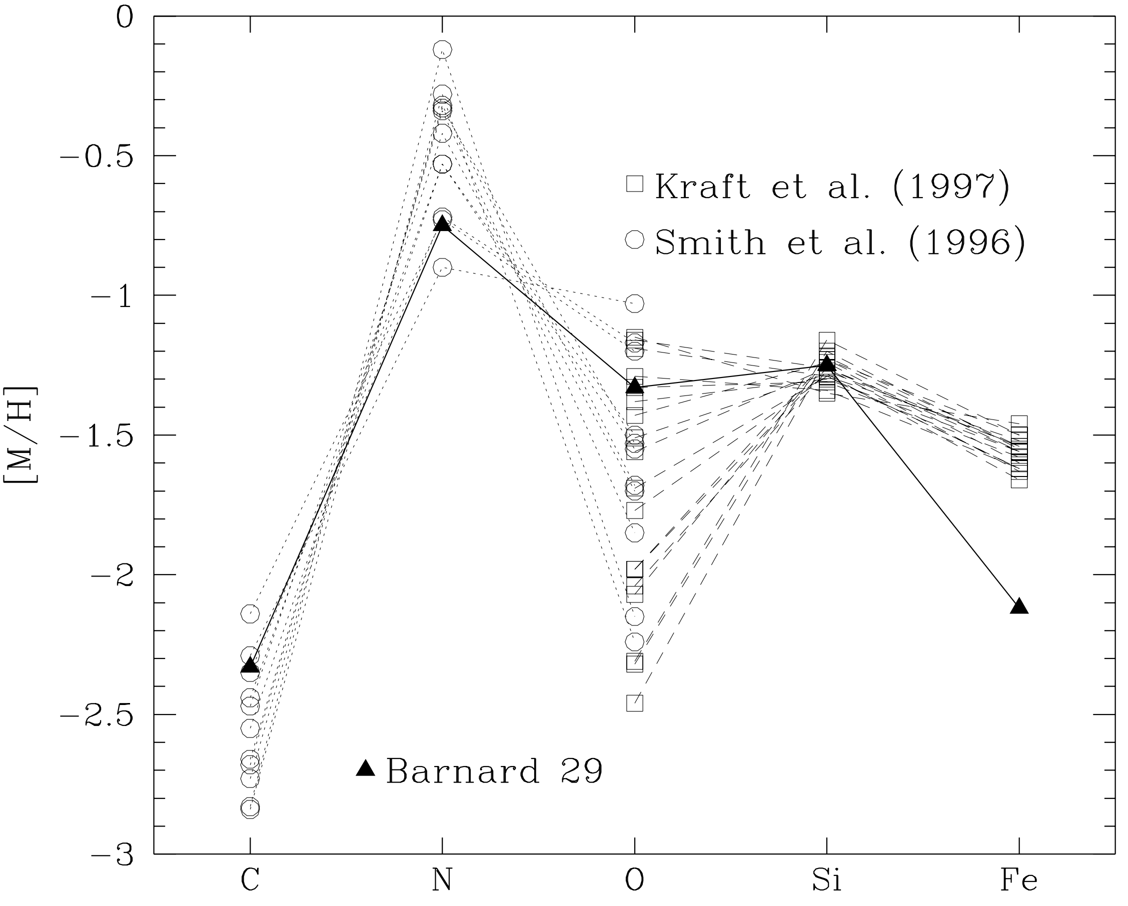

Fig. 42. The abundances derived for Barnard 29 from curve-of-growth analyses (filled triangles connected by solid line) compared to those of red giant stars in M 13. The dotted and short-dashed lines connect the abundances of the red giants taken from Smith et al. (1996, open circles) resp. Kraft et al. (1997, open squares).

7.4 Discussion

The results of our abundance analyses are given in Table 27, where we also give the results of Conlon et al. (1994) and Dixon & Hurwitz (1998) for Barnard 29. A comparison of our results with RGB and

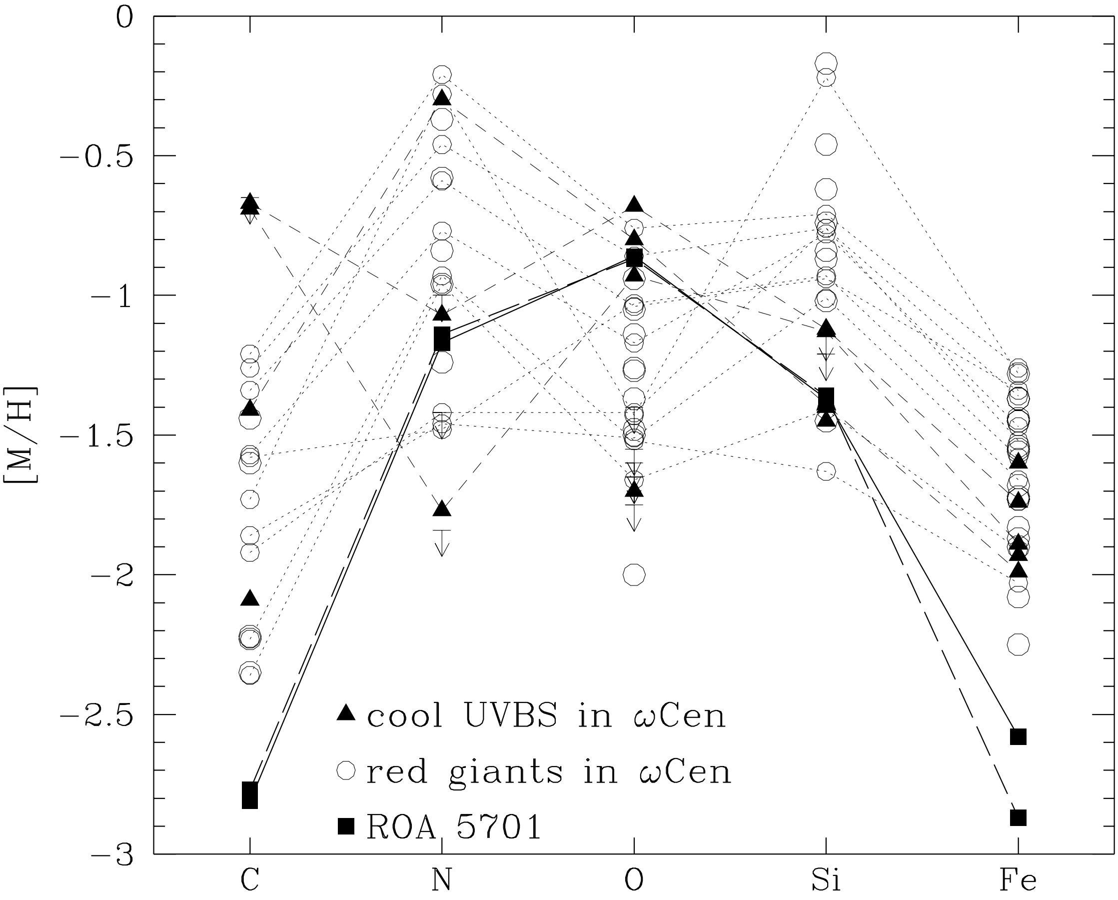

Fig. 43. The abundances derived for ROA 5701 compared to those of other stars in ω Cen. The solid and long-dashed lines connect the abundances derived for ROA 5701 from curve-of-growth and spectrum synthesis analysis, respectively. The short dashed lines mark the cool UV bright stars (filled triangles), the dotted lines connect the abundances of the red giants (open circles). For references see text.

(only in ω Cen) cool UV bright stars is presented in Figs. 42 and 43. The M 13 data in Fig. 42 are from Smith et al. (1996) and Kraft et al. (1997). The ω Cen data for the giants in Fig. 43 were collected from Paltoglou & Norris (1989), Brown et al. (1991), Brown & Wallerstein (1993), and Smith et al. (1995), the data for the cool UV bright stars are from Gonzalez & Wallerstein (1994). All abundances were adjusted to a solar iron abundance of $\log \epsilon_{Fe} = 7.50$.

As can be seen from Fig. 42 Barnard 29 shows similar abundance trends (except for iron) as the red giant stars observed in M 13. This abundance pattern is likely caused by deep mixing and dredge-up of CNO-processed material on the RGB (Pilachowski et al. 1996, Sect. 4.1). However, the iron abundance we found for Barnard 29 is lower than the cluster value by 0.5 dex. This indicates that the atmosphere of Barnard 29 has become iron depleted during the star's evolution, most likely by the gas-dust separation described in the beginning of this chapter.

The interpretation of the abundance pattern of ROA 5701 is hampered by the complex patterns found in ω Cen stars in general (cf. Fig. 43). If we take as a metallicity tracer the sum of C[21], N, and O abundances (which remains unchanged by CNO processing), we find that the original metallicity of ROA 5701 should be close to the median value determined for cluster stars (cf. Fig. 44). However, the iron abundance is 0.5 dex below the lowest value found for any RGB star plotted in Fig. 43.

---

[21] One should keep in mind that the upper limit for the C abundance was derived solely from the 4267 Å line, for which NLTE effects (Eber & Butler 1988) can lead to abundances too low by up to 0.5 dex.

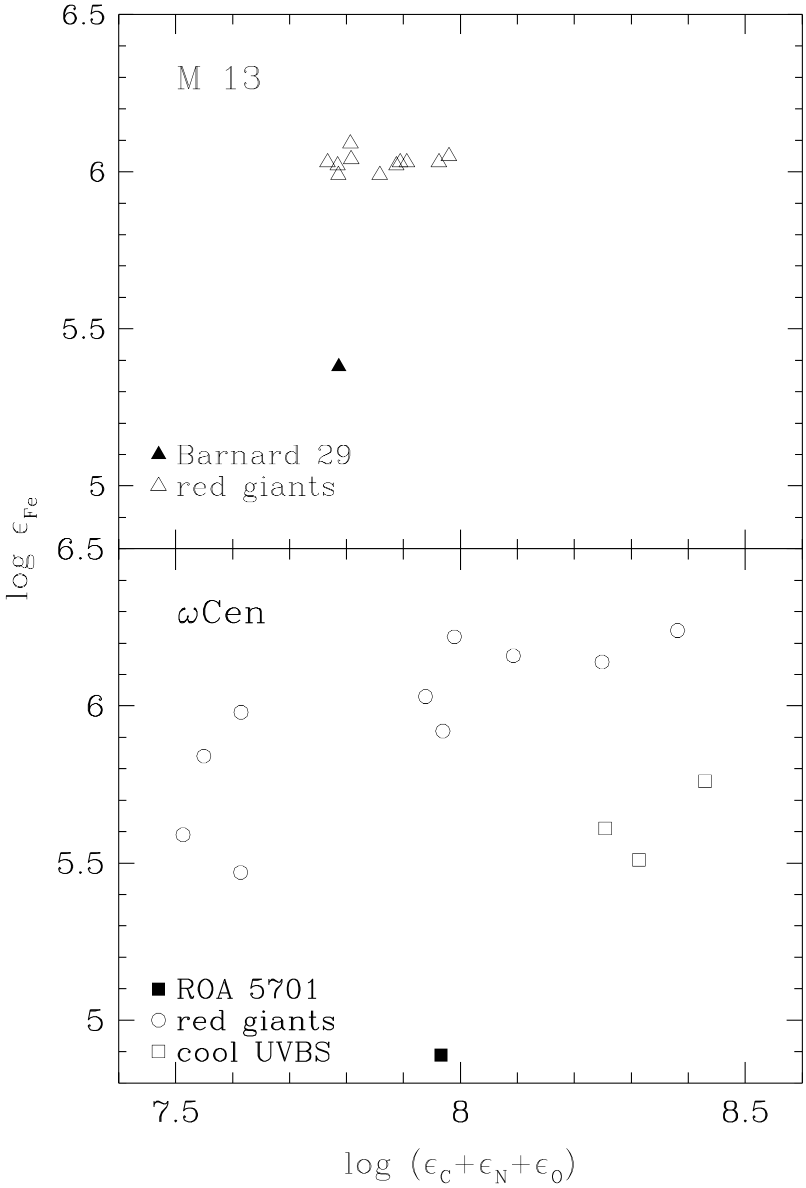

Fig. 44. Upper panel: The Fe abundances vs. the sum of CNO abundances for Barnard 29 compared to those of red giants in M 13. For references see text. **Lower panel:** The Fe abundances vs. the sum of CNO abundances for ROA 5701 compared to those of red giants and cool UVBS in ω Cen. For references see text.

This points to an iron depletion similar to that detected in Barnard 29, which also shows a similar behaviour in Fig. 44.

One should remember here, however, that Gonzalez & Wallerstein (1994) find strong enhancements of CNO and s-process elements for the brightest of the cool UV bright stars in ω Cen which they interpret as evidence for a third dredge-up. As neither ROA 5701 nor Barnard 29 show evidence for a third dredge-up (like, e.g., C enhancement) the sum of C+N+O can be taken as indicator for the original iron abundance. Fig. 44 shows that ROA 5701 and Barnard 29 were not born iron depleted.

In summary, the C, N, O, and Si abundances of Barnard 29 and ROA 5701 are in agreement with that of the respective cluster red giant stars. No third dredge-up during the AGB phase is necessary to explain these abundance patterns. However, our low iron abundances point towards a significant iron depletion, most probably caused by a gas-dust separation during the late AGB stages. One should keep in mind that there is evidence for a systematic offset between iron abundances derived from UV and from optical lines with the "UV abundances" being lower by about 0.5 dex than the optical ones

(Grigsby et al. 1996). While we followed Grigsby et al. in assuming that the UV lines yield correct iron abundances, applying an offset of 0.5 dex to the iron abundances of Barnard 29 and ROA 5701 derived here would reduce the iron depletion to insignificant values. More analyses, preferably also including optical lines, will be necessary before any firm conclusions can be drawn.

Chapter 8

White dwarfs in globular clusters

White dwarfs are the final stage of all low-mass stars (like those discussed so far) and globular clusters should thus contain many white dwarfs. However, these stars managed to evade detection until photometric white dwarf sequences were discovered recently in three globular clusters by observations with the *Hubble Space Telescope* (HST) (Paresce et al. 1995, Richer et al. 1995, 1997, Cool et al. 1996, Renzini et al. 1996). These sequences not only allow to verify time scales for the evolution of low-mass stars, but also offer a third and independent way to determine distances to globular clusters, as suggested by Renzini et al. (1996): The basic idea is to fit the white dwarf cooling sequence of a globular cluster to an appropriate empirical cooling sequence of local white dwarfs with well determined trigonometric parallaxes. The procedure is analogous to the classical main sequence fitting discussed in Sect. 4.3 but has two main advantages:

1. White dwarfs have – due to gravitational settling – very simple atmospheres that are either hydrogen-rich (DA) or helium-rich (DB/DO). Thus one can avoid the problem to find local calibrators with the same metallicities as the globular cluster stars.
2. White dwarfs are locally much more abundant than metal-poor subdwarfs, thus enlarging the reference sample.

Photometric observations alone, however, are not sufficient to select the appropriate local calibrators: Hydrogen-rich DA's and helium-rich DB's in principle can be distinguished by their photometric properties alone in the temperature range $10,000\,K \le T_{\rm eff} \le 15,000\,{\rm K}$ (see Bergeron et al. 1995a) and Renzini et al. (1996) classified two white dwarfs in NGC 6752 as DB's by this method. However, without a spectral classification, those two stars can also be explained as high-mass DA white dwarfs, possibly a product of merging. Richer et al. (1997) speculate that the brightest white dwarf in M 4 (V=22.08) might be a hot (27,000K) DB star.

The location of the white dwarf cooling sequence is also sensitive to the white dwarf mass. Renzini et al. (1996) argued that the white dwarf masses in globular clusters are constrained to the narrow range $0.51\,{\rm M}_\odot \le {\rm M}_{\rm WD} \le 0.55\,{\rm M}_\odot$, but some systematic differences between clusters are obvious: At a given metallicity some globular clusters (e.g. NGC 6752) possess very blue horizontal branches (HB's) with HB star masses as low as $0.50\,{\rm M}_\odot$. Such extreme HB stars evolve directly to low mass C/O white dwarfs (bypassing the AGB) and shift the mean white dwarf mass closer to $0.51\,{\rm M}_\odot$. Other clusters show only red HB stars, which will evolve to the AGB and form preferably white dwarfs with masses of $\approx 0.55\,{\rm M}_\odot$.

Also other channels may exist to produce white dwarfs with masses above or below the cluster mean: Low mass white dwarfs ($M < 0.45\,{\rm M}_\odot$) with a degenerate He core (instead of the "normal" C/O core) are produced, if the red giant branch evolution is terminated by binary interaction before the helium core exceeds the minimum mass for the onset of helium burning. Recently, Cool et al. (1998) found 3 faint UV-bright stars in NGC 6397 which they suggest could be helium-core white dwarfs

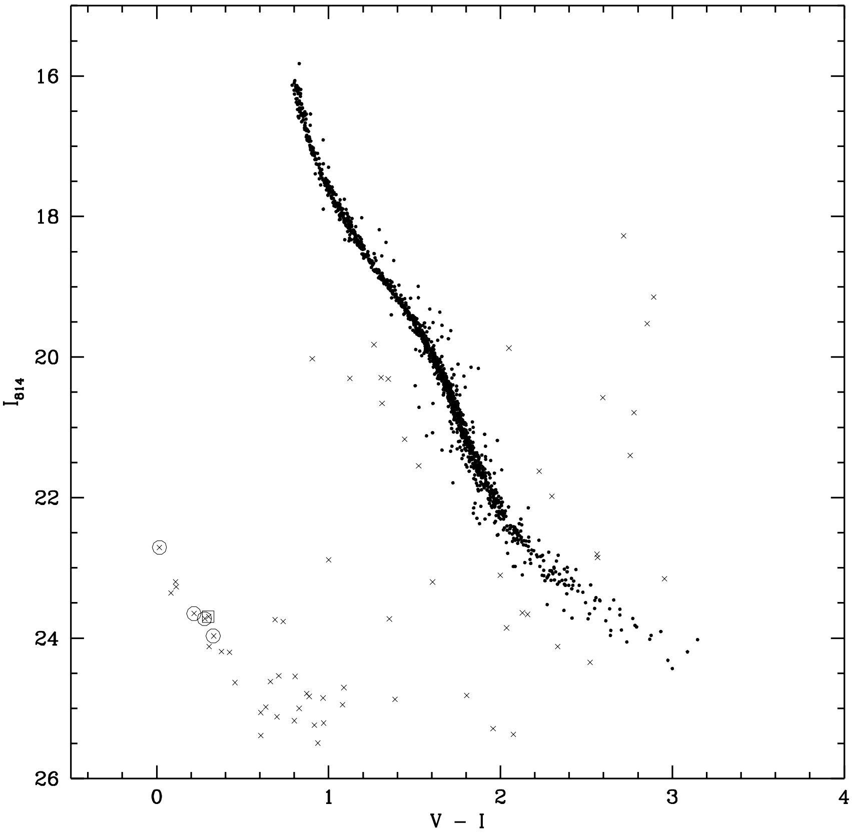

Fig. 45. Colour-magnitude diagram of NGC 6397 (King et al. 1998, their Fig. 2). Open circles mark the four white dwarfs for which spectra could be obtained, the open square marks WF4-205 (see text)

(supported by Edmonds et al. 1999). Massive white dwarfs on the other hand may evolve from blue stragglers or result from collisions of white dwarf-binaries with subsequent merging (e.g. Marsh et al. 1995).

Only a detailed spectroscopic investigation can provide masses and absolute luminosities of the individual globular cluster white dwarfs. We started an observing programme at the ESO *Very Large Telescope (VLT)* to obtain spectra of white dwarfs in globular clusters. The programme consists of two parts: First, low S/N ($\approx$ 10) spectra of the white dwarf candidates are obtained to verify their spectral type and estimate their effective temperatures. In a second run we plan to observe higher S/N ($\approx$ 30) spectra that will allow to derive $\log g$ with an internal error of $\leq$ 0.1dex. Here we report on the very first results for NGC 6397.

8.1 Observations and Data Reduction

Cool et al. (1996) discovered the white dwarfs in NGC 6397 using the Wide Field and Planetary Camera 2 (WFPC2) onboard the HST. From the improved colour-magnitude diagram of King et al. (1998) targets brighter than $V \approx 25^{\mathrm{m}}$ were selected. The WFPC2 images were convolved to a seeing of $0\farcs5$ to select targets that are sufficiently uncrowded to be observable from the ground (see Table 28, Figs. 45 and 46). The stars were observed with the FOcal Reducer/low dispersion Spectrograph (FORS) at Unit Telescope 1 of the ESO Very Large Telescope (VLT) using the high resolution collimator ($0\farcs1$/pixel) to allow better extraction of the spectra and get a better handle on cosmic rays. We used the multi-object spectroscopy (MOS) mode with the grism 300V and a slit width

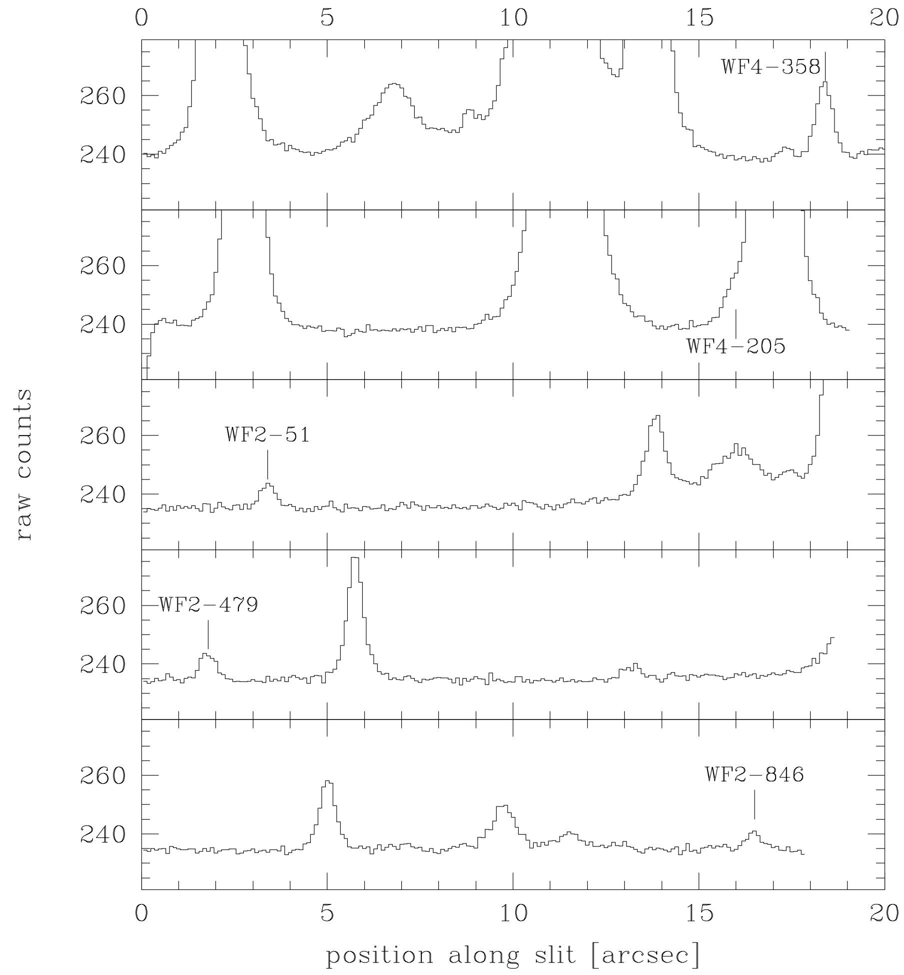

Fig. 46. Traces through the slits along the spatial axis. The lines mark the white dwarf spectra (WF4-205 unfortunately lies on the wing of a much brighter star).

Table 28. Target coordinates and photometric data from Cool (priv. comm.).

Star	α_{2000}	δ_{2000}	V	$V-I$
WF4-358	$17^{\rm h}40^{\rm m}58^{\rm s}.52$	$-53^\circ 42' 25''.3$	$22^{\rm m}.73$	$+0^{\rm m}.02$
WF2-479	$17^{\rm h}41^{\rm m}07^{\rm s}.06$	$-53^\circ 44' 45''.1$	$23^{\rm m}.87$	$+0^{\rm m}.22$
WF4-205	$17^{\rm h}41^{\rm m}01^{\rm s}.58$	$-53^\circ 43' 15''.3$	$23^{\rm m}.99$	$+0^{\rm m}.30$
WF2-51	$17^{\rm h}41^{\rm m}04^{\rm s}.52$	$-53^\circ 43' 55''.8$	$24^{\rm m}.00$	$+0^{\rm m}.28$
WF2-846	$17^{\rm h}41^{\rm m}01^{\rm s}.78$	$-53^\circ 44' 47''.2$	$24^{\rm m}.30$	$+0^{\rm m}.33$

of $0''.8$. The slit width was chosen to be larger than the required seeing ($0''.5$) in order to avoid slit losses due to imperfect pointing of the telescope. The data were obtained in service mode under excellent conditions (seeing below $0''.55$, no moon) with a total exposure time of 90 minutes. The spectral resolution as judged from a wavelength calibration spectrum obtained with a $0''.5$ slit is ≈11.5 Å. A trace along the spatial axis of the slitlets at about 4550 Å is plotted in Fig. 46. Unfortunately WF4-205 lies so close to a bright star that even at this excellent seeing its spectrum cannot be extracted.

The spectra were corrected for bias, flat-fielded, wavelength calibrated, and extracted in the same way as the long-slit spectra described in Sect. 3.3.1. Due to the use of slit blades instead of fibers or masks the MOS slitlets are very well defined and can be treated like long slits. We find only a diffuse and rather low sky background without any strong sky lines below 5150 Å. The spectra were relatively flux calibrated using LTT 7987 (Hamuy et al. 1992) and are plotted in Fig. 47 together with a

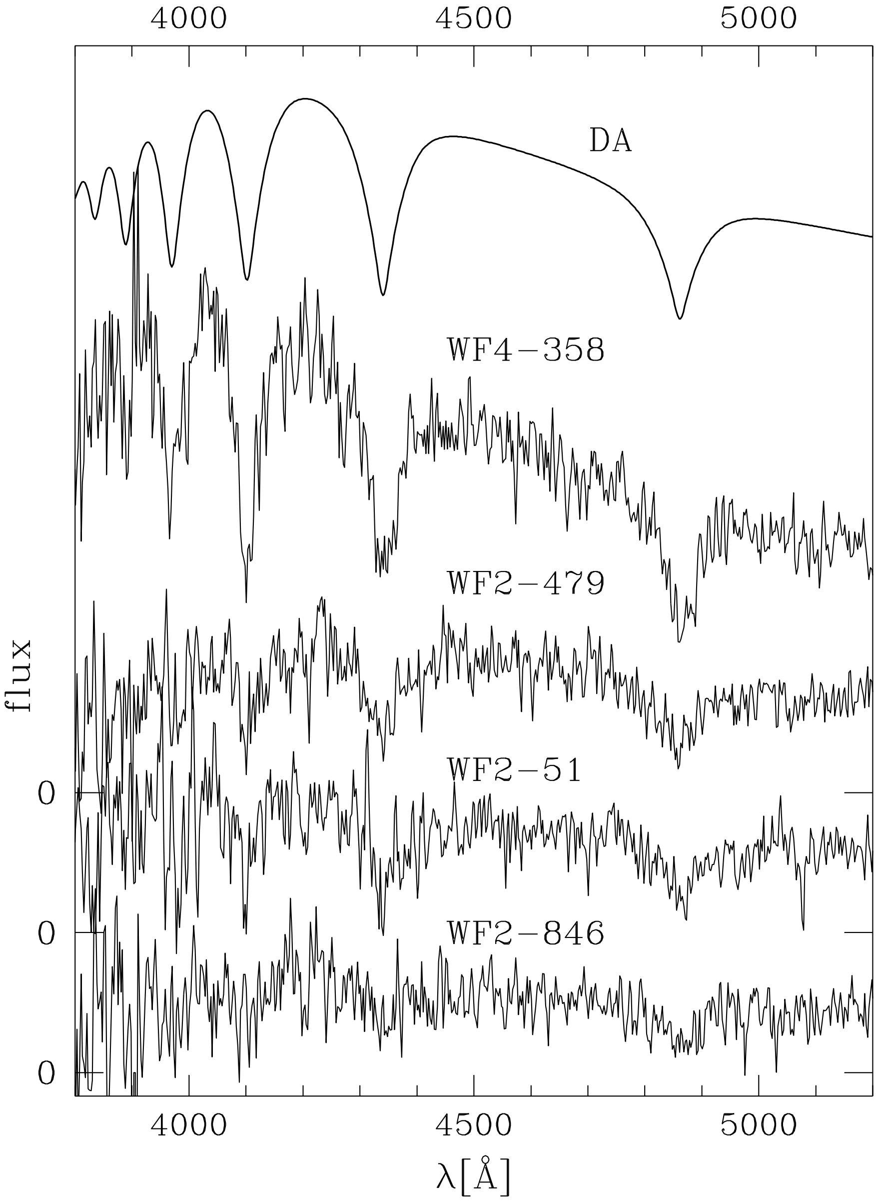

Fig. 47. The (relatively flux-calibrated) spectra of the white dwarfs in NGC 6397. The spectra of the three faintest stars are offset from each other as they would otherwise overlap. WF4-358 has no additional offset relative to WF2-479. A theoretical spectrum for a DA white dwarf convolved to the same resolution as the observed spectra is shown at the top.

theoretical DA spectrum. All four stars display strong broad Balmer lines only, which is characteristic for hydrogen-rich white dwarfs (DA stars).

8.2 Atmospheric parameters

Although the white dwarf spectra have low signal-to-noise they are sufficient for rough parameter estimates. The atmospheric parameters were obtained by simultaneously fitting profiles of the observed Balmer lines with model spectra (see Sect. 4.4.2). We used Koester's LTE models as described in Finley et al. (1997) and as a check repeated the analysis of the hottest star in our sample (WF4-358) with the NLTE grid described in Napiwotzki et al. (1999). Since the NLTE code does not treat convection

Table 29. Atmospheric parameters, masses, and absolute magnitudes for the white dwarfs. We also give the reduced χ^2 of the line profile fits (see text for details) and the distance moduli determined from the individual white dwarfs. The masses are obtained from theoretical tracks of Blöcker (1995) and Driebe et al. (1998) and absolute magnitudes are derived from Bergeron et al. (1995a). Using Bergeron et al.'s (1995a) Table 3 we derived $T_{\rm eff,(V-I)_0}$ from $(V-I)_0$, which was calculated from $V-I$ assuming $E_{\rm V-I} = 0^{\rm m}.225$ (resp. $E_{\rm B-V} = 0^{\rm m}.18$)

star	$\log g$ [cm/s^2]	$T_{\rm eff}$ [K]	χ^2	$T_{\rm eff,(V-I)_0}$ [K]	M [M$_\odot$]	M_V	$(m-M)_V$	$(m-M)_0$
NGC6397-WF4-358[1]	7.3	18200	0.93		0.36	$9^{\rm m}.7$	$13^{\rm m}.03$	$12^{\rm m}.45$
NGC6397-WF4-358	7.2	17800	1.02		0.32	$9^{\rm m}.6$	$13^{\rm m}.13$	$12^{\rm m}.55$
NGC6397-WF4-358	7.5	18900	1.04		0.42	$10^{\rm m}.0$	$12^{\rm m}.73$	$12^{\rm m}.15$
NGC6397-WF2-479	7.5	10800	1.15		0.39	$11^{\rm m}.1$	$12^{\rm m}.77$	$12^{\rm m}.19$
NGC6397-WF2-51	7.5	10900	1.46		0.39	$11^{\rm m}.1$	$12^{\rm m}.90$	$12^{\rm m}.32$
NGC6397-WF2-846	7.5	10500	0.71		0.38	$11^{\rm m}.2$	$13^{\rm m}.10$	$12^{\rm m}.52$
NGC6397-WF4-358	7.7	19500	1.07		0.48	$10^{\rm m}.3$	$12^{\rm m}.43$	$11^{\rm m}.85$
NGC6397-WF2-479	7.7	11000	1.14		0.46	$11^{\rm m}.4$	$12^{\rm m}.47$	$11^{\rm m}.89$
NGC6397-WF2-51	7.7	11100	1.46		0.46	$11^{\rm m}.4$	$12^{\rm m}.60$	$12^{\rm m}.02$
NGC6397-WF2-846	7.7	10600	0.71		0.46	$11^{\rm m}.5$	$12^{\rm m}.80$	$12^{\rm m}.22$
NGC6397-WF4-358	8.0	20300	1.13	19400	0.62	$10^{\rm m}.7$	$12^{\rm m}.03$	$11^{\rm m}.45$
NGC6397-WF2-479	8.0	11200	1.14	11500	0.59	$11^{\rm m}.8$	$12^{\rm m}.07$	$11^{\rm m}.49$
NGC6397-WF2-51	8.0	11300	1.47	10800	0.59	$11^{\rm m}.8$	$12^{\rm m}.20$	$11^{\rm m}.62$
NGC6397-WF2-846	8.0	10800	0.71	10300	0.59	$11^{\rm m}.9$	$12^{\rm m}.40$	$11^{\rm m}.82$

[1] H_ϵ is included in this fit.

and ignores molecular opacities no reliable NLTE atmospheric models can be calculated for the three cooler white dwarfs.

Fitting the lines H_β to H_ϵ for WF4-358 gives 18,200±1300 K and 7.30±0.36 for $T_{\rm eff}$ and $\log g$, respectively. The errors given here are 1σ errors obtained from the χ^2 fit (see Sect. 5.1.2). Omitting H_ϵ from the fit results in 17,800 K and 7.19 with more or less unchanged errors. The results of the NLTE analyses are essentially identical to those obtained with Koester's models, differing only by small fractions of the formal errors ($\Delta\ T_{\rm eff} \approx 500\,$K, $\Delta\ \log g \approx 0.07\,$dex). The surface gravity is surprisingly low – if verified WF4-358 could be a low-mass helium-core white dwarf. For the remaining three stars the S/N is too low to determine $T_{\rm eff}$ and $\log g$ simultaneously. We thus fitted H_δ, H_γ, H_β (H_ϵ being too noisy) for WF2-51, WF2-479, and WF2-846 for three fixed values of $\log g$ (8.0, 7.7, 7.5). These $\log g$ values correspond to C/O white dwarfs of $\approx 0.6\,{\rm M}_\odot$, low-mass C/O white dwarfs of $\approx 0.5\,{\rm M}_\odot$, and He white dwarfs of $\approx 0.4\,{\rm M}_\odot$, respectively (see below). The 1σ errors are about 600 K for WF2-479, WF2-846, and WF4-358 and about 900 K for WF2-51. The errors for the cooler stars are relatively small (despite their low S/N) as the line profiles are much more sensitive to effective temperature variations at $T_{\rm eff}$ ≈11,000 K than at $T_{\rm eff}$ ≈18,000 K. The temperatures derived from the Balmer lines for $\log g = 8.0$ agree quite well with those obtained from $(V-I)_0$ using the theoretical colours of Bergeron et al. (1995a, $\log g = 8.0$). The masses given in Table 29 were derived by interpolation between the evolutionary tracks of C/O white dwarfs calculated by Blöcker (1995) and the He white dwarf tracks of Driebe et al. (1998). Finally, absolute magnitudes M_V were calculated for each parameter set with the photometric calibration of Bergeron et al. (1995a).

8.3 The distance to NGC 6397

As can be seen from Table 10 (p. 60) NGC6397 is a good example for the large differences between old and new distances to globular clusters with distance moduli varying between $11^{\rm m}.71$ and $12^{\rm m}.24$. Table 29 shows that the long distance scale would only be supported by our analyses if all white dwarfs analysed here were low-mass He-core white dwarfs, which we consider rather unlikely. Keeping in mind that NGC 6397 has an almost exclusively blue horizontal branch and a UV-bright star that is well fit by a $0.565\,M_\odot$ post-AGB track (ROB 162, Heber & Kudritzki 1986) we consider it also unlikely that the white dwarfs have an average mass as high as $0.6\,M_\odot$. Thus the most probable case in our opinion are low-mass C/O white dwarfs, which yield a distance almost exactly between the old and new values ($(m-M)_0 = 12\overset{m}{.}0 \pm 0\overset{m}{.}17$ for $E_{B-V} = 0\overset{m}{.}18$). This distance, however, would be too short to reconcile the spectroscopically derived masses of blue HB stars in NGC 6397 with canonical HB theory (de Boer et al. 1995, Heber et al. 1997, see also Sect. 3.4 and 4.3). The variation of the derived distance moduli among the four stars (for a fixed $\log g$) may reflect the fact that the stars very probably *do not* all have the same surface gravity. From their different apparent magnitudes (resulting in different absolute magnitudes) it is plausible that WF4-358 will have the smallest $\log g$ resp. mass and WF2-846 will have the largest $\log g$ resp. mass.

8.4 Conclusions

Using VLT-FORS1 multi object spectroscopy we have confirmed four white dwarf candidates to be hydrogen-rich DA white dwarfs. The gravity determined for the brightest star, WF4-358, suggests that it is a He-core white dwarf with a mass of $(0.36 \pm 0.12)\,M_\odot$. Temperatures derived for the three cooler and fainter stars for fixed $\log g$ would put them near the red edge of the ZZ Ceti instability strip, for which Bergeron et al. (1995b) determine a temperature range of 11,160 K to 12,460 K using their preferred ML2/α=0.6 prescription for the treatment of convection. Therefore, a search for photometric variability of the cooler white dwarfs – if successful – could place important additional constraints on these stars. From Table 29 it is obvious that the assumption of a constant mass for all white dwarfs in a globular cluster may bias a distance determination: If a luminous, low-mass He-core white dwarf like WF4-358 is compared to a local C/O-core white dwarf the distance to NGC 6397 would be underestimated. Once higher quality spectra are available, which will allow more accurate parameter (and thus mass) determinations, analyses of white dwarfs in globular clusters will become a powerful tool for independent distance estimates.

Chapter 9

Summary

Globular clusters are the closest approximation in astronomy to a physicist's laboratory: They contain several thousand to more than one million stars, which are old and essentially coeval. They are thus ideally suited to study the evolution of low-mass stars. We discuss here three types of hot stars observed in globular clusters, that cover all stages of stellar evolution at high temperatures after the main sequence: **horizontal branch stars**, **UV bright stars**, and **white dwarfs**.

While the distribution of stars along the horizontal branch in first approximation moves towards hotter temperatures as metallicity decreases, colour-magnitude diagrams of many metal-poor globular clusters show a large variety of (blue) horizontal branch morphologies, namely blue tails, i.e. extensions towards hotter temperatures, and gaps along the horizontal branches. These variations at low and essentially identical metallicities are not predicted by standard stellar evolution. Some scenarios suggest that the stars below the gaps along the horizontal branch (HB) are not "true" HB stars (i.e. descendants of red giants), but stars created by some other mechanism. The different scenarios predict different mass and temperature distributions for the stars along the blue tails. As photometry does not provide sufficient information to distinguish between the various scenarios we decided to obtain spectra of stars along the blue tails in the globular clusters M 15 and NGC 6752 to verify their evolutionary status and mass.

The stars below the gap in M 15 show atmospheric parameters that are best described by hot HB evolutionary models, i.e. stars that burn helium in the core and hydrogen in a shell. Their surface gravities, however, are systematically lower than predicted by canonical HB models and the derived masses lie on average significantly below canonical HB masses. Neither the atmospheric parameters nor the masses can be explained by any of the non-HB scenarios.

The stars below the gap in NGC 6752 turn out to be significantly hotter than those in M 15 and are well described by evolutionary tracks for extreme HB stars, i.e. HB stars that have too little hydrogen envelope left to sustain hydrogen shell burning. The masses derived for these stars are in excellent agreement with canonical predictions. The stars above the gap in NGC 6752 turn out to be similar to those below the gap in M 15 in temperature, surface gravity, and mass, i.e. they show the same offset toward lower gravities and masses as the stars in M 15. All stars analysed in NGC 6752 are helium deficient by factors ranging from 3 to more than 100, indicative of gravitational settling of helium.

A comparison with data for horizontal branch stars in other clusters shows that the discrepancies between observational results and theoretical predictions do not depend on a star's position relative to some gap, but rather on its temperature: Stars with effective temperatures between 11,500 K and 20,000 K show low gravities and masses, while hotter stars agree well with theoretical predictions. This situation became clear only with our observations as the older data from the literature did not cover the whole range in temperature, but were mainly dealing with cooler, visually brighter stars. The stars below 11,500 K show gravities and temperatures consistent with stellar evolutionary theory, but deviate towards low mass values.

Combining all available data sets also shows that most of the gaps seen along the horizontal branches are not mirrored by any gaps in the distribution of physical parameters. The only two exceptions are a gap at ≈20,000 K separating extreme HB stars (sdB's) from hot HB stars and a narrow gap at $T_{\rm eff}$ ≈10,000 K – 12,000 K. Thus the gaps seen along the HB's in colour-magnitude diagrams are in most cases due to statistical fluctuations. Three possible scenarios to explain the behaviour described above are discussed:

1. **Helium mixing on the red giant branch**, which would produce hotter and more luminous HB stars than canonical evolution. As more luminous stars show lower surface gravities tracks with helium mixing can well explain the low gravities of the hot HB stars. The extreme HB stars are unaffected by this explanation as the lower gravities result from a higher energy production in the hydrogen-burning shell, which is inactive in extreme HB stars. The observed parameters for stars hotter than 11,500 K are well reproduced by evolutionary tracks, that take into account helium mixing. Cooler stars are better described by canonical tracks. As mixing increases the temperature of the resulting HB stars cooler HB stars may descend from unmixed red giants.
2. **Distances to globular clusters** directly affect the mass determination: underestimating the cluster distance results in too low masses. Especially the stars cooler than 11,500 K, which show "canonical" gravities, but low masses, support this solution.
3. **Radiative levitation of heavy elements** in the atmospheres of the HB stars would change the metallicities of the stellar atmospheres. If the metallicity of the theoretical model atmosphere deviates significantly from that of the observed atmosphere systematic errors in effective temperature and surface gravity are introduced. The low surface gravities in this case would be artifacts from the metallicity mismatch between theoretical and observed stellar atmospheres. Cooler stars may not be affected by diffusion, as their atmospheres may not be stable enough.

NGC 6752 is a perfect test case for the above mentioned scenarios: Its stars below the gap show a mean mass consistent with canonical EHB theory and its distance is undebated. The analysis of a sufficiently large sample of hot HB stars in that globular cluster should thus allow to distinguish between helium mixing (in which case stars with low gravities should show canonical masses) and diffusion (in which case the erroneous low gravities would yield low masses)

We observed and analysed 32 more hot horizontal branch (HB) stars in the globular cluster NGC 6752 and found that the atmospheric parameters derived from the analysis with metal-poor model atmospheres are consistent with helium mixing, but yield low masses. All analysed stars are helium deficient, which indicates the presence of diffusion. While a lack of helium does not change the structure of the atmospheres significantly, diffusion may enrich the heavy elements in the stellar atmosphere via radiative levitation. For 19 stars Mg II and Fe II lines are detected in our spectra, indicating an iron enrichment by a factor 50 on average with respect to the cluster abundance whereas the magnesium abundances are consistent with the cluster metallicity.

This finding suggests that radiative levitation of heavy elements plays a significant role in the atmospheres of hot HB stars. Using model atmospheres with a solar metallicity moves the stars closer to the canonical evolutionary tracks and thus solves part, but not all, of the problem of anomalously low gravities and masses along the hot HB: The physical parameters of horizontal branch stars with temperatures between 11,500 K and 15,500 K now agree well with canonical evolution theory, but some discrepancies (low gravities and masses) remain for the temperature range 15,500 K to 19,000 K. As the change in abundances due to radiative levitation depends on the temperature of the star, these remaining deviations may indicate changes in the relative abundance patterns which are not well approximated by our simple model atmospheres.

The HB stars cooler than about 11,500 K (which should be unaffected by diffusion) in the globular clusters M 92, NGC 288, and NGC 6397 still strongly support the long distance scale for globular clusters, as their derived masses are significantly too low otherwise.

As mentioned above the distribution of stars along the horizontal branch moves towards cooler temperatures as metallicity increases. Hot horizontal branch stars are therefore generally rare in metal-rich globular clusters, but the observed UV excess of (metal-rich) elliptical galaxies suggests that hot HB and/or extreme HB stars can also be produced at high metallicities. The discovery of hot HB star candidates in several metal-rich cluster therefore prompted us to study them spectroscopically to verify their evolutionary status:

The colour-magnitude diagrams observed in the central regions of the bulge globular clusters NGC 6388 and NGC 6441 show long blue tails, that are completely unexpected for such metal-rich systems. In addition the horizontal branches are sloped towards brighter magnitudes for hotter stars, which cannot be explained by standard evolutionary theories. Several scenarios have been suggested to explain not only the presence of so many hot HB stars in metal-rich globular clusters, but also the slope in brightness along the HB. As these scenarios predict different atmospheric parameters for these stars we performed spectroscopic analyses for several hot HB stars in these two clusters. Comparing the results of our spectroscopic analyses to the theoretical predictions shows that their atmospheric parameters are only marginally inconsistent with the predictions of canonical evolutionary theory, but disagree strongly with all non-canonical scenarios that reproduce the sloped horizontal branches seen in the colour-magnitude diagrams of these clusters. There is thus a severe discrepancy between results from photometric and from spectroscopic observations, that cannot be resolved with the currently available observations and theoretical scenarios.

Far-UV observations with the Ultraviolet Imaging Telescope showed the presence of hot stars in the globular clusters 47 Tuc and NGC 362, which so far have been known to contain primarily red HB stars. As both clusters have positions on the sky close to the Small Magellanic Cloud (SMC) photometric data alone cannot decide whether the blue objects are HB stars within the globular clusters or massive stars in the SMC. Spectroscopic analyses of these stars show that unfortunately most of the hot stars seen in NGC 362 do not belong to the cluster, but are probably members of the SMC. The number of cluster members turns out to be quite small (3 stars in each cluster). The parameters of the member stars, however, agree well with canonical HB evolution and thus differ from the HB stars observed in the bulge clusters NGC 6388 and NGC 6441. The agreement with canonical evolution suggests that the stars in 47 Tuc and NGC 362 are probably produced from red giants with unusually high mass loss, which is also consistent with the small number of hot stars seen in the two clusters.

Turning towards the evolutionary stages after the horizontal branch we observed **UV-bright stars** discovered by Ultraviolet Imaging Telescope in globular clusters. Searches in the UV are very efficient to detect hot stars, which due to their large bolometric corrections can be quite faint visually. Comparing the effective temperatures, surface gravities, and helium abundances of these UIT-selected UV bright stars to evolutionary tracks shows that none of these stars is a “true” post-AGB star. All stars lie along either post-extended horizontal branch (post-EHB) or post-early AGB evolutionary tracks. Comparing the parameters of the UV bright stars discovered by UIT to those known from optical searches shows that the optical searches for hot UV bright stars are severely biased towards the most luminous evolutionary stages. The analysis of optically selected UV bright stars thus gives a wrong impression of the importance of the various evolutionary phases that contribute to the UV flux of old stellar populations. The lack of “true” post-AGB stars within the UIT selected sample could also explain the lack of planetary nebulae in globular clusters. The predominance of post-early AGB stars over “true” post-AGB stars suggests that mass loss on the AGB may be higher than assumed in standard evolution (resulting in an early termination of the AGB phase). However, as the lifetimes of post-early AGB stars are also considerably longer than those of “true” post-AGB stars a larger sample will be needed before firm conclusions can be drawn about the mass loss on the AGB.

To get more information on the AGB phase of stellar evolution (esp. on the question of third dredge-up) we analysed two hot post-AGB stars, ROA 5701 (ω Cen) and Barnard 29 (M 13). We determined abundances of He, C, N, O, and Si for ROA 5701 from optical spectra and iron abundances for both stars from UV spectra. The iron abundances lie significantly below the mean cluster abundance in both stars. Barnard 29 shows the same abundance pattern as the red giant stars in M 13, except for its stronger iron deficiency, while the interpretation of the abundance pattern for ROA 5701 is hampered by the star-to-star abundance variations seen in ω Cen. Nevertheless the abundance patterns of both stars would be consistent with iron depletion due to gas-dust separation in the AGB star's atmosphere. Such separation may happen if iron condensed into dust grains which were then removed from the atmosphere of the AGB star by a radiatively driven wind.

Finally we observed the very first spectra of stars along the **white dwarf** sequences discovered by HST observations of globular clusters. All four white dwarf candidates under study turn out to be hydrogen-rich DA stars and the spectrum of the brightest star even allows to derive effective temperature and surface gravity simultaneously. Comparing these parameters to evolutionary tracks suggests that the brightest star analysed in NGC 6397 may be a luminous, low-mass ($0.36\,M_\odot$) white dwarf with a helium core (instead of the more common C/O cores). The low S/N of the spectra of the fainter stars does not allow to derive effective temperature and gravity simultaneously. Keeping the gravity fixed we can still obtain an estimate of the effective temperature for these stars, which puts them close to the ZZ Ceti instability strip. As it is rather implausible that *all* analysed white dwarfs are low-mass helium-core white dwarfs, there probably exists a spread in mass among the white dwarfs in NGC 6397. As the brightness of a white dwarf depends strongly on its mass the assumption of a constant mass for white dwarfs in a globular cluster can thus introduce large bias into a distance determination.

Acknowledgements. I want to thank Prof. U. Heber for the possibility to prepare this thesis and all colleagues at the Dr. Remeis-Sternwarte for the good climate at the institute. I am grateful to W.B. Landsman and A.V. Sweigart for many useful discussions. Thanks go also to the staff of the Calar Alto (DSAZ) observatory, Hubble Space Telescope, and ESO observatories at La Silla and Paranal for their support during and after observations. I gratefully acknowledge financial support for this work by the DFG (grants Mo 602/1,5,6), DARA/DLR (grant 50 OR 96029-ZA), Alexander von Humboldt-Foundation (Feodor Lynen fellowship) and Dr. R. Williams as director of the Space Telescope Science Institute (DDRF grant).

References

Adams S., Seaton M.J., Howarth I.D., Auriére M., Walsh J.R., 1984, MNRAS 207, 471

Alcaino G., Buonanno R., Caloi V., et al., 1987, AJ 94, 917

Altner B., Matilsky T.A., 1993, ApJ 410, 116

Anders E., Grevesse N., 1989, GeCoA 53, 197

Armosky B.J., Sneden C., Langer G.E., Kraft R.P., 1994, AJ 108, 1364

Arp H.C., 1955, AJ 60, 317

Bahner K., 1967, in *Handbuch der Physik*, ed. S. Flügge, (Springer Verlag, Berlin), Vol. 29, p. 227

Bailyn, C., 1995, ARAA 33, 133

Bailyn C.D., Grindlay J.E., Cohn H., Lugger P.M., 1988, in *The Harlow-Shapley Symposium on Globular Cluster Systems in Galaxies*, eds. J.E. Grindlay & A.G.D. Philip, IAU Symp. 126 (Kluwer, Dordrecht), p. 676

Bailyn C.D., Iben I., 1989, ApJ 347, L21

Bailyn C.D., Sarajedini A., Cohn, H., Lugger P., Grindlay J.E., 1992, AJ 103, 1564

Barnard E.E., 1900, ApJ 12, 176

Baschek B., Norris J., 1975, ApJ 199, 694

Battistini P., Bregoli G., Fusi Pecci F., Lolli M., 1985, A&AS 61, 487

Becker S.R., Butler K., 1989, A&A 209, 244

Becker S.R., Butler K., 1990, A&A 235, 326

Behr B.B., Cohen J.G., McCarthy J.K., Djorgovski S.G., 1999a, ApJ 517, L135

Behr B.B., Djorgovski S.G., Cohen J.G., et al., 1999b, `astro-ph/9907211`

Bell K.L., Hibbert A., Stafford R.P., McLaughlin B.M., 1994, Physica Scripta 50, 343

Bell R.A., Dickens R.J., Gustafsson B., 1979, ApJ 229, 604

Bell, R.A., Hesser, J.E., Cannon, R.D., 1984, ApJ 283, 615

Bell R.A., Briley M.M., Norris J.E., 1992, AJ 104, 1127

Bergeron, P., Saffer, R.A., Liebert, J., 1992, ApJ 394, 228

Bergeron P., Wesemael F., Beauchamp A., 1995a, PASP 107, 1047

Bergeron P., Wesemael F., Lamontagne R., et al., 1995b, ApJ 449, 258

Blöcker T., 1995, A&A 299, 755

Bohlin R.C., Harris A.W., Holm A.V., Gry C., 1990, ApJS 73, 413

Bohlin R.C., 1996, AJ 111, 1743

Bond H.E., 1991, in *Evolution of Stars: the Photospheric Abundance Connection*, eds. G. Michaud, A. Tutukov, IAU Symp. 145 (Kluwer, Dordrecht) p. 341

Bowen G.H. 1988, ApJ 329, 299

Briley M.M., Bell R.A., Hoban S., Dickens R.J., 1990, ApJ 359, 307

Briley M.M., Smith G.H., 1993, PASP 105, 1260

Brown J.A., Wallerstein G., Oke J.B., 1990, AJ 100, 1561

Brown J.A., Wallerstein G., Cunha K., Smith V.V., 1991, A&A 249, L13

Brown J.A., Wallerstein G., 1992, AJ 104, 1818

Brown J.A., Wallerstein G., 1993, AJ 106, 133

Brown T.M., Ferguson H.C., Davidsen A.F., Dorman B., 1997, ApJ 482, 685

Buonanno R., Corsi C.E., Fusi Pecci F., 1981, MNRAS, 196, 435

Buonanno R., Buscema G. Corsi C., Iannicola G., Fusi Pecci F., 1983a, A&AS 51, 83

Buonanno R., Buscema G. Corsi C., Iannicola G., Smriglio F., 1983b, A&AS 53, 1

Buonanno R., Corsi C.E., Fusi Pecci F., Alcaino G., Liller W., 1984, A&AS 57, 75

Buonanno R., Corsi C.E., Fusi Pecci F., 1985, A&A 145, 97

Buonanno R., Caloi V., Castellani V., et al., 1986, A&AS 66, 79

Buonanno R., Corsi C.E., Buzzoni A., et al., 1994, A&A 290, 69

Buonanno R., Corsi C.E., Bellazzini M., Ferraro F.R., Fusi Pecci F., 1997, AJ 113, 706

Burki G., Rufener F., Burnet M., et al., 1995, ESO Messenger 80, 34
Burstein D., Bertola F., Buson L.M., Faber S.M., Lauer T.R., 1988, ApJ 328, 440
Cacciari C., Caloi V., Castellani V., Fusi Pecci F., 1984, A&A 139, 258
Cacciari C., Bruzzi A., 1993, A&A 276, 87
Cacciari C., Fusi Pecci F., Bragaglia A., Buzzoni A., 1995, A&A 301, 684
Caloi V., 1972, A&A 20, 357
Caloi V., 1999, A&A in press
Caloi V., D'Antona F., Mazzitelli I., 1997, A&A 320, 823
Cannon R.D., Croke B.F.W., Bell R.A., Hesser J.E., Stathakis R.A., 1998, MNRAS 298, 601
Carbon D.F., Romanishin W., Langer G.E., et al., 1982, ApJS 49, 207
Cardelli J.A., Clayton G.C., Mathis J.S., 1989, ApJ 345, L245
Carretta E., Gratton R.G. 1997, A&AS 121, 95
Carretta E., Gratton R., Clementini G., Fusi Pecci F., in *Harmonizing Cosmic Distance Scales in a Post-HIPPARCOS Era*, eds. D. Egret & A. Heck, ASP Conf. Ser. 167, p. 255
Cassisi S., Castellani V., Degl'Innocenti S., Weiss A., 1998, A&AS 129, 267
Cassisi S., Castellani V., Degl'Innocenti S., Salaris M., Weiss A., 1999, A&AS 134, 103
Catelan M., 1998, ApJ 495, L81
Catelan M., de Freitas Pacheco J.A., 1996, PASP 108, 166
Catelan M., Borissova J., Sweigart A.V., Spassova N., 1998, ApJ 494, 265
Cavallo R.M., Sweigart A.V., Bell R.A., 1998, ApJ 492, 575
Charbonneau P., Michaud G., 1988, ApJ 327, 809
Charbonnel C., 1994, A&A 282, 811
Charbonnel C., Meynet G., Maeder A., Schaller G., Schaerer D., 1993, A&AS 101, 415
Charlot S., Worthey G., Bressan A., 1996, ApJ 457, 625
Code A.D., Welch G.A., 1979, ApJ 228, 95
Cohen J.G., 1999, AJ 114, 2434
Cohen J.G., McCarthy J.K., 1997, AJ 113, 1353
Conlon E.S., 1994, in *Hot Stars in the Galactic Halo*, eds. S. Adelman, A. Upgren, C.J. Adelman, (Cambridge University Press, Cambridge), p. 309
Conlon E.S., Dufton, P.L., Keenan, F.P., 1994, A&A 290, 897
Cool A.M., Piotto G., King I.R., 1996, ApJ 468, 655
Cool A.M., Grindlay J.E., Cohn H.N., Lugger P.M., Bailyn C.D., 1998, ApJ 508, L75
Cottrell P.L., Da Costa G.S., 1981, ApJ 245, L79
Crocker D.A., 1991, in *The Formation and Evolution of Star Clusters*, ed. K. Janes, ASP Conf. Ser. 13 (San Francisco), p. 253
Crocker D.A., Rood R.T., O'Connell R.W., 1986, ApJ 309, L23
Crocker D.A., Rood R.T., O'Connell R.W., 1988, ApJ 332, 236
Cudworth K.M., Rees, R. 1990, AJ 99, 1491
D'Antona F., Caloi V., Mazzitelli I., 1997, ApJ 477, 519
d'Cruz N.L., Dorman B., Rood R.T., O'Connell R.W., 1996, ApJ 466, 359
Da Costa G.S., Demarque P., 1982, ApJ 259, 193
Da Costa G.S., 1997, in *The Interaction between Observations and Theory*, ed. T.R. Bedding, IAU Symp. 189 (Sydney: University of Sydney), p. 193
Daou D., Wesemael F., Bergeron P., Fontaine G., Holberg J.B., 1990, ApJ 364, 242
de Boer K.S., 1982, A&AS 50, 247
de Boer K.S., 1985, A&A 142, 321
de Boer K.S., 1987, in *The 2^{nd} Conference on Faint Blue Stars*, eds. A.G.D. Philip, D.S. Hayes, J. Liebert, (L. Davis Press, Schenectady), p. 95
de Boer K.S., Schmidt J.H.K., Heber U., 1995, A&A 303, 95

de Boer K.S., Tucholke H.-J., Schmidt J.H.K., 1997, A&A 317, L23

Denissenkov P.A., Denissenkova S.N., 1990, Soviet Astron. Lett. 16, 275

Denissenkov P.A., Da Costa G. S., Norris J.E., Weiss A., 1998, A&A 333, 926

Dickens R.J., Bell R.A., Gustafsson B., 1979, ApJ 232, 428

Dixon W.V.D., Davidsen A.F., Ferguson H.C., 1994, AJ 107, 1388

Dixon W.V.D., Davidsen A.F., Ferguson H.C., 1995, ApJ 454, L47

Dixon W.V., Davidsen A.F., Dorman B., Ferguson H.C., 1996, AJ 111, 1936

Dixon W.V., Hurwitz M., 1998, ApJ 500, L29

Djorgovski S., 1993, in *Structure and Dynamics of Globular Clusters*, eds. S.G. Djorgovski & G. Meylan, ASP Conf. Ser. 50 (San Francisco), p. 373

Dorman, B., Lee Y.-W., VandenBerg D.A., 1991, ApJ 366, 115

Dorman B., 1992a, ApJS 80, 701

Dorman B., 1992b, ApJS 81, 221

Dorman B., 1997, in *The Nature of Elliptical Galaxies (2nd Stromlo Symposium)*, eds. M. Arnaboldi; G. S. Da Costa, P. Saha, ASP Conf. Ser. 116 (San Francisco), p. 195

Dorman, B., Rood, R.T., O'Connell, W.O., 1993, ApJ 419, 596

Dorman B., O'Connell R.W., Rood R.T., 1995, ApJ 442, 105

Dorman B., Shah R.Y., O'Connell R.W., et al., 1997, ApJ 480, L31

Drake J.J., Smith V.V., Suntzeff N.B., 1992, ApJ 395, L95

Driebe T., Schönberner D., Blöcker T., Herwig F., 1998, A&A 339, 123

Drilling J.S., 1996, in *Hydrogen-Deficient Stars*, eds. C.S. Jeffery, U. Heber, ASP Conf. Ser. 96 (San Francisco), p. 461

Durrell P.R., Harris W.E., 1993, AJ 105, 1420

Eber F., Butler K., 1988, A&A 202, 153

Edmonds P.D., Grindlay J.E., Cool A., et al., 1999, ApJ 516, 250

Ekberg J.O., 1993, A&AS 101, 1

Farthmann M., Dreizler S., Heber U., Hunger K., 1994, A&A 291, 919

Faulkner J., 1966, ApJ 144, 978

Ferraro F.R., Clemintini G., Fusi Pecci F., Buonanno R., Alcaino G., 1990, A&AS 84, 59

Ferraro F.R., Paltrinieri B., Fusi Pecci F., et al., 1997, ApJ 484, L145

Ferraro F.R., Paltrinieri B., Fusi Pecci F., et al., 1998, ApJ 500, 311

Finley D.S., Koester D., Basri G., 1997, ApJ 488, 375

Freeman K.C., Norris J., 1981, ARAA 19, 319

Fujimoto M.Y., Aikawa M., Kato K., 1999, ApJ 519, 733

Fusi Pecci F., Ferraro F.R., Bellazzini M., et al., 1993, AJ 105, 1145

Gies D.R., Lambert D.L., 1992, ApJ 387, 673

Gingold R.A., 1976, ApJ 204, 116

Glaspey J.W., Demers S., Moffat A.F.J., Shara M., 1985, ApJ 289, 326

Glaspey J.W., Michaud G., Moffat A.F.J., Demers S., 1989, ApJ 339, 926

Gonzalez G., Wallerstein G., 1994, AJ 108, 1325

Gonzalez G., Wallerstein G., 1998, AJ 116, 765

Graham J.A., Doremus C., 1966, AJ 73, 226

Gratton R., 1998, MNRAS 296, 739

Gratton R., Carretta E., Castelli F., 1997, A&A 314, 191

Gratton R.G., Fusi Pecci F., Carretta E., et al., 1997, ApJ 491, 749

Gray D.F., 1992, *The observation and analysis of stellar atmospheres*, Cambridge University Press, p. XIII

Greenstein J.L., 1939, ApJ 90, 387

Greenstein J.L., 1971, in *White Dwarfs*, ed. W.J. Luyten, IAU Symp. 42, (Reidel), p. 46

Greenstein G.S., Münch G., 1966, ApJ 146, 518

Greenstein G.S., Truran J.W., Cameron A.G.W., 1967, Nature 213, 871

Greggio L., Renzini A., 1990, ApJ 364, 35

Grigsby J.A., Mulliss C.L., Baer G.M., 1996, PASP 108, 953

Groenewegen M.A.T., Salaris M., 1999, A&A 348, L33

Grundahl F., Catelan M., Landsman W.B., Stetson P.B., Andersen M., 1999, ApJ 524, 242

Haas S., 1997, PhD thesis, University of Erlangen-Nürnberg, Germany

Hamuy M., Walker A.R., Suntzeff N.B., et al., 1992, PASP 104, 533

Harrington J.P., Paltogou G. 1993, ApJ 411, L103

Harris H.C., Nemec J.M., Hesser J.E., 1983, PASP 95, 256

Harris W.E., 1996, AJ 112, 1487

Harris W.E., Bell R.A., VandenBerg D.A., et al., 1997, AJ 114, 1030

Heber U., 1983, A&A 118, 39

Heber U., 1986, A&A 155, 33

Heber U., 1987, Mitt. Astron. Ges. 70, 79

Heber U., Hunger K., Jonas G., Kudritzki R.P., 1984, A&A 130, 119

Heber U., Kudritzki R.P., Caloi V., et al., 1986, A&A 162, 171

Heber U., Kudritzki R.P., 1986, A&A 169, 244

Heber U., Werner K., Drilling J.S., 1988, A&A 194,223

Heber U., Dreizler S., Werner, K., 1993, Acta Astron. 43, 337

Heber U., Moehler S., Reid I.N., 1997, in *HIPPARCOS Venice '97*, ed. B. Battrick, ESA-SP 402, p. 461

Heber U., Napiwotzki R., 1997, in *The 3rd Conf. on Faint Blue Stars*, eds. A.G.D. Philip, J. Liebert & R.A. Saffer (L. Davis Press, Schenectady), p. 439

Heitsch F., Richtler T., 1999, A&A 347, 455

Herwig F., Blöcker T., Schönberner D., El Eid M., 1997, A&A 324, L81

Hill R.S., Cheng K.-P., Smith E.P., et al., 1996, AJ 112, 601

Hollowell D., Iben I.Jr., Fujimoto M.Y., 1990, ApJ 351, 245

Horne K., 1986, PASP 98, 609

Howarth I.D., MNRAS 203, 301

Howarth I.D., Heber U., 1990 PASP 102, 912

Hoyle F., Schwarzschild M., 1955, ApJS 2, 1

Huenemoerder D.P., de Boer K.S., Code A.D., 1984, ApJ 89, 851

Hummer D.G., Mihalas D., 1988 ApJ 331, 794

Iben I. Jr., 1986, ApJ 304, 201

Iben I. Jr., 1990, ApJ 353, 215

Iben I.Jr., Rood R.T., 1970, ApJ 161, 587

Iben I.Jr., 1991, ApJS 76, 55

Iben I. Jr., Tutukov A.V., 1984, ApJS 54, 335

Iben I. Jr., Tutukov A.V., 1985, ApJS 58, 661

Iben I. Jr., Tutukov A.V., 1986, ApJ 311, 753

Iben I. Jr., Livio M., 1993, PASP 105, 1373

Iben I. Jr., Tutukov A.V., 1993, ApJ 418, 343

Ivans I., Sneden C., Kraft R.P., et al., 1999, AJ 118, 1273

Jacoby G.H., Morse J. A., Fullton L.K., Kwitter K.B., Henry R.B.C, 1997, AJ 114, 2611

Jordan S., Koester D., 1986, A&AS 65, 367

Kaluzny J., Krzemisńki W., Mazur B., Wysocka A., Stepień K., 1997, AcA 47, 249

Keenan F.P., 1992, QJRAS 33, 325

Keenan F.P., 1997, in *The 3^{rd} Conf. on Faint Blue Stars*, eds. A.G.D. Philip, J. Liebert & R.A. Saffer (L. Davis Press, Schenectady), p. 199

Kilian J., 1994, A&A 282, 867

King I.R., Anderson J., Cool A.M., Piotto G., 1998, ApJ 492, L37

Kraft R.P., 1994, PASP 106, 553

Kraft R.P., Sneden C., Langer G.E., Prosser C.F., 1992, AJ 104, 645

Kraft R.P., Sneden C., Langer G.E., Shetrone M.D., 1993, AJ 106, 1490

Kraft R.P., Sneden C., Langer G.E., Shetrone M.D., Bolte M., 1995, AJ 109, 2586

Kraft R.P., Sneden C., Smith G.H., et al., 1997, AJ 113, 279

Kraft R.P., Sneden C., Smith G.H., Shetrone M.D., Fulbright J., 1998, AJ 115, 1500

Kraft R.P., Peterson R.C., Guhathakurta P., et al., 1999, ApJ 518, L53

Kudritzki R.P., Simon K.P., Lynas-Gray A.E., Kilkenny D., Hill P.W., 1982, A&A 106, 254

Kurucz R.L., 1979, ApJS 40, 1

Kurucz R.L., 1992, in *The Stellar Populations of Galaxies*, eds. B. Barbuy & A. Renzini, IAU Symp. 149 (Kluwer:Dordrecht), 225

Lambert D.L., McWilliam A., Smith V.V., 1992, ApJ 386, 685

Landsman W.B., O'Connell R.W., Whitney J.H., et al., 1992, ApJ 395, L21

Landsman W.B., Sweigart A.V., Bohlin R.C., et al., 1996, ApJ 472, L93

Landsman W.B., Bohlin R.C., Neff S.G., et al., 1998, AJ 116, 789

Langer G.E., Kraft R.P., Carbon D.F., Friel E., Oke J.B., 1986, PASP 98, 473

Langer G.E., Hoffman R., Sneden C., 1993, PASP 105, 301

Langer G.E., Hoffman R.D., 1995, PASP 107, 1177

Langer G.E., Hoffman R.E., Zaidins C.S., 1997, PASP 109, 244

Lanz T., Hubeny I., Heap S.R. 1997, ApJ 485, 843

Layden A.C., Ritter L.A., Welch D.L., Webb T.M.A., 1999, AJ 117, 1313

Lee Y.-W., Demarque P., Zinn R., 1994, ApJ 423, 248

Leone F., Manfrè M., 1997, A&A 320, 257

Liebert J., Saffer R.A., Green E.M., 1994, AJ 107, 1408

Luck R.E., 1993, in *Luminous High-Latitude Stars*, ed. D.D. Sasselov, ASP Conf. Ser. 45 (San Francisco), p. 87

Lutz T.E., Kelker D.H., 1973, PASP 85, 573

Lyons M.A., Bates B., Kemp S.N., Davies R.D. 1995, MNRAS 277 113

Marsh T.R., Dhillon V.S., Duck S.R., 1995, MNRAS 275, 828

Martins D.H., Fraquelli D.A., 1987, ApJS 65, 83

Mathis J.S., Lamers, H.J.G.L.M., 1992, A&A 259, L39

Mazzali P.A., Lennon D.J., Pasian F., et al., 1996, A&A 316, 173

McCausland R.J.H., Conlon E.S., Dufton P.L., Keenan F.P., 1992, ApJ 394, 298

McWilliam A., Geisler D., Rich R.M., 1992, PASP 104, 1193

Mengel J.G., Norris, J., Gross P.G., 1976, ApJ 204, 488

Menzies J., 1974, MNRAS 168, 177

Michaud G., 1982, ApJ 258, 349

Michaud G., Vauclair G., Vauclair S., 1983, ApJ 267, 256

Mihalas D.M., 1966, ApJS 13, 1

Mitchell K.J., 1998, ApJ 494, 256

Moehler S., 1999, RvMA 12, p. 281

Moehler S., Richtler T., de Boer K.S., Dettmar R.J., Heber U., 1990a, A&AS 86, 53

Moehler S., Heber U., de Boer K.S., 1990b, A&A 239, 265

Moehler S., Heber U., de Boer K.S., 1994, in *Hot Stars in the Halo*, eds. S.J. Adelman, A. Upgren & C.J. Adelman, (Cambridge University Press, Cambridge), p. 217

Moehler S., Heber U., de Boer K.S., 1995a, A&A 294, 65
Moehler S., Heber U., Durrell P., 1997a, A&A 317, L83
Moehler S., Heber U., 1998, A&A 335, 985
Napiwotzki R., 1997, A&A 322, 256
Napiwotzki R., Heber U., Köppen, J., 1994, A&A 292, 239
Napiwotzki R., Green P.J., Saffer R.A., 1999, ApJ 517,399
Newell E.B., 1973, ApJS 26, 37
Newell E.B., Graham J.A., 1976, ApJ 204, 804
Norris J., 1974, ApJ 194, 109
Norris J., 1981, ApJ 248, 177
Norris J., 1987, ApJ 313, L65
Norris J., Cottrell P.L., Freeman K.C., Da Costa G.S., 1981, ApJ 244, 205
Norris J., Freeman K.C., 1982, ApJ 254, 143
Norris J., Smith G.H., 1983a, ApJ 272, 635
Norris J., Freeman K.C., Da Costa G.S., 1984, ApJ 277, 615
Norris J., Smith G.H., 1984, ApJ 287, 255
O'Connell R.W., Dorman B., Shah R.Y., et al., 1997, AJ 114, 1982
Oke J.B., 1974, ApJS 27, 21
Paczynski B., 1971, Acta Astron. 21, 1
Paltoglou G., Norris J.E., 1989, ApJ 336, 185
Paresce F., de Marchi G., Romaniello M., 1995, ApJ 440, 216
Parise R.A., Bohlin R.C., Neff S.G., et al., 1998, ApJ 501, L67
Pease F.G., 1928, PASP 40, 342
Peterson R.C., 1980, ApJ 237, L87
Peterson R.C., 1985, ApJ 289, 320
Peterson R., Crocker D.A., Rood R.T., 1994, in *Hot Stars in the Halo*, eds. S.J. Adelman, A. Upgren & C.J. Adelman, (Cambridge University Press, Cambridge), p. 319
Peterson R.C., Rees R.F., Cudworth K.M. 1995a, ApJ 443, 124
Peterson R.C., Rood R.T., Crocker D.A., 1995b, ApJ 453, 214
Pilachowski C.A., Sneden C., Green E.M., 1984, PASP 96, 932
Pilachowski C.A., Sneden C., Kraft R.P., Langer G.E., 1996, AJ 112, 545
Pintado O.I., Adelman S.J., 1993, MNRAS 264, 63
Piotto G., Sosin C., King I.R., et al., 1997, in *Advances in Stellar Evolution*, eds. Rood R.T., Renzini A., (Cambridge University Press, Cambridge), p. 84
Ponz D., Brinks E., 1986, ESO Messenger 43, 31
Pont F., Mayor M., Turon C., VandenBerg D.A. 1998, A&A 329, 87
Pritzl B., Smith H.A., Catelan M., Sweigart A.V., 2000, ApJ Letters (in press, `astro-ph/9912217`)
Pryor C., Meylan G., 1993, in *Structure and Dynamics of Globular Clusters*, eds. Djorgovski S. & Meylan G., ASP Conf Ser. 50 (San Francisco), 357
Rees R. 1996, in *Formation of the Galactic Halo ... Inside and Out*, eds. H. Morrison, A. Sarajedini, ASP Conf. Ser. 92 (San Francisco), 289
Reid I.N. 1997, AJ 114, 161
Reid I.N. 1998, AJ 115, 204
Reid I.N., Gizis J.E., 1998, AJ 116, 2929
Remillard R.A., Canizares C.R., McClintock J.E., 1980, ApJ 240, 109
Renzini A., 1985, in *Horizontal Branch and UV-Bright Stars*, ed. A.G. Davis Philip (L. Davis Press, Schenectady), p. 19
Renzini A., Voli, M., 1981, A&A 94, 175
Renzini A., Bragaglia A., Ferraro F.R., et al., 1996, ApJ 465, L23

Rich R.M., Minniti D., Liebert J., 1993, ApJ 406, 489

Rich R.M., Sosin C., Djorgovski S.G., et al., 1997, ApJ 484, L25

Richer H.B., Fahlmann G.G., Ibata R.A., et al., 1995, ApJ 451, L17

Richer H.B., Fahlmann G.G., Ibata R.A., et al., 1997, ApJ 484, 741

Rood R.T., 1973, ApJ 184, 815

Rood R.T., Crocker D.A., 1989, in *The Use of Pulsating Stars in Fundamental Problems of Astronomy*, ed. E.G. Schmidt (Cambridge University Press, Cambridge), p. 103

Rose J.A., Deng S., 1999, AJ 117, 2213

Rufener F., 1986, A&A 165, 275

Saffer R.A., Bergeron P., Koester D., Liebert J., 1994, ApJ 432, 351

Saffer R.A., Keenan F.P., Hambly N.C., Dufton P.L., Liebert J., 1997, ApJ 491, 172

Salaris M. Weiss A., 1998, A&A 335, 943

Sandage A.R., Wallerstein G., 1960, ApJ 131, 598

Sargent W.L.W., 1967, ApJ 148, L147

Sasselov D.D., Beaulieu J.P., Renault C., et al., 1997, A&A 324, 471

Savage B.D., Mathis F.S., 1979, ARAA 17,73

Schmidt J.H., Moehler S., Theissen A., de Boer K.S., 1992, in *The Atmospheres of Early-Type Stars*, eds. U. Heber & C.S. Jeffery, Lecture Notes in Physics 401 (Springer Verlag, Berlin), 254

Schönberner D., 1983, ApJ 272, 708

Schulz H., Heber U., Wegner, G., 1991, PASP 103, 435

Schwarzschild M., Härm R., 1970, ApJ 160, 341

Searle L., Rodgers A.W., 1966, ApJ 143, 809

Shapley H., 1915a, Contr. Mt. Wilson 115

Shapley H., 1915b, Contr. Mt. Wilson 116

Shapley H., 1930, *Star Clusters*, (The Maple Press Company, York, Pennsylvania, USA)

Shetrone M.D., 1996a, AJ 112, 1517

Shetrone M.D., 1996b, AJ 112, 2639

Shetrone M.D., 1997, in *Fundamental Stellar Properties: The Interaction between Observation and Theory*, IAU Symp. 189 (poster proceedings) (Kluwer, Dordrecht), p. 158

Smith G.H., 1987, PASP 99, 67

Smith G.H., Norris J., 1982, ApJ 254, 149

Smith G.H., Norris J., 1982b, ApJ 254, 594

Smith G.H., Norris J., 1983, ApJ 264, 215

Smith G.H., Shetrone M.D., Bell R.A., Churchill C.W., Briley M.M., 1996, AJ 112, 1511

Smith G.H., Shetrone M.D., Briley M.M., Churchill C.W., Bell R.A., 1997, PASP 109, 236

Smith V.V., Cunha K., Lambert D.L., 1995, AJ 110, 2827

Sneden C., Kraft R.P., Prosser C. F., Langer G.E., 1991, AJ 102, 2001

Sneden C., Kraft R.P., Prosser C.F., Langer G.E., 1992, AJ 104, 2121

Sneden C., Kraft R.P., Shetrone M.D., et al., 1997, AJ 114, 1964

Sosin C., Dorman B., Djorgovski S.G., et al., 1997a, ApJ 480, L35

Stecher T., Cornett R.H., Greason M.R., et al., 1997, PASP 109, 584

Steffen M., Szczerba R., Men'shchikov A., Schönberner D. 1997, A&AS 126, 39

Stoeckley R., Greenstein J.L., 1968, ApJ 154, 909

Stone R.P., 1977, ApJ 218, 767

Storm J., Carney B.W., Latham D.W., 1994, A&A 290, 443

Strocke G.W., 1967, in *Handbuch der Physik*, ed. S. Flügge, (Springer Verlag, Berlin) Vol. 29, p. 426

Strom S.E., Strom K.M., 1970, ApJ 159, 195

Strom S.E., Strom K.M., Rood R.T., Iben I.Jr., 1970, A&A 8, 243

Suntzeff N.B. 1981, ApJS 47, 1

Suntzeff N.B. 1993, in *The Globular Cluster-Galaxy Connection*, eds. G.H. Smith & J.P. Brodie, ASP Conf. Ser. 48 (San Francisco), p. 167

Suntzeff N.B., Smith V.V., 1991, ApJ 381, 160

Sweigart A.V., 1987, ApJS 65, 95

Sweigart A.V., 1994, in *Hot Stars in the Galactic Halo*, eds. S. Adelman, A. Upgren, C.J. Adelman, (Cambridge University Press, Cambridge), p. 17

Sweigart A.V., 1997a, ApJ 474, L23

Sweigart A.V. 1997b, in *The 3^{rd} Conf. on Faint Blue Stars*, eds. A.G.D. Philip, J. Liebert & R.A. Saffer (L. Davis Press, Schenectady), p. 3

Sweigart A.V. 1998, to appear in *New Views on the Magellanic Clouds*, eds. Y.-H. Chu, J. Hesser & N. Suntzeff, IAU Symp. 190 ASP Conf. Ser. (San Francisco)

Sweigart A.V., Mengel J.G., Demarque P., 1974, A&A 30, 13

Sweigart A.V., Gross P.G., 1974, ApJ, 190, 101

Sweigart A.V., Gross P.G., 1976, ApJS 32, 367

Sweigart A.V., Mengel J.G., 1979, ApJ 229, 624

Sweigart A.V., Catelan M., 1998, ApJ 501, L63

Sweigart A.V., Catelan M., 1999, in prep.

ten Bruggencate P., 1927, *Sternhaufen*, (Julius Springer Verlag, Berlin)

Theissen A., Moehler S., Heber U., de Boer K.S., 1993, A&A 273, 524

Theissen A., Moehler S., Heber U., Schmidt J.H.K., de Boer K.S., 1995, A&A 298, 577

Traving G., 1962, ApJ 135, 439

Trefzger D.V., Langer G.E., Carbon D.F., Suntzeff N.B., Kraft R.P., 1983, ApJ 266, 144

Tuchman Y., 1985, ApJ 288, 248

Tucholke H.-J., 1992a, A&AS 93, 293

Tucholke H.-J., 1992b, A&AS 93, 311

Tüg H., 1977, ESO Messenger 11, 7

VandenBerg D.A., Swenson F.J., Rogers F.J., Iglesias C.A., Alexander D.R., 2000, ApJ subm.

van Winckel H., Waelkens C., Waters L.B.F.M., 1995, A&A 293, L25

Vassiliadis E., Wood P.R., 1993, ApJ 413, 641

Villeneuve B., Wesemael F., Fontaine G., 1995, ApJ 450, 851

Vink J.S., Heap S.R., Sweigart A.V., et al., 1999, A&A 345, 109

Wallerstein G., Leep E.M., Oke J.B., 1987, AJ 93, 1137

Werner K. 1986 A&A 161, 177

Werner, K., Dreizler, S., 1996, in *Computational Astrophysics Vol. II (Stellar Physics)*, eds. R.P. Kudritzki, D. Mihalas, K. Nomoto, F.-K. Thielemann, (Springer Verlag), in press

Whitney J.H., Rood R.T., O'Connell R.W., et al., 1998, ApJ 495, 284

Yan Y., Taylor K.T., Seaton M.J., 1987, J. Phys. B 20, 6399

Zinn R., 1974, ApJ, 193, 593

Zinn R.J., Newell E.B., Gibson J.B., 1972, A&A 18, 390

Zinn R., West M.J. 1984, ApJS 55, 45

Appendix A

Evolution of low-mass stars

We present here a very brief and simplified summary of the evolution of low mass stars that should help the reader unfamiliar with this topic to better understand this thesis. It is by no means an exhaustive discussion.

Stars start their life consisting mainly of hydrogen (90% by number, 75% by mass) and helium (10% by number, 25% by mass). Energy is first created by conversion of hydrogen to helium in the core (CORE HYDROGEN BURNING). The more massive a star is at this stage the brighter it is and the shorter is the time it spends in this stage. Stars that obtain their energy from core hydrogen burning show a one-to-one relationship between effective temperature and surface gravity (at a given composition) and thus form a narrow sequence in colour-magnitude diagrams. As stars spend about 90% of their life burning hydrogen in their cores this sequence is called the **main sequence**.

During this phase the particle number in the core decreases as hydrogen is transformed into helium. As the pressure due to the gravity of the outer layers remains constant, the core contracts and heats up, thereby increasing the energy production in the core. While hydrogen vanishes at the center the core pulls adjacent regions closer and heats them up thereby starting the conversion of hydrogen to helium in these still hydrogen-rich shells (HYDROGEN SHELL BURNING). The (now inert) core continues to contract and heat, thereby increasing the temperature in the H-burning shell. This increase in shell temperature leads to an increase in energy production there and thus to an expansion of the outer regions of the star and a cooling of its surface. The star appears as a so-called **subgiant**, i.e. brighter and somewhat cooler than on the main sequence.

The cooling of the outer hydrogen layers of the star leads to the onset of convection in the stellar envelope. The convection zone extends to increasing depths thereby transporting nucleosynthesis products from the preceding main sequence phase to the surface of the star ($1^{\rm st}$ DREDGE-UP). The He core continues to grow in mass (due to the H-burning, i.e. He-producing, shell) and to contract, thereby increasing the temperature in the H-burning shell. The luminosity of the star increases dramatically and the star becomes a **red giant**. During this phase the star loses some mass.

During the red giant stage the hydrogen burning shell moves outward leaving behind an ever increasing helium core. This core still contracts and heats up. The increase in density causes electron degeneracy in the core, thereby decoupling pressure and temperature in the core. When the core has reached a mass of about 0.45 – 0.50 $M_\odot$ temperatures are sufficient to allow the conversion of helium into carbon and oxygen (HELIUM CORE BURNING, 3α PROCESS). Due to the electron degeneracy in the core region the increase in temperature caused by the helium core burning is not compensated by an increase in pressure and subsequent expansion of the core. Instead the energy production increases due to the increased temperature, resulting in a runaway effect (HELIUM CORE FLASH). At sufficiently high temperatures the electron degeneracy is removed and the core starts to cool and expand, thereby decreasing the temperature at the base of the hydrogen shell. The star is now quietly burning helium in the central region of its core and hydrogen in a shell. Due to the cooling at the base of the hydrogen

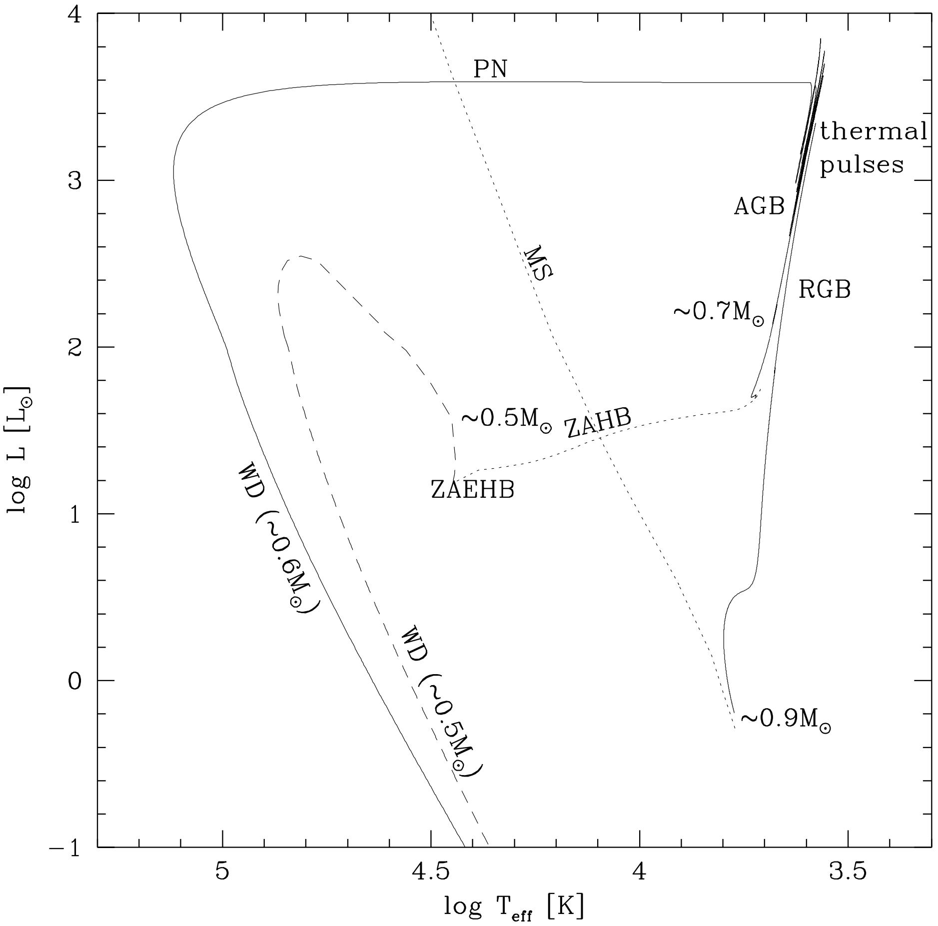

Fig. 48. Schematic evolution of a low-mass star (solid line). The dotted lines mark sequences of stars with varying mass, but same evolutionary stage (main sequence resp. zero-age horizontal branch). The dashed line gives the further evolution of an extreme horizontal branch star. The acronyms stand for main-sequence (**MS**), red giant branch (**RGB**), zero-age horizontal branch (**ZAHB**), zero-age extended HB (**ZAEHB**), asymptotic giant branch (**AGB**), planetary nebula stage (**PN**), white dwarf (**WD**). The mass values noted are meant as indication for the stellar mass at the respective evolutionary stage, not as precise values.

shell, however, the energy production there decreases and the outer envelopes of the star contract and heat up. Stars in this stage are called **horizontal branch** stars for reasons described in Chapter 1.

The zero-age horizontal branch marks the position where the horizontal branch stars have settled down and started to quietly burn helium in the core and hydrogen in a shell. Such stars are discussed in much more detail in Chapters 3, 4, and 5. They have a roughly constant core mass but a hydrogen envelope of varying thickness. Stars with more massive hydrogen envelopes are cooler than stars with less massive ones. The hottest horizontal branch stars have so little hydrogen envelope left that they cannot sustain hydrogen shell burning.

The sequence of events following now resembles that described above for core hydrogen burning: After helium vanishes in the core (terminal-age horizontal branch) helium burning starts in a shell and the star again evolves to the red giant domain. In colour-magnitude diagrams these stars populate a sequence very close to, but slightly brighter than the red giant branch, which is called **asymptotic giant branch**.

If the stars are massive enough they will evolve far enough up the asymptotic giant branch to experience so-called THERMAL PULSES caused by the alternating burning of the hydrogen and helium shells, which lead to increased mass loss. During such thermal pulses the convection zone may reach deep enough into the interior to access the products of the helium burning and move them to the surface (3^{rd} DREDGE-UP). The 2^{nd} DREDGE-UP happens early on the asymptotic giant branch and reaches only the product of the hydrogen burning shell, which lies farther out. Stars discussed in this thesis usually leave the AGB before the third dredge-up due to their low mass (see Chapters 6 and 7).

The low-mass stars discussed here are not massive enough to achieve temperatures in the core that allow the conversion of carbon into neon and magnesium. Due to the mass loss that takes place on the asymptotic giant branch (and is stronger than on the red giant branch as the stars are more extended now) the star at some time has lost so much mass that the hydrogen burning shell is hardly covered. Thus the hot core becomes increasingly exposed (as the two shells continue to burn outward and thereby still increase the core mass) and a hot stellar wind sets in. The material ejected on the asymptotic giant branch is compressed and heated by the remaining core, which continues to contract and heat (as no core energy sources are left except gravitational energy). Thus the compressed ejected material will be excited and will become visible as a so-called **planetary nebula**. During this phase degeneracy in the core sets in.

After the shell sources are extinguished the star continues to contract until the degeneracy in the core effectively stops any further contraction. The gravitational energy is not enough to sustain the star's luminosity and the star thus starts to cool and become fainter, having entered the final stage of its life as **white dwarf**. White dwarfs in globular clusters are the topic of Chapter 8.

Stars not massive enough to sustain hydrogen shell burning on the horizontal branch do not evolve to the asymptotic giant branch but evolve directly to white dwarfs.

Appendix B

Photometric systems and definitions

Photometric data used in this work are obtained either in the Strömgren (*uvby*) or Johnson (*UBV*) filter system, where the letters denote the filters (see also Fig. 49). Apparent brightness and colour are defined as follows

$$m_X = X = -2.5 \ \log \int_0^\infty F_{\lambda,obs.} X_{(\lambda)} d\lambda$$

and

$$m_X - m_Y = X - Y = -2.5 \ \log \frac{\int_0^\infty F_\lambda X_{(\lambda)} d\lambda}{\int_0^\infty F_\lambda Y_{(\lambda)} d\lambda} + const_{X-Y}$$

with $X_{(\lambda)}$ being the transmission curve of filter X. The zero points are defined in a way that colours of 0 correspond to stars with $T_{\rm eff} \approx 9500$ K and *not* to a flat spectrum. Usually $m_V/m_B/m_u$, etc. are shortened to $V/B/u$ and correspondingly $B-V$ is used for $m_B - m_V$. Fig. 49 shows how different stellar spectra yield different colours and that colours, which measure the slope between two regions of the spectrum, often can be used as temperature indicators. Hot stars, whose flux increases to shorter wavelengths, thus appear "bluer" than cooler, "redder" stars. Astronomers distinguish between apparent brightness (e.g. m_V) and absolute brightness (M_V, the brightness that a star would have if it were at a distance of 10 pc, i.e. 32.6 light years, from us):

$$\begin{aligned} m_V - M_V = \ (m-M)_V &= 5(\log d - 1) + A_V \\ (m-M)_0 &= 5(\log d - 1) \end{aligned}$$

where d is the distance to the star in pc and A_V notes the interstellar extinction, i.e. absorption and scattering of the stellar light by interstellar material (gas and dust). $(m-M)_V$ and $(m-M)_0$ are the apparent resp. true distance modulus. As the interstellar extinction is wavelength dependent it also changes the colour of a star and the colour excess (e.g. for $B-V$) is defined by

$$E_{\rm B-V} = (B-V)_{observed} - (B-V)_{true}.$$

Usually photometric observations of stars in globular clusters are used to produce so-called colour-magnitude diagrams, where the apparent brightness is plotted vs. the colour of the stars. Fig. 1 (p. 5) shows an exemplary colour-magnitude diagram.

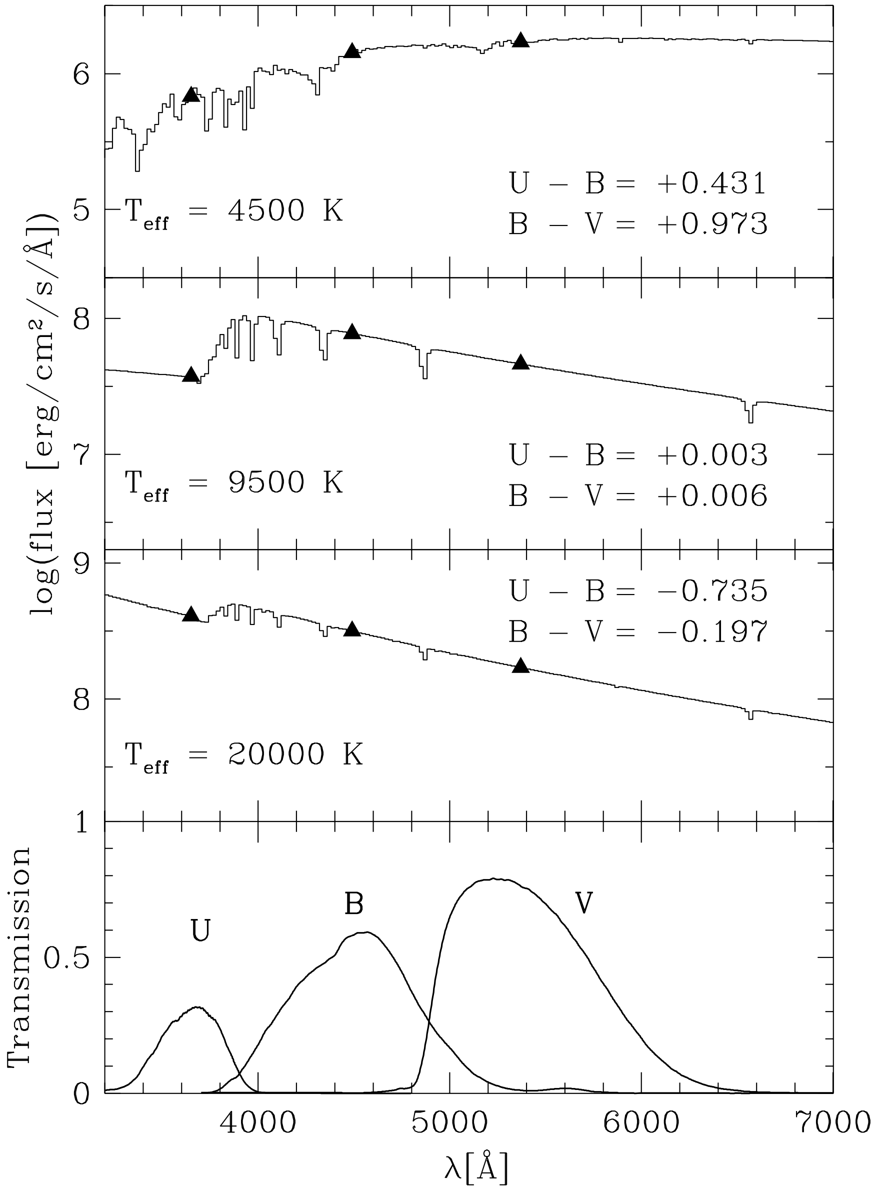

Fig. 49. The Johnson photometric filter system (*UBV*). Shown are theoretical stellar flux distributions for a metallicity of [M/H] = −2 and solar helium content. The colours obtained from photometric observations of stars with the given effective temperatures are noted and the transmission curves of the filters are shown.

Appendix C

Model atmospheres

"The remarkable nature of stars is transmitted to us by the light they send. The light escapes from the outer layers of the star – called, by definition, the atmosphere. The complete atmosphere of a star can be viewed comprehensively as a transition from the stellar interior to the interstellar medium. And yet almost the whole visible spectrum comes from a relatively thin part called the photosphere. Obviously we cannot disconnect the photosphere from the adjacent portions of the atmosphere, but in actual fact it is the only region we can study extensively for most stars." (Gray, 1992)

We usually discuss stars in this work in terms of (logarithmic) surface gravity, $\log g$ [cm/s^2], and effective temperature, $T_{\rm eff}$ [K], which are defined by

$$g = G \cdot \frac{M}{R^2}$$

and

$$\int_0^\infty F_\nu d\nu = \sigma_{\rm SB} T_{\rm eff}^4 \qquad \text{(Stefan-Boltzmann law)}$$

The definition of $T_{\rm eff}$ is linked to the total radiant power emitted by a star per unit area (= flux F) and $T_{\rm eff}$ thus corresponds to the temperature of a blackbody emitting the same total flux as the star. The stellar flux distribution F_ν as a function of frequency, however, will usually differ strongly from that of a blackbody.

A model atmosphere has to describe the transport of energy to the radiating surface under the constraints imposed by the conservations of energy, momentum, and particle number. In principle three methods of energy transport are possible: conduction (usually negligible in stellar atmospheres), convection and radiative transport. For most of the stars discussed here energy is transported through the atmosphere by radiation. To facilitate the necessary calculations the following assumptions are made:

1. plane-parallel geometry, i.e. all physical variables depend only on one space coordinate.
2. hydrostatic equilibrium, i.e. no large scale accelerations comparable to the surface gravity take place in the atmosphere (no significant mass loss, no pulsations). This also means that the pressure gradient (buoyancy) at any point of the atmosphere (e.g. gas pressure, radiation pressure) has to counterbalance the gravity, thereby constraining the pressure and density distribution within the atmosphere.
3. fine structure (e.g. starspots) and magnetic fields can be ignored.

We need an equation that describes the interaction of the energy with the atmospheric matter and the resulting changes in energy distribution. Astronomers generally use the specific intensity I_ν when calculating radiative transport which is per definition constant along a ray if *neither sources nor sinks of energy* are present. The flux then derives from this intensity

$$F_\nu = \oint I_\nu \cos\theta d\omega$$

where θ is the angle between the line-of-sight to the observer and the normal on the stellar surface and ω is the solid angle, which is integrated over all directions. In a stellar atmosphere energy will be absorbed and emitted by the atoms/ions and the intensity will thus change along the way. Concerning absorption one has to distinguish between *true absorption* (coefficient κ_a, a photon is absorbed by an atom/ion and its energy is at least partly transformed into, e.g., kinetic energy, i.e. the photon, that is re-emitted some time later differs from the absorbed one in energy and direction) and *scattering* (κ_s, the re-emitted photon has the same energy as the absorbed one, but a different direction). The most important scattering process in hot stars is Thomson scattering of free electrons (all other scattering processes are ignored here). Energy sources are *thermal emission* (ε_{th}) and *re-emission of scattered photons* (ε_s).

Under the assumption of strict thermal equilibrium (no scattering) the thermal emission coefficient ε_{th} and the true absorption coefficient κ_a (both per unit mass) are linked by Kirchhoff's law ($\varepsilon_{th(\nu)} = \kappa_{a(\nu)}B_{(\nu,T)}$) with the Planck function $B_{(\nu,T)}$. While the radiation field in stellar atmospheres is usually not in strict thermal equilibrium, it is often a good assumption that it is in thermal equilibrium at the *local* temperature. In this case (local thermal equilibrium = LTE) ε_{th} and κ_a do not depend on the radiation field but only on the state of the *local* matter, which greatly facilitates the calculations of radiative transport. Most of the stars discussed here are in a temperature–gravity range where LTE is a valid approximation for the calculation of model atmospheres (Napiwotzki 1997, see Sect. 6.2.1 for more details).

The change dI_ν in intensity over a matter element ρds can be described by the *radiative transfer equation* as

$$\begin{aligned} dI_\nu &= \rho\varepsilon_\nu ds - I_\nu\kappa_\nu\rho ds \\ \varepsilon_\nu &= \varepsilon_{th(\nu)} + \varepsilon_{s(\nu)} \\ \kappa_\nu &= \kappa_{a(\nu)} + \kappa_{s(\nu)} \end{aligned}$$

The absorption term $\kappa_\nu\rho ds$ is dimensionless and is related to the *optical depth* $d\tau_\nu$:

$$\begin{aligned} v &= \cos\theta \\ d\tau_\nu &= -\rho\kappa_\nu v ds = -\rho\kappa_\nu dx \\ v\frac{dI_\nu}{d\tau_\nu} &= \frac{\varepsilon_\nu}{\kappa_\nu} - I_\nu \end{aligned}$$

Without any scattering (i.e. strict thermal equilibrium)

$$\begin{aligned} v\frac{dI_\nu}{d\tau_\nu} &= \frac{\varepsilon_{th(\nu)}}{\kappa_{a(\nu)}} - I_\nu \\ &= B_{(\nu,T)} - I_\nu \end{aligned}$$

the radiative transfer equation can easily be solved for I_ν at a given temperature. In the more general LTE case a source function S is defined as

$$\begin{aligned} S_\nu &= \frac{\varepsilon_\nu}{\kappa_\nu} = \frac{\varepsilon_{th(\nu)} + \varepsilon_{s(\nu)}}{\kappa_{a(\nu)} + \kappa_{s(\nu)}} \\ v\frac{dI_\nu}{d\tau_\nu} &= S_\nu - I_\nu, \end{aligned}$$

which due to the scattering processes also depends on the radiation field. Since Thomson scattering is isotropic we can use

$$\varepsilon_{s(\nu)} = \kappa_{s(\nu)} J_\nu$$

with the mean intensity J_ν defined as

$$J_\nu = \frac{\oint I_\nu d\omega}{\oint d\omega}$$

This assumption allows to simplify the source function S_ν to

$$\begin{aligned} S_\nu &= \frac{\varepsilon_{th(\nu)}}{\kappa_{a(\nu)} + \kappa_{s(\nu)}} + \frac{\kappa_{s(\nu)}}{\kappa_{a(\nu)} + \kappa_{s(\nu)}} J_\nu \\ &= \frac{\kappa_{a(\nu)}}{\kappa_{a(\nu)} + \kappa_{s(\nu)}} \frac{\varepsilon_{th(\nu)}}{\kappa_{a(\nu)}} + \frac{\kappa_{s(\nu)}}{\kappa_{a(\nu)} + \kappa_{s(\nu)}} J_\nu \\ &= \frac{\kappa_{a(\nu)}}{\kappa_{a(\nu)} + \kappa_{s(\nu)}} B_{(\nu,T)} + \frac{\kappa_{s(\nu)}}{\kappa_{a(\nu)} + \kappa_{s(\nu)}} J_\nu \end{aligned}$$

The general form of the radiative transfer equation has the formal solution

$$I_{\nu(v,\tau_\nu)} = I_{\nu(v,\tau_{1\nu})} e^{(\tau_\nu - \tau_{1\nu})/v} - \int_{\tau_{1\nu}}^{\tau_\nu} S_{\nu(\tau'_\nu)} e^{(\tau_\nu - \tau'_\nu)/v} \frac{d\tau'_\nu}{v},$$

which can be solved numerically and yields $I_{\nu(\tau_\nu)}$ once $S_{\nu(\tau_\nu)}$ is known. This requires the knowledge of ε_ν and κ_ν, which in turn depend on the temperature. So before we can really employ the formal solution for $I_{\nu(\tau_\nu)}$ we have to know the temperature distribution within the atmosphere.

A first estimate of the temperature distribution for a given $T_{\rm eff}$ and $\log g$ can be obtained from a so-called *grey atmosphere* for which $\kappa_a, \kappa_s \neq f_{(\nu)}$ is assumed. As absorption coefficient κ the *Rosseland* absorption coefficient κ_R

$$\frac{1}{\kappa_R} = \frac{\pi}{4\sigma_{\rm SB} T^3} \int_0^\infty \frac{dB_\nu}{dT} \frac{d\nu}{\kappa_\nu}$$

is often used, which is formally the harmonic mean of κ_ν with the weighting function dB_ν/dT. It can easily be calculated once κ_ν is known from the atomic data. Integrating over ν yields $J = S$ and simplifies the radiative transfer equation to

$$v \frac{dI}{d\tau_R} = J - I$$

Assuming that the asymptotic solution obtained for J for large optical depths is valid for the whole atmosphere (Eddington approximation) and strict LTE yields an approximate temperature distribution

$$T^4_{(\tau)} = \frac{3}{4} T^4_{\rm eff} (\tau + \frac{2}{3})$$

The approximate temperature distribution obtained that way is used to solve the hydrostatic equation

$$\frac{dP}{dx} = g\rho \qquad \Leftrightarrow \qquad \frac{dP}{d\tau_R} = g/\kappa_R$$

which constrains the pressure and density distribution within the stellar atmosphere.

The pressure in the atmospheric layers of a star is usually small ($\leq 1 N/m^2$) which allows the use of the perfect gas law. If the gas is (at least locally) in thermal equilibrium (i.e. collisional interactions

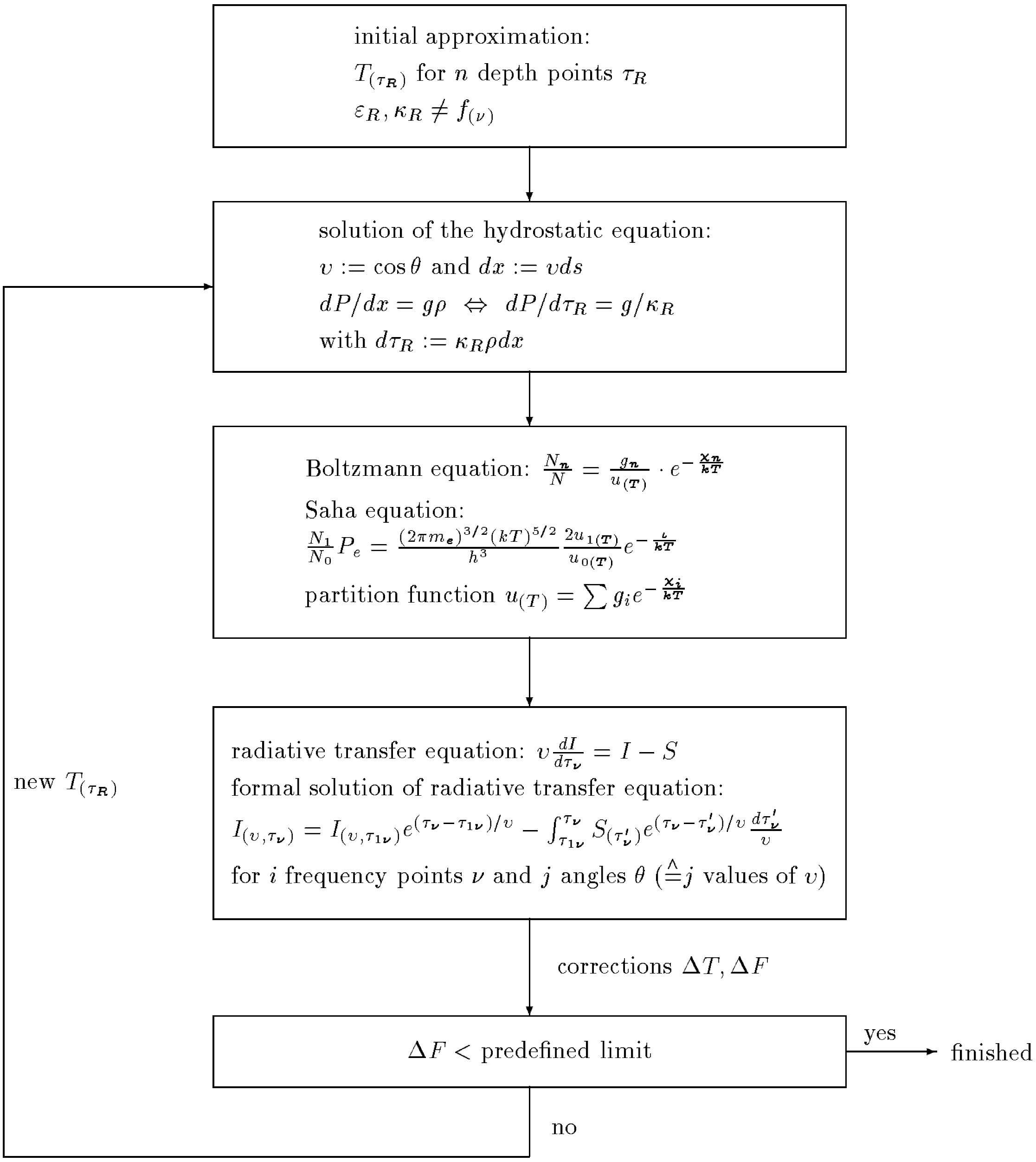

Fig. 50. Simplified diagram for the calculation of LTE model atmospheres

between atoms/ions dominate over radiative ones) the relative population of excitation and ionization levels of its atoms can be described by the Boltzmann equation (number N_n of atoms per unit volume at excitation level n compared to total number N of atoms per unit volume of this element)

$$\frac{N_n}{N} = \frac{g_n}{u_{(T)}} \cdot e^{-\frac{\chi_n}{kT}}$$

and the Saha equation (number of singly ionized to neutral atoms per unit volume of an element)

$$\frac{N_1}{N_0} P_e = \frac{(2\pi m_e)^{3/2}(kT)^{5/2}}{h^3} \frac{2u_{1(T)}}{u_{0(T)}} e^{-\frac{\iota_1}{kT}}$$

ι and χ are the ionization and excitation potentials and P_e is the electron pressure ($= N_e kT$ with number of electrons per unit volume N_e). $u_{(T)}$ is the partition function defined as

$$u_{(T)} = \sum_i g_i e^{-\frac{\chi_i}{kT}},$$

with the statistical weights g_i of the excitation states i. u_1 and u_0 are the ionic resp. neutral partition function.

Knowing the temperature and pressure distribution within the atmosphere thus allows to calculate the relative occupation numbers of the various excitation (Boltzmann equation) and ionization states (Saha equation). From those numbers the correct (frequency-dependent) absorption coefficients can be derived, which are then used for the formal solution of the radiative transfer equation for as many frequencies as required to realistically describe the entire flux distribution. This solution yields a new temperature distribution and thus a new total flux, which has to fulfil the original definition for T_{eff}, i.e.

$$\int F_{new(\nu)} d\nu = \sigma_{\text{SB}} T^4_{\text{eff},orig}$$

at all depth points. If the integrated flux F is not constant at all depth points (within a predefined accuracy) corrections for the temperature distribution are derived and the iteration is repeated with the new temperature structure. The spectrum that finally emerges from the model atmosphere is then calculated from the definition of the flux.

The absorption process can affect the continuum only (free-free and bound-free transitions) or result in spectral lines (bound-bound transitions). The *shape* of the spectral lines is affected by various broadening mechanisms (besides the natural line width) that can give us information on the state of the atmosphere:

1. *Doppler broadening* is caused by the thermal motion of the atoms/ions
2. *Pressure broadening* becomes important if the time between two collisions is less than the lifetime of the state of the atom/ion. Two types of pressure broadening play a rôle for the spectroscopic analysis of hot stars:

   quadratic Stark effect: The perturbing particle distorts the electron distribution of the atom/ion and thus creates a dipole moment. The interaction of this induced dipole moment with the electric field of the perturbing particle is then $\sim E^2$ (E being the electric field strength). The perturbers in this case are typically electrons and lines of almost all atoms/ions, especially in hot stars, are affected.

   linear Stark effect: Atoms/Ions that have an inherent dipole moment (like H I or He II) show an interaction with the perturber (typically protons or electrons) that is $\sim E$.
3. *Rotational broadening* is caused by the systematic variation of Doppler shifts due to the rotation of the star and will affect all lines.